NATIONAL KAPODISTRIAN UNIVERSITY OF ATHENS
SCHOOL OF SCIENCE
DEPARTMENT OF GEOLOGY AND GEOENVIRONMENT
SECTION OF MINERALOGY AND PETROLOGY

BSc Thesis

New petrological data and a revised interpretation of the Styra-Ochi Unit in central Evia Island, Greece

Pavlos Zampras
Registration no.: 1114201900151

Supervisors:
Dr. P. Pomonis (Professor)
Dr. D. Kostopoulos (Associate Professor)

Athens, 2024

Table of Contents

Introduction:

The study and research area are located in Central Evia near the detachment fault in Octonia-Achladeri-Avlonario. It is above the fault (Upper Plate) in the village of Trachili and mainly in the metamorphic core excavated below the fault (Lower Plate) in the area of Petries.

The purpose of this paper is to review these areas, particularly the area in the Lower Plate where the Styra-Ochi unit occurs, now named Makrotantalo-Ochi. Chemical analyses of whole rock near the Petries survey area showed that the rocks are not typical of schist rock. Evidence of chemical elements such as sodium and suspected sodic-clinopyroxenes-amphiboles suggests that these minerals are only formed in acidic, granitoid, and alkaline rocks. This section is characterized by high-pressure, low-temperature metamorphism that began about 50 million years ago.

The rocks found in the central Evia region are granitic, mafic mainly metavolcanic, limestone, marble, clay, and volcano-sedimentary complex. The underlying rocks forming the crystalline basement are Carboniferous-Permian orthogneisses, which seem to have formed prior to the magmatism of the subduction zone between the overlying Laurasia and the underlying PaleoTethys. The age of the magmatism is the same as that of the Pelagonian, indicating that it is the result of Triassic magmatism due to partial melting of the mantle wedge of the overlying continental block due to dehydration of the oceanic lithospheric plate. The rise of the asthenospheric mantle created thermal events, and the period is identical to the formation of two oceans, Pindos and Axios.

This event introduces us to the second type of rock to be examined, which is metabasalts. Observations of metabasaltic veins and sills located within the granitic host rock indicate extensional eruption and simultaneous generation of sedimentary rocks with ages around the Triassic. The partial melting of these rocks created the volcano-sedimentary complex in the Upper Plate. In general, the existence of acid and mafic magmatism must be related to a continental rift geotectonic setting, where the tectonic setting is a combination of post-tectonic and within-plate granites, mainly towards southern Evia.

Methodology:

In the thin, polished sections, specific points for point analysis using transmitted light microscopy were carefully chosen. The different parts of the microscope are depicted in Figure 1. Each sample consists of a thin slice of rock, 30 μm thick, which will be affixed with resin to a glass slide. The principles of light physics enable us to identify minerals. The absorption or non-absorption of radiation of a particular wavelength results in coloration. Variances in the speed of light as it travels through different mediums (the sample) create relief, while variations in transmission speed between fast and slow rays produce polarization colors. When the polarization direction aligns with a crystallographic axis, the quenching effect occurs. In transmitted light microscopy, we observe minerals that are anisotropic due to their structure, resulting in properties that change in all three directions. The crystallization system of the minerals impacts their optical properties. Minerals in the monoclinic, triclinic, and orthorhombic systems exhibit three colors of pleochroism, while those in the trigonal, hexagonal, and tetragonal systems exhibit two colors. Due to their symmetry, minerals of the cubic system are permanently quenched.

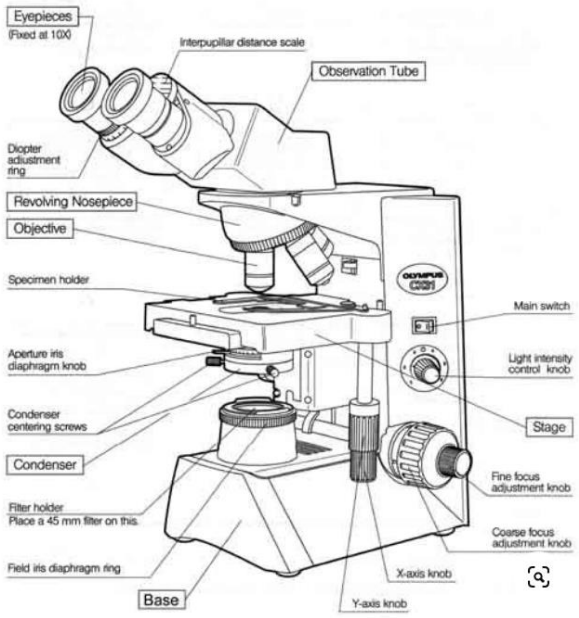

Figure 1: Parts of an optical microscope.
Aggeliki Papoutsa (course leader of EKPA: Methods of rock and ore analysis - Fluid inclusions), et al. 2023

The X-ray diffraction in crystalline powder (PXRD Powder XRays Diffraction) method is used for qualitative mineral diagnostic analysis of rock samples. The sample is first powdered and then subjected to irradiation by an electron beam in the X-ray spectrum of a specific wavelength λ, under specific geometric arrangements and conditions. Throughout the analysis, the sample is continuously scanned, and the reflected diffracted radiation (at an angle of 2θ) is measured and recorded as the angle of incidence θ of the X-ray beam on the sample is continuously varied at a fixed and constant rate. Essentially, a continuous diagram records the positions (i.e., the angles 2θ and the corresponding spacings d-spacings) at which the X-rays are diffracted by the crystal lattice of the sample grains. This process is schematically represented in figure 2. The recorded diagram is known as the radiation diagram. The evaluation and mineralogical identifications are made on the X-ray diagram with the assistance of the EVA software program, as well as certain useful characteristics of the reflections (peaks), respectively.

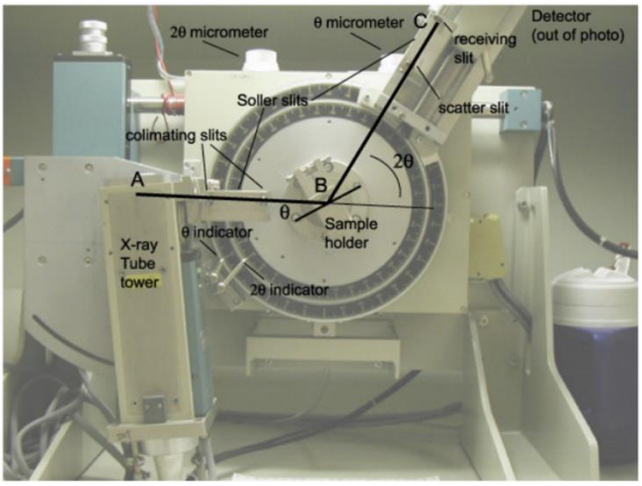

Figure 2: XRD during operation
Aggeliki Papoutsa (course leader of EKPA: Methods of rock and ore analysis - Fluid inclusions), et al. 2023

The mineral samples underwent chemical analysis at the University of Mainz in Germany utilizing a JEOL JXA 8200 Electron Microprobe. The microanalyzer utilizes a filament to generate an electron beam, which is then focused by a series of electromagnetic lenses and directed at the sample. This process generates X-rays, which are diffracted into the analytical crystal within the spectrometer.

Chapter 1

Unit 1.1 General Geology

The plate tectonic model here provides valuable insights into dynamic plate boundaries and synthetic paleo-iso-chrons, yielding new information on ocean widths, the timing of major tectonic events, and the processes responsible for their existence and disappearance.

The rift of a ribbon of superterranes along the Gondwana margin led to the rollback of the Rheic and Asiatic oceanic slabs, resulting in the opening of the PaleoTethys as a back-arc basin. In the early Paleozoic era, constraints for PaleoTethys opening emerged during the Late Ordovician and Silurian periods. Leading to the splitting of the Hun terranes into the European and Asiatic components. Subsequently, the European and Asiatic Hunic terranes were transferred and dismembered along the Eurasian margin. The Variscan orogeny in Europe did not result from a continent/ continent collision but rather from the accretion of these terranes. (Stampfli et al., 2002)

The deformation of surrounding foreland basins provides a well-recorded account of the Gondwana-Laurasia collision during the Late Carboniferous period. The ultimate closure of PaleoTethys in the Tethyan domain occurred during the Cimmerian (Triassic to Jurassic) orogenic cycle (Fig. 3). The Late Carboniferous to Early Permian calc-alkaline intrusions and volcanism observed in the Variscan Alpine Mediterranean domain are linked to the northward subduction of the PaleoTethys. The subsequent rollback of the PaleoTethys slab precipitated the collapse of the pre-existing Variscan cordillera and facilitated the opening of the NeoTethys. Notably, the NeoTethys superseded the PaleoTethys while Pangea remained stable during the Permian and Triassic periods, underscoring the significant impact of slab pull forces on oceanic evolution and, consequently, plate distribution (Fig. 4) (Stampfli et al., 2002).

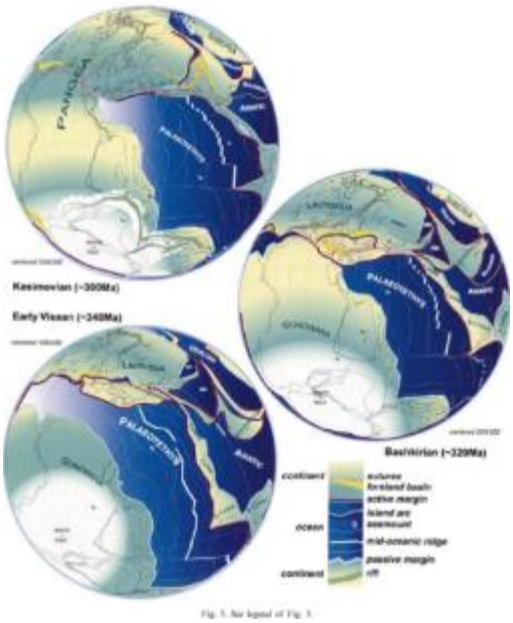

Figure 3: Gondwana-Laurasia collision in the Late Carboniferous, Stampfli et al., 2002

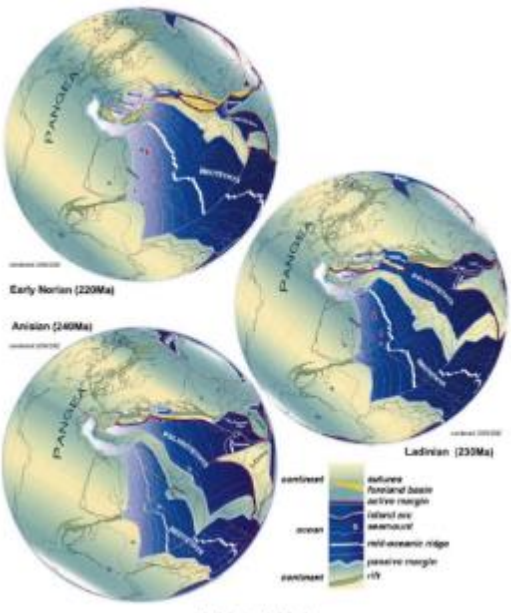

Figure 4: The replacement of the PaleoTethys from NeoTethys, Stampfli et al., 2002

The significant changes in plate tectonics from the Late Jurassic to Early Cretaceous are linked to the diachronous subduction of the active NeoTethys ridge along the northern margin of Eurasia. The formation of the Alpides mountain range (Alps, Carpathian and Balkans) is directly linked to the evolution of the Maliac-Meliata/Vardar region and the southward subduction of the Maliac-Meliata slab. The orogenic prism moved from the Austro-Carpathian area to the Alpine Tethys and extended westward to the western Alps in Late Cretaceous time. In contrast, the Tethysides system is associated with the north-directed subduction of the NeoTethys and the back-arc basins (e.g., Semail and Spongtang). The large NeoTethys slab was entirely subducted, leaving little ophiolitic traces; all NeoTethyan ophiolites being derived from Cretaceous back-arc basins. (Stampfli et al., 2002)

The subduction of the NeoTethys resulted in the opening of the Argo Abyssal Plain and the detachment of the Argo-Burma terrane from Australia, possibly along with the Indian plate. The subsequent Valanginian rotation of east Gondwana relative to Africa led to intra-oceanic subduction within the NeoTethys south of Iran and the onset of spreading of the Semail Marianna-type back-arc ocean. (Stampfli et al., 2002)

Unit 1.2 Subduction depth-thickness data

The Cimmerian blocks mentioned earlier are a key focus of this thesis as they help us better understand the Alpine Paleogeographic Evolution and Nappe Stacking of the Hellenides. This terrane detached from a passive margin by slab pull, consists of two passive margins. Only after the subduction of the active ridge, does the slab pull become strong enough to detach a terrane. The sedimentary record of the terrane provides timing information about the rifting of both oceans, thus giving us a good control on the spreading rate. (Stampfli et al., 2002)

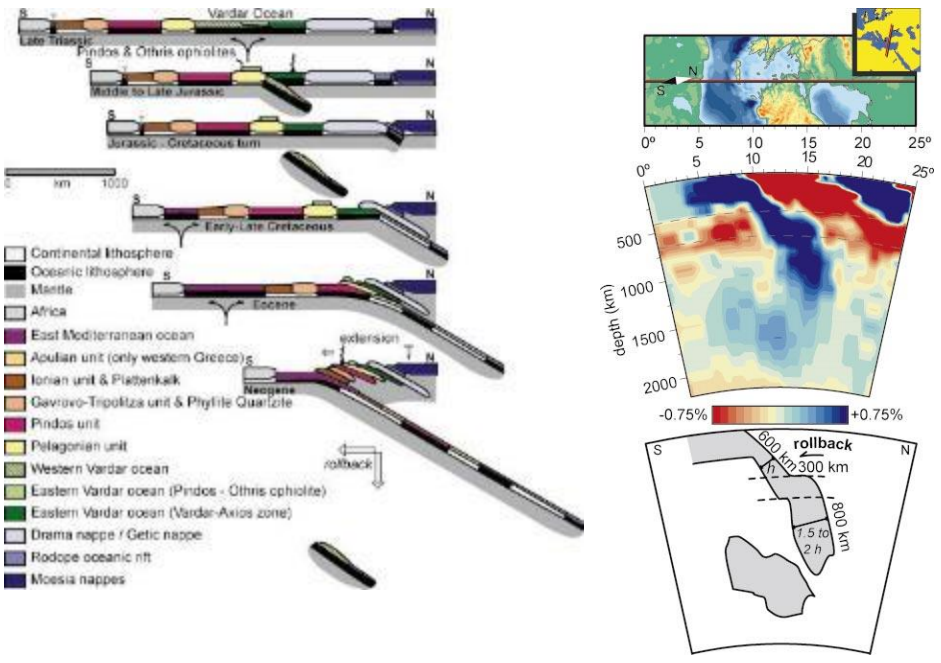

Figure 5: Schematic Subduction model and Geophysical tomography, van Hinsbergen et al., 2005

Understanding this model gives us specific data about the slab rollback, under the Aegean, which is caused by the pull forces of the plate. The tomographic model of Bijwaard in 1998, gives us a cross-section of the Aegean mantle, parallel to the convergence direction inferred from the nappe stack (Fig. 5).

This section uncovers a high-velocity anomaly extending to a depth of 1500 km, with well-defined spatial characteristics. Researchers, such as De Jonge in 1994, have shown that interpreting these anomalies as images of subducted lithosphere is justified. The upper mantle segment of the dipping slab measures 600 km in length. The tomographic image further suggests that the slab is horizontally extended over the 660 km discontinuity for 300 km, suggesting a possible 300 km slab rollback, which aligns with the late Cenozoic north-south extension in the Aegean region. In the lower mantle, the anomaly spans 800 km in length and is 1.5 to 2 times thicker than the upper mantle slab. If we consider only slab thickening, disregarding thermal effects from mantle cooling surrounding the subducted slab, the entire slab anomaly could represent 2100–2500 km of convergence. An approximate two-fold increase in the thickness of the subducted lithosphere in the lower mantle concurs with the findings of Hafkenscheid (2004), who accounted for temperature effects in predicting the present thermal volume of subducted Aegean lithosphere. The anomaly model proposed by Bijwaard et al. (1998), Faccenna et al. (2003) interpreted the anomaly as a result of drag folding of the slab at the 660 km discontinuity in response to northward trench motion.

Unit 1.3 Explanation of Internal-External Hellenides

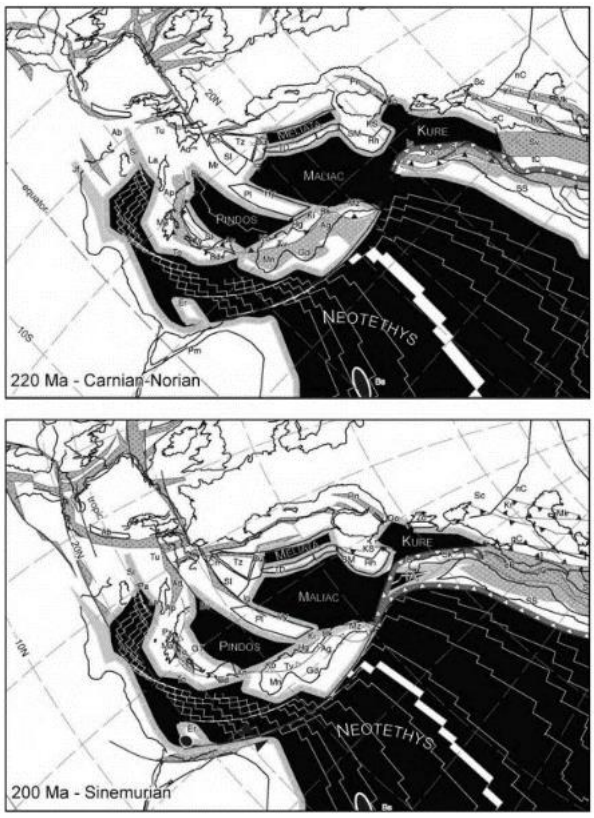

Figure 6: Reconstruction of Pindos, Maliac and Meliata, Plate Tectonics of the Apulia–Adria Microcontinents, Stampfli, 2005

This unit explores the formation and development of oceanic and continental crust over geological time in the Hellenic Subduction zone. The differences between oceanic and continental crust, as well as their interactions, give rise to two categorized units known as the Internal and External Hellenides, which will be discussed further below.

It is important to note that the external Hellenides have been undergoing sedimentation since the Mesozoic era, particularly during the Cenozoic period and experienced tectonization only during the Eocene-Miocene. In contrast, the Internal Hellenides have been shaped by two tectonic events, with

the first occurring during the Upper Jurassic-Late Cretaceous period. Specifically, the units to the south, such as those in the footwall of the Pelagonian-Lycian Block, do not have a Cretaceous orogenic history. They became involved in subduction orogenesis and associated high-P metamorphism at least 20 Ma later than the Pelagonian-Lycian Block and the Vardar-Izmir Oceanic Unit. The Pindos Oceanic Unit is complex paleogeographic domain comprising oceanic crust and continental basement-cover sequences. These distinct units are part of an accretionary complex that formed between approximately 55 and 30 Mya. In the Cyclades, the uppermost part of the Pindos Oceanic Unit is the highly attenuated ophiolitic Selçuk Mélange (Okrusch & Brocker 1990), which now marks the suture between the Pindos Oceanic Unit and the overlying Pelagonian-Lycian Block (Ring & Layer 2003). Slivers of oceanic crust such as gabbro, plagiogranite, and basalt that formed around 80–65 Ma are incorporated in the ophiolitic Selçuk Mélange. Beneath the Selçuk Mélange, the continental rocks of the Cycladic Blueschist Unit constitute the most deeply exhumed parts of the Hellenides. (Ring et al., 2010)

The Cycladic Blueschist Unit comprises a crystalline basement, and a passive margin of the Pindos Ocean as the Pelagonian block to the north. In SW Turkey, this sequence is unconformably overlain by mid to late Paleocene flysch (~62–56 Mya) (Ozer et al. 2001), which slightly predates the sedimentation in the Meso-Hellenic and Thrace forearc basins. These sediments were deposited as a response to the inception of subduction of the Pindos Oceanic Unit. The Tripolitza Block represents a continental platform unit of Triassic to Eocene age (~250– 40 Mya), partly covered by late Eocene to early Oligocene flysch (~35–25 Mya) (Jacobshagen 1986). The undertreating of the Tripolitza Block began around 35–30 Mya (Thomson et al. 1998a, Sotiropoulos et al. 2003). In the Cyclades, high-pressure (HP) rocks of the Tripolitza Block are locally exposed in tectonic windows through the overlying Cycladic Blueschist Unit (Godfriaux 1968, Shaked et al. 2000, Ring et al. 2001). In the Peloponnese and Crete, the Tripolitza Block and the Pindos Oceanic Unit are only slightly metamorphosed. The Ionian Block comprises mainly limestone and late Eocene to Miocene flysch (~35–10 Mya) (Jacobshagen 1986). Ultimately, during the Miocene and early Pliocene, the later Hellenic active subduction zone caused the Ionian unit to thrust over the pre-Apulian slope of the Apulian platform. This platform was absent in the eastern part of Greece, where the lithosphere of the Eastern Mediterranean basin had been subducting since the early or middle Miocene (Le Pichon et al., 2002; Underhill, 1989). The Mediterranean Ridge Accretionary Complex, the southernmost part of the Hellenides, saw the onset of accretion at around 19 Mya during the ongoing subduction of the Triassic (~250–200 Mya) oceanic crust of the East Mediterranean Ocean (van Hinsbergen et al. 2005). The tectonic plates with units, during the Triassic subduction are shown above in (Fig. 6). Along the central Mediterranean Ridge, this oceanic crust of the East Mediterranean Ocean has been completely consumed, and the leading edge of the African passive continental margin is currently entering the subduction zone. (Ring et al., 2010)

Unit 1.4 Metamorphic Basement of Units and Displacement of the Volcanic Arc

In this section, we will explore the metamorphic basements of geological units and the movement of the volcanic arc as factors contributing to the subduction process. The rollback

of the plate that as mentioned previously, caused the displacement of the arc, resulting in the formation of mountain building processes, known as orogeny.

The Srednogorie, Rhodope, and Sakarya continental fragments were amalgamated with Eurasia between ~185 and >100 Mya (Mposkos & Kostopoulos 2001, Krohe & Mposkos 2002). During the Cretaceous period, a complex north dipping Rhodope nappe stack developed: Ricou et al. (1998) subdivided the nappe into (1) a lower nappe of continental basement, overlain by a sedimentary cover (Drama nappe), and (2) an overlying mixed unit of continental and oceanic origin. (Ricou et al. 1998) suggested that the two continental units were separated by a narrow oceanic rift, and that Cretaceous shortening in the Rhodope was 500 km. (Ring et al., 2010)

The Vardar-Izmir Oceanic Unit was subducted beneath the Srednogorie and Rhodope-Sakarya blocks during the Cretaceous period (approximately 145–65 million years ago). This unit includes mainly Jurassic ophiolitic rocks and indicates a suprasubduction zone environment. A volcanic arc associated with the subduction of the Vardar-Izmir Oceanic Unit commenced in southern Bulgaria around 90–75 million years ago (von Quadt et al. 2005). The oldest nappe, formed by an ophiolite that is as much as 10 km thick and 100 km wide, was deposited on top of the Pelagonian unit during the Jurassic period, originating from the Vardar Ocean in the north (Ricou et al., 1998; Robertson and Shallo, 2000). In the Late Cretaceous, the remaining northern half of Vardar closed, resulting in a 100-km-wide Vardar-Axios nappe (Ricou et al., 1998). The original north-south width of Vardar was estimated as 1000 km by Stampfli and Borel (2004), with an estimated 700 km of Jurassic and 300 km of Late Cretaceous contraction. It is suggested that the subducted southern part of Vardar detached in the Jurassic along the northern margin of Pelagonia (Ring et al., 2010).

The Pelagonian-Lycian Block is located structurally below the Vardar-Izmir Oceanic Unit. Both the Vardar-Izmir Oceanic Unit and parts of the Pelagonian-Lycian Block underwent metamorphism under blueschist-facies conditions between approximately 125 and 85 million years ago (Lips et al. 1999, Sherlock et al. 1999, Ring & Layer 2003). The MesoHellenic and Thrace troughs formed as forearc basins at the onset of the Eocene (around 56-50 million years ago) above the southern edge of the Pelagonian-Lycian Block (Vamvaka et al. 2006, Huvaz et al. 2007). The units to the south, in the footwall of the Pelagonian-Lycian Block, lack a Cretaceous orogenic history and became involved in subduction orogenesis and associated high-pressure metamorphism at least 20 million years later than the Pelagonian-Lycian Block and the Vardar-Izmir Oceanic Unit. After the accretion of the Vardar-Axios unit in the Late Cretaceous, the Pelagonian unit and overlying Jurassic ophiolites were underthrusted in the Paleogene. The Pelagonian unit is made up of Variscan continental basement covered by Paleozoic and Mesozoic carbonates (Jacobshagen, 1986). The minimum width of the Pelagonian zone is approximately 200 km, measured from its westernmost exposure on the Pindos unit to its easternmost exposure in the Paikon window (Bornovas and Rontogianni-Tsiabaou, 1983; Ring et al., 2010).

The Pindos Oceanic Unit is a heterogeneous paleogeographic domain that involves oceanic crust and continental basement-cover sequences. This complex formed between approximately 55 and 30 million years ago. In the Cyclades, the uppermost part of the Pindos Oceanic Unit is the highly stretched ophiolitic Selçuk Mélange (Okrusch & Bröcker 1990), which now marks the boundary between the Pindos Oceanic Unit and the overlying Pelagonian-Lycian Block (Ring & Layer 2003). The Cycladic Blueschist Unit includes a basement of schist and orthogneiss dating back to the Carboniferous period (approximately 360–300 million years ago), as well as a late

Carboniferous to post-Carboniferous passive-margin sequence of marble, metapelite, and volcanics (Durr et al. 1978, Ring & Layer 2003).

During the Eocene, the Pindos unit underthrusted the Pelagonian unit, with the subducted portion of the Pindos unit being metamorphosed into the Cycladic blueschist. This rock formation is now exposed in the Cyclades and Evia. As we move towards Mount Ossa, Mount Olympos, and the Paikon window in northern Greece, the Pindos unit shows a lower grade greenschist to prehnite metamorphic facies (e.g., Jolivet et al., 2004; Kisch, 1981; Ricou et al., 1998). The Pindos unit contains radiolarites, indicating deposition below calcium compensation depth, suggesting an original oceanic basement (Robertson and Shallo, 2000).

The Cycladic blueschist unit is underlain by continental basement, possibly representing the late Carboniferous to post-Carboniferous passive margin of the Pindos basin (Ring et al., 1999). The basement of Cycladic Blueschist consists of schist and orthogneiss, and the passive-margin of marble, metapelite, and volcanics. Restored sections across the Pindos unit, displayed an original width of 160 km for the parts exposed in western Greece (Skourlis & Doutsos 2003). In the Oligocene, the Pindos unit was underthrusted by the Tripolitza unit, comprising of 3 km of platform carbonates and 4–5 km of flysch (Jacobshagen, 1986). The Tripolitza unit may have been the stratigraphic continuation of the metamorphic Phyllite Quartzite unit of the Peloponnese and Crete (Van Hinsbergen et al., 2005b), which is 2 km thick (Krahl et al., 1983) and unconformably overlies slivers of continental pre-Alpine basement on eastern Crete (Finger et al., 2002). In the Cyclades, high-pressure rocks of the Tripolitza Block are locally exposed in tectonic windows through the overlying Cycladic Blueschist Unit (Ring et al., 2010).

The Ionian unit's oldest section consists of the Kastania phyllites that lie beneath the Plattenkalk unit (Kowalczyk and Dittmar, 1991). These phyllites were thought to be sediments from a passive margin. In this area, the Cretan detachment separates the Tripolitza Block from the underlying high-pressure rocks of the Ionian Block, which are approximately 25–20 million years old (Fassoulas et al. 1994, Jolivet et al. 1996, Thomson et al. 1999). The Ionian Block consists of Late Carboniferous to possibly Triassic rocks (approximately 310–220 million years old), covered by limestone and late Eocene to Miocene flysch (around 35–10 million years old) (Jacobshagen 1986) (Van Hinsbergen et al., 2005).

Across the central Mediterranean Ridge, this oceanic crust of the East Mediterranean Ocean has been completely consumed, and the leading edge of the African passive continental margin is currently entering the subduction zone (Van Hinsbergen et al., 2005).

Unit 1.5 General information about metamorphism and tectonics of Evia

On the island of Evia, high-pressure metamorphism began around 50 million years ago (Maluski et al. 1981). The Cycladic Blueschist Unit experienced high-pressure conditions until about 33 million years ago, after which the rocks began to be exposed and eventually re-equilibrated under greenschist-facies conditions around 21 million years ago (Ring & Layer 2003, Ring et al. 2007a). Recent data for the Cyclades islands suggest that the Cycladic Blueschist Unit may have an internal structure, comprising different tectonometamorphic slices (cf. Forster & Lister 2005). For instance, in northern Syros, high-pressure rocks provide strong evidence for early high-pressure metamorphism around 53 million years ago, based on U-Pb zircon and Ar-Ar phengite data (Tomaschek et al. 2003, Putlitz et al. 2005). The earliest

greenschist facies overprint on Syros is dated at about 40 million years ago (our own unpublished Rb-Sr mineral data). A similar situation is observed in Samos in the eastern Aegean, where high-pressure metamorphism took place before 45 million years ago (Ring & Layer 2003). The initial exposure of high-pressure rocks began around 42 million years ago under high-pressure conditions and continued under greenschist-facies conditions until about 32 million years ago (Ring et al. 2007b). In contrast, in northern Sifnos in the southwest Cyclades, the earliest high-pressure metamorphism occurred at about 42 million years ago, followed by a transition from blueschist- to greenschist-facies around 30 million years ago (Altherr et al. 1979, Wijbrans et al. 1990, Lister & Raouzaios 1996, Forster & Lister 2005). The age pattern observed in northern Sifnos is akin to that of the Cycladic Blueschist Unit in Tinos. There was HP metamorphism around 44–40 million years ago (Mya), followed by early transformation from blueschist to greenschist facies at approximately 30 Mya (Brocker et al., 1993). In the southern part of Sifnos, there exists another high-P unit (Schmadicke & Will, 2003), located structurally beneath the high-P complex in the northern region, which is about 42 million years old. This southern unit experienced high-P overprinting at 30 Mya or later, followed by reworking into greenschist facies at around 22–19 Mya (Altherr et al., 1979; Wijbrans et al., 1990). The data suggests that a significant amount of time, estimated to be between 5 to 15 million years, passed before each high-P layer was exhumed sufficiently to enable decompression-related mineral reactions. Analyses of structural and geochronologic data from Sifnos indicate that both high-P and exhumation ages decrease with lower structural position within the Cycladic Blueschist Unit. The younger high-P and exhumation ages are observed in deeper tectonic slices, moving from the ophiolitic Selçuk Mélange to the underlying basement-cover sequence of the Cycladic Blueschist Unit. Interestingly, this downward younging trend is consistent with a similar trend observed in the subduction system and the magmatic arc progressing towards the south. In the tectonic windows of the Cyclades, Rocks of the Tripolitza Block, located beneath the Cycladic Blueschist Unit, exhibit high-pressure metamorphism at 8–10 kbar and 350–400◦C (Shaked et al. 2000). Age data for this high-pressure metamorphism consistently falls between approximately 24 and 21 million years ago (Ring et al. 2001, Ring & Reischmann 2002, Ring & Layer 2003; Ring et al., 2010).

Studies conducted at the western and eastern edges of the Aegean, in Evia as well as Samos and adjacent western Turkey (Ring et al. 2007 a,b), revealed that extrusion wedges were formed during the Eocene at approximately 42–32 million years ago (Samos/western Turkey) and in the early Oligocene at around 33–21 million years ago (Evia). Both extrusion-wedge systems were active for roughly 10 million years. The extrusion wedge on Evia led to approximately 8–15 kilometers of syn-subduction exhumation. In the cases of Cycladic and Cretan extrusion wedges, it was observed that normal faulting at the top of the extruding wedges did not lead to the development of extensional graben in their hanging walls, indicating that these normal faults were not a result of regional horizontal extension, but rather were shortening-related.

The reported cases of extrusion-wedge formation showed that the wedges commonly accomplished more than 50% of the exhumation of high-pressure rocks in or above the subduction channel. In the examples from Evia and Samos/western Turkey, the normal fault at the top of the extrusion wedges developed in the ophiolitic Selçuk Mélange, representing an ancient subduction thrust. As the subduction trench retreated, this former subduction thrust was reactivated as a shortening-related normal fault. Ring & Reischmann (2002) proposed a similar scenario for the Cretan detachment, emphasizing the significant

relationship between extrusion wedges, pronounced tectonic exhumation, and the subduction system (Ring et al., 2010).

Unit 1.6 Geology of Central Evia

During the late Paleozoic to early Mesozoic era, the regional tectonic setting of Tethys in the southern Mediterranean region (including Sicily, Crete, Peloponnese, and Evia) was studied to explore alternative models using sedimentary evidence. The local Pelagonian sequence, ranging from Late Permian to Mid-Triassic age, comprises metasiliciclastic sandstones, shale, ribbon chert, redeposited carbonates (including debris flows), andesitic-rhyolitic metavolcanic rocks, and tuffaceous-volcaniclastic sediments, indicating a rift-related origin. This sequence transitions into a several-kilometer-thick unit of platform carbonates from the Late Triassic to Jurassic age, which is characteristic of the Pelagonian zone in general (Fig. 7b). Stratigraphically, this entire succession is underlain by schists and granitic rocks (referred to as 'Hercynian basement') and coarse 'basal' clastic sediments derived from these rock types (Fig. 7e). These processes began when extensive magmatism affected the crystalline basement in the Late Triassic (300 Mya), leading to its transformation into an oceanic environment (Robertson, 2006).

It is suggested that southward subduction beneath the north margin of Gondwana was active during the Late Paleozoic Hercynian 'orogeny'. The subduction signature of Triassic basalts is thought to be related to melting of subduction-contaminated lower crust and upper mantle. These volcanic rocks may represent small melt fractions strongly influenced by the composition of the underlying crust and mantle lithosphere (Dixon & Robertson, 1993). The south Aegean and Balkan region were characterized by calc-alkaline magmatism, such as extensive granite extrusion and andesitic volcanism, during Late Paleozoic time related to the Hercynian orogeny (Mountrakis, 1986; Kotopouli et al., 2000). This pre-existing magmatism may have been the source of the subduction signature in some of the Triassic rift-related volcanic rocks rather than contemporaneous Triassic subduction (Fig. 8). During the Upper Paleozoic (Early Carboniferous), subduction may have occurred both northwards and southwards, i.e. beneath both Gondwana and Laurasia (Eurasia). This resulted in complete closure of the 'Hercynian' ocean in the west, while Tethys (PaleoTethys) remained partly open further east. Subsequent subduction was northward-directed beneath Eurasia during the Triassic and the late Mesozoic-Early Cenozoic. It is proposed that a relict south-facing Hercynian slab might have remained along the north Gondwana margin and, if so, was reactivated during Triassic rifting, resulting in subduction-influenced volcanism in some areas of the Balkans (e.g. eastern Crete but not western Crete; southern Pindos but not northern Pindos, etc.). In summary, the Eastern Tethyan rifts cannot be considered as subduction-related back-arc marginal basins; where present, a subduction influence is seen as being relict from previous, probably 'Hercynian', subduction (Robertson, 2006).

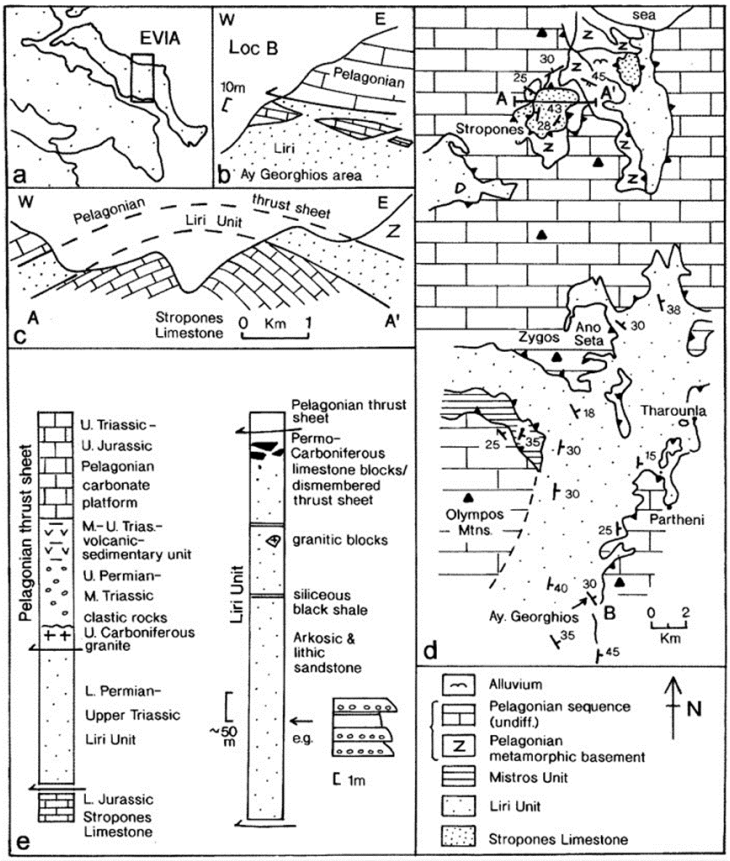

Figure 7: Geology of Central Evia, Sedimentary evidence from the south…, Robertson, 2006

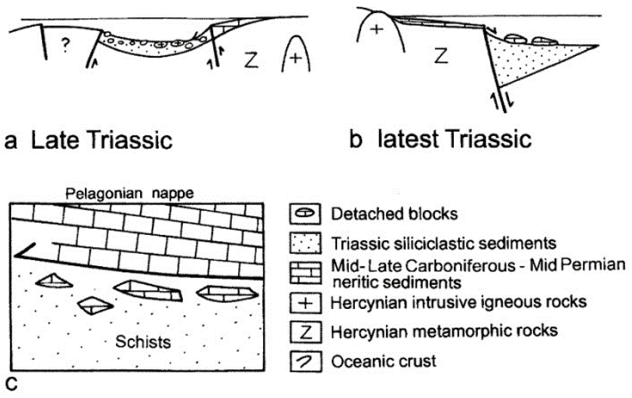

Figure 8: Triassic rifting and magmatism, Sedimentary evidence from the south…, Robertson, 2006

Chapter 2

Unit 2.1 Upper Plate

In Central Evia, there is a rift that divides the region into an Upper Plate (Hanging Wall) in the Sub Pelagonian zone to the north, and a Lower Plate (crystalline basement) forming the Foot Wall. Our research is primarily focused on the Lower Plate in the vicinity of Agious Apostolous. Specifically, we are studying the tectonostratigraphy of Evia, encompassing the lowermost Almyropotamos Unit, the overlying South Evia Blueschist Belt (Lower Plate), and the uppermost Pelagonian Unit. These units together form a nappe pile that was tectonically stacked during the Alpine orogenesis.

In accordance with Bradley in 2012, the upper plate mainly consists of 5 units (Fig. 9): Dirfys, Servouni, Liri-Mistros, Gerontas (Olympos), and Pounta Units. Starting from the structurally highest unit and moving to the lowest, the Dirfys Unit is extensively present in western Central Evia and comprises a typical Sub-Pelagonian sequence. It is made up of very low-grade Permo-Triassic clastic, volcaniclastic, and volcanic rocks that are overlain by Late Triassic to Jurassic neritic carbonates. This sequence is covered by Late Jurassic deep-water radiolarites and red shales, which are part of the tectono-sedimentary Pagondas Mélange (Bradley et al. 2012).

The Servouni Unit, which is of great interest due to its volcano-sedimentary nature, is found in most of eastern central Evia and forms the immediate basement of the Kymi-Aliveri basin. The unit's stratigraphy has been well-documented. Starting from the bottom, there are discontinuous, often strongly cataclastic outcrops of the Late Carboniferous Skotini Granite, which serve as the crystalline basement. This is unconformably overlain by the Permian arkoses and carbonates of the Ano Mavropoulon Formation, and further overlain by the Middle Triassic Volcano-sedimentary Complex and a Middle Triassic through Jurassic platform carbonate sequence. Additionally, a bauxite-mantled erosion surface, Cenomanian neritic carbonate platform, Maastrichtian pelagic limestone, and Paleogene flysch can also be observed (Bradley et al. 2012).

We should discuss some distinctions between Dirfy's and Servouni's units. Unlike the Dirfy's Unit, the Servouni's Unit Later-Cretaceous unconformity is not covered by an abducted ophiolitic mass. However, there are sporadic patches of red shales, small pockets of serpentinite and gabbro, and Cretaceous bauxites found locally on the unconformity surface (Katsikatsos et al., 1981). The Upper Jurassic-Lower Cretaceous obduction event is primarily evidenced by the truncation of large-scale folds affecting the Triassic-Jurassic carbonates by the Late Cretaceous unconformity (Bradley et al. 2012).

Above the Servouni unit there is the Liri-Mistros Unit, which is composed of conglomerates, arkosic sandstones, and flysch-type turbidites of Permian to Late Triassic age (the Liri Unit; de Bono, 1998) that were laid down on top of a Carboniferous gneisses and schists crystalline basement intruded by undated mafic dykes (the Mistros Unit; de Bono, 1998). The upper ~200m of the Liri Unit contains disconnected, internally folded blocks of Carboniferous limestone and granite, ranging from meter to sub-kilometer scale, which are interpreted either as olistostromes shed from a Triassic rifted margin (de Bono, 1998), or, more likely, as fault-bounded slivers derived from an overlying thrust sheet (Robertson, 2006). The Liri Unit reached lowermost greenschist facies and is influenced by a variably developed foliation that is continuous within argillic units as a spaced cleavage in coarse conglomerates and arkoses

or not at all. Regarding tectonics, this foliation is most strongly developed near the base and top of the unit, where an E-W to NE-SW trending intersection lineation is weakly developed, running parallel to the hinge lines of isoclinal and intrafolial folds. Phacoid flattening fabrics are common throughout the Liri Unit (Robertson, 2006), especially in northern exposures where the unit is structurally thinnest (Bradley et al. 2012).

Geochronological data (U-Pb and Ar-Ar) from the Pelagonian basement in Evia (Greece) give us geodynamic significance for the evolution of PaleoTethys). The samples from Liri come from olistoliths belonging to the Permo-Triassic Liri unit. situated about 3.5 km in the NE of Kato Seta village or 1 km west of Manikia village. The granitic blocks and pebbles included in the Liri flyschoid sequence are mineralogically similar to the granites from Skotini. However, there are some differences like Liri granites are less affected by deuteric processes and some samples have not been affected by static recrystallization. The Skotini granites are very interesting because they were collected from the outcrops stratigraphically resting at the base of the Neopaleozoic units of central Evia (De Bono. 1998: De Bono et al., 1999). They located about 6km NE of Kato Seta village (Steni Dirfios, HAGS ed. 1971). They are homogeneous. coarse grained hypersolvus granites. Their paragenesis include quartz, albite, alkali-feldspar, biotite, white mica, chlorite, stilpnomelane, titanite, apatite, zircon and calcite. Their granitic textures are badly preserved and these rocks are seldom not foliated. The study Skotini granites shows that the quartz there has been at least one event of static recrystallization followed by a dynamic recrystallization. Secondary processes such as hydrothermalism, affect the mineralogy of the rocks and resulted in the transformation of feldspars to sericite and kaolinite and the formation of veins of stilpnomelane, quartz, aciculate white micas, chlorite and calcite. Biotite is usually altered to chlorite and associated with neoformed stilpnomelane. Almost every mineral shows undulate extinction and deformation features such as lamellae in quartz. Consequently, these granites went through low-grade metamorphic conditions.

Gerontas Unit consists of maybe Permian gypsiferous coarse clastics, overlain by a probably Triassic volcano-sedimentary sequence with interbedded limestones, which is in turn overlain by a shallowing-upward succession of Triassic-Jurassic carbonates (Katsikatsos, 1999). Along the northeastern flank of Olympos Mountain, Upper Jurassic to Early Cretaceous radiolarian cherts and reworked carbonate sediments depositionally overlie Jurassic neritic platform carbonates (de Bono, 1998). The previously mentioned cherts are structurally overlain by an undated volcano-sedimentary mélange that consists of Jurassic (Ladinian) limestone blocks (de Bono, 1998). The structural windows of the Stropones-Metochi area bring to light Jurassic marbles ladeled the Stropones Limestone (de Bono, 1998) that are in brittle fault contact with, and lie structurally beneath, the highly attenuated Liri-Mistros Unit (Robertson, 2006; Guernet, 1979). The Stropones-Metochi marbles are overturned, but do not exhibit penetrative ductile fabrics and preserve authentic bedding structures and fossil forms (de Bono, 1998), ruling out correlation with the mylonitic marbles of the ACC. In addition, discontinuous patches are observed of knocker-bearing serpentinite mélange decorating the fault contact between the Liri-Mistros Unit and the Stropones Limestones, suggesting a correlation between the Stropones Marbles and the Gerontas Unit.

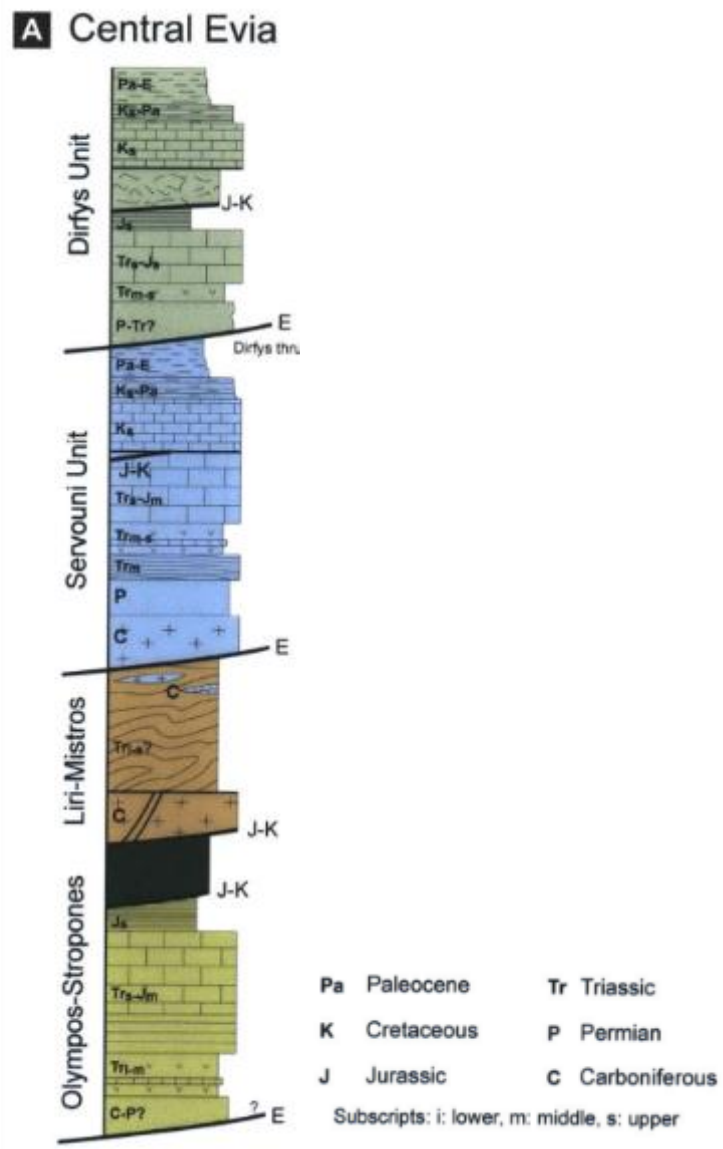

Figure 9: Column of Upper Plate's Units, Bradley et al. 2012.

Pounta unit being the final unit on the top, is related to Octonia Detachment, a low-angle fault exposed only over a small area along the coastline east of Octonia. The footwall of this fault consists primarily of nearly pure calcite marbles with volumetrically minor quartz, plagioclase, and graphite. In the area occurs discontinuous, plurimeter intercalations of fine-grained muscovite schist, phyllite, and fine-grained metabasite. The exposed Pounta Unit formation has less than 400m structural thickness. Remnants of bedding are locally evident as meter-scale dark-light banding, cherty stringers, and dolomitic layers. The marbles typically bear a NE/SW-directed, gently plunging lineation that lies in the plane of a variably-developed schistosity and parallels the hinge lines of isoclinal to open, mostly upright folds that lack axial planar fabrics. In most outcrops an intersection lineation can locally be shown to also be a stretching lineation. The ductile sense of shear recorded at outcrop scale is inconsistent, varying locally from top-to-the-NE to top-to-the-SW. The Pounta marbles are affected by NW-SE striking, an echelon, calcite-filled tension fractures and lineation perpendicular joints. The marbles and schists of the Pounta Unit are separated from distended rocks of the Servouni Unit and Kymi-Aliveri basin by the Octonia Detachment. This fault dips ~15' westward, except

where it is strongly folded and attains steep northwestward dip of the South Evia-North Attica Fault, against which it is truncated. The immediate hanging wall of the Octonia Fault consists of a 0-20m thick shear zone containing fragmented blocks of the Servouni and Liri-Mistros Units. Moreover, calcite mineral lineation, frictional-slip striae, and microbreccia streaks on the low-angle fault surface are oriented SW/NE. Small-offset, synthetic normal faults on the fault surface indicate transport of the hanging wall toward the southwest. The hanging wall rocks are affected by SW-dipping normal faults with dip-slip kinematics, some of which attain shallow dip (~30') near the detachment surface. These structures are dominantly synthetic to the top-to-the-SW sense of displacement recorded on the main low-angle fault surface. Within 30 meters of the fault surface, the marbles of the Pounta Unit are affected by a strong cataclastic overprint that obscures the older ductile fabrics. The Pounta Unit exhibits structural characteristics, including L-S tectonites and lineationparallel folds, that are absent from the thrust sheets of the Sub-Pelagonian zone but are within the polymetamorphic rocks of the adjacent Attic-Cycladic Complex. We tentatively correlate the NE-SW directed ductile stretching and upright folding (greenschist-facies) deformation in the ACC. However, the Pounta Marbles are lithologically distinct from the cipolines of the Styra and Almyropotamos Units (Maluski et al., 1981), and we have identified no HP-LT 28 minerals within the Pounta Unit. This suggests that the Pounta Unit represents a deep-seated part of the Pelagonian zone (s.l.) that is most directly related to the scarce rocks preserved in the hanging wall of the ACC detachments (Bradley et al. 2012).

The Octonia Detachment is exposed along the eastern margin of the Kymi-Aliveri basin. This basin developed between ~16.5 Ma and -13 Ma, and is separable into three inconsistent bounded sequences characterized by different sedimentary facies and clast provenances (Bradley et al., in prep.). The Octonia Detachment truncates oligomictic conglomerates and thin lacustrine sand-clay interbeds of the ~16.5-14 Ma Prinias and Mantzari Groups, but has no contact with the debris flow conglomerates that comprise the less than 14 Ma Koustoumalou Group. Where the Miocene conglomerates directly overlie the Octonia Detachment, they lose their sedimentary textures and instead exhibit brittle grain-flow fabrics, anastomosing gouge zones and trains of broken clasts (Bradley et al. 2012).

Unit 2.2 Tectonic and volcanism of Central Evia

Unit 2.2.1 Local Tectonics

In the geological cross-section of a two-dimensional basin, we can see a fault that divides the area into an Upper and Lower plate. This fault also shows how the two blocks are deformed above and below a subduction zone (Fig. 10).

It seems like the tectonic development of Evia led to various geological processes. In 2012, Bradley noted that certain faults in Central Evia from the Late Jurassic-Early Cretaceous and Eocene periods were reactivated during regional extension. This reactivation has influenced the tectonic evolution of Central Greece since the middle Miocene. The movement of the NW-striking normal faults and the restored position of these faults have affected the region's tectonic development. The compression in the E-W direction is related to the westward movement of Anatolia, which likely began during the middle Miocene. This compression aligns with the structures affecting molasse basins and granitic intrusions during the middle Miocene. The extensional direction, orthogonal to the Hellenic trench, suggests that the

extension was influenced by the retreat of the Aegean trench. The observed distribution of deformation, with pure extensional structures away from strike-slip localizing shortening corridors, may be influenced by tectonic inheritance. The Pelagonian strike-slip corridor is positioned in the main contact between Adria/Pindos and Pelagonia. During the rollback and curvature of the trench, block rotation has likely been accommodated by NE-striking dextral faults. The structural data indicate that the Pelagonian fault acted as a major dextral strike-slip fault during the middle Miocene. Later on, the fault accommodated different amounts and styles of continental extension. This includes widespread extension in Cyclades/South Evia/Attica, accommodated by detachment faulting, and less extension in Central Greece, mainly accommodated by high-angle normal faults. Throughout the Plio-Quaternary period, Central Greece evolved into a purely extensional tectonic regime, with almost radial extension and no E-W shortening. This suggests that the North Anatolian Fault fully accommodated the westward extrusion of Anatolia, leading to the formation of the Anatolia/Aegean microplate. The middle Miocene normal faults were repurposed to define NW-striking oblique rifts, with newly formed E-striking normal faults (Fig. 11). The Pelagonian Fault delineates the Pelagonian and Adria/Pindos terranes in both Evia and Attica.

As a result, the system of the Corinth and Evia rifts are related to progressive strain localization at lithospheric scale controlled by both the presence of inherited structures and a change in the direction of extension. The progressive trench curvature and block rotation during trench retreat cannot explain the change in direction from NE-SW to N-S during the Pliocene-Quaternary. This is probably related to slab deformation at depth, as exemplified by the formation of the Kephalonia strike-slip fault (Bocchini et al., 2018; Evangelidis, 2017; Faucher et al., 2021).

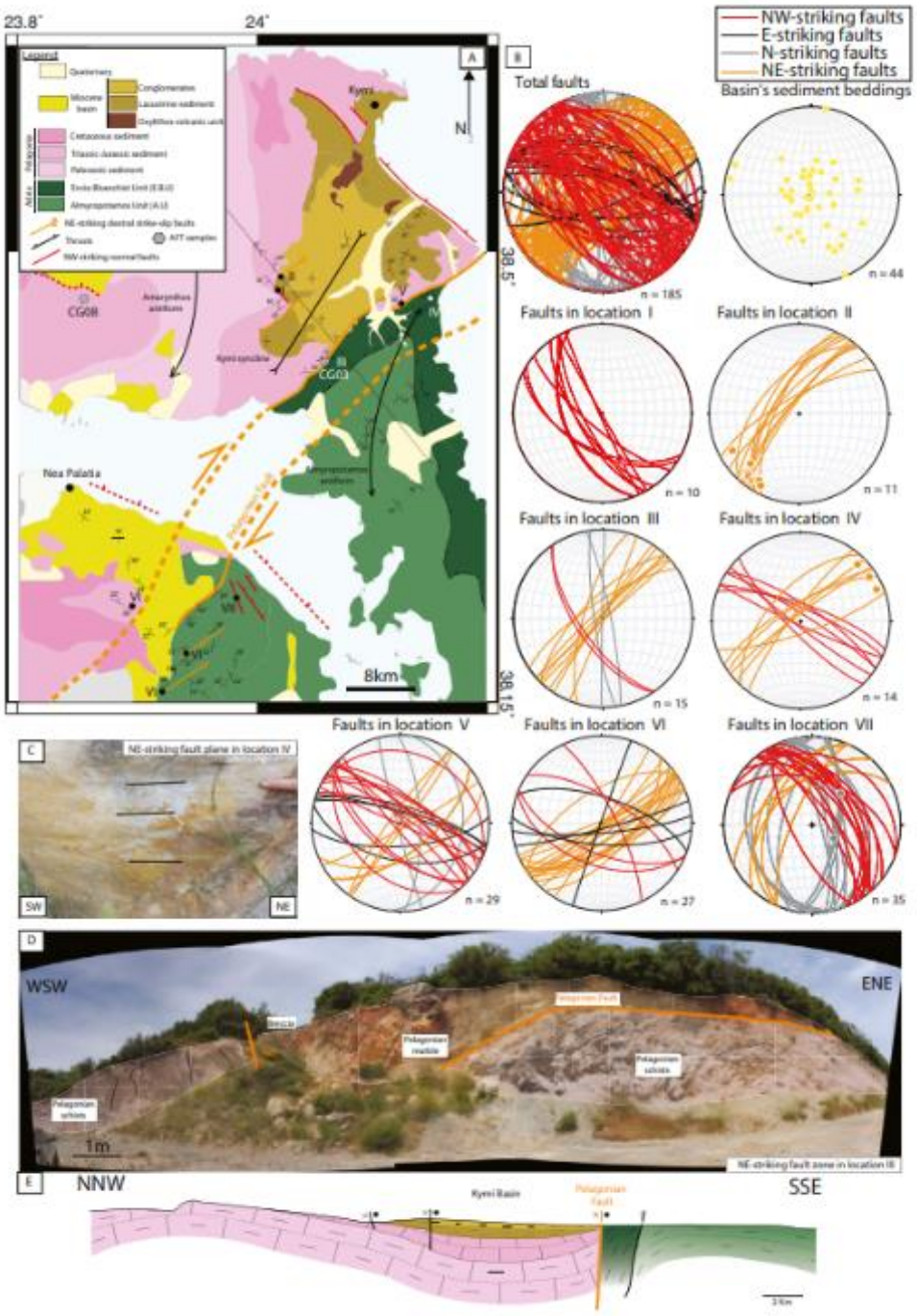

Figure 10: Structural features of the Kymi basin with inferred main NW-striking normal faults and NE-striking dextral strike-slip faults, basin bedding and basement foliations. Picture A: Digitized geological map where we see the dextral strike and other faults in Evia and Attica. Picture B: Stereographic representation of the level of the faults. Picture C: NE-striking fault plane photo from fieldwork. Picture D: Fieldwork photo of upper and lower plate in Central Evia. Picture E: Digitized two-dimensional geological section where Pelagonian Fault delimits the upper the lower plate in Central Evia.

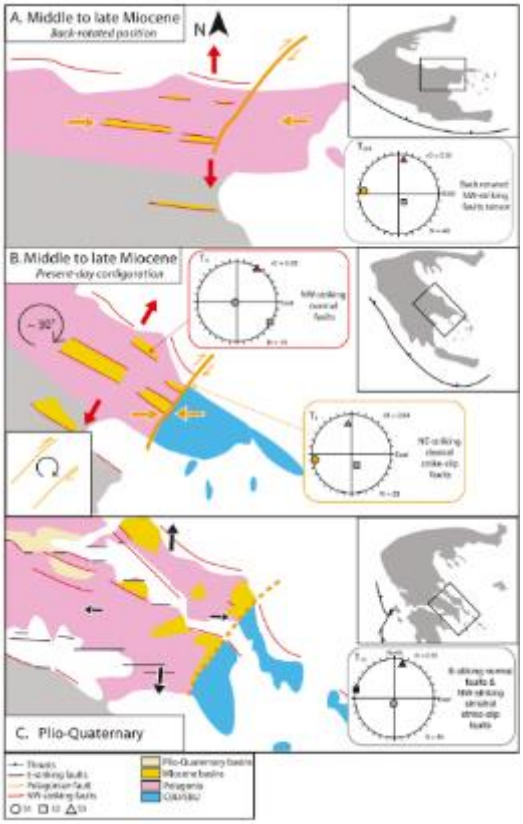

Figure 11: Tectonic development of Evia throughout the geological era, Faucher et al., 2021.

Unit 2.2.2 Correlation between Dextral strike and Attica fault

Two main units compose the Pelagonia, from bottom to top. The crystalline basement composed of a paragneiss and orthogneiss with Cambrian ages and a metasedimentary cover with Permian metasediments and metavolcanics, Triassic to Jurassic marbles. These units are thrusted on top of the Mesozoic to Lower Tertiary Beotian and Parnassos Flysch. During the early Cretaceous these units have undergone greenschist facies metamorphism and locally underlie ophiolites. Middle Miocene basins in Evia and Attica are also observed close to the NE-striking Pelagonian Fault (Fig. 12), which is initially a thrust formed during subduction nappe stacking, separating Adria and Pelagonia. The age of the activity of the Pelagonian Fault is controversial, with a potential middle Miocene age (Kokkalas, 2001; Xypolias et al., 2003). The Pelagonian Fault was characterized as a normal fault because of differential exhumation in the footwall CBU and hangingwall (Pelagonia) (Diamantopoulos et al., 2009; Papanikolaou and Royden, 2007; Shaked et al., 2000) (Faucher et al., 2021).

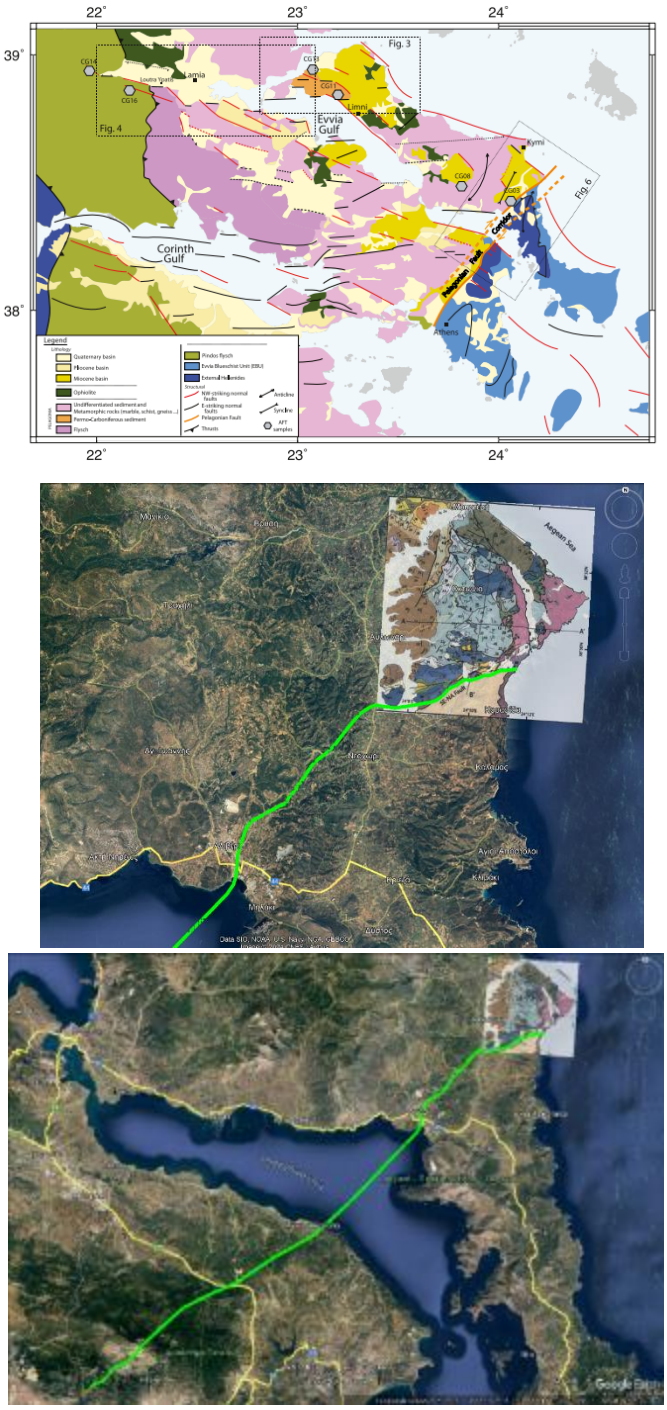

Figure 12: Picture A: Dextral strike exposed to Attica (Faucher et al. 2021). Picture B: Picture from google earth pro with used map from (Bradley et al. 2012). Picture C: Zoom out picture B, to compare two verions of the same Pelagonian fault from Faucher and Bradley.

Unit 2.2.3 Volcano-sedimentary complex

In central Evia there is a Variscan crystalline basement which is found at the base of many units both in the upper plate and even more so in the lower plate in the Makrotantalo-Ochi unit. This basement started to fade due to diatreme material. This the area began to fracture as normal faults were created and along with veins of diabase material, pelagic sediments were mixed in due to tectonic movements. Analyses on Ar found testify to an earlier stage of metamorphism. Metaplutonic rocks of similar age have also been reported not only in central Evia but also on islands of the Cyclades, in the area of Verdikousa in northern Thessaly as late carbonate granodiorite and their chemical affinities with magma associated with subduction were characterized. Similar chemical signatures to the high Ti continental flood basalts are also present in diorites and gabbroic diorites. These rocks probably crystallized during the Late Carboniferous, but are not related to the granodiorite because they often appear to truncate and sometimes precede the diorites and gabbros. In addition, the Naxos metamorphic core complex includes a Miocene amphibole controlled by the type I granitoids of Variscan type I.

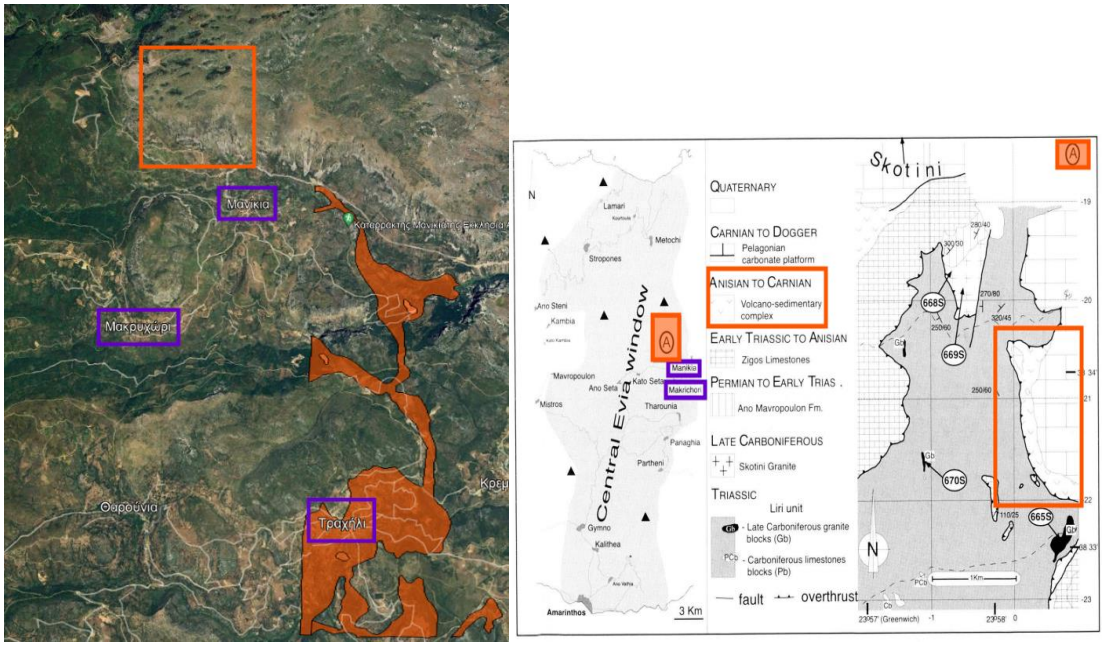

Figure 13: In these two pictures we can see that the volcano-sedimentary complex is located North-West from Manikia and Makrichori. This complex continuous East to Trachili village (metabasalts- colored red formation) (Vavasis et al., 2000).

The upper plate of Central Evia is characterized by volcanic rocks overlain by a Late Triassic to Middle/Late Jurassic carbonate platform. These volcanic rocks likely originated from the Variscan basement, specifically the Flambouron Unit, which is primarily composed of ortho- and paragneiss, as well as Late Carboniferous granitic intrusions (Skotini granites). These formations overlay the Cyclades Complex. Analysis of the Triassic volcanic rocks (De Bono 1998) indicates that they belong to the group of alkaline to sub-alkaline basalts typically found in within-plate environments, as previously demonstrated by Pe-Piper & Panagos (1989). In

the two photos above (Fig. 13) are seen the volcano-sedimentary locations in upper plate. These Permo-Triassic volcanic rocks have been further classified into two main lithostratigraphic units: the Seta Group and the Volcano-sedimentary Complex (De Bono et al. 1998). We have the Seta Group, in which the upper boundary is represented by the first occurrence of volcanic rocks (volcano-sedimentary complex) above and within the Zygos limestones. The age of the entire Group is from Permian to Anisian. Zigos limestones in the Kambia area lenses still occur within the volcanic rocks as a sharp boundary (Fig. 14) (De Bono et al. 1998).

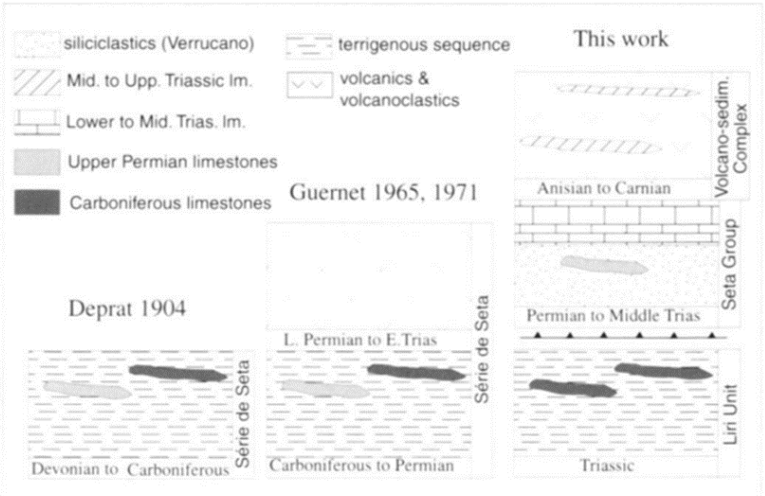

Figure 14: Positions of (the Seta Group and the Volcano-sedimentary Complex in relation to limestones in upper plate from Devonian to Triassic. (De Bono et al. 1998).

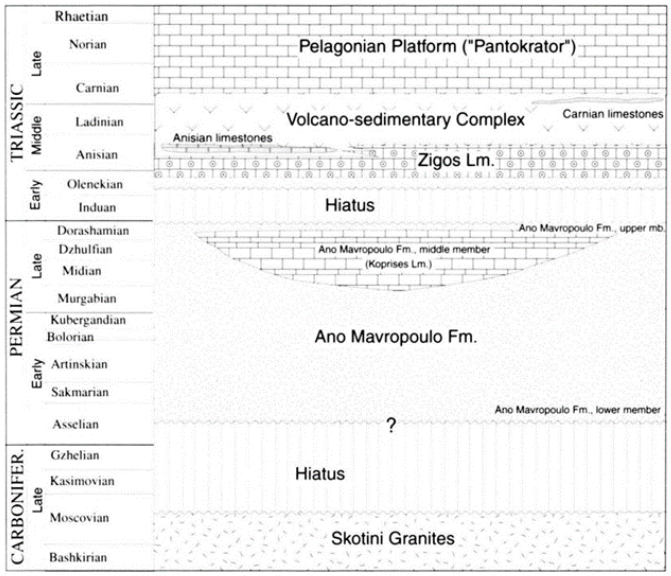

Figure 15: Lithostratigraphy column of upper plate (De Bono et al. 1998).

The volcanic rocks and associated sediments of central Evia form a new unit known as the Volcano-sedimentary Complex. This complex dates from the Anisian period and locally extends to the Carnian period. It is composed of tuffs interbedded with thick limestone beds of various facies and ages, along with sporadic basalt flows, pillow lavas, dolerites, and

gabbros (refer to Fig. 15). The lower limit is marked by the first occurrence of volcanic material over the Zigos Lm., while the upper limit is defined by the initial strata of Upper Triassic limestones of the Pelagonian platform of "Pantokrator". (De Bono et al., 1998).

The volcanic rocks and associated sediments of central Evia form a new unit known as the Volcano-sedimentary Complex. This complex dates from the Anisian period and locally extends to the Carnian period. It is composed of tuffs interbedded with thick limestone beds of various facies and ages, along with sporadic basalt flows, pillow lavas, dolerites, and gabbros (refer to Fig. 16). The lower limit is marked by the first occurrence of volcanic material over the Zigos Lm., while the upper limit is defined by the initial strata of Upper Triassic limestones of the Pelagonian platform of "Pantokrator". (De Bono et al. 1998).

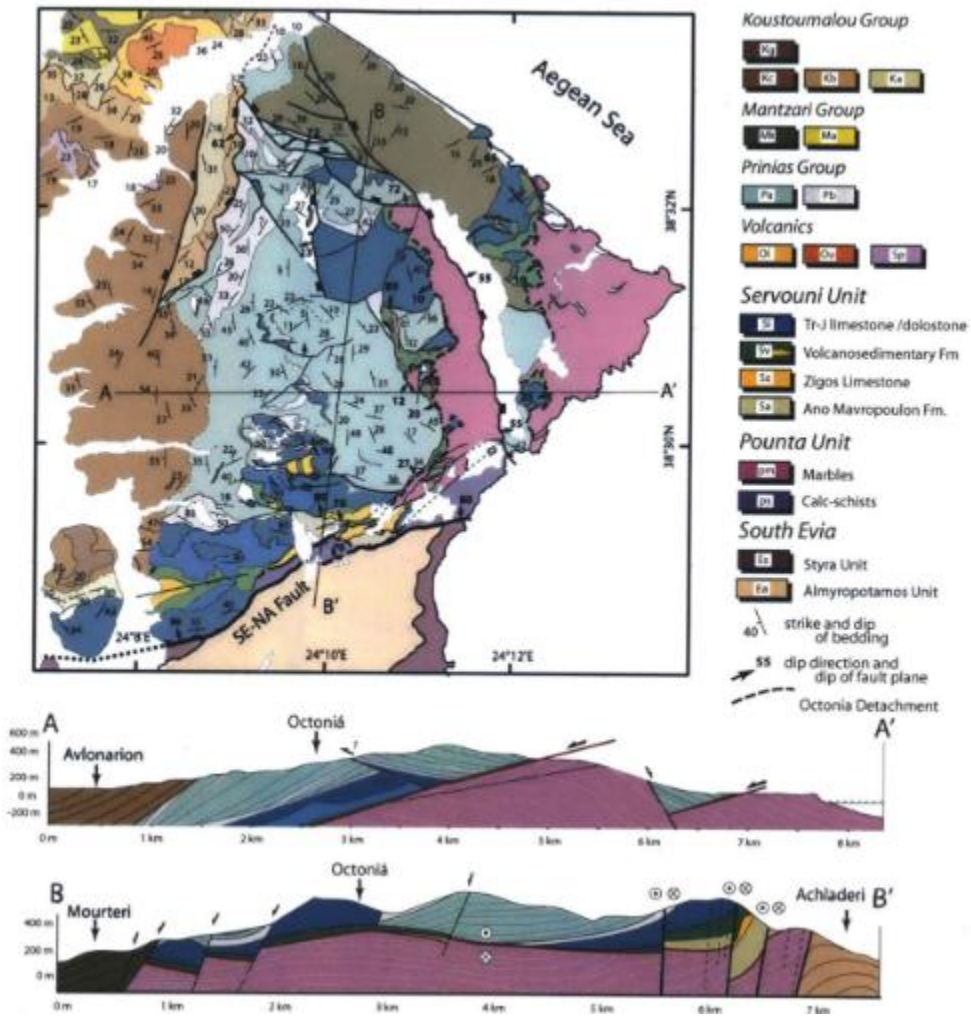

Figure 16: On the geological map in Central Evia the detachment of Ochtonia appears. Geological sections A and B show the geological structure of the area in two dimensions (Bradley et al. 2012).

Unit 2.3

Unit 2.3.1 Lower Plate

Our research area focuses on the lower plate in Central Evia, which is a foot-wall under the Ochtonia detachment. This plate consists of three main units: the Almyropotamos Unit, the South Evia Blueschist Belt, and the Pelagonian Unit.

The Almyropotamos unit in central Evia is a paraautochthonous unit that is exposed in a tectonic window. This unit deposited sediments during the Mesozoic–Eocene era and is thought to pertain to the external part of the Hellenides. It experienced only low-pressure metamorphism. The tectonic contact between the Almyropotamos Unit and the overlying blueschist unit is a thrust fault.

The geological data suggests that a high-pressure stage of Late Cretaceous–Middle Eocene age was followed by a lower pressure event during the Oligocene/Miocene. In south Evia, the main high-pressure metamorphic event is associated with 45–55 Ma, and the blueschists are estimated to be at 10–11 kbar and 300–350 °C. Other estimates suggest varying pressures and temperatures.(Lensky et al. 1997) (Shaked et al., 2000).

The Almyropotamos Unit is a thick (~ 2000 m) series of Mesozoic–Cenozoic platform carbonates that have now transformed into marbles due to metamorphism. These marbles are covered by a 1500 m thick sequence of metaquartzites and metapelites with a couple of marble layers, forming a metaflysch. At the top of the marble, there are rudists and a nummulitic hard ground, indicating that sedimentation continued in the Almyropotamos area at least until Middle Eocene times (Ypresian–Lutetian) according to Dubois & Bignot, 1979. The metamorphism affecting this unit is believed to have taken place after the Eocene epoch. In terms of its sedimentary history and structural position, the Almyropotamos Unit is considered a part of the external Hellenides based on Papanikolaou, 1984, 1986, Katsikatsos et al. 1986, and Okay, 1989. It is thought to represent the continental edge of the Apulian microplate overthrusted by the metamorphic rocks of the internal Hellenides. The Almyropotamos Unit is believed to be similar to the para-autochthonic Olympos Unit that underlies Late Cretaceous–Eocene high-pressure metamorphic rocks in northern Greece. The metaflysch is composed of phengite, quartz, chlorite, and albite, along with occasional calcite, stilpnomelane, epidote, sphene, opaques, graphite, and zircon. In a location near the contact with the Styra formation in the village of Krieza, glaucophane and albite porphyroblasts are rarely found, indicating evidence of high-pressure conditions affecting the Almyropotamos Unit. Albitic porphyroblasts may have crystallized either during the final stages of deformation or statically after deformation ceased, enclosing relics of earlier foliation and minerals such as phengite, graphite, and chlorite. Chlorite is interleaved with phengite or appears in aggregates. In this region, it is observed that relict glaucophane is replaced by biotite and chlorite. The Almyropotamos marbles mainly consist of almost pure, coarse-grained calcite with small amounts of detrital quartz, muscovite, and chlorite. In schist intercalations within the marbles, mineral assemblages include chlorite, calcite, albite, phengite, and quartz. Glaucophane inclusions in albite porphyroblasts found near Koskina indicate that glaucophane formation occurred throughout the Almyropotamos Unit (Shaked et al., 2000).

The Almyropotamos window provides a unique view of the underlying autochthonous unit beneath the Cycladic Blueschist Unit (represented here by the South Evia Blueschist Belt), indicating back arc extension. The contact between the Almyropotamos Unit and the South Evia Blueschist Belt is a thrust fault that brings Cretaceous–Eocene high-pressure metamorphic rocks over Eocene sediments. Consequently, the Almyropotamos Unit also underwent blueschist-facies metamorphism. The metamorphism in the Almyropotamos Unit, estimated at approximately 10 kbar/350 °C, resulted from the underthrusting of the South Evia Blueschist Belt at depth. Both units likely followed similar development paths from there (Shaked et al., 2000).

The last information about Almyropotamos unit, according to Bradley in 2012, is that this unit is related to Attica (Fig 17). In Evia, the Basal Unit as it has been named Almyropotamos unit and Attica together consists of a thick sequence of marbles and phyllites, collectively termed the Almyropotamos Unit, that originated as Middle Triassic through Late Eocene platform carbonates depositionally overlain by undated olistostromal flysch (Dubois and Bignot, 1979; Katsikatsos, 1986, 1987; Shaked, 2000). The structure and deformational history

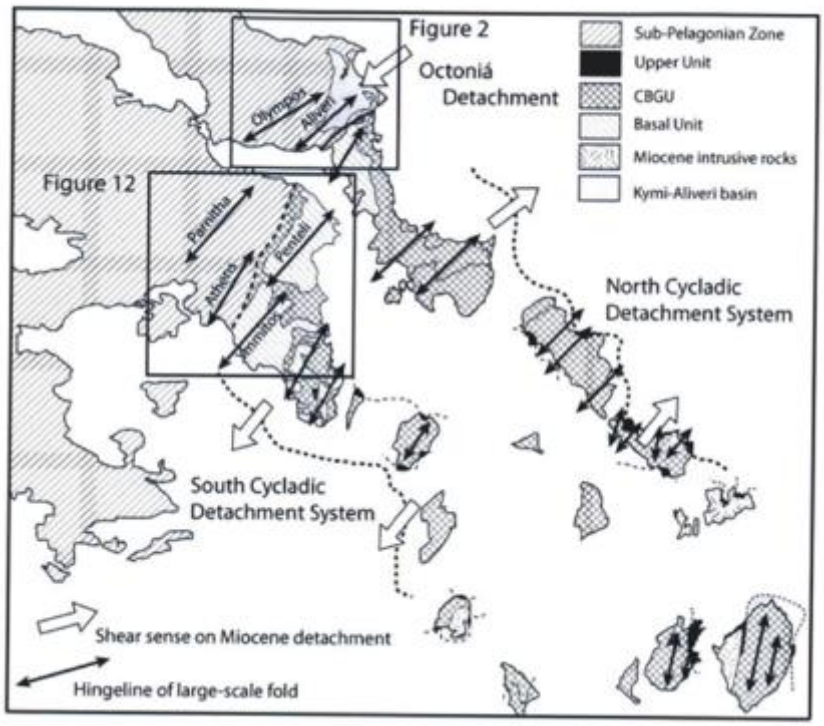

Figure 17: Basal Unit comprised Almyropotamos and Attica due to the South Evia-North Attica fault , Kyle Edward Bradley et al. 2012

of the Basal Unit has been described in both Attica and South Evia as we mentioned before (Lozios, 1993; Xypolias and Kokkalas, 2003; Ring et al., 2007; Xypolias et al., 2010). Phengite from the Basal Unit yields consistent Early Miocene (~22-21 Ma) $^{40}Ar/^{39}Ar$ ages, which were originally interpreted as resulting from deep underthrusting in HP/LT conditions (10 kbar, 350-400 °C), requiring a large amount of post-Early Miocene exhumation (Ring and Reischmann, 2002; Ring et al., 2007), but have since been reinterpreted as reflecting the timing of regional greenschist-facies retrogression.

The next one unit which overlain the Almyropotamos unit is the Styra unit. The structurally lower Styra nappe is a 2.000 m thick included from interbedded marbles and pelitic to

psammitic schists with rare intercalations of metabasic blocks near its base (U–Pb single zircon ages and geochemistry of metagranitoid rocks in the Cycladic Blueschists (Evia Island): Implications for the Triassic tectonic setting of Greece). The Styra unit is defined by the unity of the Pillars which appears in the east and north side of the map and consists of orthogneissic, quartzites, shale formations and the overlying marbles. Underlying all of the above are marble-rich pyroxenic shales and Na-rich meta-granites. Precisely, we have Spiritual formation and quartzites on the roof. The underlying formations are orthogneisses which are molybdenum altered and quartzites but there are not everywhere in the area. The quartzites occupy a larger area than the gneissic formation. Slates and Marbles are overlain and they constitute the upper parts of the unit and occupy the eastern side of the map. The shales always occur in contact with the overlying marbles. In several places there are shale interbeds within the marbles, indicating isoclinal folding. The Pillar Marbles overlie all the formations and cover a large area. In several places they appear folded, creating sheath folds. Alkaline post-granitic formations cover a large area and are subject to all the pillar formations. It occurs throughout the northeastern side (Agios Nikolaos Bay) of the map and is in contact with Sodium-rich clinopyroxenes phreatic schists. Phengitic pyroxenic shales in contact with the above formations, there are phengite pyroxenic shales which differ from the muscovite, chlorite shales which will be described below. The difference lies in the fact that these formations are composed of also composed of Sodic-clinopyroxene (Mpounti et al., 2011)

About the metamorphic rocks and metamorphic events in the section Pillars are metamorphosed under high-pressure-low-temperature conditions and then under low-pressure-high-temperature conditions. More specifically, it is observed that the discovery of phengite in phyllite and phengite in the Cycladic shales is an indication of blueschist metamorphism. In the metamorphosed gneissic formations, the paragenesis encountered are Sodic-amphibole (glauconite, crossite and rhyme), epidote, zoisite, albite, white mica, opaque minerals, and minor quartz that define the blueschist metamorphism and the minerals albite, chlorite and epidote define the transition to the greenschist phase of metamorphism. In the meta-granites, albite, potassic feldspar, quartz, sodium pyroxene (aegir and jadeite), white mica, biotite and allanite were observed. In the meta-granites there is the paragenesis of quartz, potassic feldspar, biotite and fengite, so that the geobarometer of Massonne & Schreyer (1987) and Parra T., Vidal O., Agard Ph. (2002) can be applied. Below were taken the average temperatures for the area from previous surveys of about 370°C. Based on the Massonne & Schreyer geobarometer, a pressure of 11.5-13.5 kbar (diagonal pressure 11.5-13.5 kbar) was found and the metamorphism was blueschist at the boundary with the eclogite, while based on Parra T., Vidal O., Agard Ph. the pressure was found to be much lower, about 8kbar and the metamorphism was blueschist. (Mpounti et al., 2011)

Unit 2.3.2 Crystalline basement of upper plate according to Katsikatsos

The information selected from the book by Katsikatsos refers to the crystalline background of the Pelagonian zone (Upper Plate). In this plate, the crystalline basement occurs in the Galitsades-Aidipsos area of Northern Evia and in the Stophon-Metochia area of Central Evia. The age of the formations of this basement and their metamorphism is Late Middle Carboniferous. In the area of Central Evia, Neoproterozoic formations with fossils of Middle-Middle Carboniferous age were found above the bedrock. The basement formations in North

Evia are 800 m thick. These rocks are mainly biotitic gneisses and gneiss-schists metamorphosed into migmatites. In Central Evia there are marble intercalations above the parent rock. The Neopaleozoic formations are partially or slightly metamorphosed and occur with unconformable accretions over the parent rock. They are classic rocks with limestone intercalations in the Permian. The Neo-Paleozoic formation series consists of fine-grained sandstones and shaly sandstones, arkoses and graywackes, and in places clayey shales and phyllites and interbeds with conglomerate-gneiss-gneiss shales of Hercynian origin. The overburden is argillaceous at the base, mafic explosive as tophiform due to submarine outcrops, and finally the top is covered by lenticular shallow limestones in the Late-Middle Triassic (Katsikatsos et al., 1992).

Unit 2.3.3 Lower plate according to Katsikatsos (Ochi Unit)

What we knew about the geology of upper plate (Neohellenic cover) according to Katsikatsos (1992) was that given the absence of the Middle - Upper Cretaceous from the Neohellenic cover series, which is characteristic of the Interval Hellenes, we conclude that this thick series must belong to the External Hellenides considering that the middle-upper Cretaceous accretion is missing and that above the Styra unit the younger Ochi unit evolves which is overlying it. However, the Upper Cretaceous, which has been established by the above radiocarbon dating, with Sr isotopes, for the original sediments of the formations of the upper part of the marble horizon -sipolines of the Styra's of the Neohellenic cap does not agree with the age of the first metamorphism of these formations, because it is not possible to determine the age of the original sediments can be younger (Upper Cretaceous) than the age of the first of the first metamorphism of these sediments, which was found to be below -Mesocretaceous (120-85m.y.). These results, (Upper Cretaceous) for upper part of the marble-siliciclastic horizon of the Styra), do not agree with the results of the microtectonic study of these formations (G. l<ATSIKATSOS, J. MERCIER, & P. VERGELY, 1976a, 1 976b). This study shows that the Pillar-Ochi Formations have undergone two tectonic phases, one Tertiary and one older, Upper Jurassic-Lower. However, this is not justified, because the age of the original sediments of these formations cannot be Upper Cretaceous, as radiocarbon Sr isotope dating has shown, but Upper Jurassic or even older.

Lithostratigraphic horizons of the Styroi - Ochi units of the Neohellenic cap of South Evia, which, as mentioned above, from the basement to the roof are: The Tsaki schists, the Styra marbles, the sipolines, the Ochi formations. Lithostratigraphically, the Tsaki schists form the lower part of the Styron - Ochi Series, while tectonically they form the base of the Neoellinic tectonic cover, which is deposited in the indigenous section of Almyropotamos - Attica). Thestones of the Tsaki schists in the area of the southern part of the sheet "Aliveri" map ΙΓΜΕ 1991 (Fig.18), are incubated on the marbles of the Upper Cenomanian - Middle Eocene of the Unit Almyropotamos - Attica. On the contrary, further north, in the area of the northern part of the "Aliveri" sheet, the Tsaki schists are completely absent, so that the base of the Neolithic tectonic cover in this area is formed by the upper lithostratigraphic horizons of the Styra - Ochi unit. The Ochi formations are the upward gradational evolution of the marble-siliciclastic horizon of the Styra unit and have their main development in the southern part of the southernmost part of South Evia (Ochi - Karystos - Platanistos area) as shown in the map (Fig.19), where they form a thick series of formations, which are the most important in the

southern part of the area. They consist of mica, dolomitic, chlorite, glaucophane and quartz shale, in which there are often interspersed with allochthonous tectonic rocks of varying size and of varying lithological composition (Katsikatsos et al., 1992).

Smaller occurrences of these formations also exist in the area of Dystos - Petries, in southern Evia. The main characteristics of the Ochi formations, whose total thickness reaches 5,000 m, are the transformation of high pressure and low temperature conditions and the presence and presence in them of a large proportion of allochthonous rock fragments of various sizes and of varying lithological composition (meta-volcanic, serpentinites, radiolarians, etc.). According to R. VERGEL Y (1984), these fragments are evidence of large slides formed during the subduction that took place in the Malayan Ocean during the pre-orogenic period JE2, but this view has not been universally accepted. The Ochi formations were studied in detail by RH. and D. BAVAY (1980) in the area of their main occurrence (Ochi - Karystos - Platanistos area) (Fig. 19).(Katsikatsos et al., 1992).

Ochi row which comprises upwardly drifting from a lower set of schists, which are enriched upwardly by allochthonous mafic blocks. The schists consist of mafic and ultramafic rocks and radioclasts. There are mainly amphibolites, glaucophane and in places with losonite, muscovite, quartz (which sometimes becomes quartzite), limestone and chlorite. They also contain metatuffs and metabasalts. This is followed by a chaotic 'mix' of rock block fragments of varying size and different lithological composition, such as metabasalts, serpentinites and radiolarians. This formation is at its thickest on Mount Ochi and is absent from the Marmari area (Katsikatsos et al., 1992).

An upper set of rocks, which has been named the Paximadi series, consisting of alternating quartz - feldspar and muscovite schists and muscovite quartzites. This series is characterized by the presence in it of lenticular intercalations of acidic mineral materials. This formation is thickest on Mount Oki and is absent from the Marmari area. The Kakia Skala unit is tectonically located in the Ochi and Paximadi ranges and is composed mainly of quartzites and marbles that evolve upwards into quartz schists. It is characterised by the presence in it of blocks of radiocarbon fragments in high proportion. In the Ochi area it also includes serpentinite and metabasalts blocks. In general, the lower formations of the Kakia Skala unit are a lateral transition of the upper members of the marble-siliciclastic Styra horizon, while the upper formations are identical to the formations of the base of the Ochi Series. The Castri Range is tectonically located at the top of the Ochi Range and the Paximadi Range mentioned above. In general, it is the upward continuation of the Ochi Series and is divided into two parts. A lower part, consisting mainly of quartzite and an upper part, which is rich in large fragments (blocks) of varying lithological composition (transgressions, marbles, etc.), which are found in a schist environment, mainly of quartz schists and quartzites, with intercalations of metatuff and metabasalt sediments. At the top of this section there are also meta-arcoses and sipolines (Katsikatsos et al., 1992).

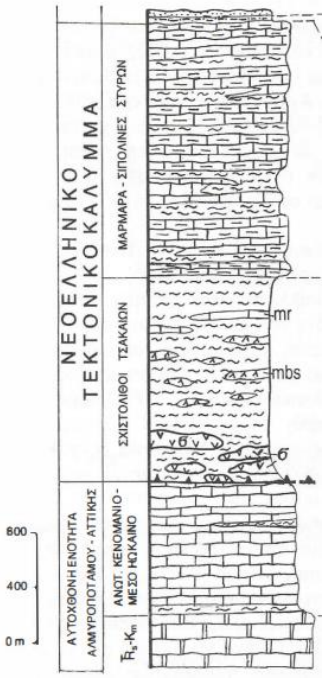

Figure 18: Geological map of ΙΓΜΕ, Evia, sheet Aliveri 1991. In map blue circled area is Tsakι schists. West of Tsaki schists is the Almyropotamos unit and east of it we have the Styra and Ochi unit and north of the map only Ochi unit. North there are no marbles in Ochi unit instead of Styra unit further South. Stromatographic column (Katsikatsos el al. 1992) shows as the units from the basement to the top.

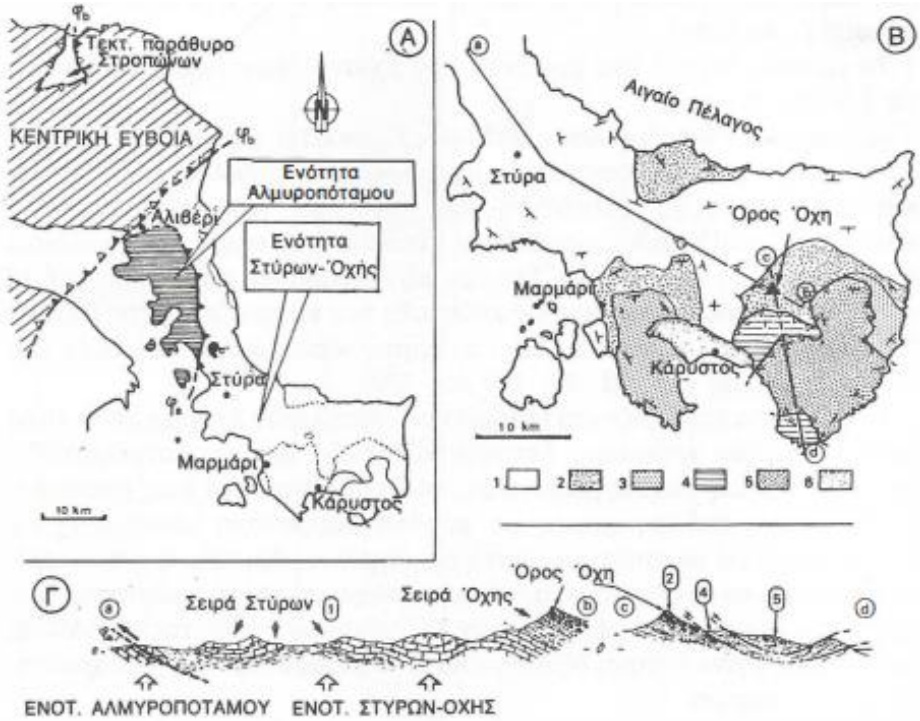

Figure 19. Formations of Neohellenic nape of S. Evia, Styra and South formation of Ochi unit. (Katsikatsos 1992)

Everything we know about Ochi unit is that on the base of the Ochi nappe, a ca. 100 m thick suite of metagranitoid rocks was mapped at a scale of 1:50.000 scale. The metagranitoid suite is intercalated with albite and mica schists, and is characterized by moderately to highly strained bodies that have concordant contacts with the adjacent schists. Both metagranitoid rocks and schists display a well-developed ESE)–WNW trending stretching lineation defined by the shape-preferred orientation of sodic amphibole needles as well as elongated crystals of feldspar and quartz. There are two different types of metagranitoid rocks. The one type is bright-colored and free of sodic amphibole while the other is dark-colored and contains sodic amphibole. In mesoscopic scale, bright-colored metagranitoids form lens- and tabular-shaped bodies of dark-colored metagranitoids, which can be several decimeters thick. Although in places concordant, the initial contact between the two metagranitoid rock types is obscured, due to subsequent pervasive Alpine ductile deformation. It is considered unlikely that this scenario applies to the Attic-Cycladic zone due to the geochemical signature of mafic rocks from the ophiolite-bearing HP-mélange (Ochi unit) on Evia and from HP-mélanges on adjacent northwest Cycladic islands. Research indicates that the geochemical signatures point to a supra-subduction zone origin. Additionally, it is suggested that a Triassic age should be assumed for some of the mafic rocks in the Blueschist unit, however, this is contradicted by the Jurassic/Cretaceous isotopic ages of gabbroic rocks in the HP-ophiolitic mélange on Syros, Tinos and Andros. It should be noted that the HP-ophiolitic mélange of the Ochi unit, based on its tectonostratigraphic position, can be considered equivalent to that on Syros. Therefore, the presence of A-type plutons seems to be more concise with a Late Triassic tectonic reconstruction. In this paleogeographic context, the position of the Blueschist unit basin depocenter remains unclear. Note that both a Pindos and a Vardar origin have been proposed for the Mesozoic protolith of the Blueschist unit. A-type felsic magmatism recognized in this study implies an incipient rift environment for the Late Triassic Cycladic area, meaning that a

stage of full oceanization was probably not attained at that time. As a result, considering various models that suggest oceanic spreading in both the Pindos and Vardar basins during the Late Triassic period, it appears that the documented felsic magmatism on Evia must have taken place in the subsiding passive margin (either eastern or western) of Pelagonia.(Fig. 2a). However, U–Pb zircon ages of ca. 80 Mya from meta-gabbroic rocks in the meta-ophiolite bearing HP-mélange cropping out on several Cycladic islands, indicate Late Cretaceous oceanic magmatism, which has not been recorded from Pindos ophiolitic rocks. A similar HP-mélange also occurs on southern Evia and together with the dated metagranitoid rocks constitute the Ochi nappe. As a result, it is reasonable to assume that the Mesozoic protolith of the Blueschist unit is linked to the Vardar rather than the Pindos ocean (U–Pb single zircon ages and geochemistry of metagranitoid rocks in the Cycladic Blueschists (Evia Island): Implications for the Triassic tectonic setting of Greece) (Katsikatsos et al., 1992).

The uppermost Ochi Formation, exposed mostly on the southernmost tip of Evia, consists mainly of metapelites with subordinate intercalations of quartzites, metatuffs, and metabasites. It also contains metabasic bodies, and serpentinites near the contact with the underlying Styra Formation (Katsikatsos et al., 1992).

Microstructures of the Styra and Ochi formations record a metamorphic-deformation history that starts at blueschist-facies conditions with the development of a fabric that includes a glaucophane lineation, and continues at lower pressure conditions in which albite and epidote porphyroblasts grew. The rocks were folded after the formation of glaucophane lineation. Albite porphyroblasts developed syn-kinematically and later statically, enclosing a deformed foliation of earlier generations and relict glaucophane prisms. Most glaucophane crystals are broken at crenulation hinges or boudinaged, and biotite grows in boudin necks. Where pressure shadows are found in blueschists, they lack a distinct asymmetry. An unequivocal sense of shear could not be deduced from microstructures in blueschists of the Styra and Ochi formations. In retrograded rocks of the Ochi Formation on the other hand, a top-to-the-SE to SSW sense of shear was deduced from S-type (Simpson, 1986) tails at pressure fringes of albite porphyroblasts. This was found in rocks having a lineation dominated by greenschist fabric crenulations and elongated quartz-feldspathic aggregates parallel to the crenulation hinges. This fabric must be associated with exhumation of the South Evia Blueschist Belt as it is a syn-tectonic overprint expressed by the growth of greenschist-facies minerals (Katsikatsos et al., 1992).

In the Almyropotamos unit, but also in the blueschist zone of South Evia, which consists of the Tsaki schists, Styra and the Ochi unit of South Evia, the only feldspar is albite. This is true for the type of occurrence of pre/post-mobile deformed porphyroclasts and the type of occurrence of co/post-mobile deformed porphyroclasts. Also, except for albite, the composition of all white mica present in the blueschist zone is similar. That is, we have phengites containing 3.2 to 3.6 Si p.f.u., such as those of the Almyropotamos unit. Also, the presence of biotite with glaucophane is a fact. Blue amphibole is found in all the formations of the blueschist zone, such as the ferruginous schist with a high content of bivalent iron and some are cross-cutting between ferruginous and riebeckite. But the most important finding is that Na-clinopyroxene was found in two locations, in a metabase block in the Tsaki Formation and in intermediate basement schist at Styra unit. This pyroxene consists of two interlocking phases: a jadeite phase and an aegirine phase. The results for our area of interest, the Ochi unit in particular, are shown in the diagram below (Fig.20). (YONATHAN SHAKED et al., 2000).

In the South Evia Blueschist Belt pressure estimates are based on the abundant presence of sodic-amphibole, the high silica Si $_{(3.6)}$ content in phengite, and jadeite (Jd) $_{(0.7)}$ pyroxene. The pressures experienced by the Blueschist Belt were at minimum 10–12 kbar (Fig 21), perhaps slightly higher than those inferred for the Almyropotamos Unit. This is apparent from the higher Si content in phengites of the Ochi Formation and the higher Jd content in Na-Cpx (YONATHAN SHAKED et al. 2000).

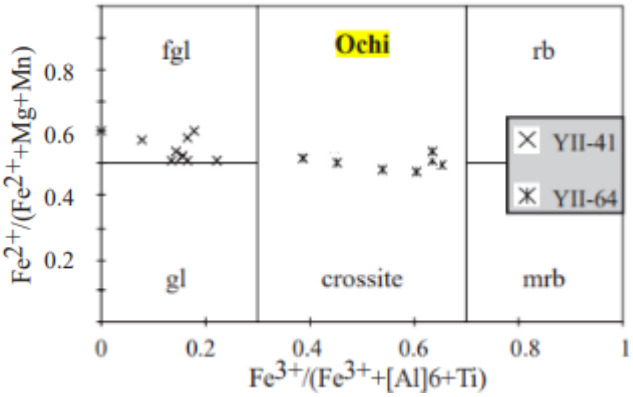

Figure 20: fgl: Ferro-glaucophane, gl: glaucophane, rb: riebeckite, mrb: magnesioriebeckite. Ochi unit of blueschist belt is characterized by fgl and crossite minerals with sodic, Fe^{2+} and most Fe^{3+} high content.

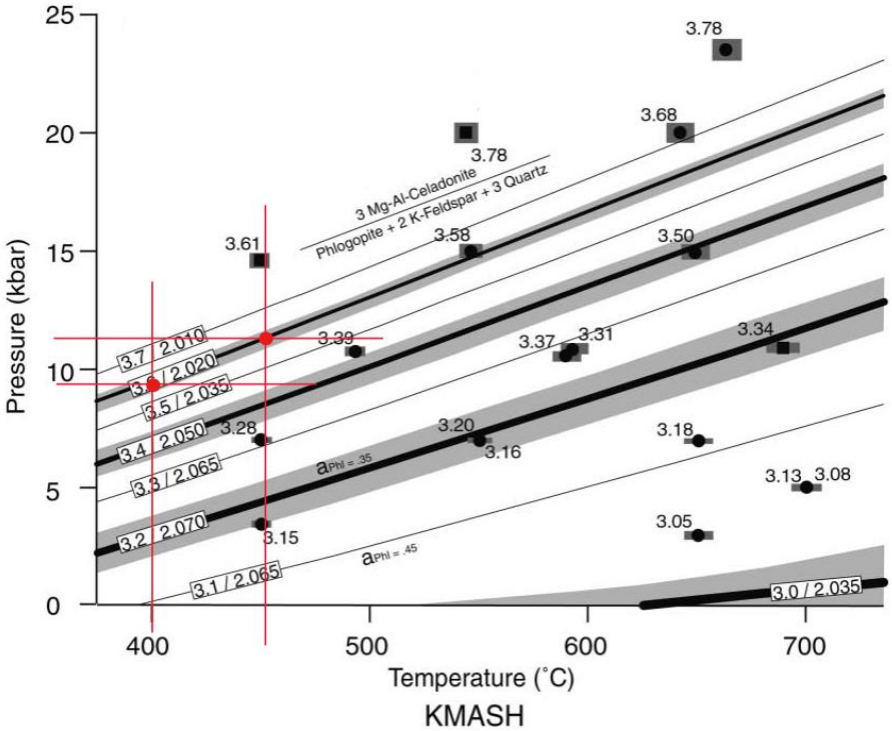

Figure 21: Samples from Ochi unit have Si content 3.6 and their minerals indicates that the unit was found under conditions of pressure 10-12 kb and temperature 400-450°C. Results on the recalculated KWM Tschermak isopleths in the presence of phlogopite–K-feldspar–quartz and water (KMASH system) (Teddy Parra et al. 2002).

Chapter 3

Unit 3.1 Preparation before fieldwork

For the purposes of fieldwork, two geological maps of ΙΓΜΕ (sheet Aliveri 1991 and sheet Kymi 1981) (Fig. 23) have been overlayed in google earth pro. The map image files had been converted into a format that the program can recognize and attached the maps in digital format onto the Google Earth Pro map. After the successful georeference of them, the polygons (vector files) of the formations of interest near Petries, Trachili, and Ochtonia were digitized. The red-colored formations are basalts, and the blue-colored formations are granitoids. Blue points which are shown below indicate the sampling locations. Some sampling points were close to points (in yellow) from previous fieldwork work in our department (Fig. 22).

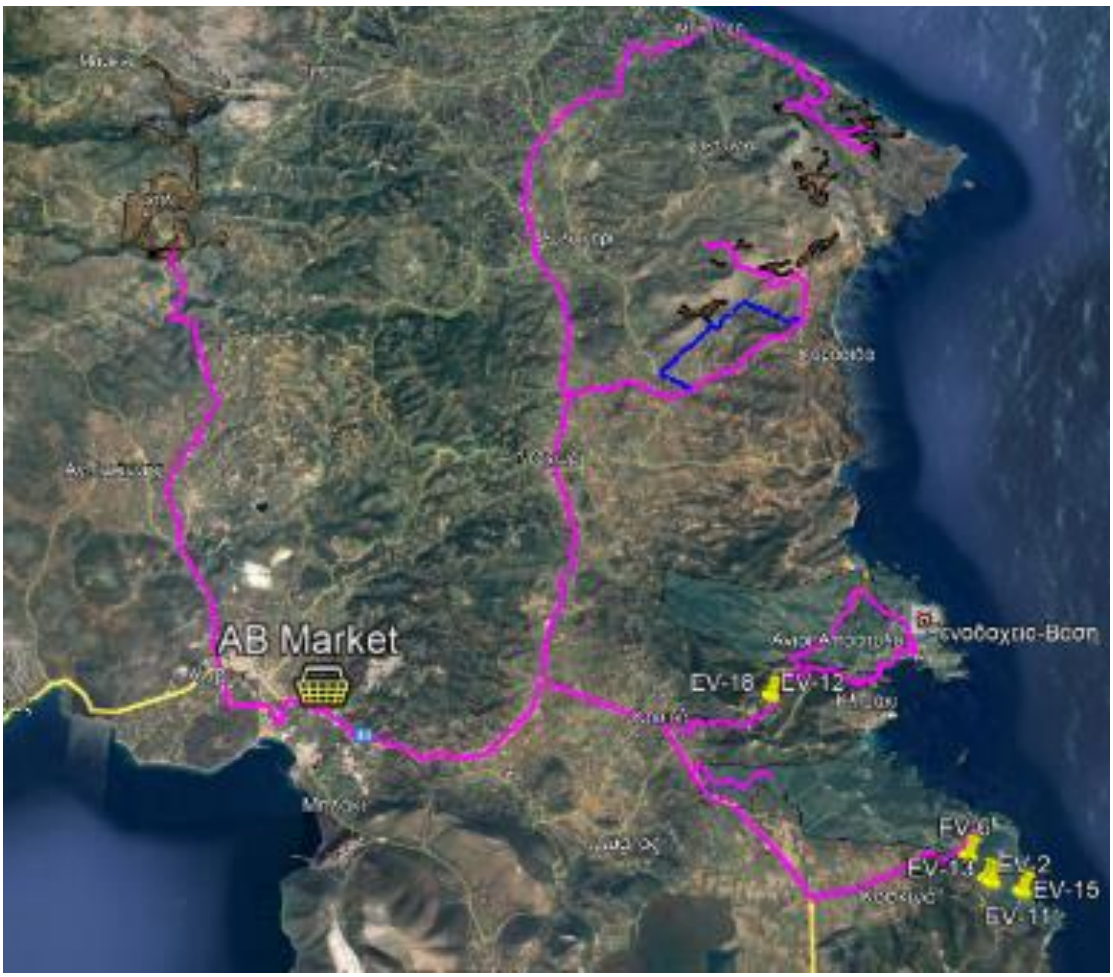

Figure 22: Metabasaltic (red colored) and metagranitic (blue colored) formations are shown on google earth pro, based on ΙΓΜΕ Kymi (1981) - Aliveri (1991) sheets.

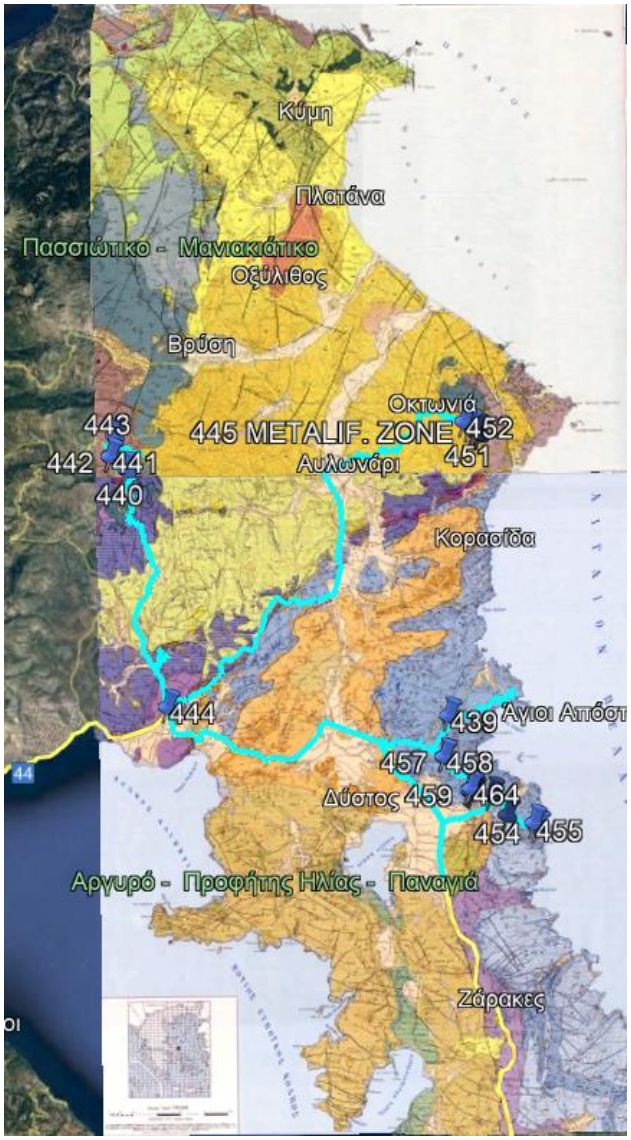

Figure 23: Map of ΙΓΜΕ (Kymi (1981) – Aliveri (1991) sheets) on google earth pro.

Unit 3.2 Fieldwork

Below there is a description of the fieldwork based on the two days plan that was scheduled and followed. The areas where the research was done in central Evia is the village of Trachili which is located north of the Paramerites and geologically according to the ΙΓΜΕ bibliography it is characterized by occurrences of volcanic mafic and ultramafic rocks (lavas) of the Lower-Middle Triassic, overlying carbonate sedimentary such as limestones of the Triassic- Jurassic and Neogene sediment with scattered olistoliths of ophiolite mélange. Near and around the Octonia rift, in accordance with the bibliography and the notes of the ΙΓΜΕ maps, there are also handles of the same composition on the surface and above them are marbles and limestones as before. Finally, according to the bibliography of Katsikatsos, near the village of Petria, which is south of Agioi Apostoli, the geology we expect is to encounter epidotetic and glaucophanitic mainly schists that will be tectonically overlain by limestone, marbles and flysch of the Styra unit.

Unit 3.2.1 Day 1

On the first day 11 stops were made, covering the Upper Plate of Central Evia: Trachili Village (4 stops) and the Mountain of Octonia-Achladeri-Avlonario (6 stops) (Fig. 24).

Figure 24: Path of first day, Kymi (1981)- Aliveri (1991), on google earth pro

At the first stop in Petries a sample 439 was taken (Fig.25). The rock type is mica marble (fengite) with fengite recrystallization (Fig.26), a sugary texture and green color. Observing from a distance we see dense banks, dense beds, strongly foliated marbles. Plastic behaviour is inferred because these marbles are deformed. This can be understood from the phengite which shows a temperature range of 300-400°C. Congruent parallel Quarz veins were observed (probably related) and foliated texture. S-type mylonite's with boudinaged courts are clearly visible with tectonic features such as Foliation 010/45 Lineation 056/20 (Fig.27). The sense of shear is top to NE.

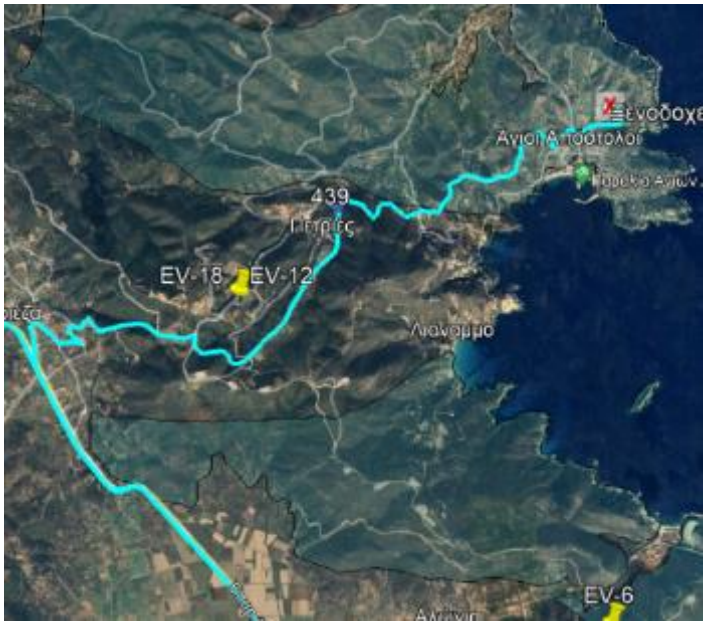

Figure 25: Map that indicates the position of the first stop for sample 439, on google earth pro.

Figure 26: Sample location no. 1, Carbonates, Phengite Marbles at first stop.

Figure 27: Carbonates, Phengite Marbles at first stop with the pencil positioned parallel to the lineation.

After the first stop, the investigation continued to the Trachili Village (Fig.28). After observing the first volcanic occurrences, we started to collect samples. As we moved northward, we continued to collect volcanic samples.

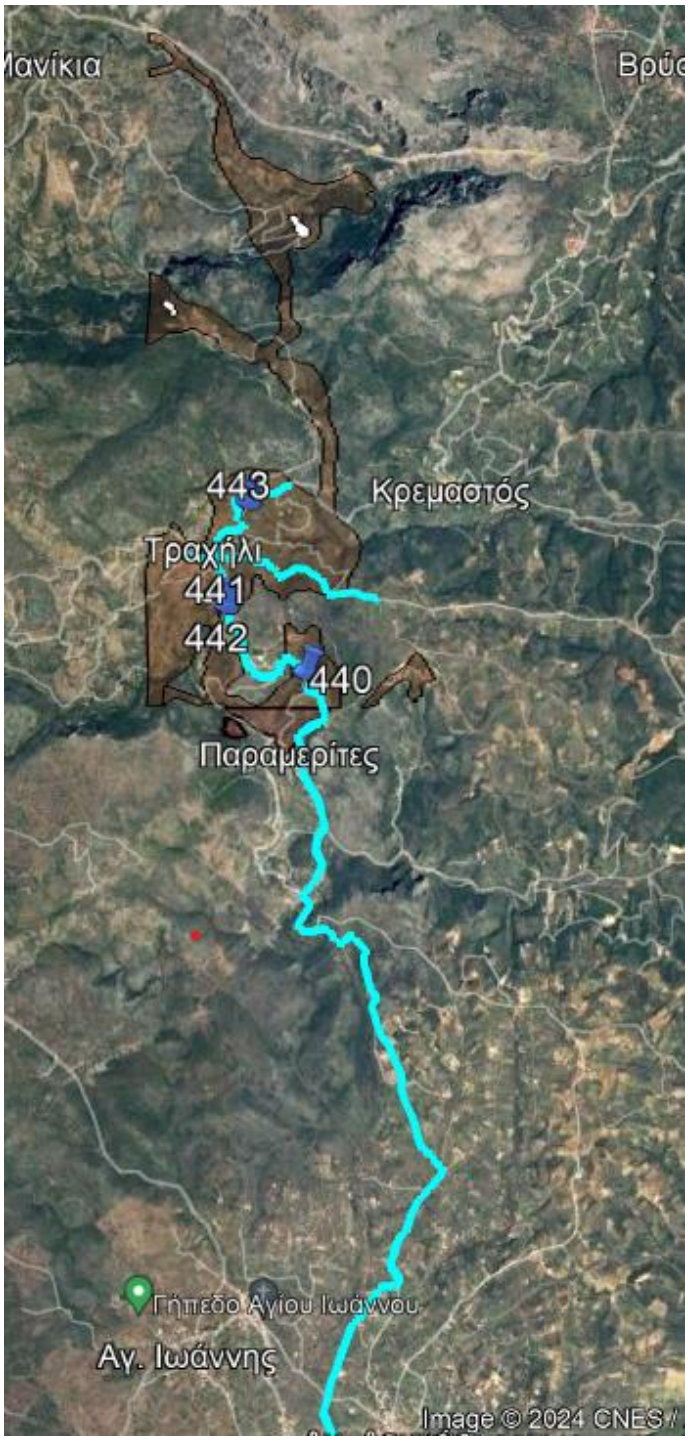

Figure 28: Map of Thrachili Village with the sample collecting stops pined, on google earth.

At the second stop, sample number 440 was taken and red, brown, green even black colored basalts were found over limestone. Secondary fluids have paid the cracks with quartz because there is pronounced crushing. Also observed is that basalts with heterogeneous structure and

strongly oxidized. East of the road there were other altered mafic-ultramafic rocks such as serpentinites.

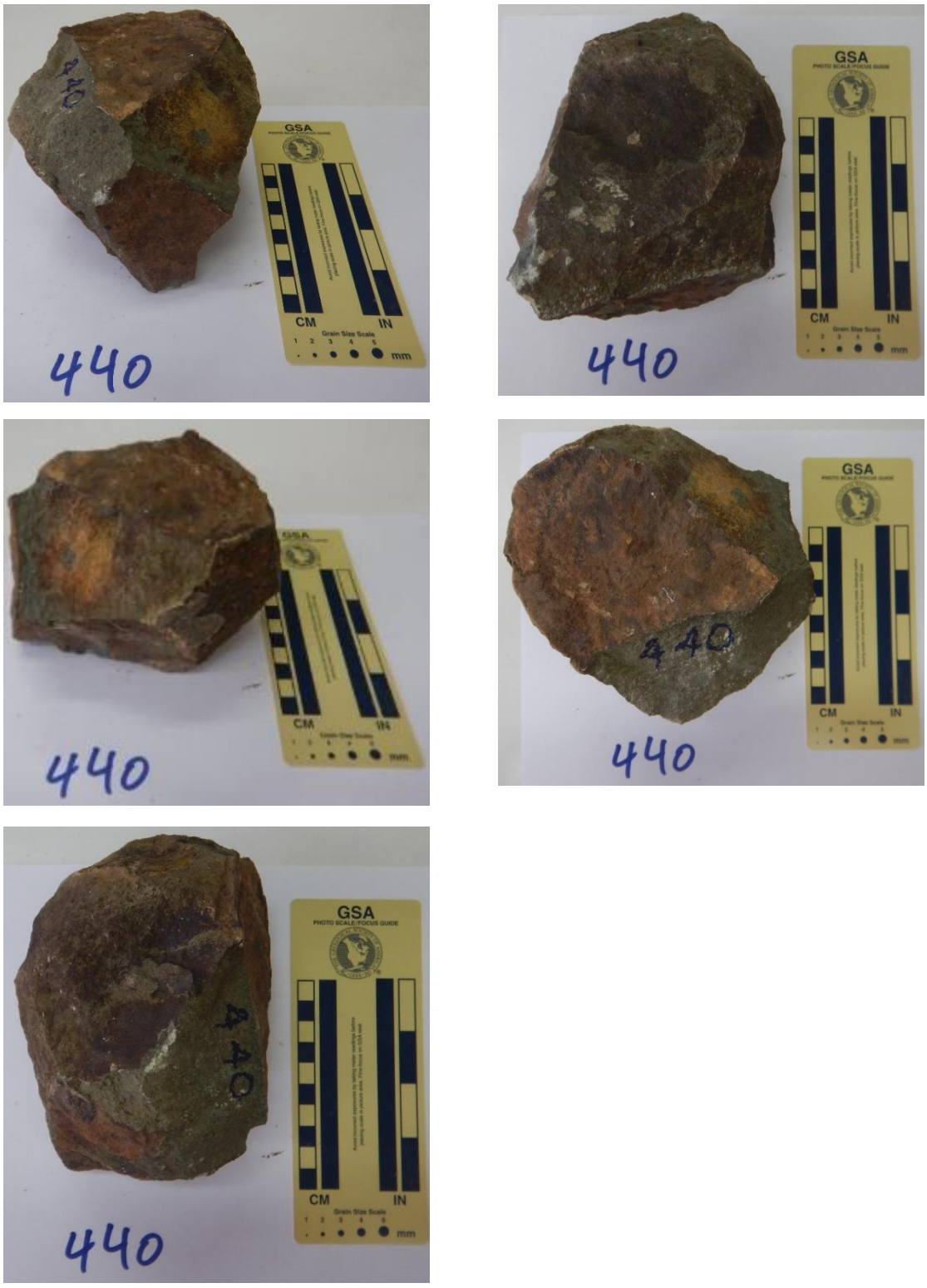

Figure 29: Sample 440: Basalt, collected from stop no.2 at the Trachili Village,

Figure 30: Sample location no.2, basalts (mafic rock) fragmented and compact formation, where the sample 440 was collected.

As we moved north to the 3rd stop (sample number 442) we found basalt flows. Solid fragments with intense fragmentation greener than those of the previous stand with reddish-

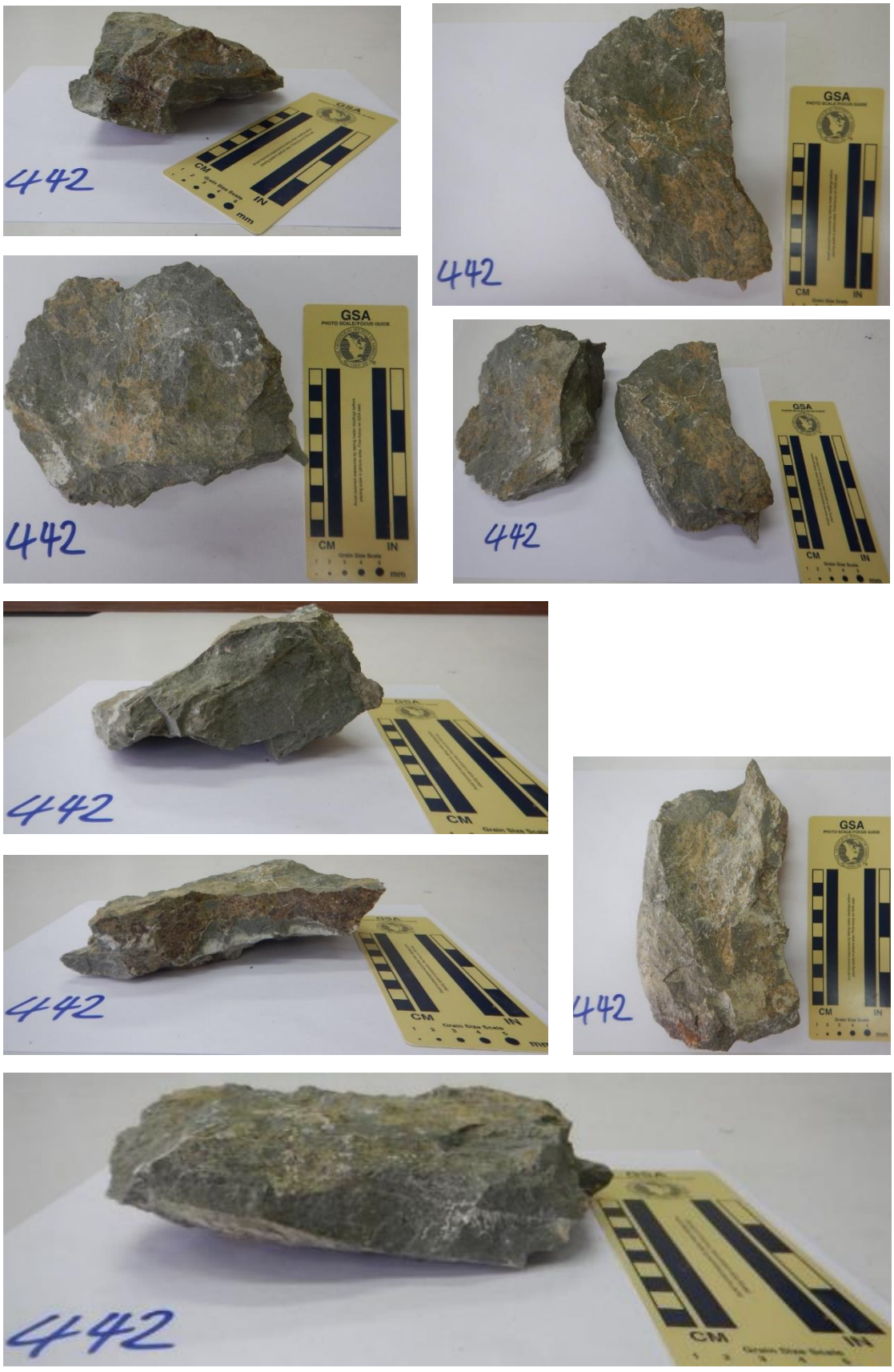

Figure 31: Sample 442: Basalt, collected from stop no.3 at the Trachili Village.,

brown shades due to oxidation by meteoric water. In the rock structure, irregular small quartz and carbonate veins are observed in the solid pieces of mafic rocks in which the rock has been fractured.

Figure 32: Location no.3, Greenish-red blocks with local breakage and oxidation. The image of the 3 stop is volcanic fragments erupting from the surrounding sedimentary (limestones) in the area.

At the forth stop the sample 443 was taken from the corner of the road where there was green-black basalts with aphanitic texture with whitewash minerals such as quartz and calcite. Macroscopic green and black minerals such as chlorite, epidote, amphiboles, pyroxenes and Plagioclase are observed.

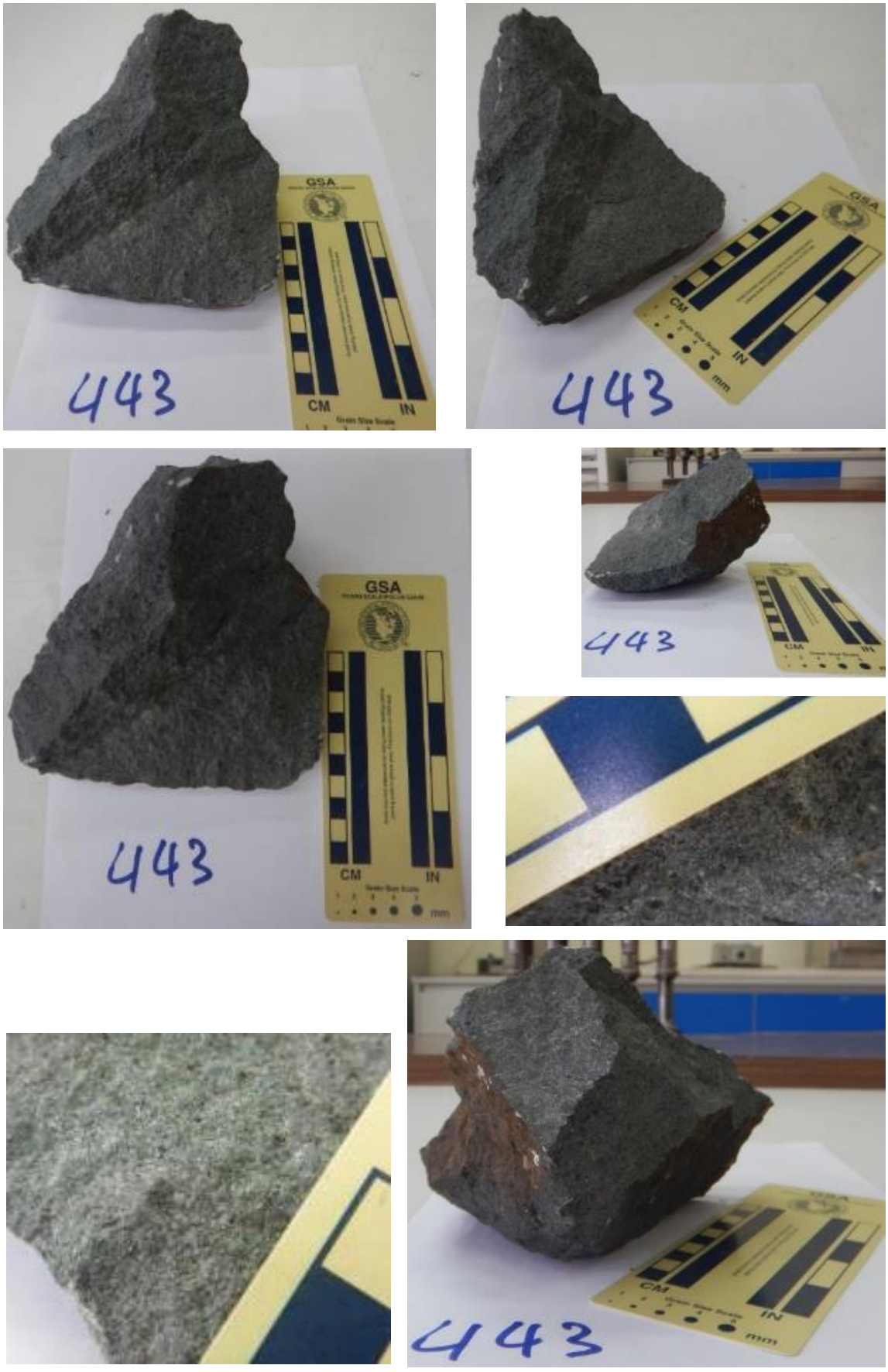

Figure 33: Metabasalt sample 443 has aphanitic texture.

Figure 34: Location no.4, solid and altered basalt rock.

The second exploration area was located near to Ochtonia detachment where there were no mafic rocks such as basalts-metabasalts, but a kind of argilites (minerals that characterize them such as kaolinites, minerals of the montmorillonite group, illite with oxides and hydroxides), due to massive alteration of basalts which are very friable microgranular rocks, white to beige color and their observation began as soon as the appearance of carbonate sediments ended. The first sample taken from this exploration area was number 444 from 5th stop.

Figure 35: Sample 444

Figure 36: Location no.5

At site 6 we observed a beginning of the metalliferous zone (sample 445) consisting of fine-grained clay minerals, white and light brown to orange colored. Near us began a huge area which is depicted as lavas according to the geological map of ΙΓΜΕ as shown below (Fig.38) in google earth pro, which turns out to be a large hydrothermal conglomerate which has emerged from the Ochtonia faults and the surrounding sedimentary mountain tops and has eroded the rocks of the area. It is evidence of alteration to clay minerals we can see there.

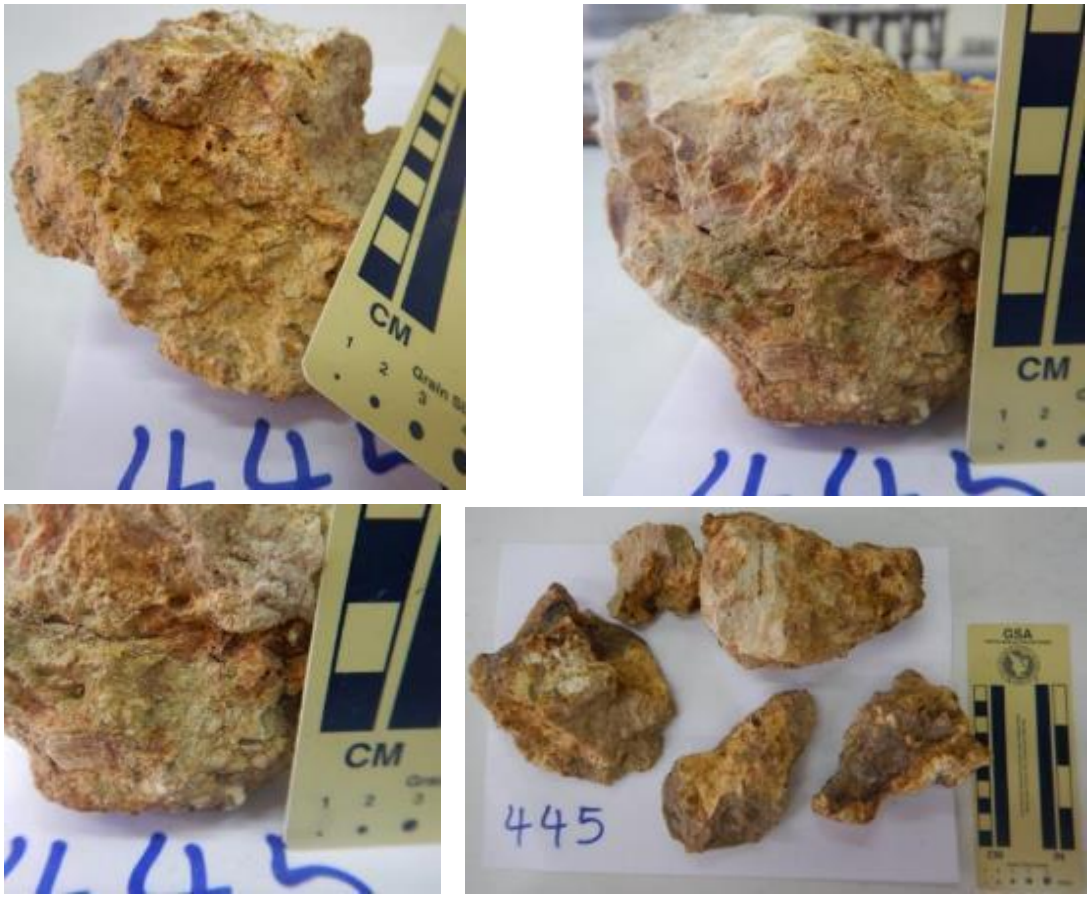

Figure 37: Sample 445 hydrothermally altered rock of yellow to orange and black color.

Following the clay alteration by taking metalliferous basalts in two samples (7th stop) 445A and 446 from the same location.

Figure 38: The path followed on google earth pro map during the sampling in lava according to ΙΓΜΕ

Figure 39: Sample 446

Figure 40: Location between 6-7 position (beginning of alteration)

At 8th stop (447) sample was not taken but the hydrothermally altered rocks were described as is shown below.

Figure 41: Location no. 8, hydrothermal breccia.

As at site 9 in the hydrothermal breccia (HWBX) (sample 448) and with sample 449 it could be confirmed that the existence of hydrothermal breccia that has basalts and (kaolinite probably) white-colored, fine-grained and metallic minerals replacing the basalts.

Figure 42: Sample 448, white to green minerals.

Figure 43: Location no. 9, hydrothermal breccia, leucocratic and altered minerals such as Sericite or Kaolinite.

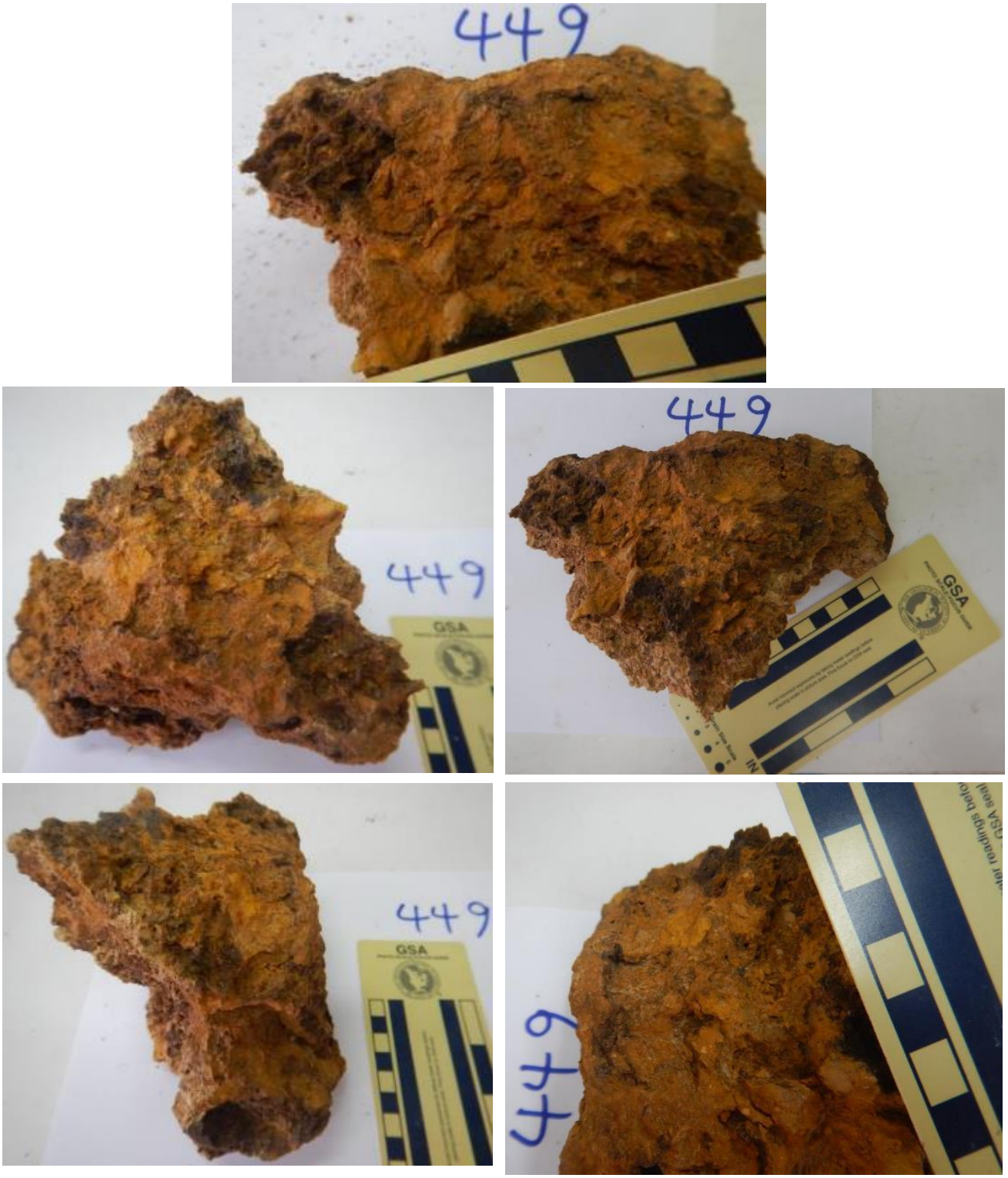

Figure 44: Sample 449, hydrothermally altered rock of yellow to orange and black colour.

We end with stop 10 (sample 450) with another metalliferous basalt.

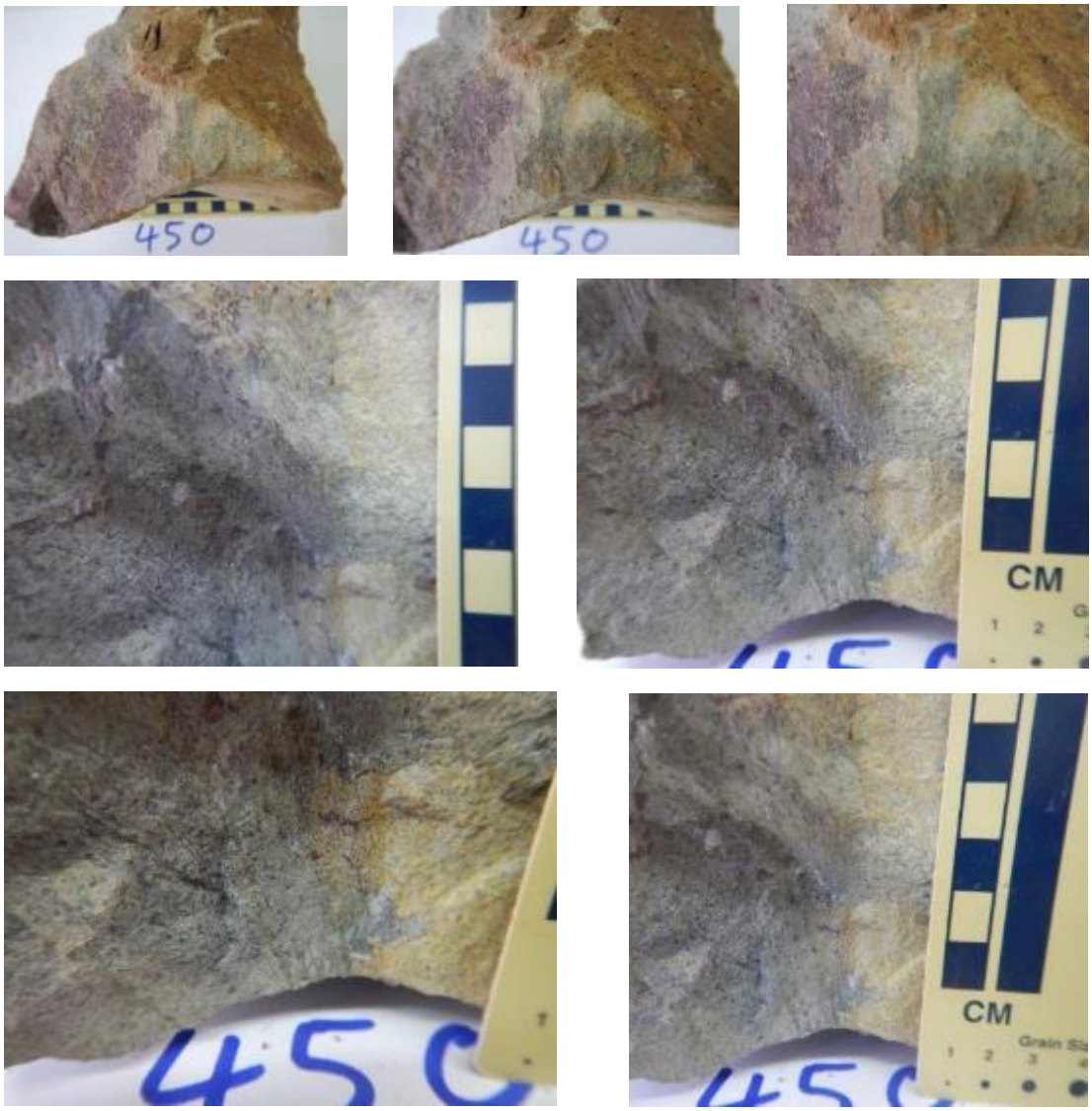

Figure 45: Sample 450, aphanitic texture and heterogeneous structure, as the secondary penetration of the vein into the basalt appears. Hence the existence of two brownish-green colors in one part of the sample and a much lighter one in the other.

Figure 46: Sample 450

Figure 47: Location no. 10

At the next stops, samples weren’t collected.

Figure 48: Location no. 11, (451) no sample from here .

Figure 49: Picture from (452) no sample location, Strong alteration with coarse grained loose material of white clay minerals

Figure 50*: Picture from (452) no sample location, there appears to have been former mining activity*

Carbonate observations during the ascent:

It is noted for the calcareous aggregate that we change from the category supported to mass supported. That is, grain contact is from branch to branch while as we ascend (increasing elevation) we notice that the grains are supported by the main mass due to basin fouling. More specifically we observe black micritic and also white grains in the branch and less black in the mass.

Initially in our attempt to check the ages of the sedimentary rocks i.e., the unmetamorphosed limestones in the hanging wall of the Pelagonian fault and the metamorphosed ones i.e., the marbles in the footwall, it is observed that in some rocks of these two groups a correlation is made while in others it is not. The ages of most of the marbles are later than those of the limestone group, which are correlated within a few million years of each other. This makes sense as the footwall of metamorphic rocks is exhumed. However, particularly in the area of the Styra unit, in almost all marble samples there is no correlation between these metamorphic and some corresponding unmetamorphic hanging wall samples. As the most recent unmetamorphic (NE of Psachna) are Late Cretaceous in age and some metamorphics mainly of the Styra unit are Medium Miocene in age which is a difference of tens of millions of years (Fig.51- Fig.52).

Sample #	Locality	Assumed age	Seawater-curve Age					Age agreement
			Age (Ma)	$^{87}Sr/^{86}Sr$	Stage/Age	Series/Epoch	System/Period	
Unmetamorphosed limestones, northern and central Euboea								
5913	NE of Psachna	Late Cretaceous	79	0,7075	Campanian	Upper	Cretaceous	Y
5879	NE of Psachna	Late Cretaceous	88	0,7073	Coniacian	Upper	Cretaceous	Y
2100E	6km SE of Prokopion	Late Jurassic	160	0,7067	Oxfordian	Upper	Jurassic	Y
2529	near Steni	Late Triassic	198	0,7076	Sinemurian	Lower	Jurassic	Y
2101E	near Aedipsos	Late Permian	253	0,7076	Changhsingian	Lopingian	U. Permian	Y
Marbles of southern Evia								
3148	Styra	Late Cretaceous	14	0,7088	Langhian	M. Miocene	Neogene	N
2747	Styra	Late Cretaceous	23	0,7082	Aquitanian	L. Miocene	Neogene	N
E100K	Styra	Late Cretaceous	0	0,7093				N
3328	Styra	Late Cretaceous	75	0,7076	Campanian	Upper	Cretaceous	Y
2592	Panagia	Late Cretaceous	16	0,7087	Langhian	M. Miocene	Neogene	N
3126	Attica (Argyron)	Jurassic to Late Cretaceous	165	0,7069	Callovian	Middle	Jurassic	Y
3145	Argyron	Jurassic to Late Cretaceous	165	0,7069	Callovian	Middle	Jurassic	Y
3152	Argyron	Jurassic to Late Cretaceous	160	0,7067	Oxfordian	Upper	Jurassic	Y
3171	Argyron	Jurassic to Late Cretaceous	167	0,707	Bathonian	Middle	Jurassic	Y
2447	St. George	Late Triassic	255	0,7072	Wuchiapingian	Lopingian	U. Permian	~Y
2448	St. George	Late Triassic	249	0,7081	Olenekian	Lower	Triassic	~Y

Figure 51: Geochronology of limestones and marbles of Evia with strontium isotopes. Comparison of ages of metamorphic and unmetamorphic rocks.

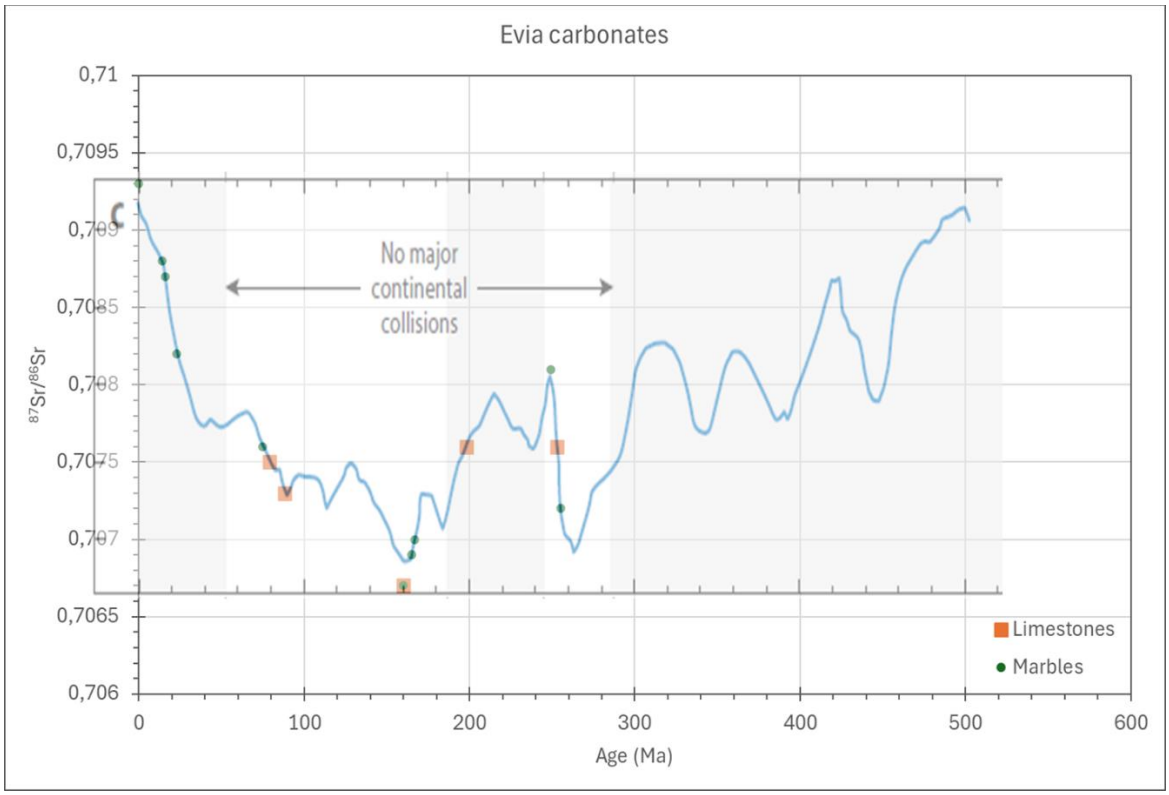

Figure 52: Projection diagram of ages of grouped limestones and marbles of Evia according to the ratio of the isotopes of strontium. As we get closer to zero, the gap between the limestones and the corresponding marbles becomes more obvious.

Unit 3.2.2 Day 2

The area of interest on the second day of the field survey was near to Petries and the route from where samples were collected was as follows:

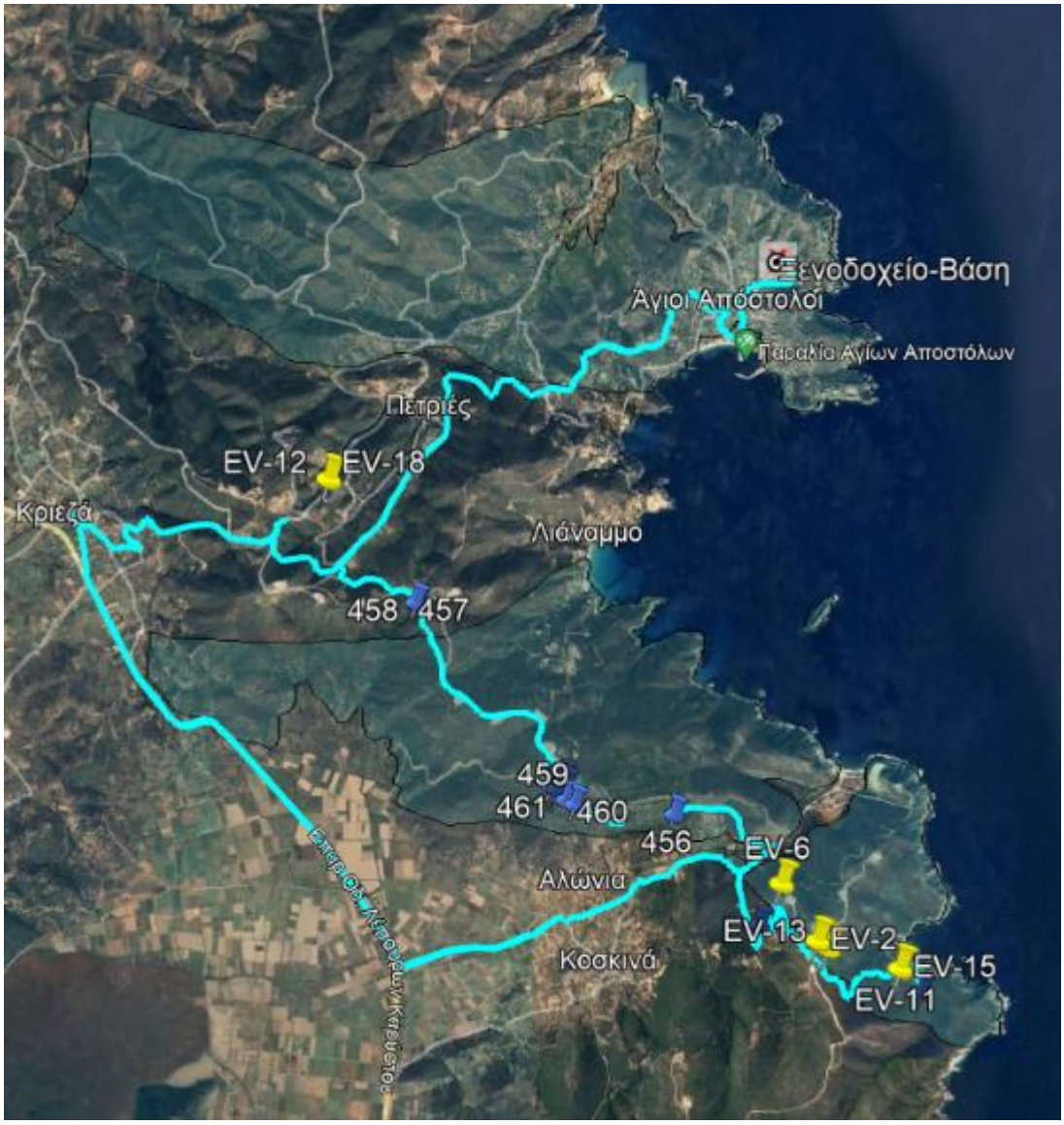

Figure 53: A map of google earth pro shows the orthogneisses of Ochi unit (blue color), the route followed and the sampling points (blue color).

We started from our base at Agioi Apostoloi and headed south-east. The points of interest are located on either side north and south of Petries. The first stop was just outside the digitized meta-granitic formation as interesting basaltic sills were observed which are trapped within granitic bodies as both together have been tectonized and deformed.

More specifically at our first location, sample 453 was taken from a Micro granite-Orthogneiss which is an acid metamorphic rock, with sugary texture and fine-grained rock which contains white, gray and green minerals such as Quartz, biotite, Potassium feldspars, white mica and hematite. Also observed were L mylonite and synfoliated (thick) Quartz veins

(cm) which are post tectonic. With foliation: 050/43 and Lineation 080/65 and sense of shear top to the SW.

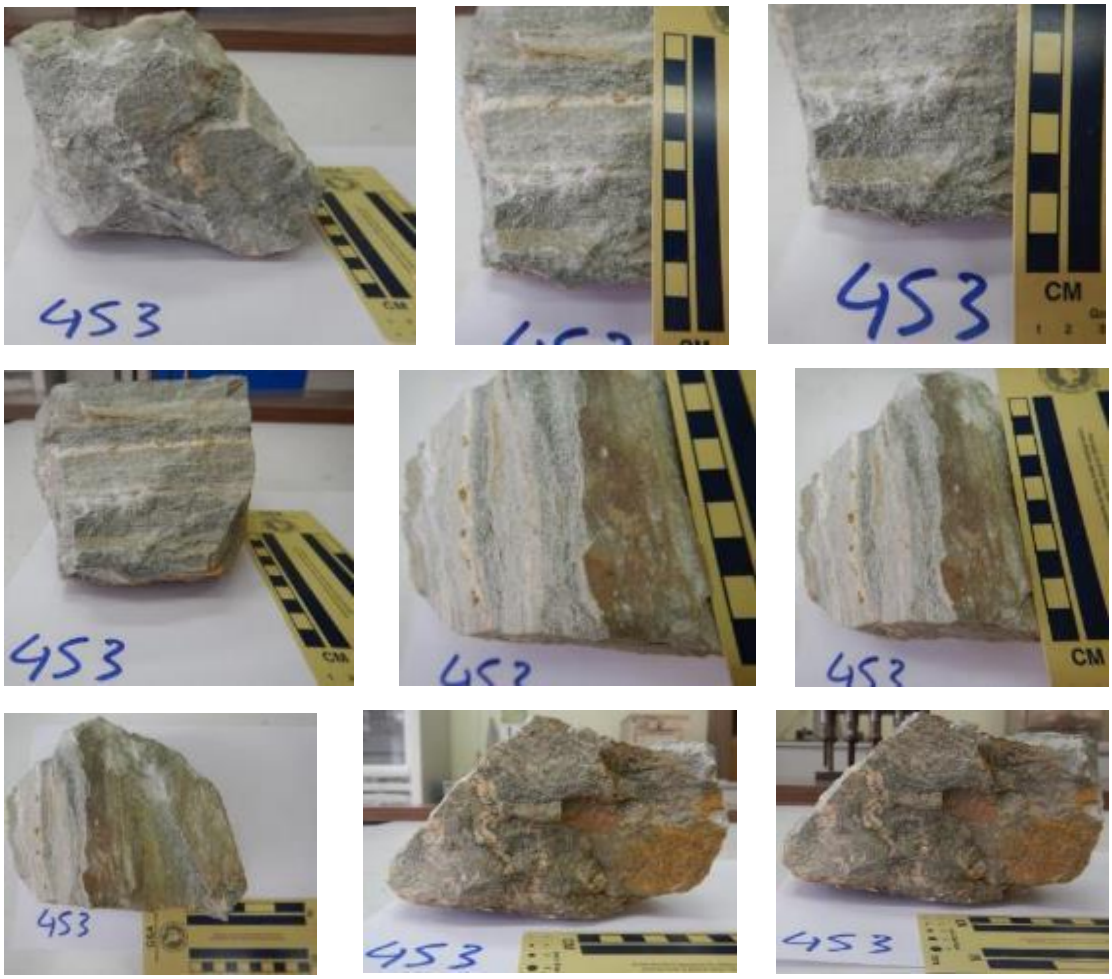

Figure 54: Sample 453, evidence is presented for strong ductile deformation and content in rounded porphyroclasts and lithic fragments of similar composition to matrix minerals.

Figure 55: Location no. 1, strongly deformed as shown by a supergiant porphyroblast

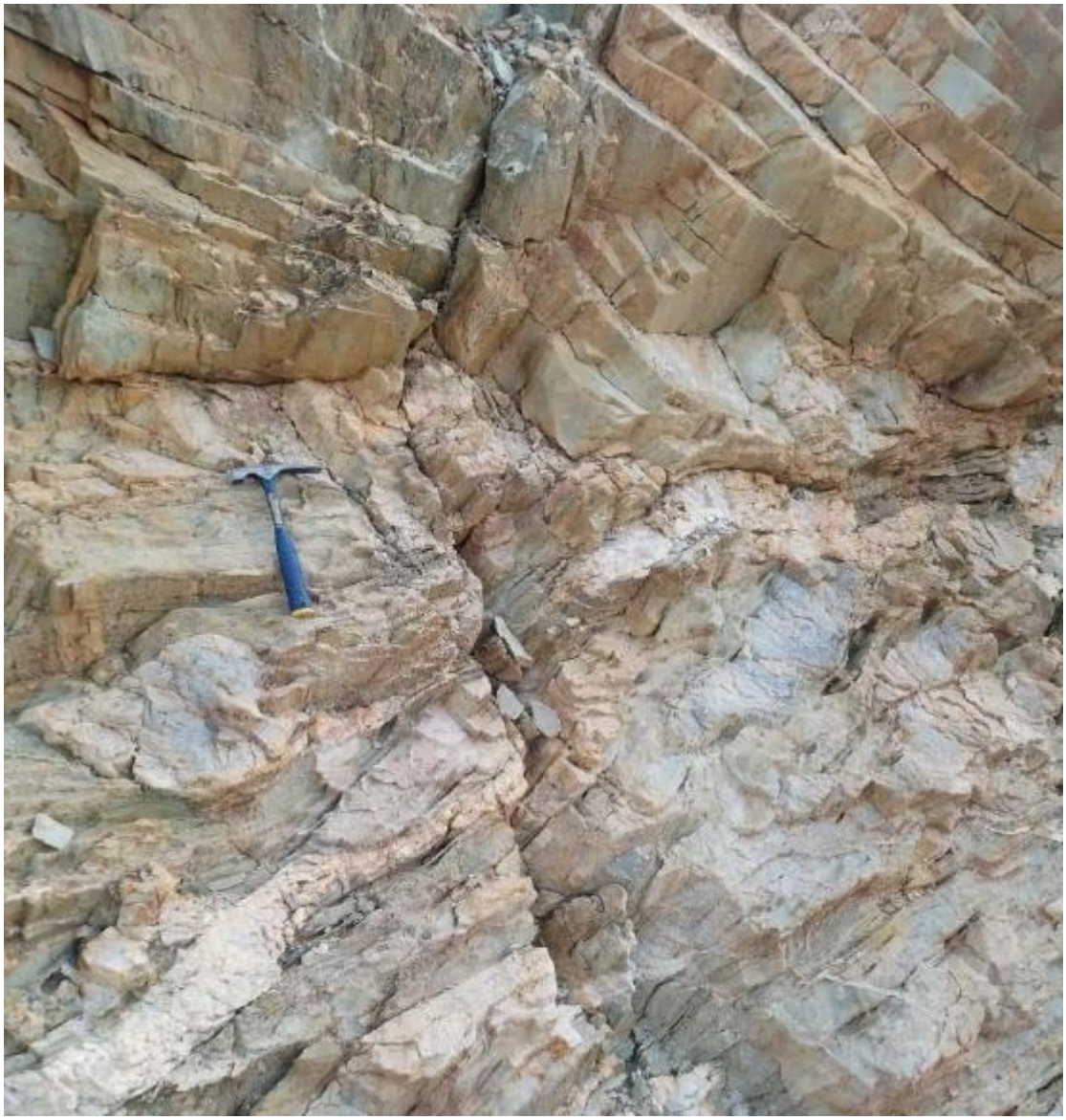

Figure 56: Location 1, fragmented deformed gneisses, where the thin bands were created by shearing are almost parallel to the foliation.

Figure 57: Sample 454

Figure 58: Location no. 2 this banded orthogneiss shows intense reflection

At third stop (location no. 3 with no sample), a point worth mentioning is the kinematic tectonic which are: foliation: 060/33 and lineation: 042/38.

At 4th stop 456 was observed horizontal foliation and lineation with kinematics tectonic: foliation: 061/10 and lineation: 061/03.

Figure 59: Sample 456, metallic minerals (hematite) inside Quartz veins.

Figure 60: Location no. 4, Intense tectonic, foliated and lineated microgranite-orthogneiss.

Figure 61: Deformed and fractured geological environment

At the 5th stop 457 are visible orthogneisses and basalts that are fine-grained and metamorphosed. Characteristic are the colors of the mafic rocks that become greener and more altered. Mafic sills are clearly folded, strongly foliated or boudinaged syntectonic during metamorphism in their host rocks that are gneiss. So, the rocks have a strongly heterogeneous structure because of the change in chemistry and mineralogy from the secondary mafic sills that due to the shearing of the gneisses filled the gap in their structure. The length of the mafic "eye" was about 30 meters and sample number 458 was collected near to 457.

Figure 62: Sample 458, dark and green minerals like chlorite, zoisite, epidote.

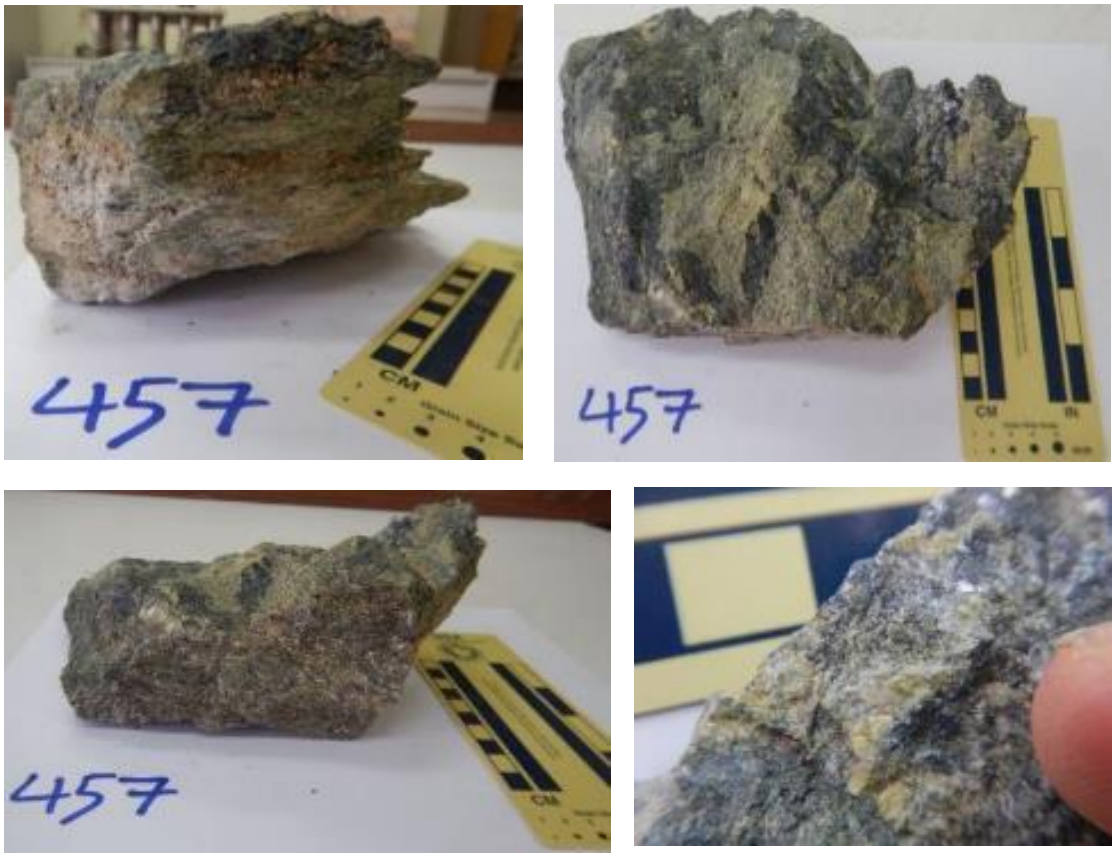

Figure 63: Sample 457.

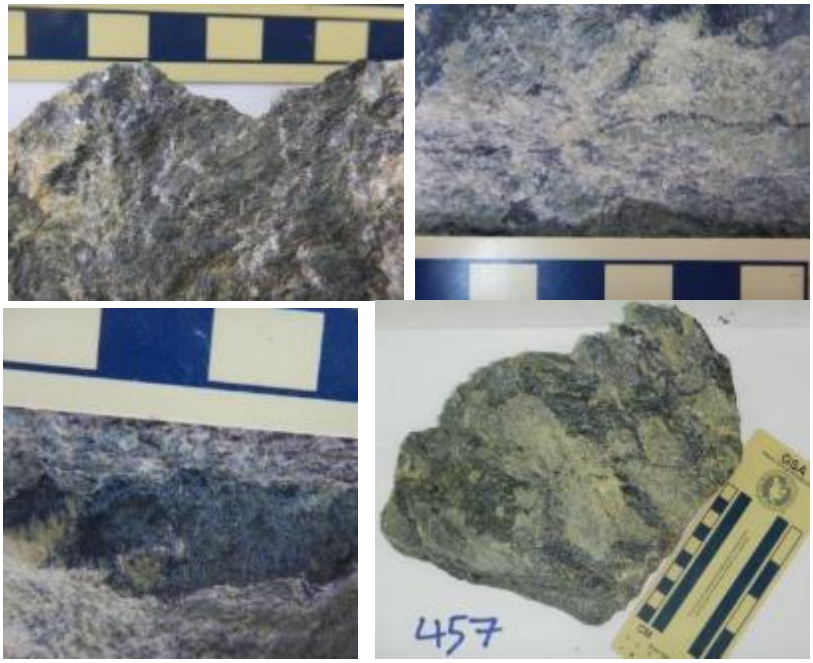

Figure 64: Sample 457, dark, green and blue minerals like chlorite, epidote (zoisite), sodic amphiboles like glaucophane.

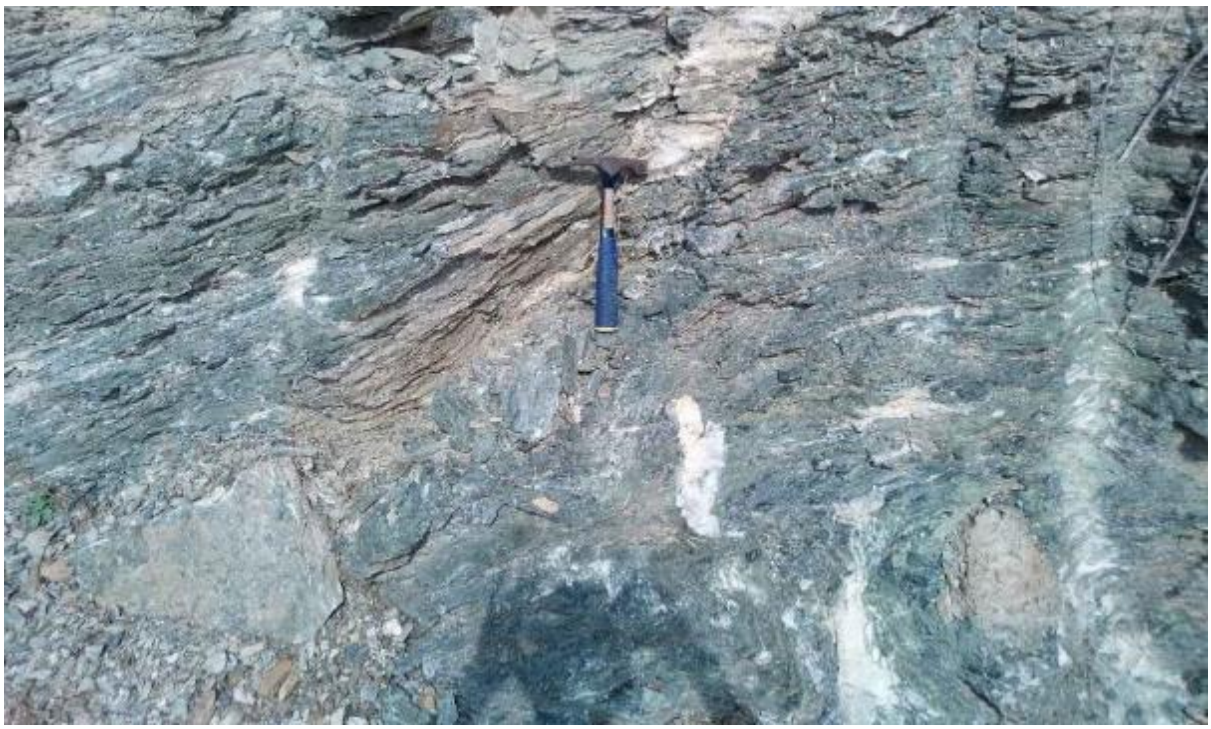

Figure 65: Location no. 5, mafic sills cause alteration of the host rock, gneiss. The rock becomes increasingly fine and sandy.

Taking sample number 459 from a chlorination area (6th stop) which contains basaltic-mafic sills clearly folded, highly foliated or boudinaged, syntectonic during metamorphism in their host rocks (orthogneiss).

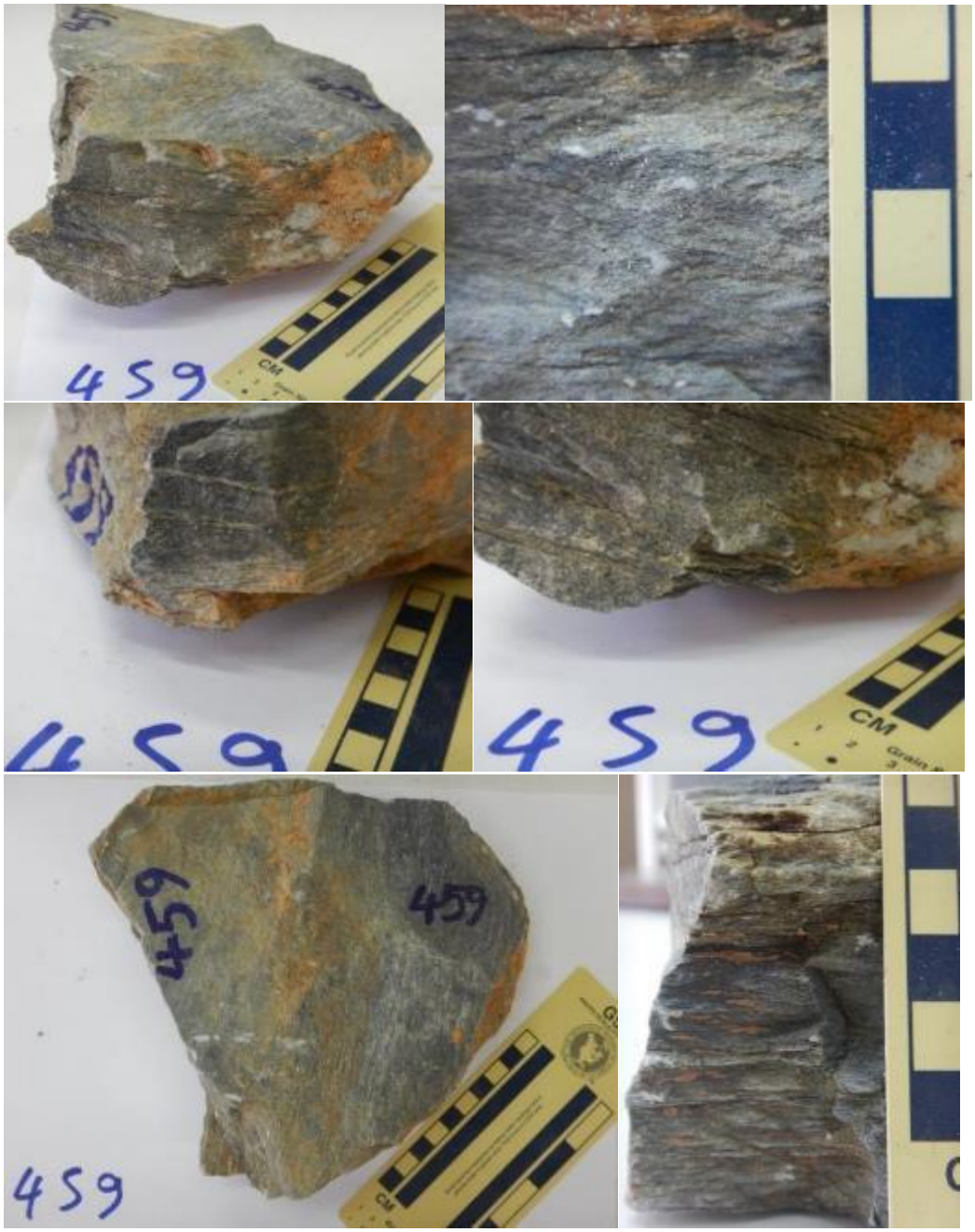

Figure 66: Sample 459.

Figure 67: Location no. 6, syntectonic (gneiss and mafic sills) and boudinaged.

Figure 68: Location no. 6, high deformation condition about 500°C.

There at 7th stop we can see clearly fine-grained Granitic Gneiss with heterogeneous texture as before and oxidized.

Figure 69: Sample 460.

The following 2 images highlight the strongly deformed rock and mineral deformation such as quartz and visible crushed volcanic tissue filling the gaps in the folds.

Figure 70: Location no. 7, Fragmented mafic sill within a gneiss fold.

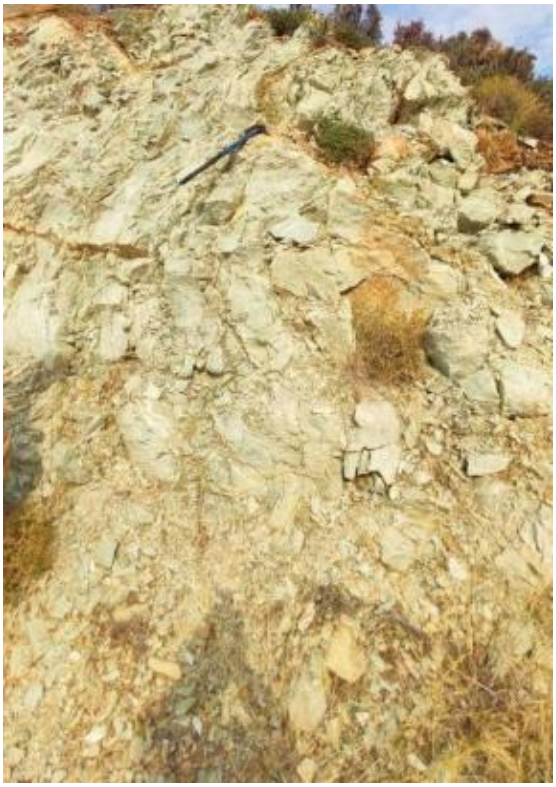

Figure 71: Location no. 7, large-scale gneiss fold.

Next stop (8th), sample number 461, we realize that Orthogneiss is a mylonite with Augen-Eyes texture. Because of a polished plate of Augen-gneiss with lenticular porphyroblasts of quartz and feldspars wrapped around by fine-graned matrix.

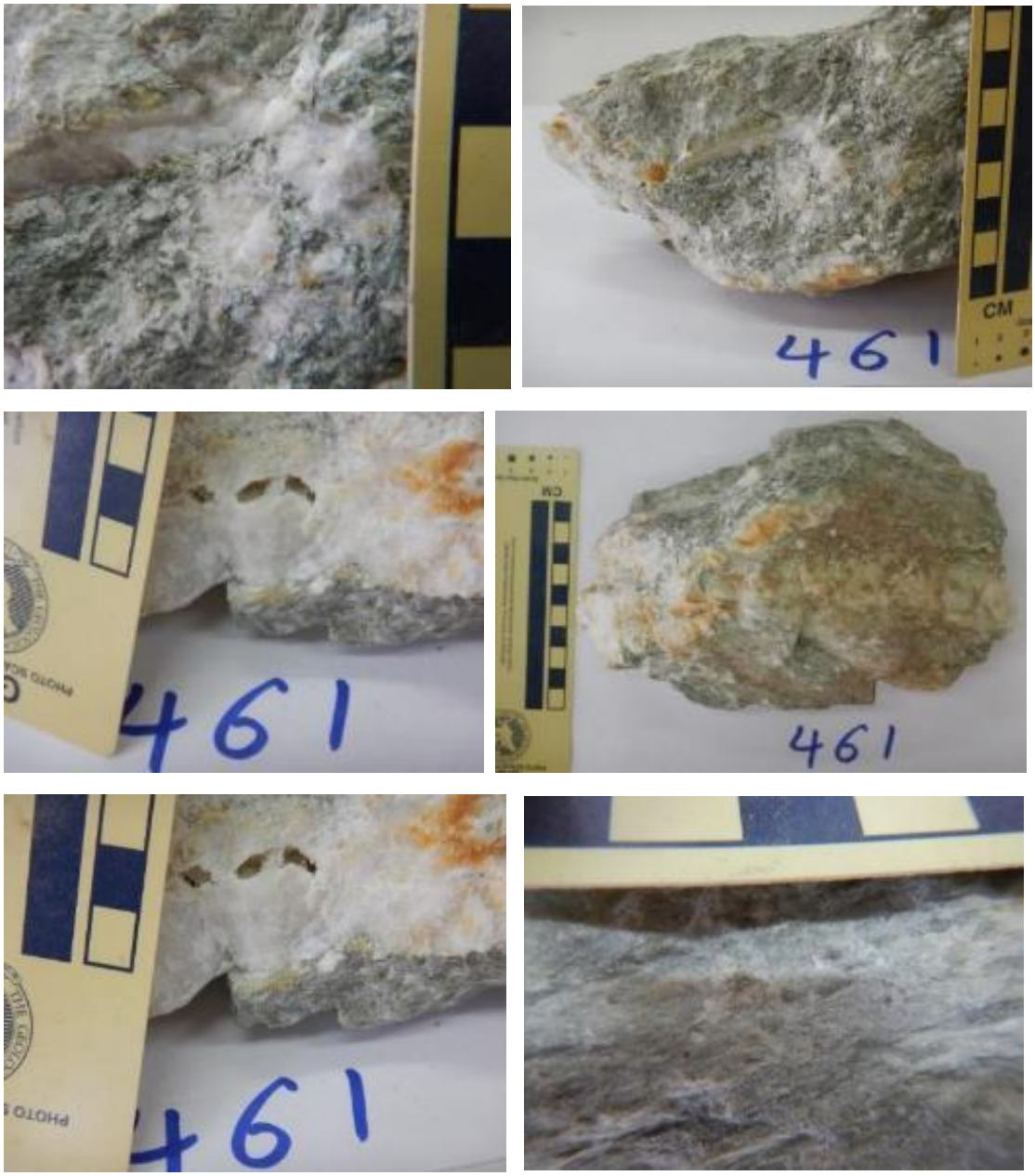

Figure 72: Sample 461, Eyes texture.

Figure 73: Location no. 8, where gneiss with Eye texture were taken.

Figure 74: Location no. 8, where gneiss with Eye texture were taken.

Figure 75: Location no. 8, mylonite, Gneiss Eyes.

Again at 9th stop we can watch Gneiss “Eyes” in Orthogneiss and synfolial (thick) Quarz veins and we can conclude to some kinematic tectonic information about area like the sense of shear that is top to the SW from 1 delta but there are more delta of sense of shear top to the NW.

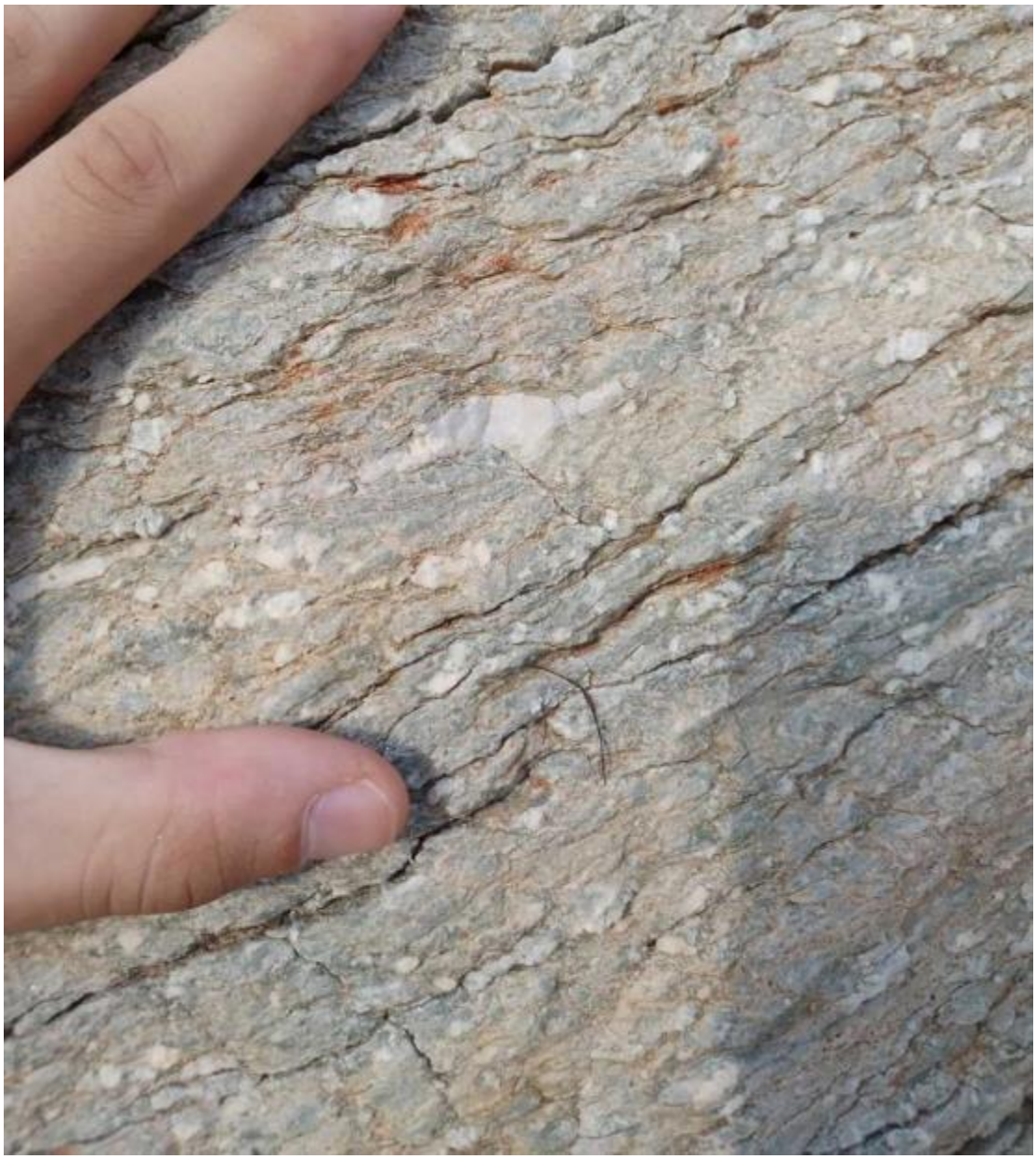

Figure 76: Location no. 9, delta (Quartz and K-Feldspar porphyroblasts)

Figure 77: *Location no. 9 sense of shear is top to the SE from 1 delta.*

Continuing the journey following these 2 mafic sills (stop 10) which are parallel to gneiss foliation, syntectonic and deformed. Foliation is 163/03. But before we arrived to stop number 10 we followed these:

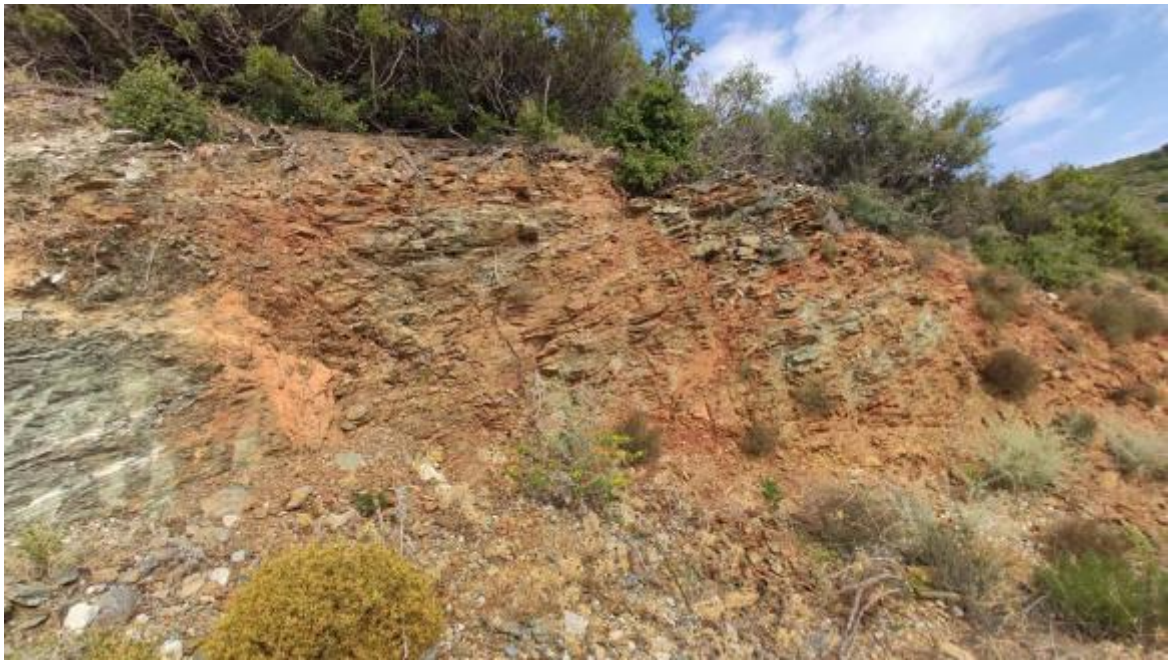

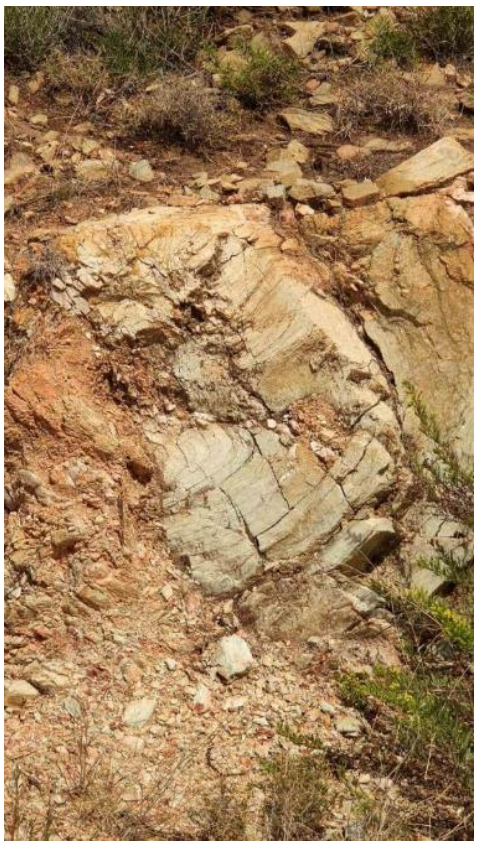

Figure 78: paraclinal folds.

Figure 79: Boudinaged Quartz veins and paraclinal folds.

Also not unnoticed was a fully contoured metamorphic granitic outcrop with large and deep holes. The geological environment is exactly the same as that of the Penteli in that it has exactly the same petrological type which has undergone exactly the same amount of linearization with exactly the same holes.

The rocks that occur in the area of Penteli Mountain are granitic, mafic, clay, metavolcanic, calcareous and marble. The underlying rocks of all and in particular the Triassic marbles, as they form a crystalline basement, are the Permian (276 Ma) granitic gneisses. They are characterized by strong tectonism, folds, foliation and, to a lesser extent, graininess, which are the result of the extension of the area due to the tensile collapse of the orogen. These conclusions were led to by the orientation and dip of the axial fold planes, the zones of large-scale mylonitization and S-mylonites with orthogneiss. The orthogneisses appear to have been generated by magmatism of the subduction zone between the overlying Laurasia and the

underlying PaleoTethys, the age of magmatism being the same as that of the Pelagonian. Then in the Triassic we have the known thermal events due to the decompression of the asthenospheric mantle at the same time as the Pindos and Axios oceans were created. This explains the observation and the later age of the post-basaltic veins which are boudinaged due to extensional eruption and the simultaneous creation of sedimentary rocks. Indeed, partial melting of these created tophi. In general, the existence of acid and mafic magmatism indicates a geotectonic environment of continental eruption. Therefore, Penteli is a part of the subduction zone in Greece which did not deepen enough only about 30 km in (HP-LT) blueschist conditions during the Late Eocene-Early Oligocene (35 Ma) and during its excavation was characterized by the greenschist phase about 10-15 Ma later. Compared to Central Evia, which is also part of the same subduction zone, as can be seen from the ages, the petrology, the tectonics and the geography that connects them, Penteli was always a little further south and a little shallower than its area Evia. So central Evia seems to reach deeper into the subduction zone with little bit older ages and was buried under similar conditions as Penteli.

Figure 80: Strongly lineated outcrops

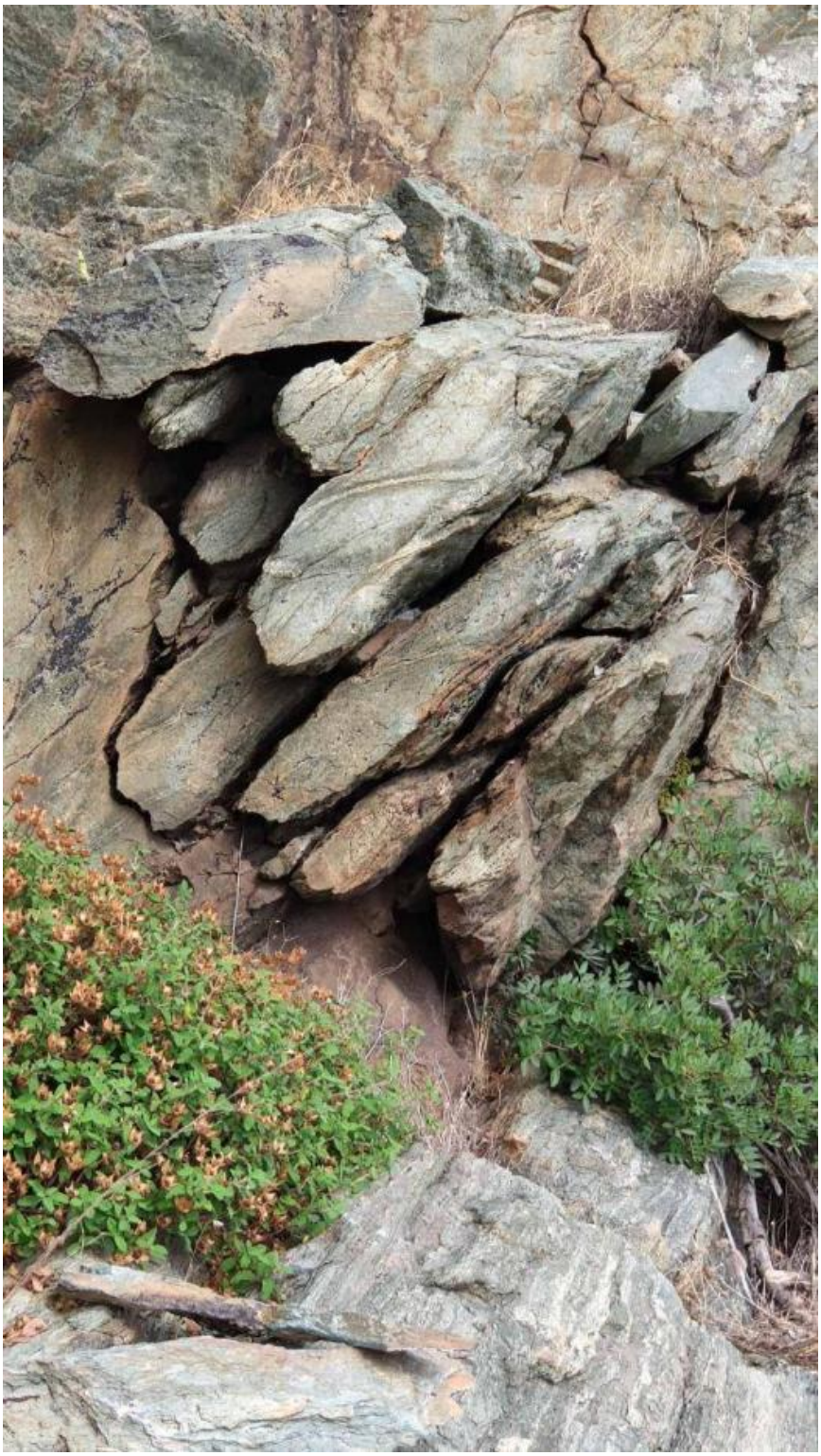

Figure 81: Gneiss strongly lineated (photo on outcrop)

Figure 82: Strongly lineated outcrops.

Figure 83: Strongly lineated outcrops.

The post tectonic setting of the granitoid geological formation with internal metabasaltic sills is beginning to prevail and this is evident from the paraclinal folds we are beginning to encounter. This is also verified by the predominance of the strong lineation.

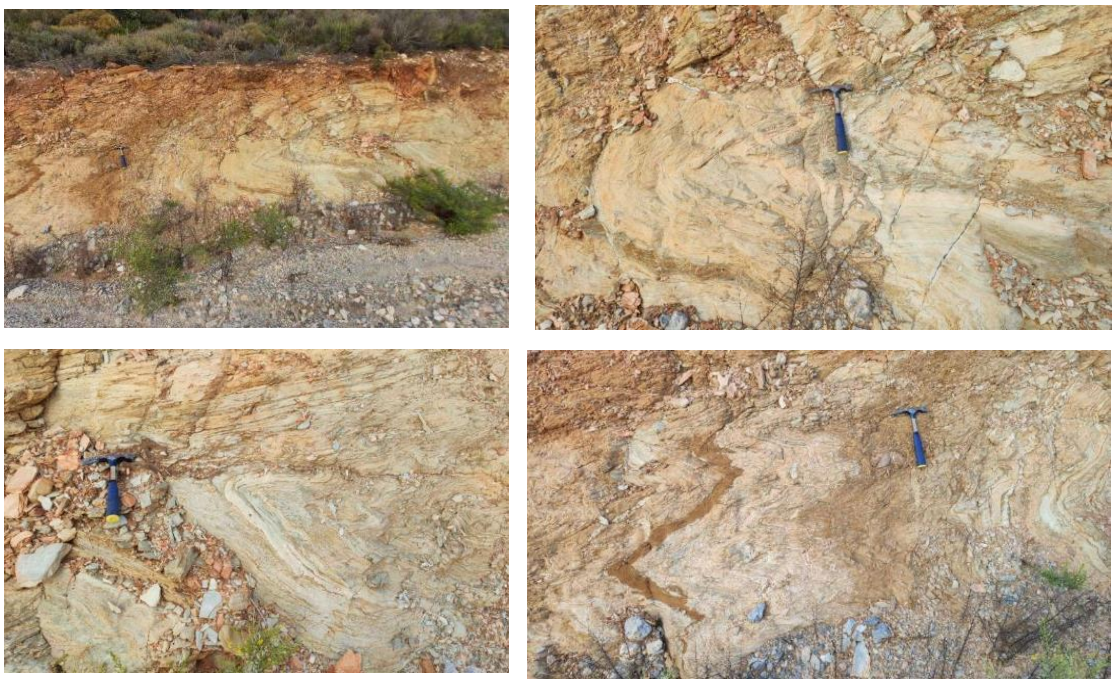

Figure 84: Paraclinal folds.

On the way back it was observed at 10th stop fine grained orthogneiss with ''Eye'' and sugary texture which comprise quartz, K-feldspars as porfyroblasts biotite, Plagioclase and probably alkaline amphibols and pyroxens because of the mafic alkaline sill inside of the host granitic rock.

Figure 85: Location no.10, mafic sill between two granitic rocks.

Figure 86: Gneiss Eyes texture, fine-graned *porphyroblasts (K-Feldspar).*

Going back taking two last samples number 464 were taken from the same place, an Orthogneiss outcrop including full of Quartz and sulfides which are inside of Quartz veins. (11th stop).

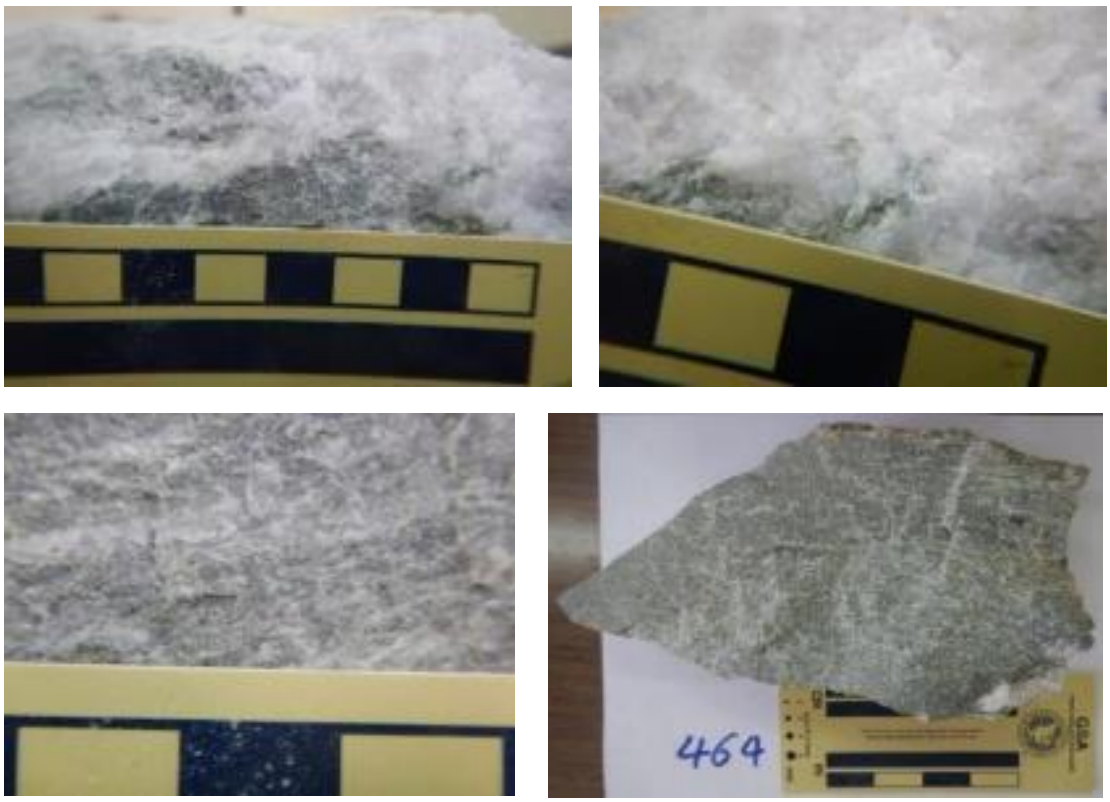

Figure 87: Quartz veins in granatic host rock.

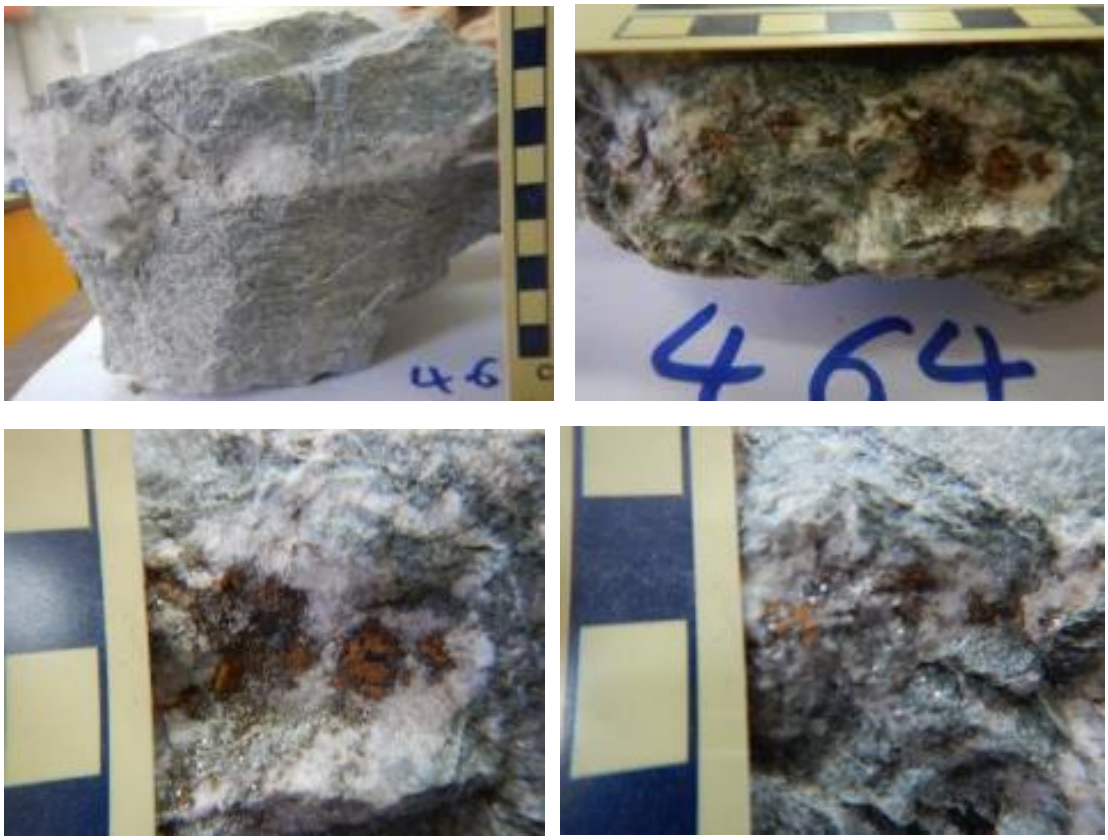

Figure 88: Sample 464, Granitic rock with quartz and hydrothermal fluids with metallic minerals.

Figure 89: Location no. 11, an outcrop near to the road.

Figure 90: Location no. 11, metalliferous quartz veins in gneiss.

Unit 3.3 After fieldwork

Unit 3.3.1 Data collection

At the same time and after the fieldwork the GPS data were transferred to google earth pro to make our daily routes visible and to note the numbers of samples, what was found and what was observed at each location. Based on the observed data about the tectonics of the area the petrology-mineralogy some assumptions were made about the model of the geotectonic environment. The samples were stored in special bags for transport always indicating a sample number on each one. (Tables of chemical analysis and mineral notes per sample in (unit 5.3 and unit 5.2). Once back at the university the field data was recorded in the above excel. This was followed by photographing the samples and processing the photos in Upscayl for higher resolution photos. After all of these steps, a literature search for our area began to determine if there was additional information from other scientists on the specific formations being studied.

Unit 3.3.2 Synthesis of the geological history of the Upper Plate units:

The purpose of the following plan is to reconstruct the stages of the subduction zone of Central Evia from the time period that we know until the picture we have today. Our knowledge starts with the existence of a crystalline basement (Carboniferous-Permian) which at (230-210 Mya) is subject to a rift known as the Triassic rift. The tectonic regime is tensile as mafic dykes enter the basement and meet faults normally as mafic sills. During rifting, basins of sedimentation of fractional products and chemical precipitation are created. The rocks formed are arkosic, limestone, argillaceous, pelitic and radiolarian. Due to the thickening of the crust that occurred and the uplift of the upper mantle, the mantle material medium veins along with these sedimentary rocks created volcanic tophi and the so-called volcano-sedimentary complex.

An attempt is made to approximate the position of the Upper Plate units in Central Evia during the Triassic rifting before they were tectonically superimposed on each other (Fig.91). To do this, the following data were exploited:

The fact that the Gerontas unit has two volcano-sedimentary horizons and even above the first one there are carbonates (Triassic-Jurassic) and then transition to radiolarians (Late Jurassic-Early Cretaceous), suggests the deepening of the area due to a non-fixed boundary of the CCD. (Then above the second volcano-sedimentary horizon follows ophiolitic mélange with overlying stratigraphic void as verified by (Fig.9).

In the Liri unit the occurrence of sedimentary rocks such as arkosic and flysch (Permian-Late Triassic) just above the crystalline basement of Carboniferous without any vol/sedimentary horizon or other deep water sedimentary formation e.g., siliciclastic, suggests a meritic sedimentary environment.

The Servouni unit contains a vol/sedimentary horizon and an overlying bauxite horizon between Mid. Triassic-Jurassic limestone and Cenomanian niritic phase carbonates. Prior to flysch deposition the environment deepens with corresponding pelagic phase rocks. Characteristic of the Dirfy unit is the carbonate layer (Late Triassic-Early Jurassic) and the overlying radiolarites with pelagic phase red schists which together are above the vol/sedimentary horizon (Permian-Triassic).

Then the lithospheric plate acquired an oceanic character as pieces of continental crust, joined by passive margins, moved apart. Finally, we have the closure of the ocean with the creation of an active margin, where oceanic lithosphere subducts under the continental one. Now arriving at today's picture where the ocean of (Paleo Tethys) has been completely closed, which with its dehydration created volcanism further north of the current volcanic arc and the continental block coming from the former Gondwana (Today's Africa) is about to collide with the continental crust of today's Eurasia. More specifically, the figure shows the current placement of the units of the Upper Plate of Subduction Zone of Central Evia, which has come to the surface.

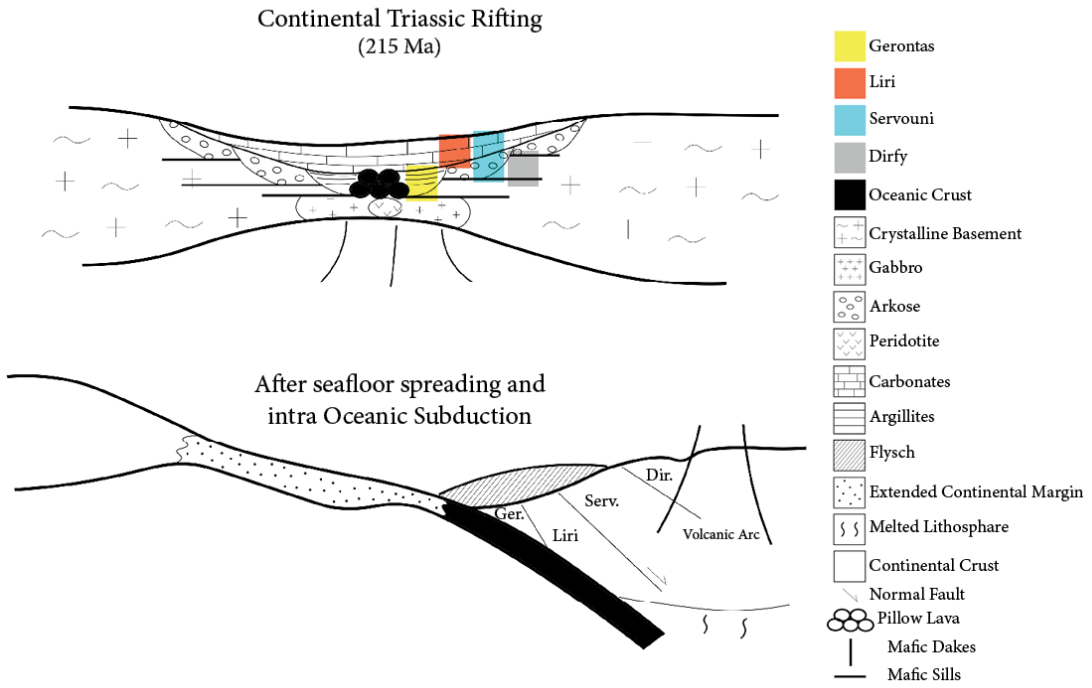

Figure 91: Synthesis of the geological history of the Upper Plate units from the age of Triassic rifting until now.

Chapter 4

Unit 4.1 Preparation for microscopy

After our samples were collected and sorted in the preparation area, the next step was to select samples that would be analysed further as they were of greater interest and more relevant to our subject than others. A selection was made of all types of grips mainly near the village of Trachili and those samples that showed to be of granitic composition mainly from the Petries area, always selecting the least weathered and oxidized rocks. The aim was that the rocks to be analysed should be as less altered as possible by the influence of sub-genetic and upper-genetic fluids. Then in the granitic rocks, the grain was marked so that they were cut parallel to and perpendicular to the foliation. After this clearing, 16 samples prevailed whose manual cutting was done on the wheel. The aim was to create thin section stems so that the specimens could be examined on a smaller scale in the transmitted light polarizing microscope. The slices-slabs cut was approximately 1-2 cm thick. Slab photos there are in appendix for each sample.

In the next preparatory step for the manufacture of thin sections, the rock slices were polished on a rotating wheel using water sandpaper starting from the size of 100 up to 1.000 going in steps and finally using special diamond sandpaper. This was followed by grinding the cuts with carbon silica to achieve an even smoother surface. On a smaller wheel, the slices were cut into small chips measuring approximately 2.5 by 4 cm to approximate the dimensions of the glass surface to which the section would adhere. Finally, after being properly stored, the chips were transported to the ΙΓΜΕ (now ΕΑΓΜΕ) where the final thin sections were made for the microscope.

Unit 4.2 Microscopy-Petrography

In this subchapter we will deal with microscopy as we will observe the tissues, structures and mineralogical description of the specimens through microscope images.

Starting with sample 440 which is mero-crystalline with purple tissue, we observe pseudomorphs due to carbonated albite and quartz. The presence of chlorite and former olivine pyroxenes is important as we can imagine their former grain boundaries that are now obliterated. In the glassy mass of the basalt, we have small crystals of blue magnesian and green chlorite. We also have the existence of former titanites, Laths (Interzertal texture) plagioclase forming prismatic crystals as the calcareous part of the plagioclase creates epidote. White marbles with small grains are observed that in parallel Nicols the relief is altered due to sericitization.

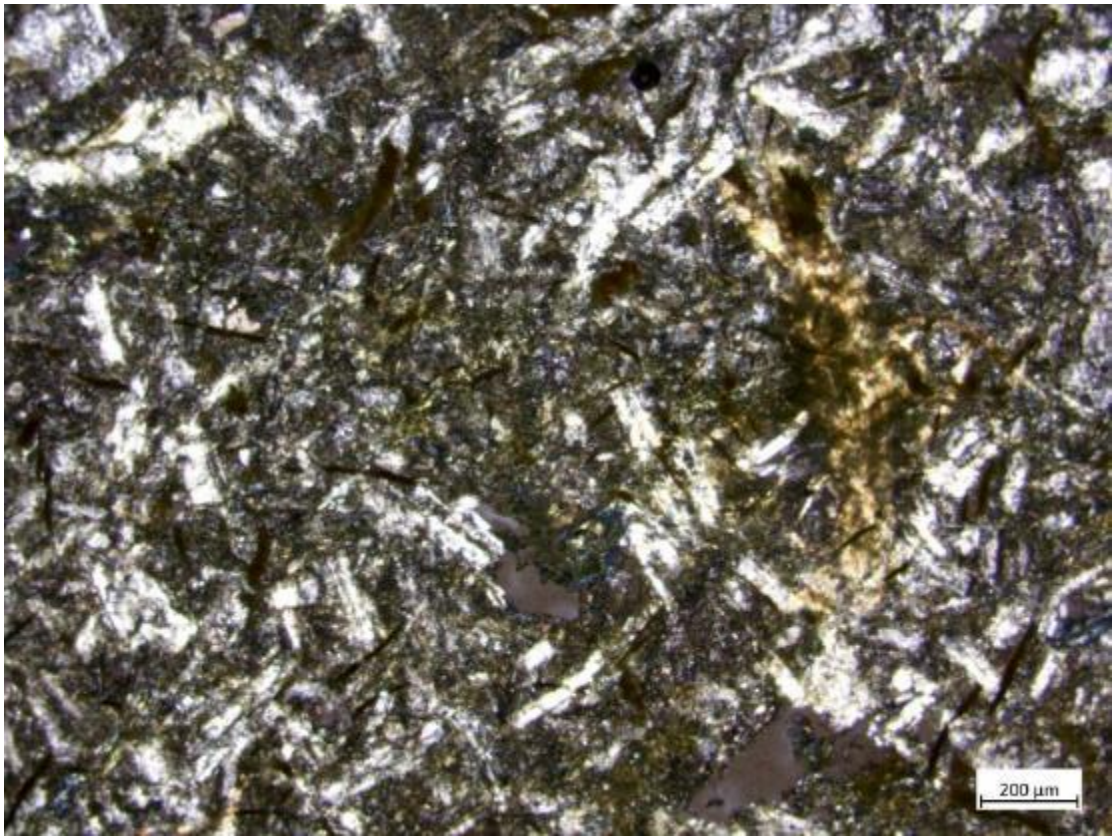

Figure 92: Section 440, altered plagioclase prismatic crystals.

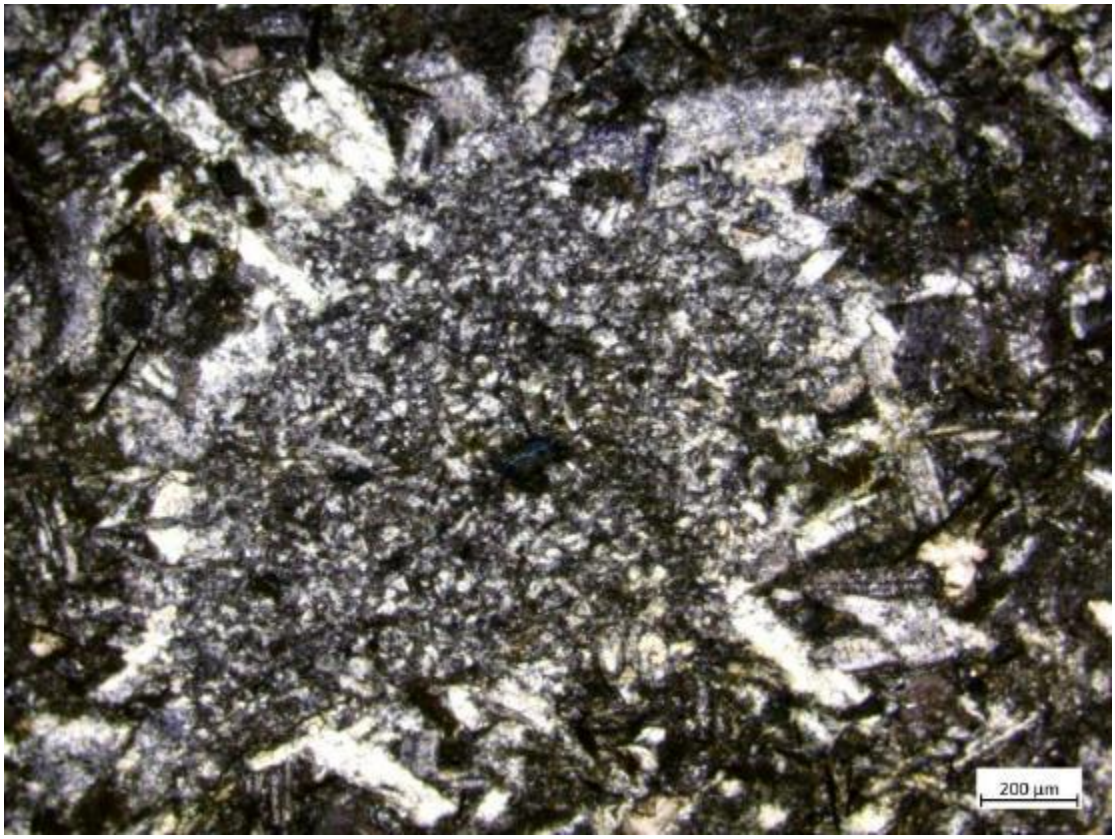

Figure 93: Section 440, plagioclase Lath.

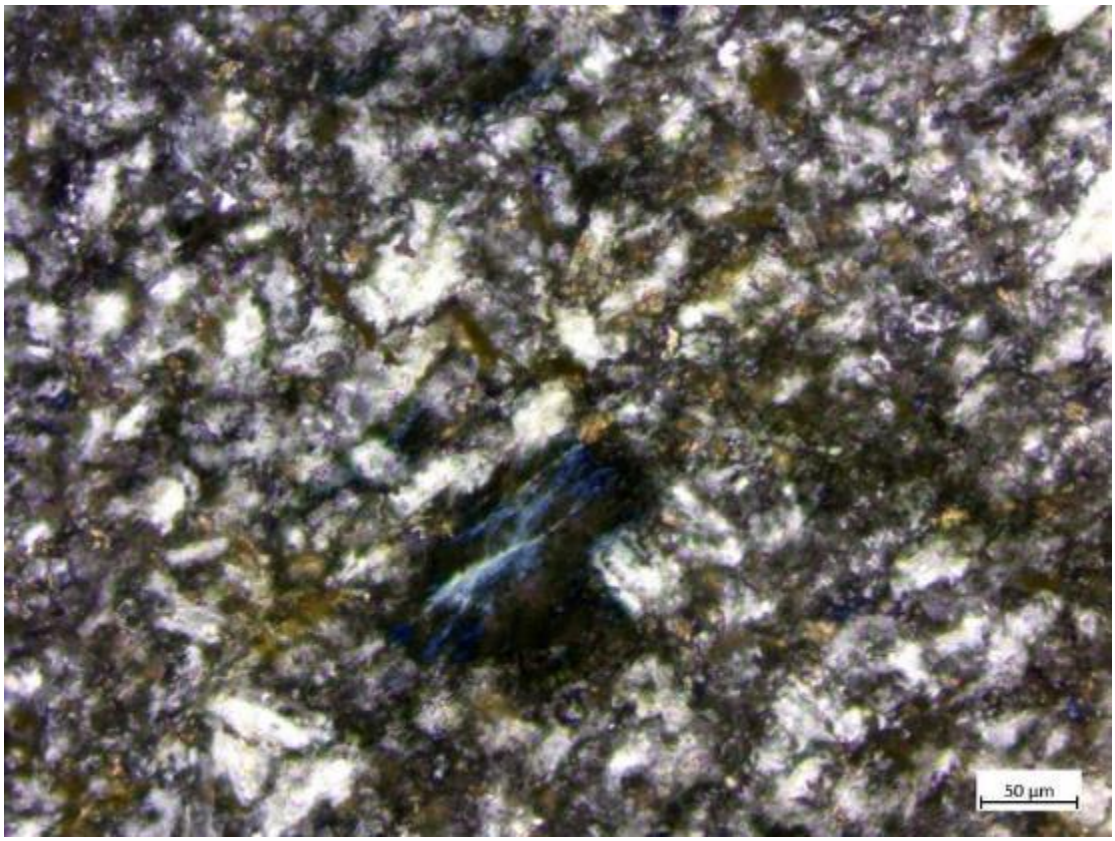

Figure 94: Section 440, magnesian chlorite.

In sample 442 we are talking about an Igneous rock, mero-crystalline, where what strikes us is the characteristic chlorite-clinochlore growth in bundles (with green and yellow polarization colors) as it is anisotropic. There is a strong alteration in the sample with minerals such as chlorite, pyroxene in plagioclase since the last two seem to form an ophite structure. In the mass of the rock, we have many clay-silicate minerals as an aggregate. Of particular interest is the microgranular quartz observed rather allotriomorph amphiboles and epidote. Our sample is not lacking in oxides.

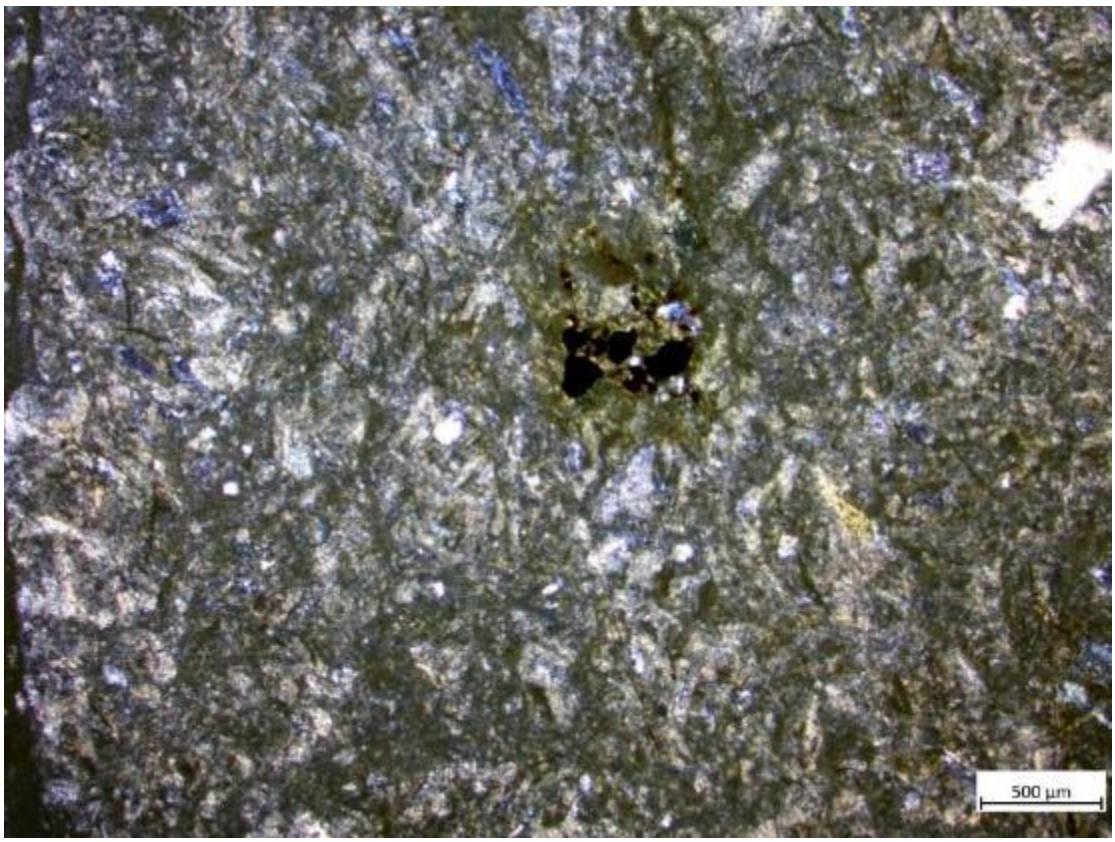

Figure 95: Section 442, existence of oxides (dark minerals).

Figure 96: Section 442, parallel Nicols.

Figure 97: Section 442, crossed Nicols.

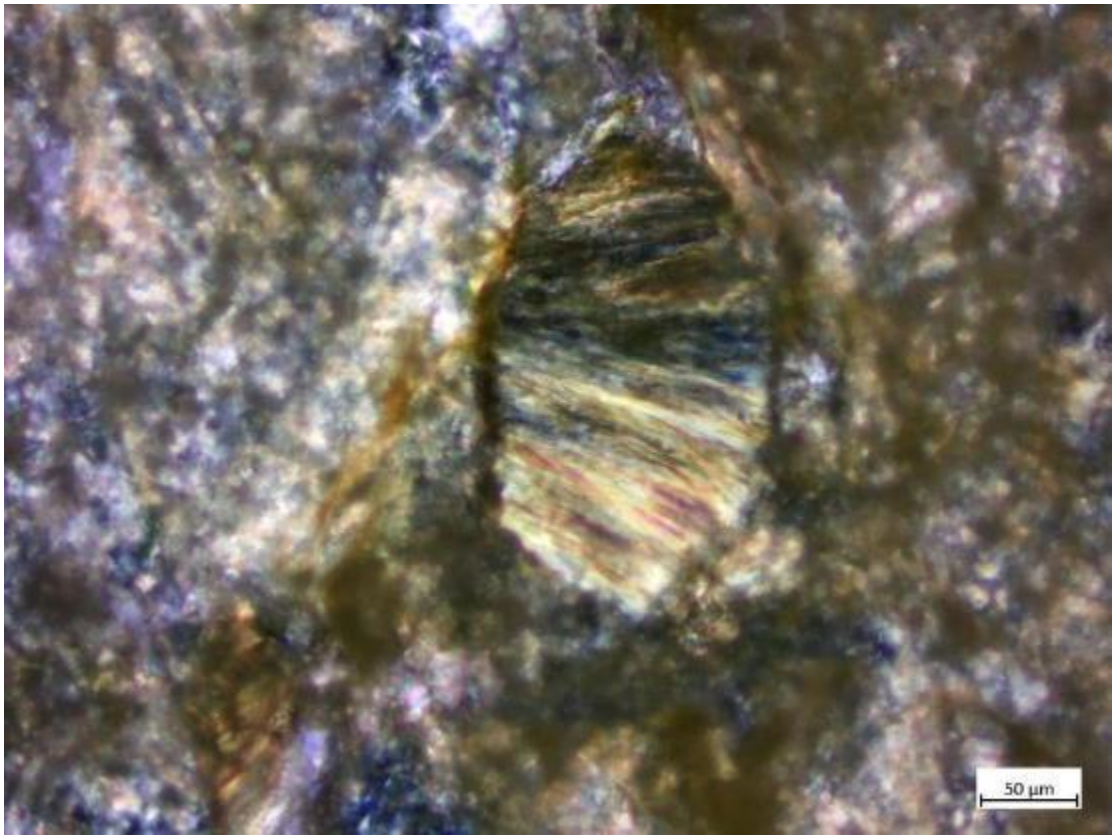

Figure 98: Section 442, polarisation colors of clinochlore growth in bundles.

In sample 443 the scheme continues as in the previous samples as it is of a similar category. Sericified plagioclasts with thousands of microgranules are observed. We have radiating chlorite growth (high polarization colors of purple, high magnesium blue and high polarization colors like yellow, brown and perhaps secondary biotite. Magnetite residues were detected in clinochlore. Pseudomorphic olivine and pyroxenes have been replaced by carbonates and clinochlore.

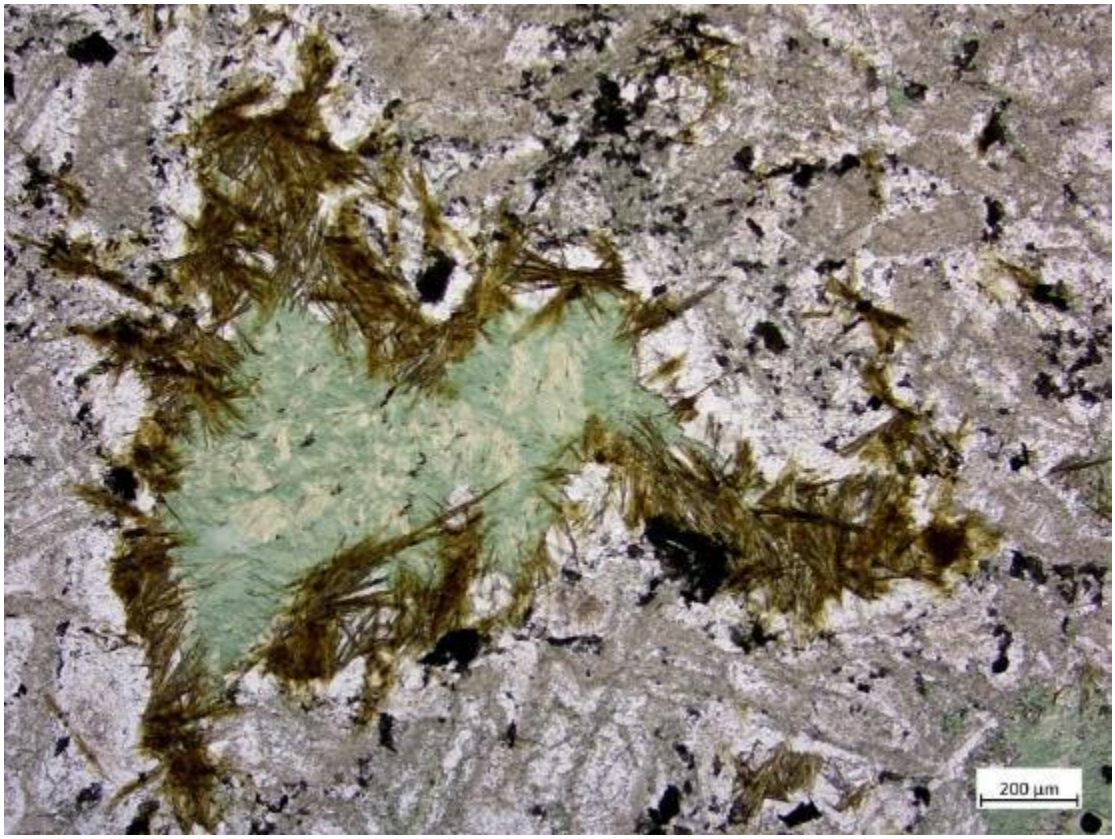

Figure 99: Section 443, 1.1 Clinochlore growth in bundles with parallel Nicols.

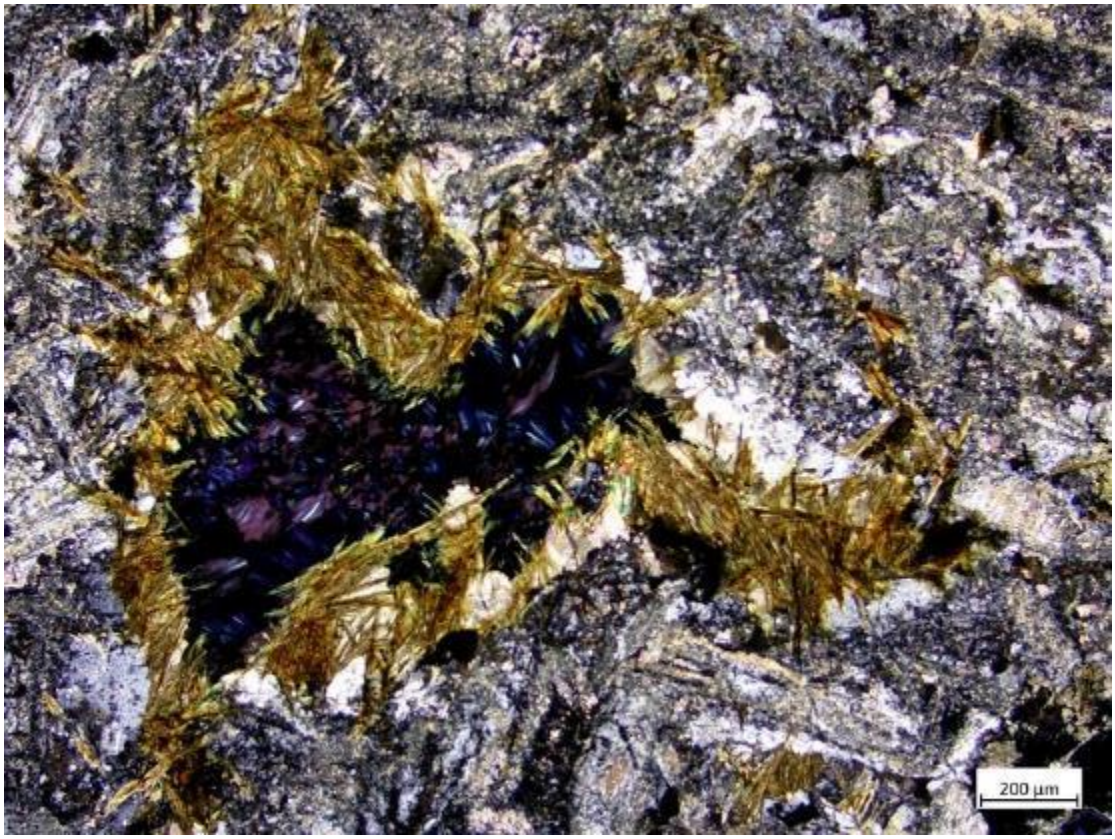

Figure 100: Section 443, 1.2 Clinochlore growth in bundles σε κάθετα Nicols.

Figure 101: Section 443, 1.3 Clinochlore growth in bundles, // Nicols.

Figure 102: Section 443, 1.4 Clinochlore growth in bundles, crossed Nicols.

Figure 103: Section 443, 2.0 Pseudomorph olivine-pyroxene grain replaced by carbonate and chlorite.

Figure 104: Section 443, 2.0 Pseudomorph granule of former olivine or pyroxene split in two.

Figure 105: Section 443, 3.0 Yellow-brown pleochroic colors of possibly secondary biotite in chlorite in //Nicols.

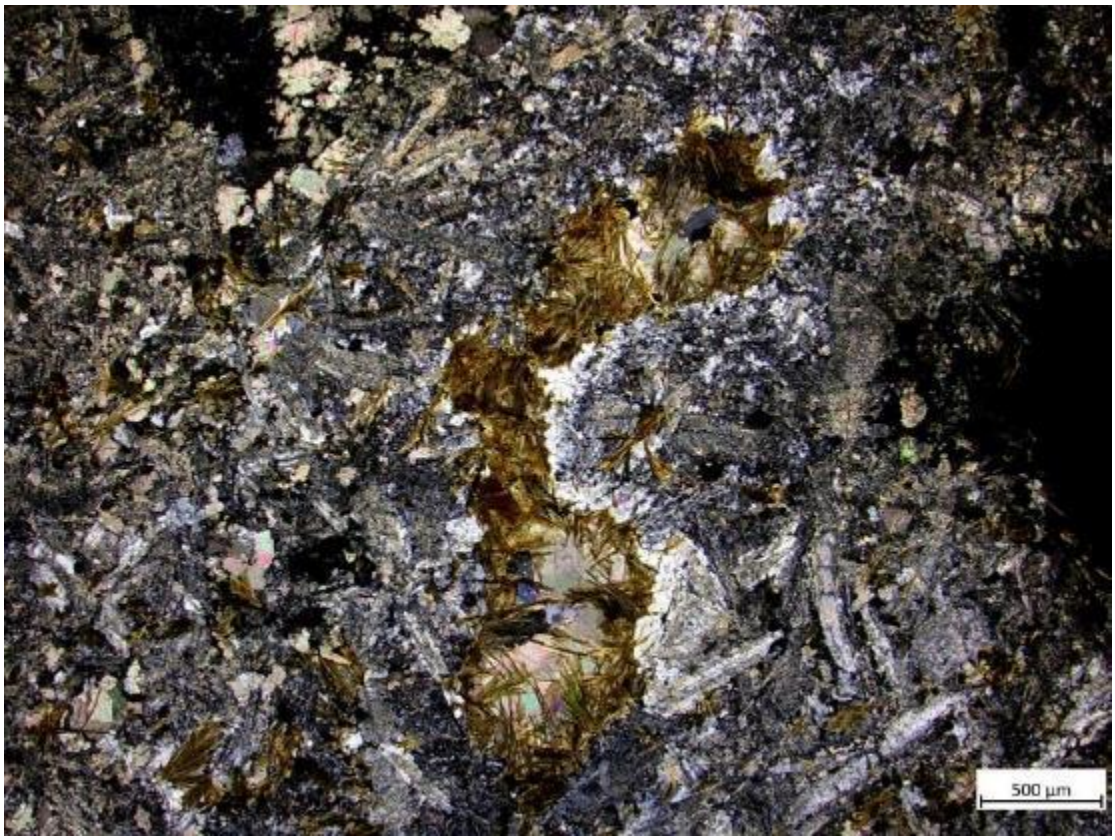

Figure 106: Section 443, 3.0 Residues of biotite in chlorite in crossed Nicols.

Figure 107: Section 443, *The points in the section where were observed the previous grains.*

Sample 450 is characterized by replacement by carbonate, albite, calcite, quartz (pervased carbonization). Existence of microgranular titanite and chlorite anisotropic and radial buffers; found at typical Greenschist (Low) = 350 °C. The outer ring of the dessert has high relief with prismatic crystals.

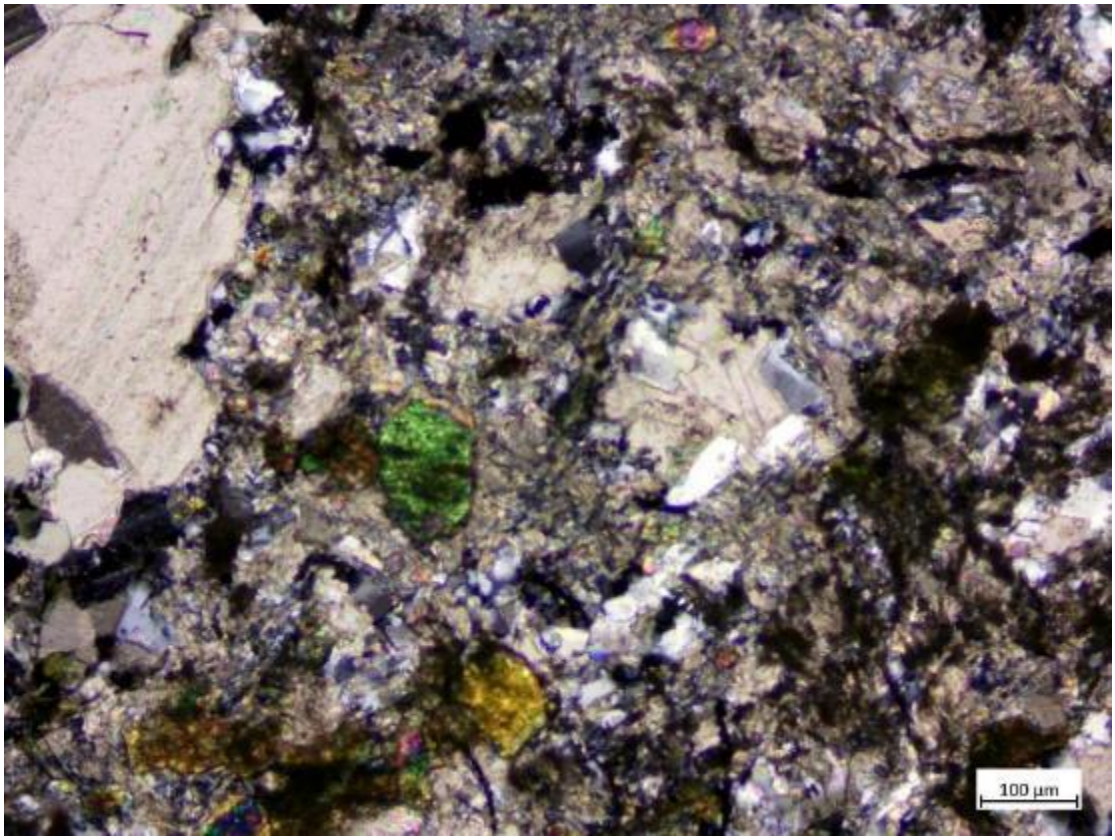

Figure 108: Section 450, Existence of an epidote with green-yellow polarization colors and high relief.

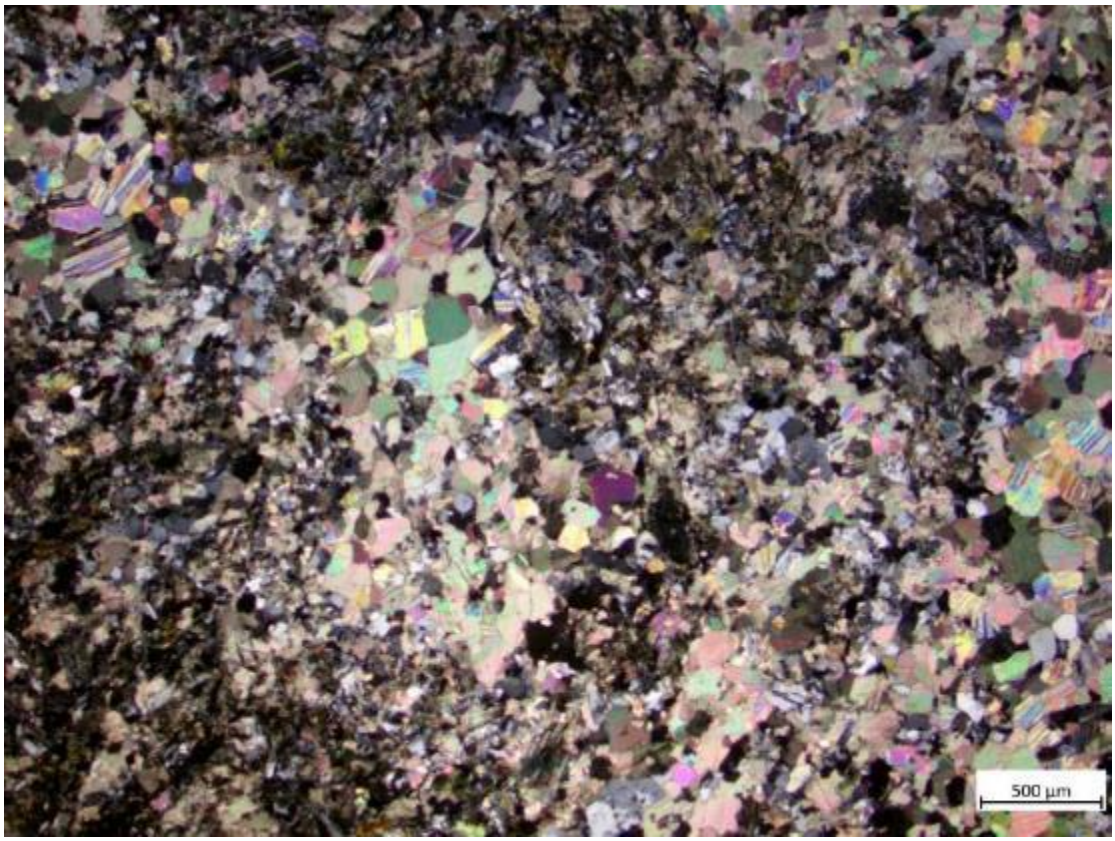

Figure 109: Section 450, Replacement of plagioclase and quartz by carbonate minerals. (High class polarization colors).

Figure 110: Section 450, Degraded plagioclase with the presence of chlorite and epidote.

Sample 453 is probably Granitic Gneiss metamorphic), all-crystalline and isocrystalline with direct grain attachment. We have minerals such as quartz, plagioclase grains due to syntectonism and creation of parallel zones with slightly more developed grains, and the grain arrangement is anisotropic and parallel (foliation parallel). Gaps are filled with mica and we have quartz reflection every 120 degrees (Ribons Quarz).

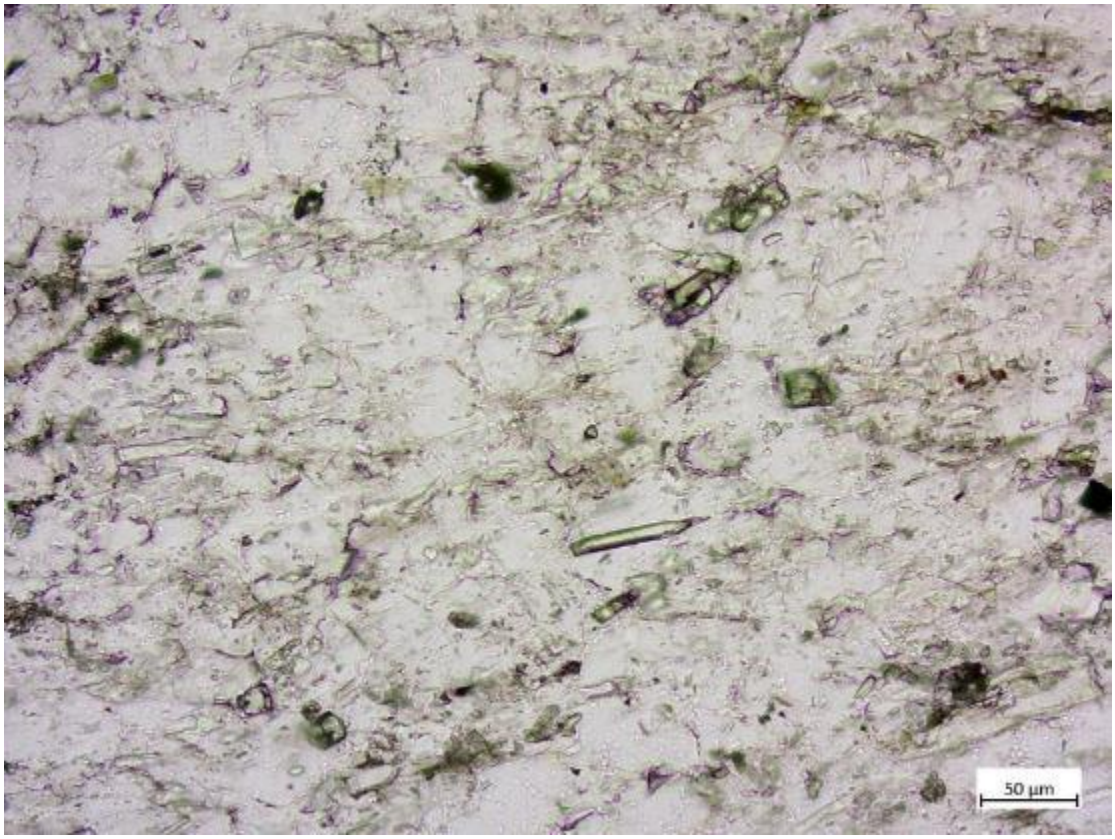

Figure 111: Section 453, Top right of the photo shows zoisites, zircons and bottom zircons with mica blade.

Sample 454 continuing with the granitic compositions is metamorphic, all-crystalline and isocrystalline. Minerals such as: Quartz in places under stress (Stressed) with wave quenching and quartz grains, plagioclase due to syntectonism and creation of parallel zones with slightly more developed grains, while their arrangement is anisotropic and parallel (foliation parallel). The gaps are filled with mica and we have quartz reflection every 120 degrees (ribons quarz). Other minerals such as mica, plagioclase (Large grains sericitized and twinned), zoisite oriented and peculiar needle-like crystals and zoisite oriented and peculiar crystals. Calcite is present in mixture with quartz.

Figure 112: Section 454, Epidote grain (high relief with //Nicols)

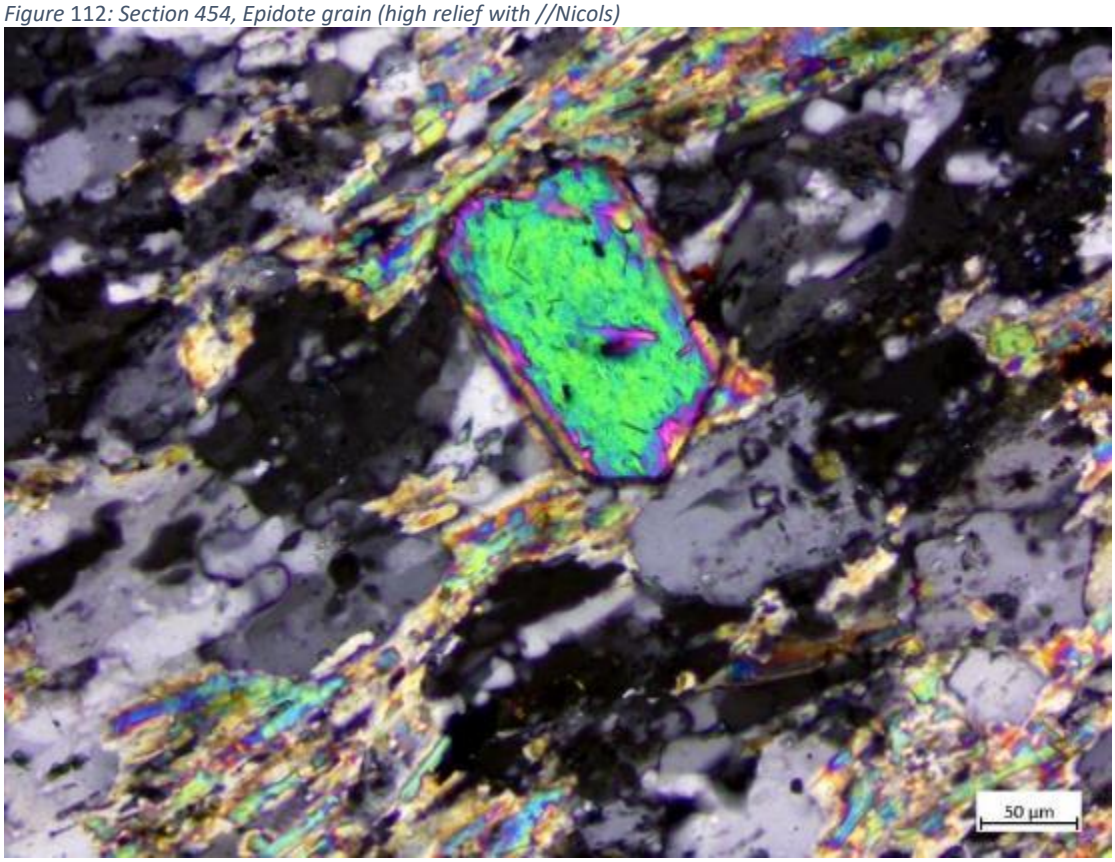

Figure 113: Section 454, Epidote grain (high relief with crossed Nicols.

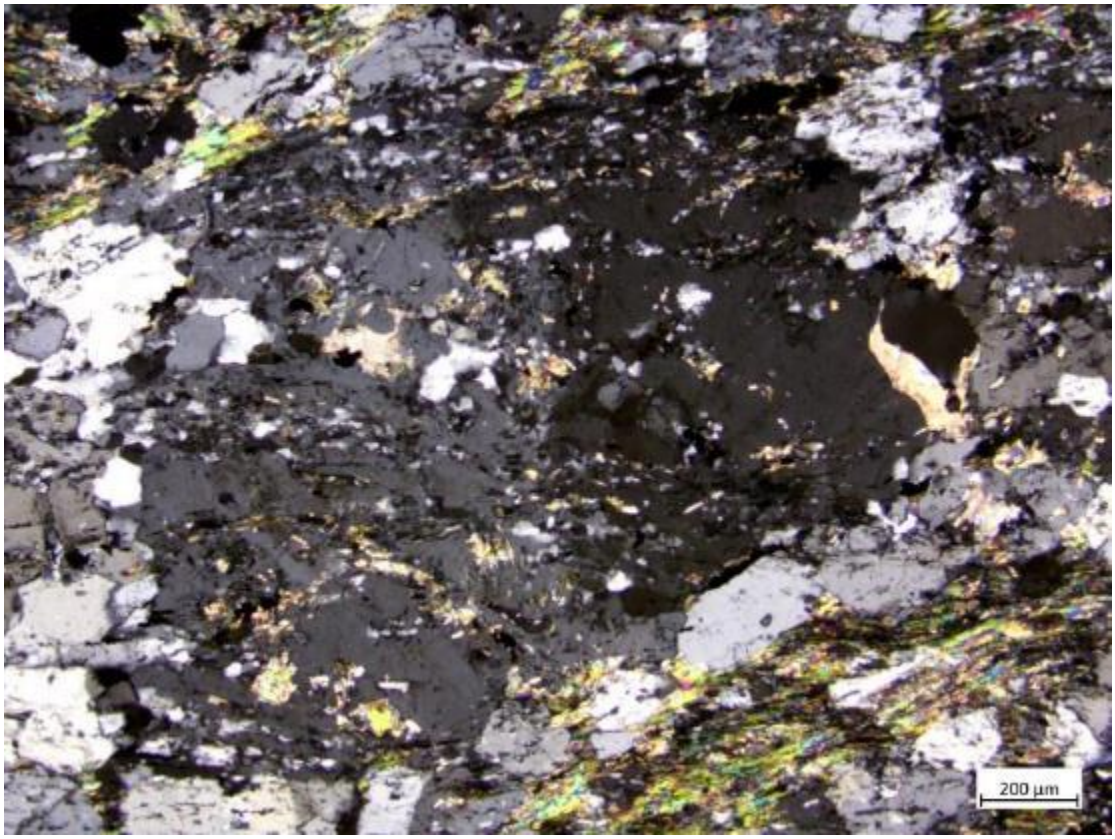

Figure 114: Section 454, Mega grain of plagioclase sericitized.

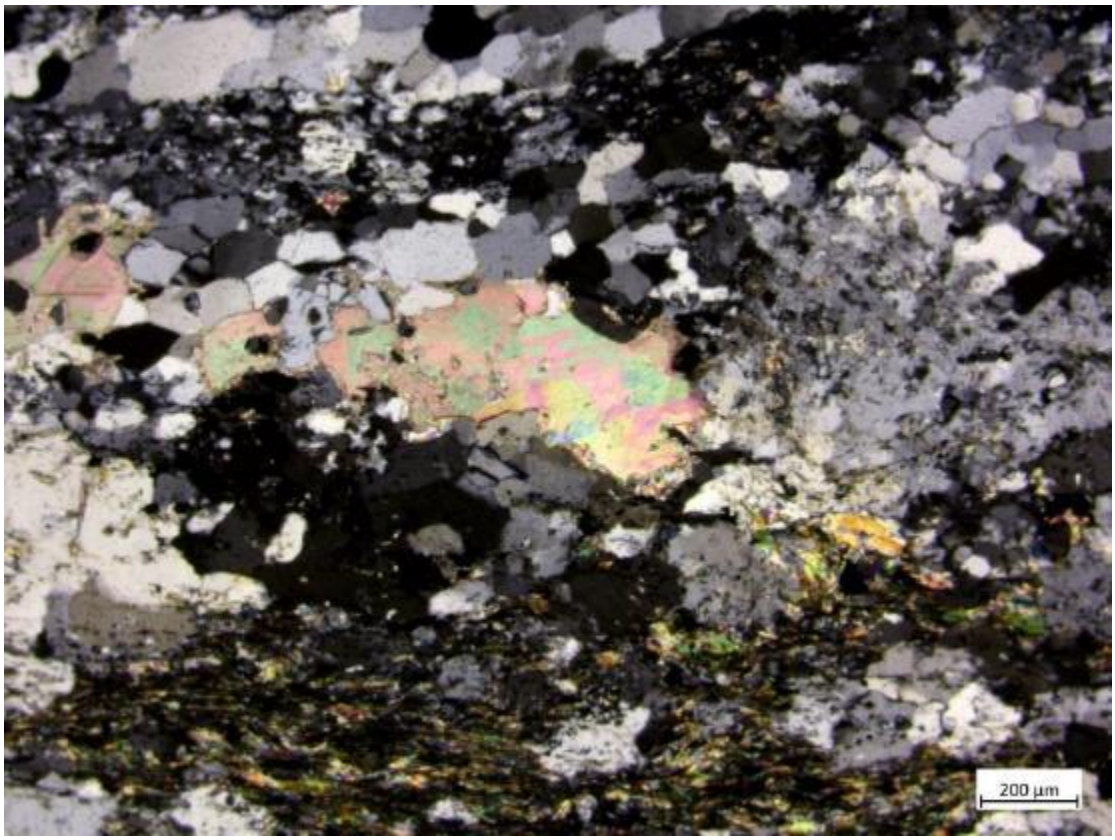

Figure 115: Section 454, Replacing carbonates in other minerals such as quartz and plagioclase.

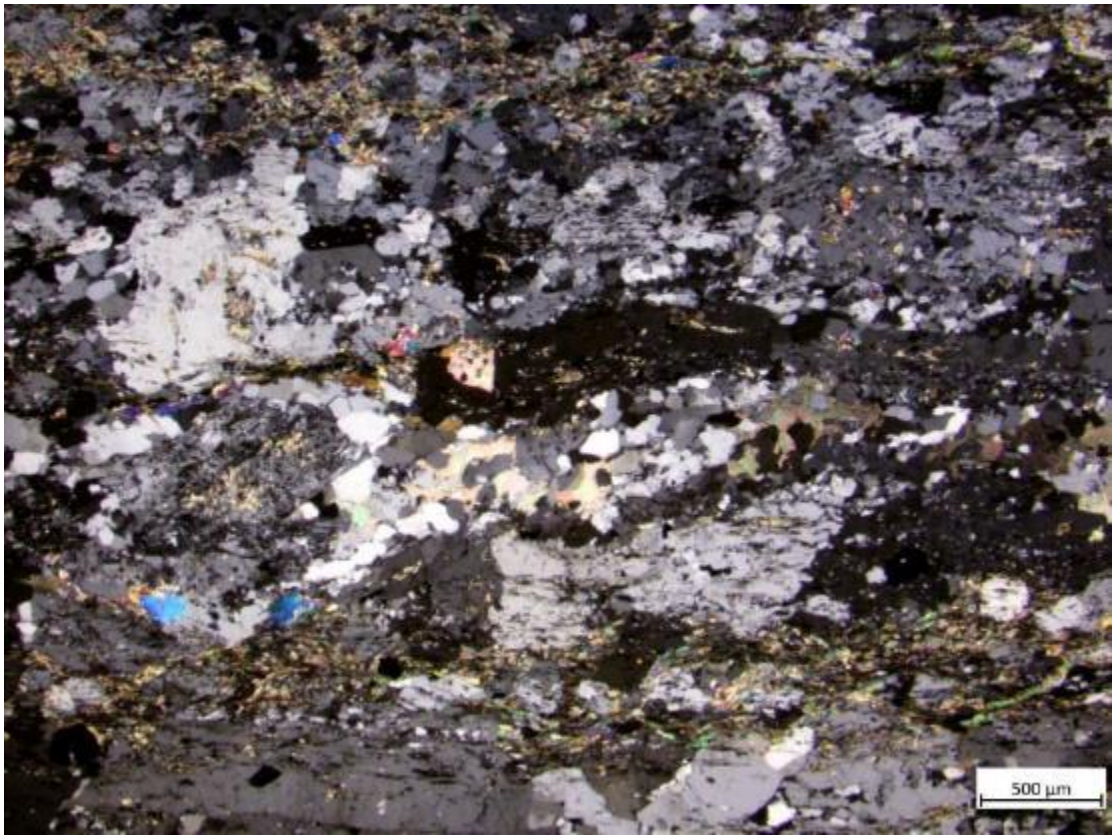

Figure 116: Section 454, stressed Quartz zone.

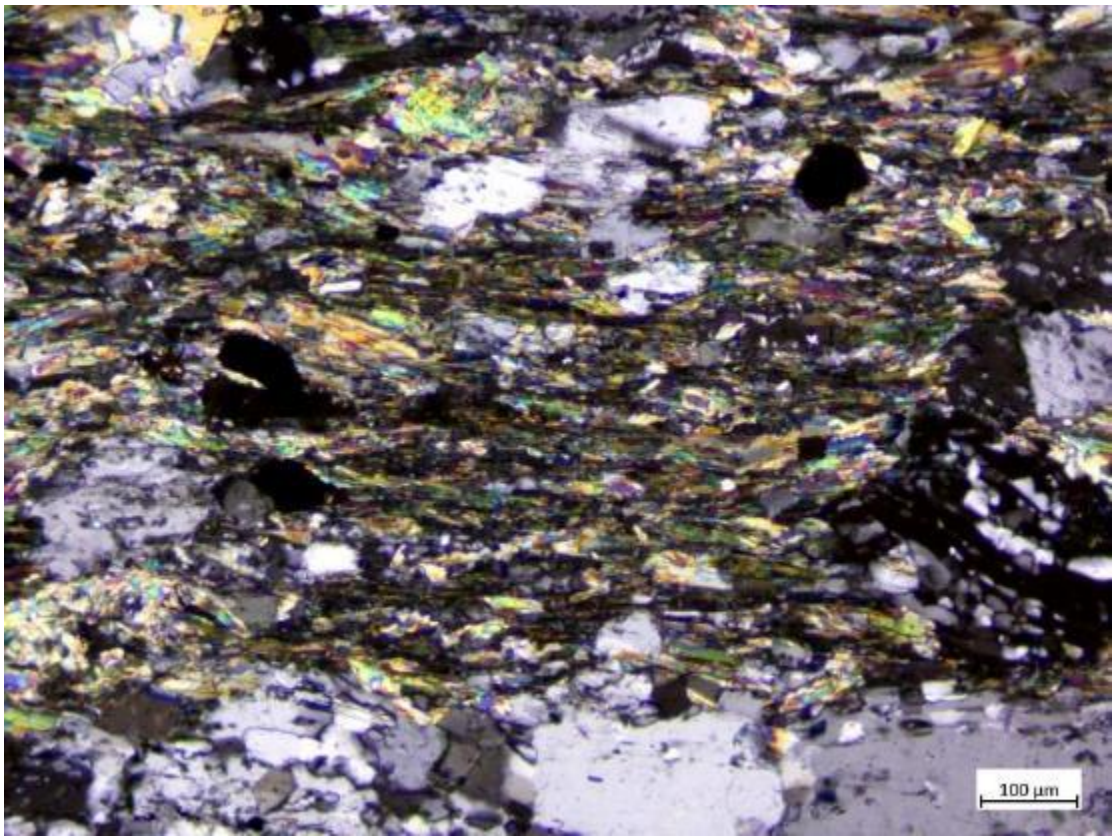

Figure 117: Section 454, Aggregate of clay-silicate minerals and mica.

In sample 458 which is metamorphic, all-crystalline, with a low percentage isocrystalline main mass and homogeneous anisotropic granitic association there is a high percentage of carbonates. Minerals such as: quartz, mica (muscovite), plagioclase and zoisite oriented belonoid crystals are observed. We have magma grains of dessert sized quartz. The last two minerals indicate a pyroxene residue.

Specimen 456 compared to 458 has more mica and not as many dessert crystals. Existence of brownish-red oxides (metallic grains) and clay silt where the presence of titanite and chlorite is possible. Huge exfoliated plagioclase grains as well as pseudomorphic chlorite which may have replaced pyroxene.

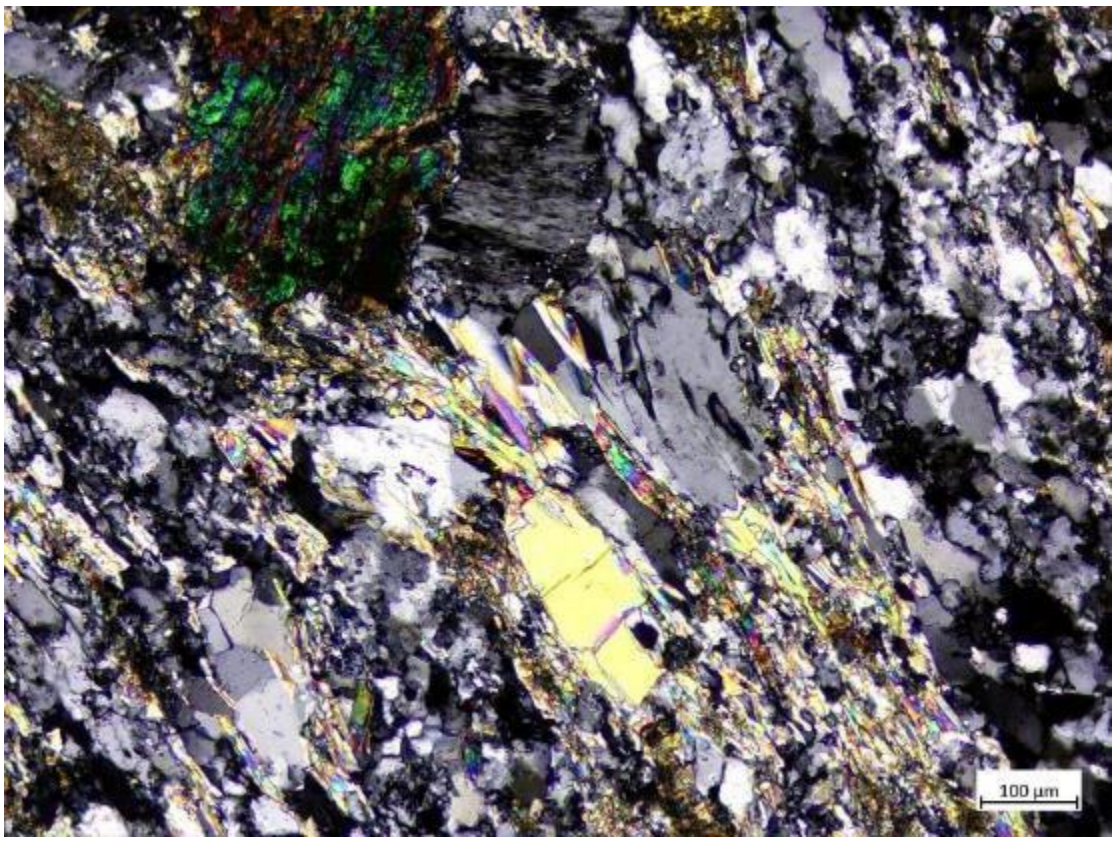

Figure 118: Section 456, Chlorite, epidote, zoisite and mica grains.

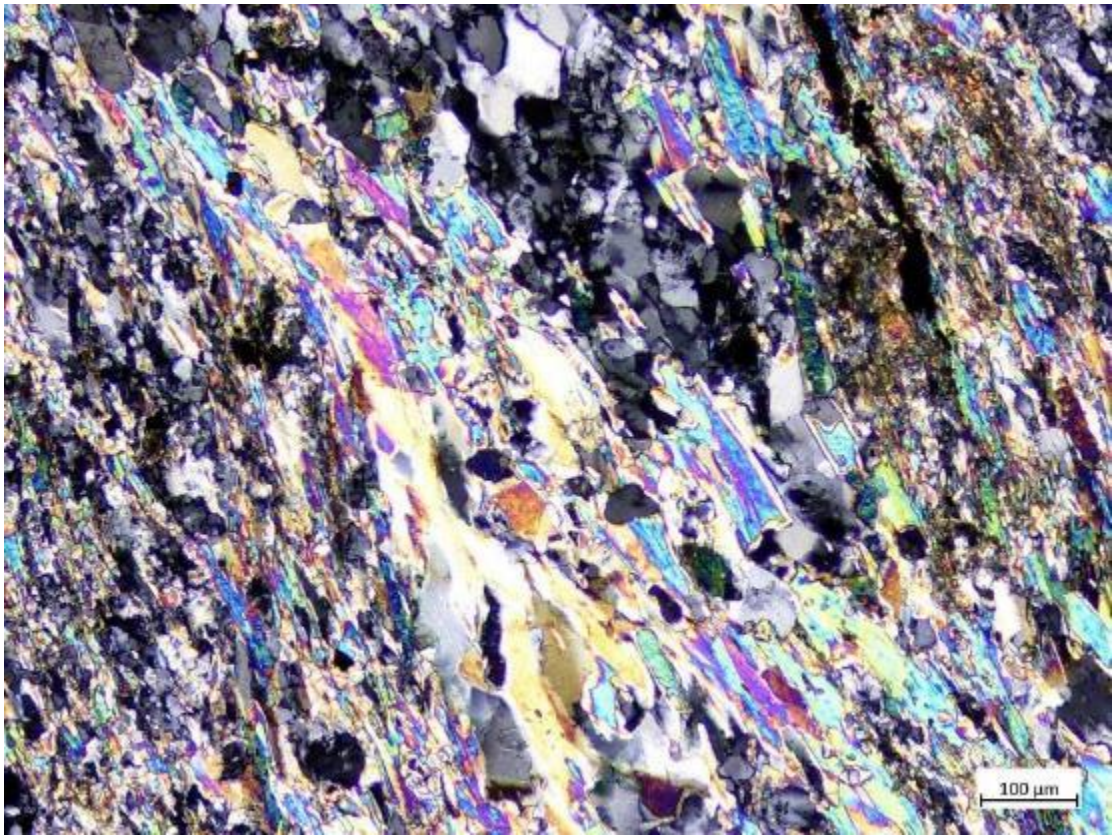

Figure 119: Section 456, Total mica granules.

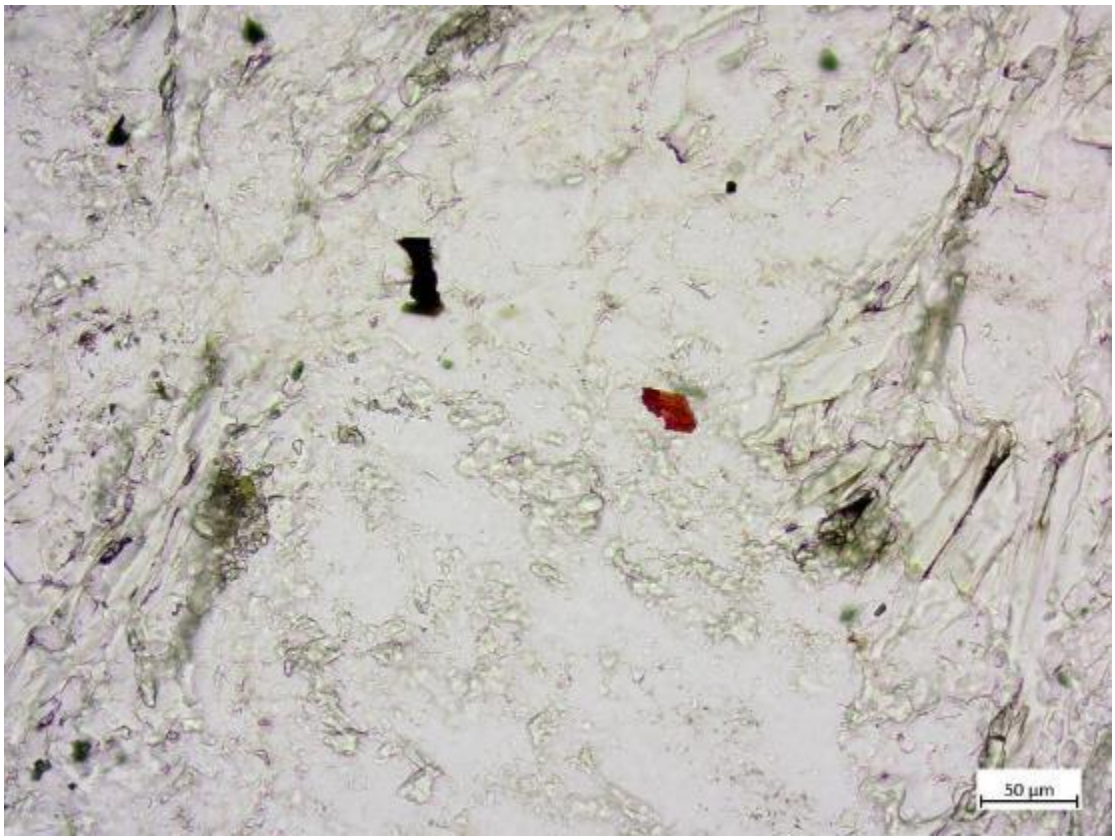

Figure 120: Section 456, Oxides-metallic minerals in //Nicols.

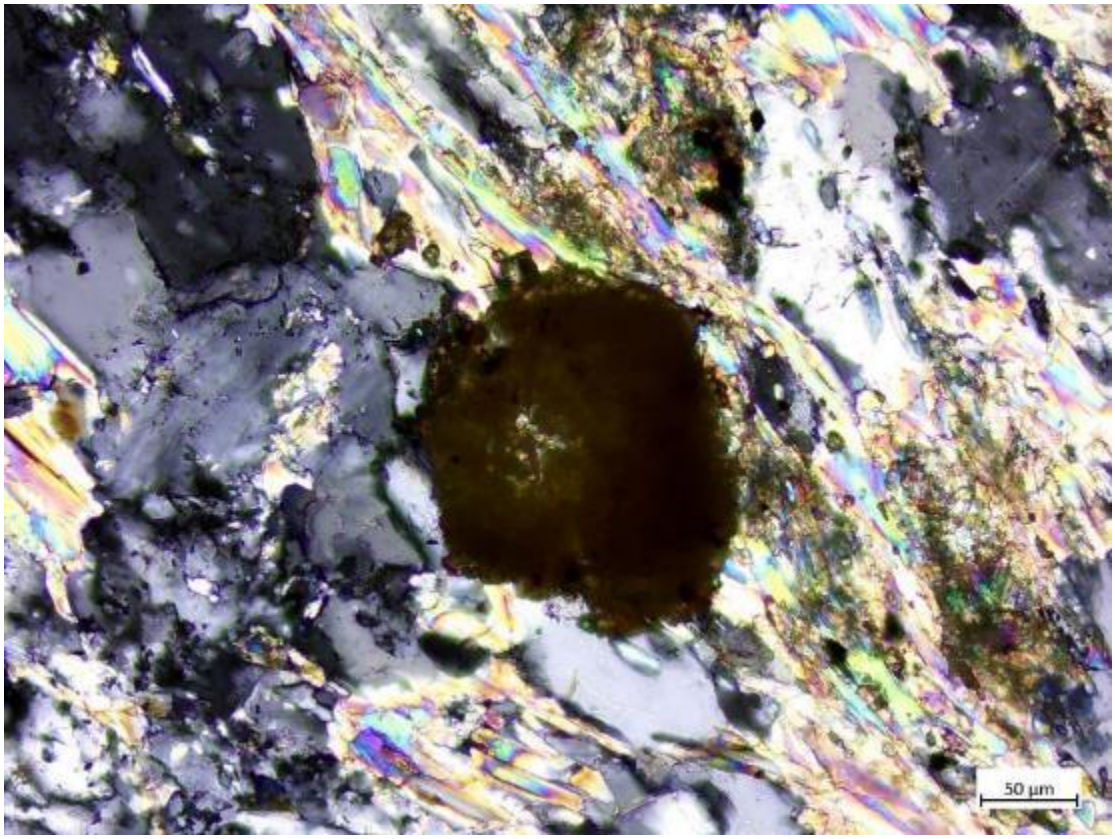

Figure 121: Section 456, Aggregate of clay-silicate minerals and mica.

Figure 122*:* Section *456*, *Giant grade of altered* plagioclase.

Figure 123: Section 456, Marked grain of this plagioclase on this section.

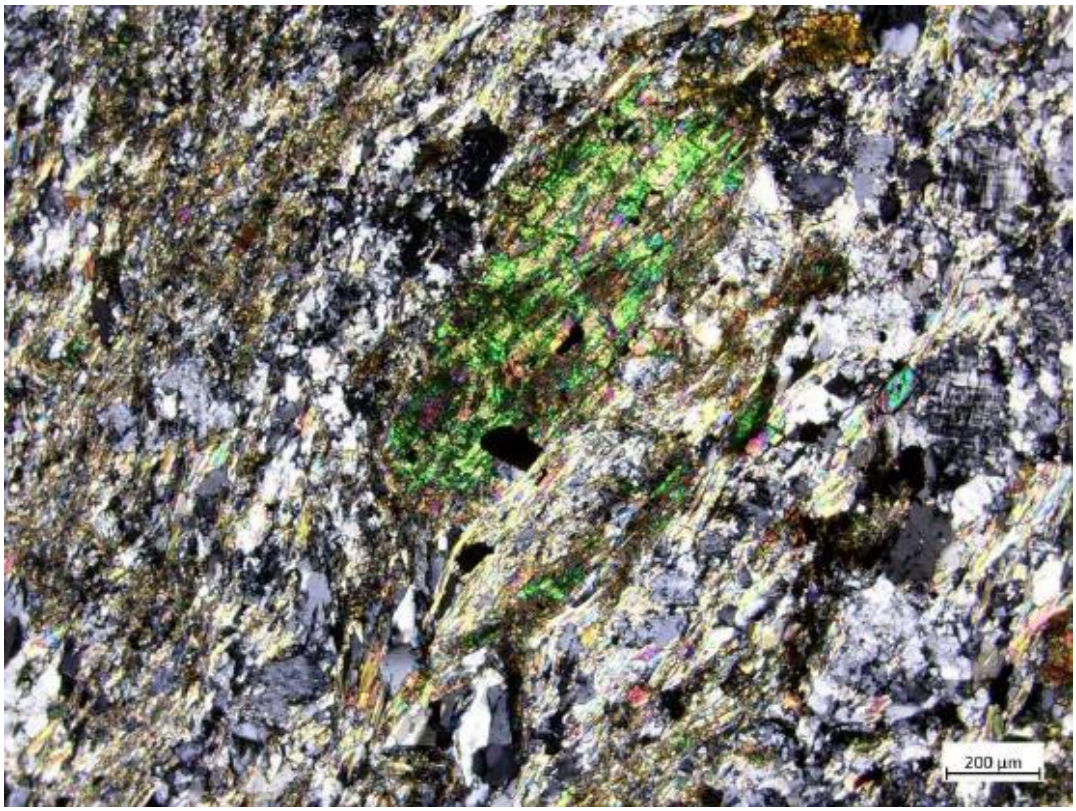

Figure 124: Section 456, Former pyroxene granules replaced by chlorite.

Figure 125: Section 456, Chlorite grain in // Nicols.

Sample 457(i) and 457(ii) (two samples of the same rock) are Igneous rock, with strong carbonate replacement, pro-grade; pro-grade; porphyritic microcrystalline with porphyritic fabric and indirect grain bonding. Large grains of epididote and chlorite indicate oxidizing environment of trivalent iron replacing Al in epididote. All in carbonate mass (rhombic cleavage and small white micas grains have yellow polarization and with internal reflections). Existence of zoisite crystals with yellow-purple (cyan) color and presence of epididote and chlorite. White mica phyllaries have slight cleavage and low relief unlike that of zoisite. 120-degree cleavage in blue amphibole like glaucophane or sodic tremolite. Phenocrysts glaucophane and of a mineral green color and polarization other than chlorite probably formerly marks former pyroxene. Existence of greenish-brown to blue amphibole probably jadeite. Of course, the zircons within Feldspars are too numerous. The plagioclases have many twinnings. A large grain of sodic-pyroxene is observed that is yellow with fission. All the above evidence points us to pressure and temperature conditions of 7-9kb, 300°C respectively.

At the intersection of 457(i) this observation was made:

Figure 126: Section 457(i), 1.1 Epidote and chlorite in // Nicols

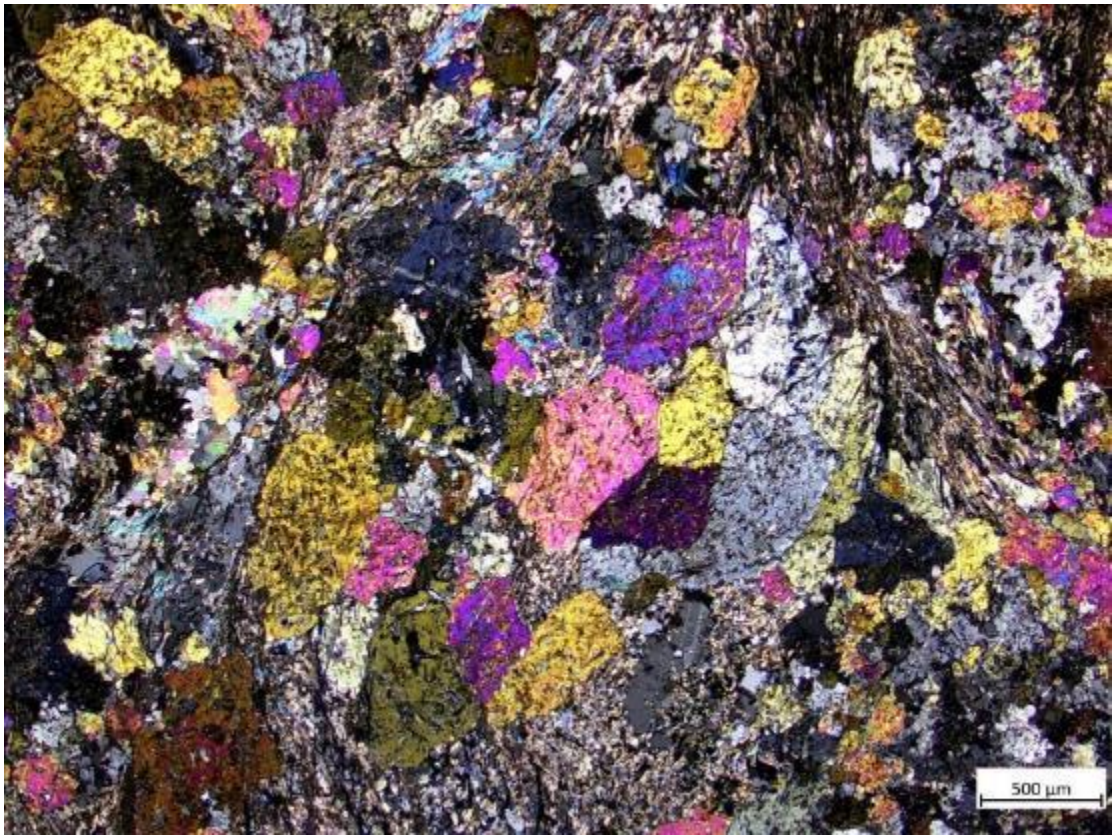

Figure 127: Section 457(i), 1.2 Epidote and chlorite in crossed Nicols.

Figure 128: Section 457(i), 2.1. Calcite with double cleavage and polarization multicolor.

Figure 129: Section 457(i), 2.2. Calcite with double cleavage and polarization multicolor.

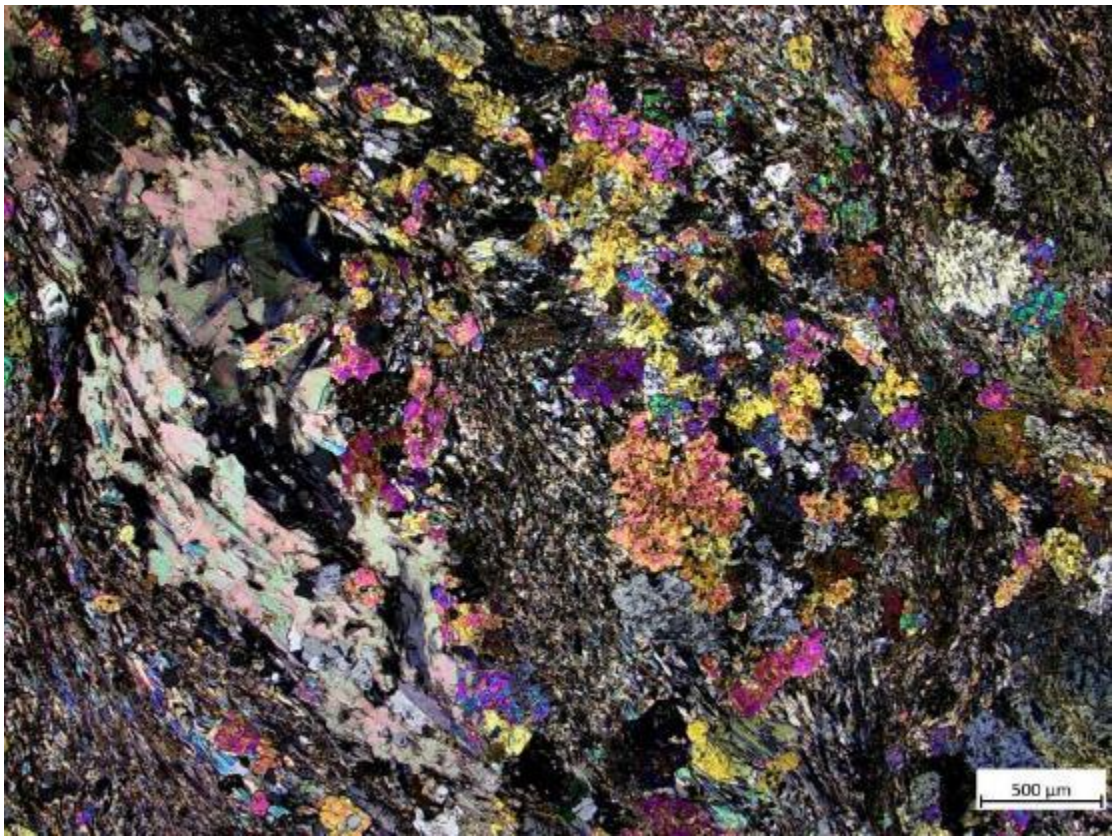

Figure 130: Section 457(i), 3.1. Epidote, chlorite, what is blue is glaucophane and other amphiboles crossed Nicols.

Figure 131: Section 457(i), 3.1 Epidote, chlorite, what is blue is glaucophane and other amphiboles in // Nicols.

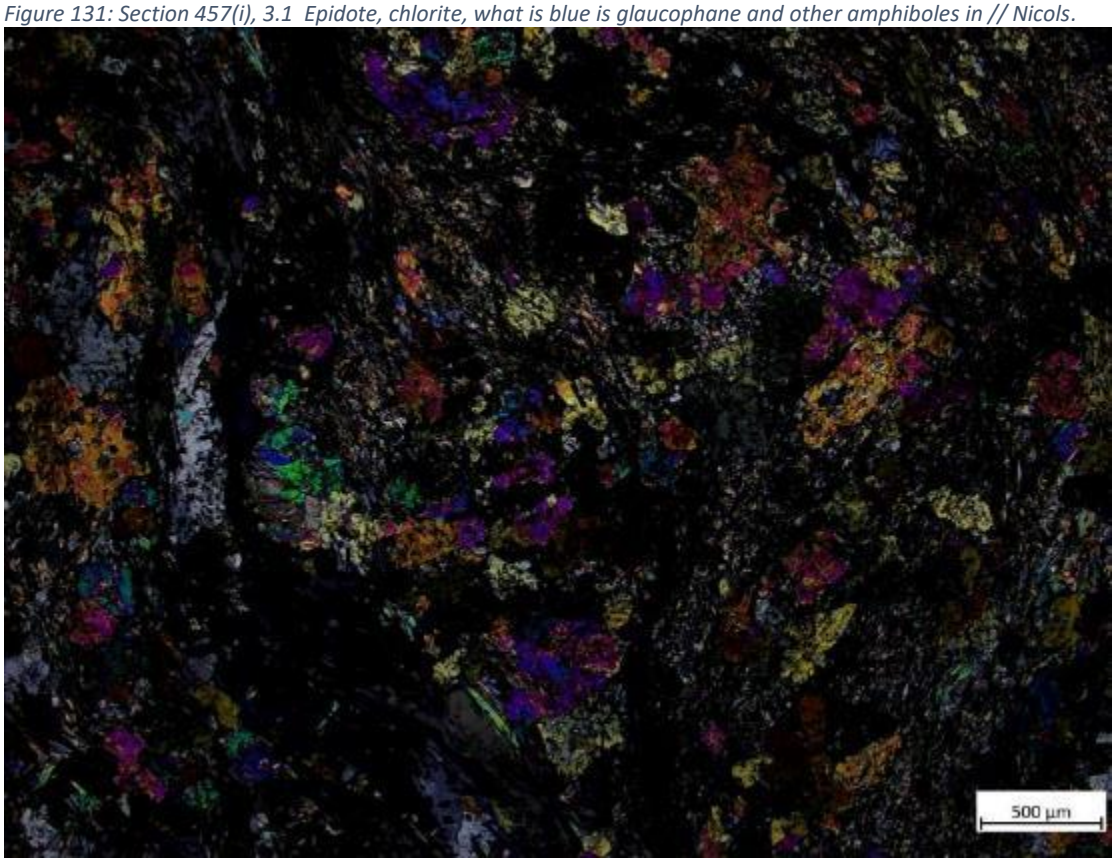

Figure 132: Section 457(i), 3.2. Epidote, chlorite, what is blue is glaucophane and other amphiboles in crossed Nicols.

Figure 133: Section 457(i), 3.2. Epidote, chlorite, what is blue is glaucophane and other amphiboles in // Nicols.

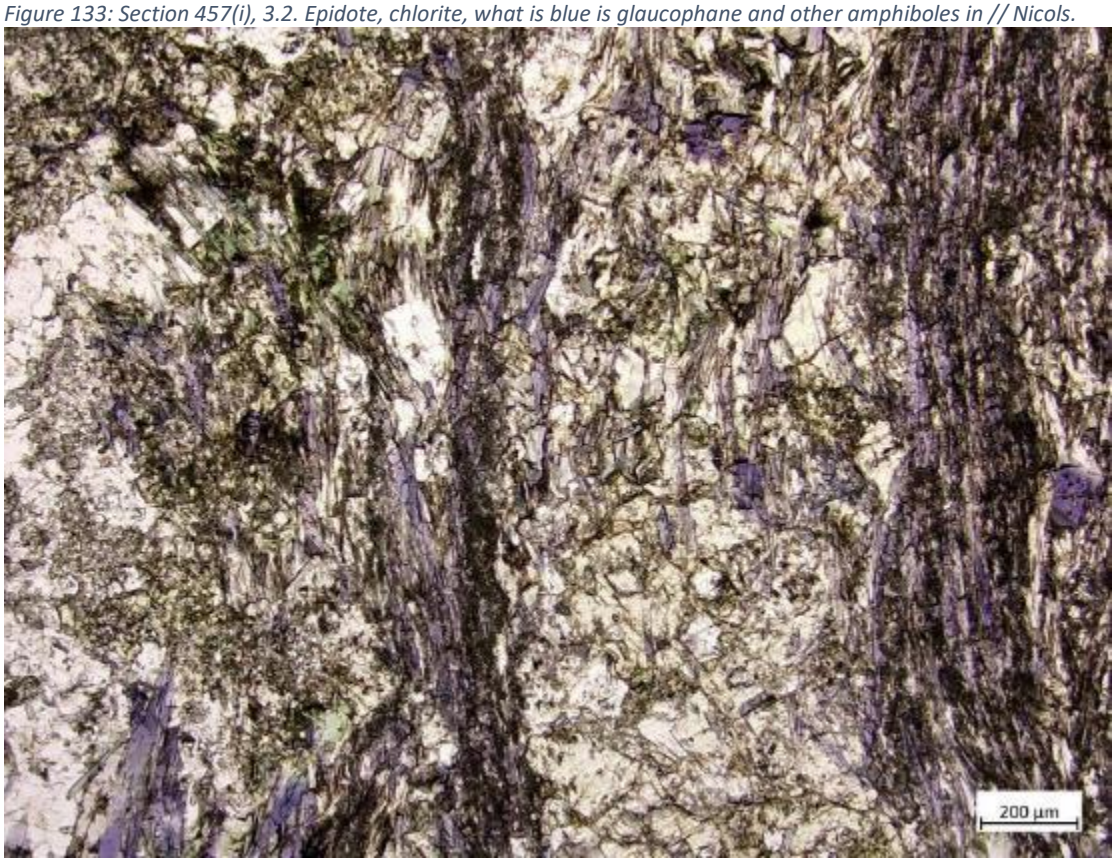

Figure 134: Section 457(i), 3.3. Epidote, chlorite, what is blue is glaucophane and other amphiboles in // Nicols.

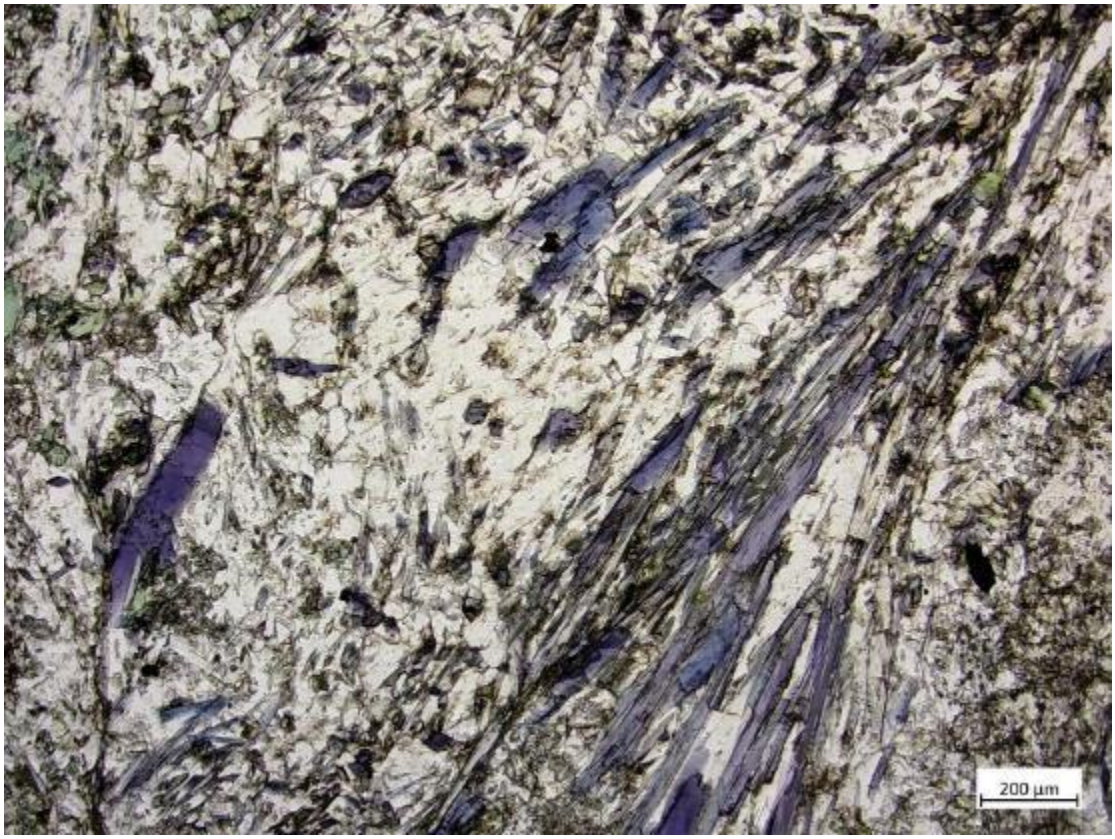

Figure 135: Section 457(i), 3.4. Epidote, chlorite, what is blue is glaucophane and other amphiboles in // Nicols.

Figure 136: Section 457(i), 3.5. Epidote, chlorite, what is blue is glaucophane and other amphiboles in // Nicols.

Figure 137: Section 457(i), 3.6. Epidote, chlorite, what is blue is glaucophane and other amphiboles in // Nicols.

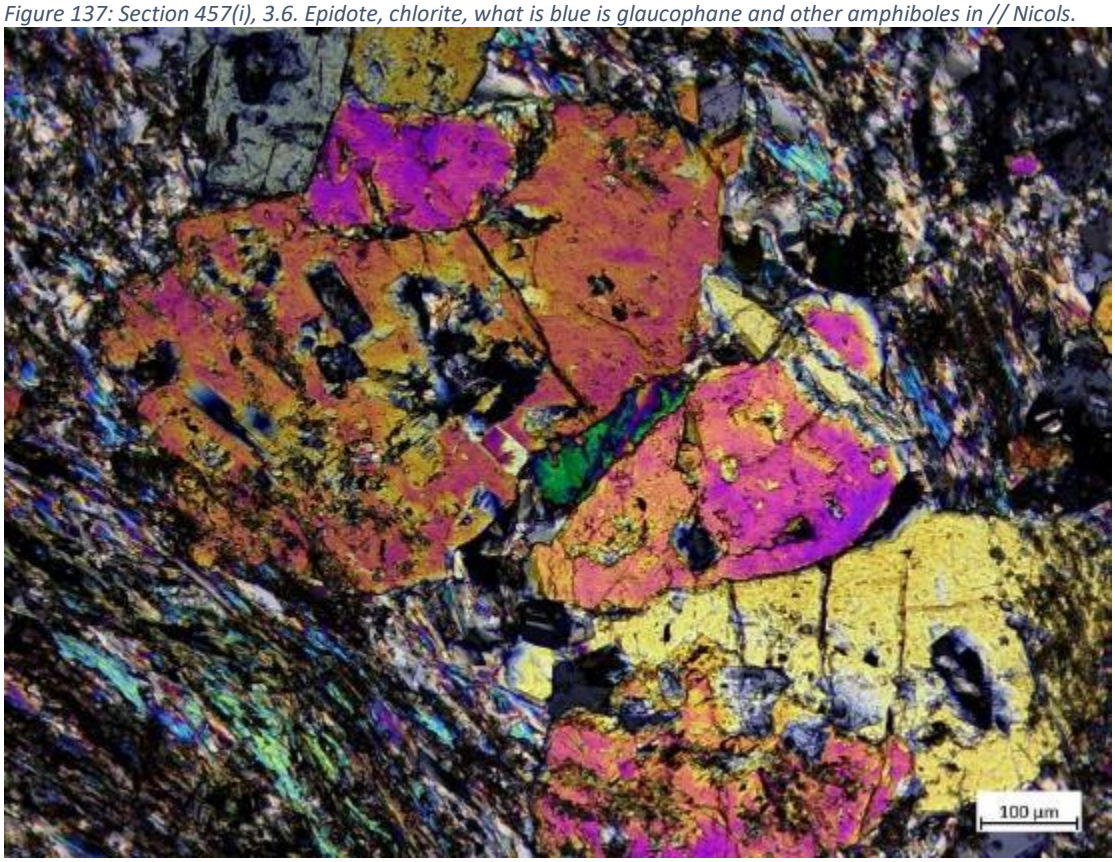

Figure 138: Section 457(i), 3.6. Zoisite with (lila-yellow polarization colors) in crossed Nicols.

Figure 139: Section 457(i), Area 1: epidote and chlorite, area 2 carbonate (calcite)

Figure 140: Section 457(i), Areas of former granules that now have chlorite and glaucophane.

Figure 141: Section 457(I), Area where zoisite was observed.

Figure 142: Section 457(I), Area with epidote, chlorite and what is blue is glaucophane and other sodic amphiboles such as tremolite.

Sample 460 is igneous rock, intermediate grain size, (medium grade) medium-micrograined, is merocrystalline, anisocrystalline, with a purple fabric. The sample is homogeneous with small grains of dessert and zoisite (high analogue). We have existence of blue amphiboles everywhere (like glaucophane) and it seems to replace clinopyroxene (with pink-yellow polarization colors). Additional minerals are titanite, white mica and microgranular existence of chlorite.

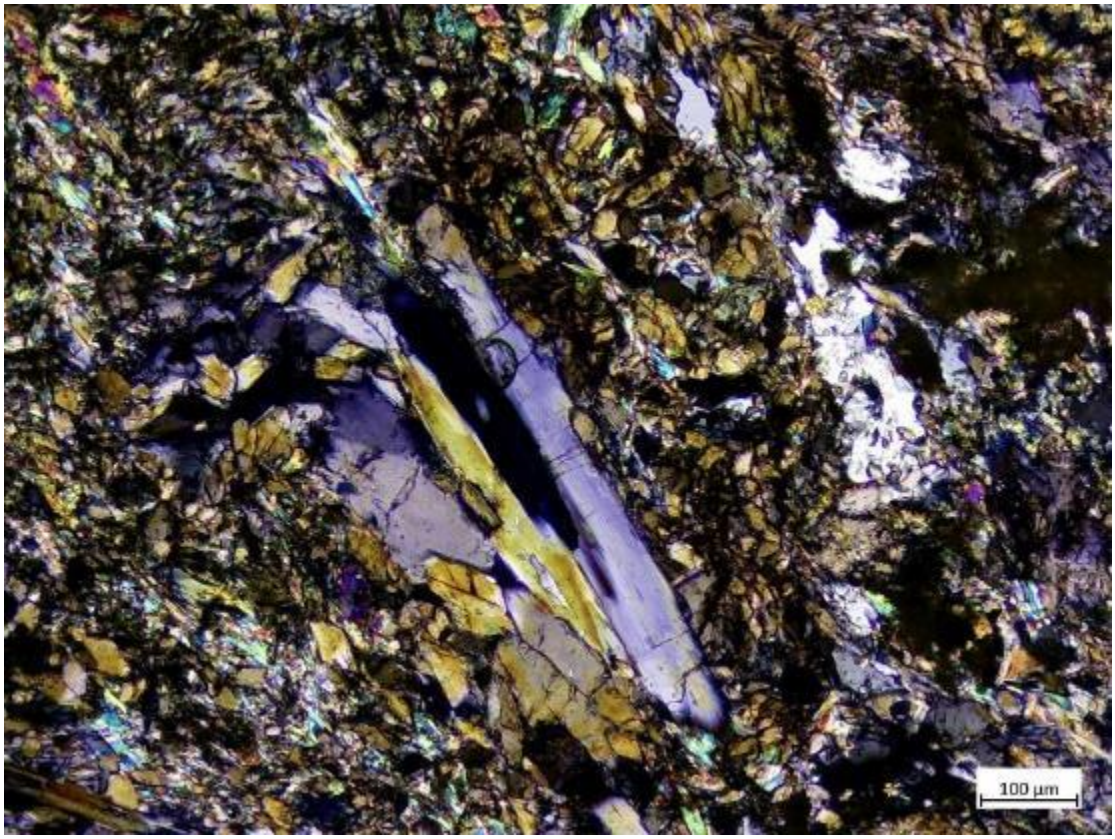

Figure 143: Section 460, 1.1. Blue amphiboles and small grains of epidote and zoisite (high relief). Epidote, titanite and zoisite replace pyroxene grains.

Figure 144: Section 460, 1.2. Blue amphiboles and small grains of epidote and zoisite (high relief). Epididote, titanite and zoisite replace pyroxene grains.

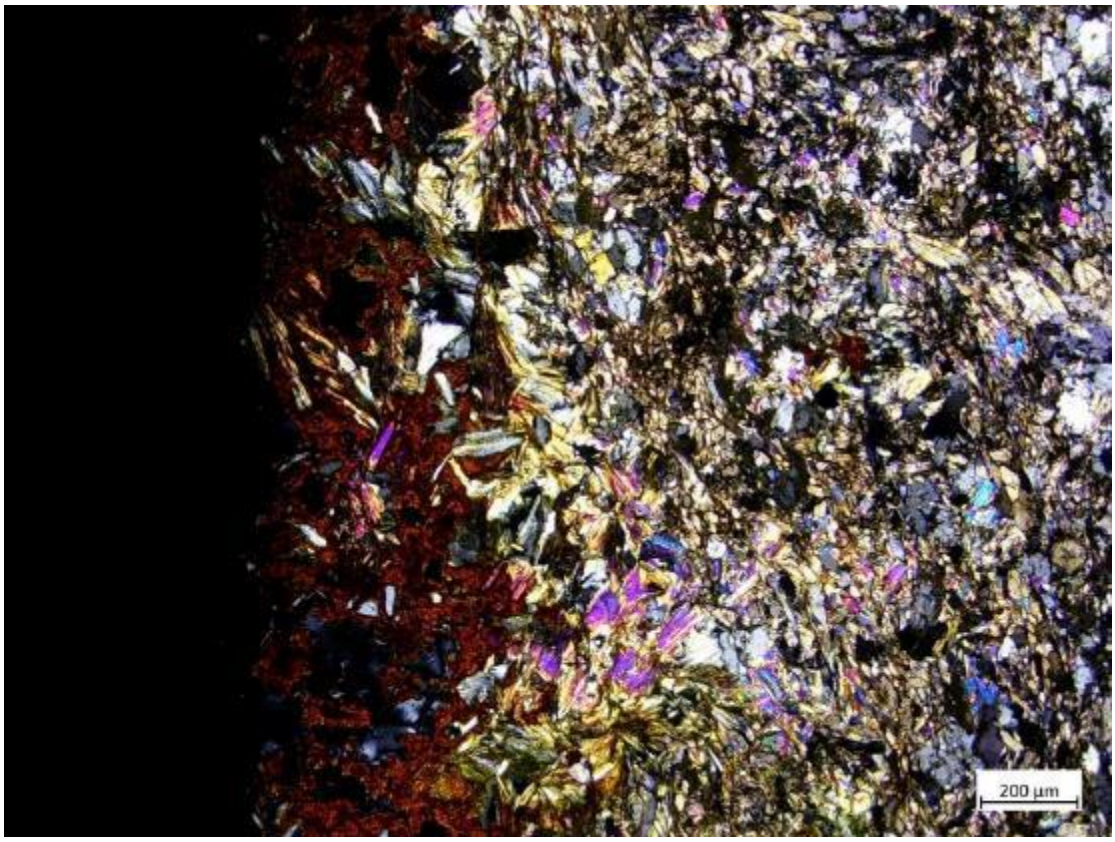

Figure 145: Section 460, 2.1 Epidote, titanite and zoisite replace pyroxene grains.

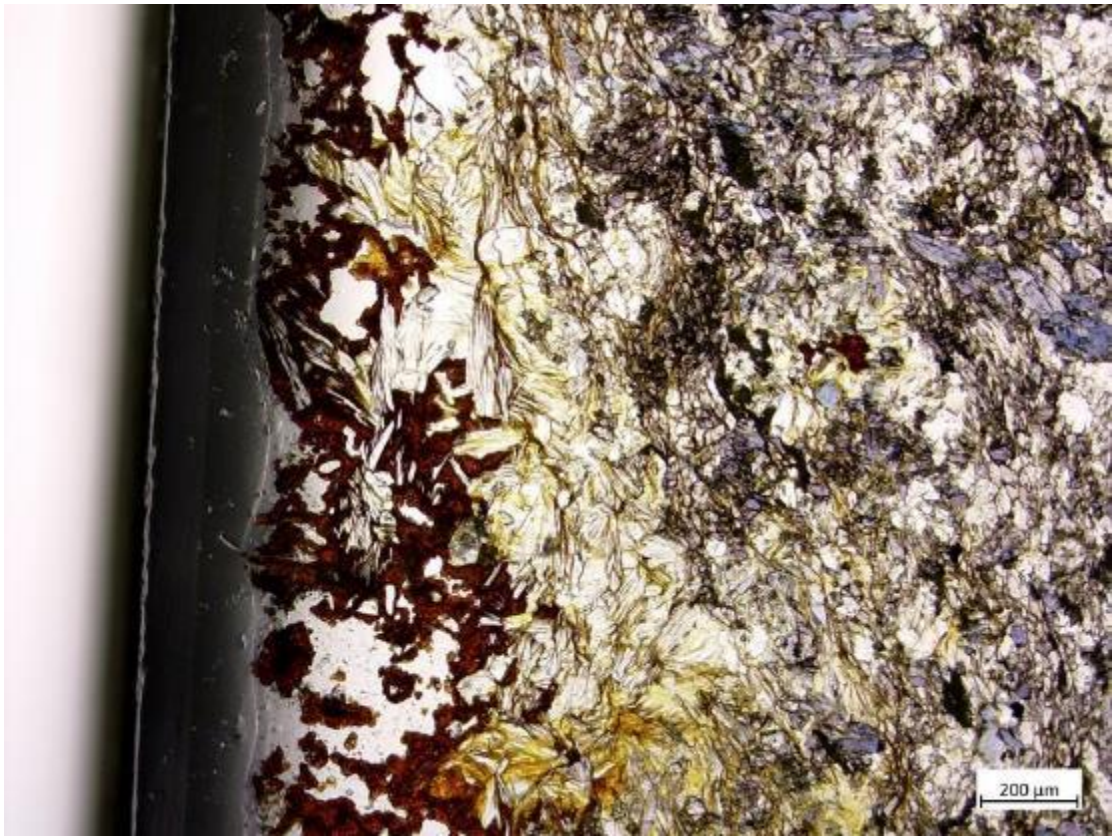

Figure 146: Section 460, 2.2. Epidote, titanite and zoisite replace pyroxene grains.

Figure 147: Section 460, Areas with the minerals in sample 460 reported.

Samples 461(i) and 461(ii) were collected from the same area and indeed are the same rock which is metamorphic, all-crystalline with purple tissue, anisocrystalline and of mineral observe: Plagioclase with perthitic structure and twinning. The moonstone forms large prismatic crystals. The so-called annealing structure that creates tectonized quartz at 120 degrees characterizes almost all the extent of the section. And finally, we have titanite and zircon grains in the sample.

Starting with photos of section 461(i):

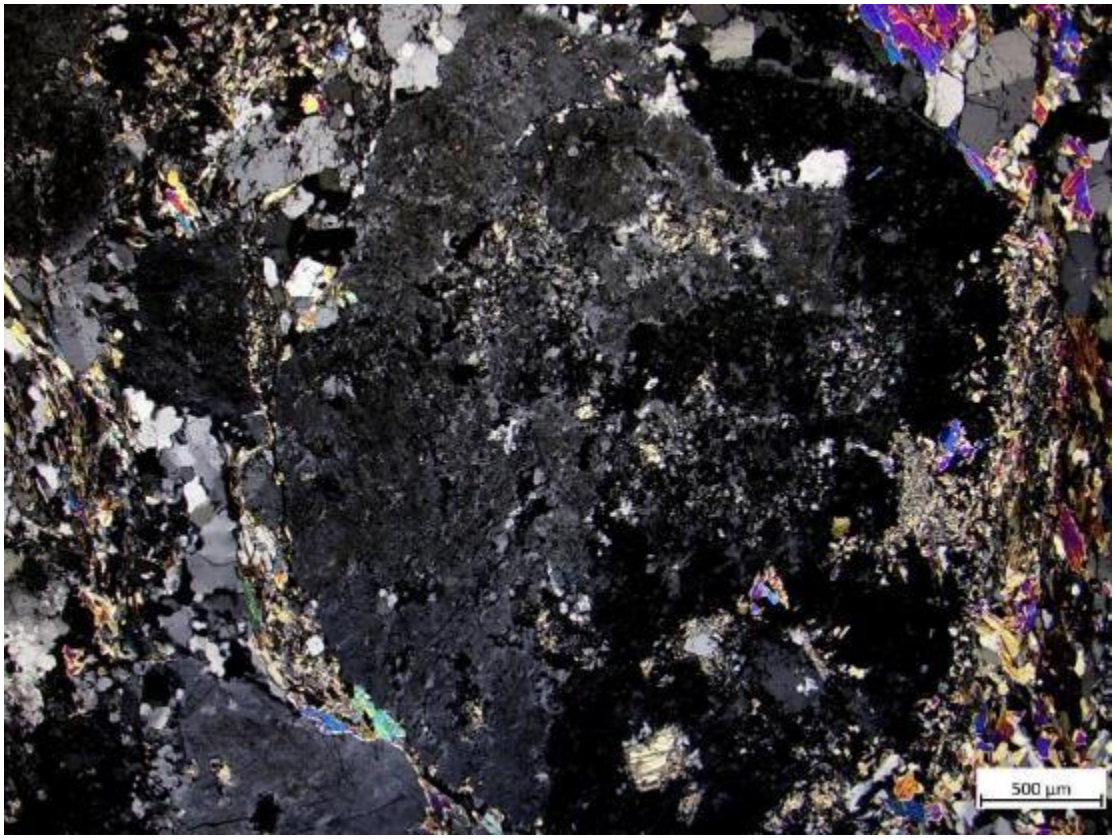

Figure 148: Section 461(I), 1.1. Plagioclase with perthitic structure and twinning in crossed Nicols.

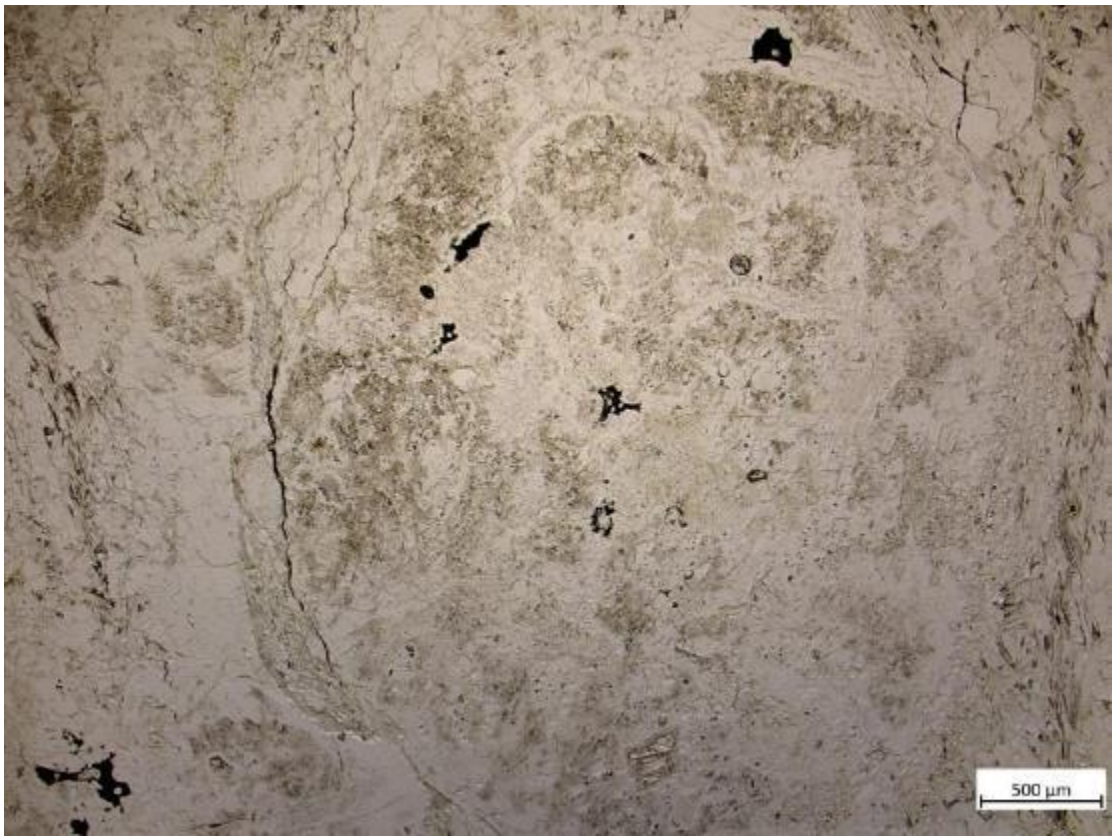

Figure 149: Section 461(i), 1.2. Plagioclase with perthitic structure and twinning in // Nicols.

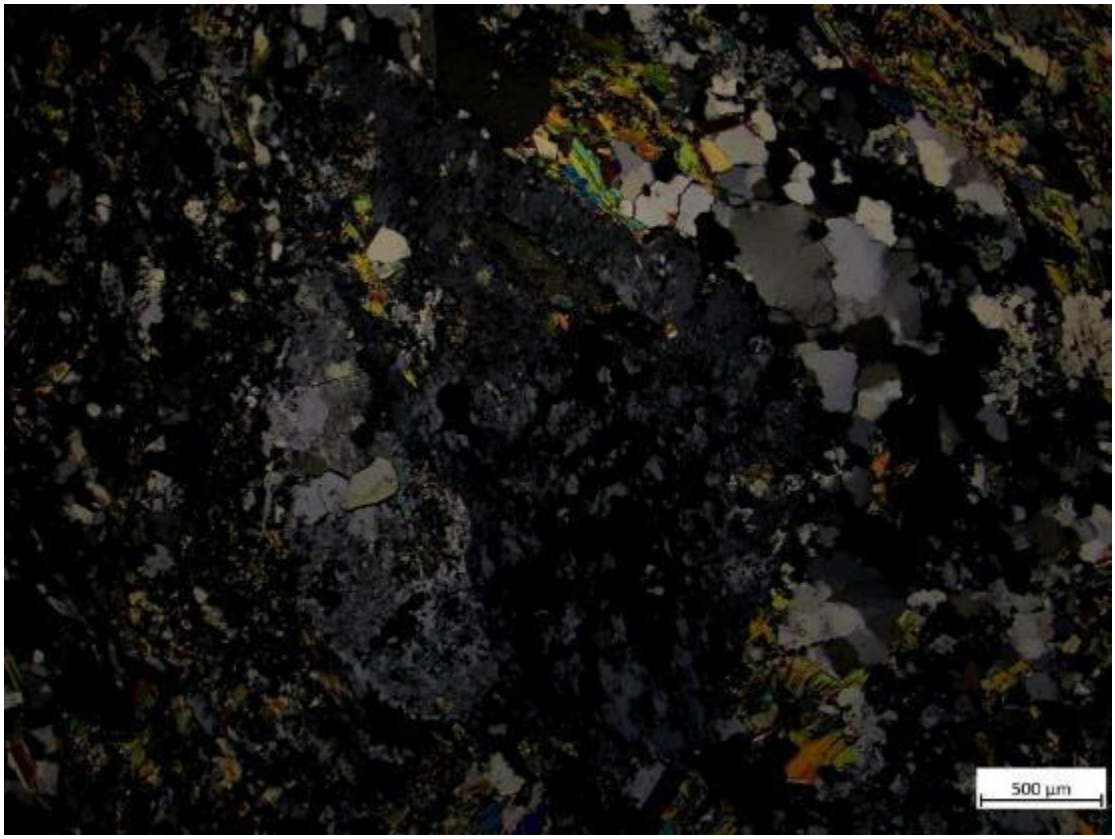

Figure 150: Section 461(i), 1.3 Plagioclase with perthitic structure and twinning in crossed Nicols, 2.1. Prismatic fengite crystals

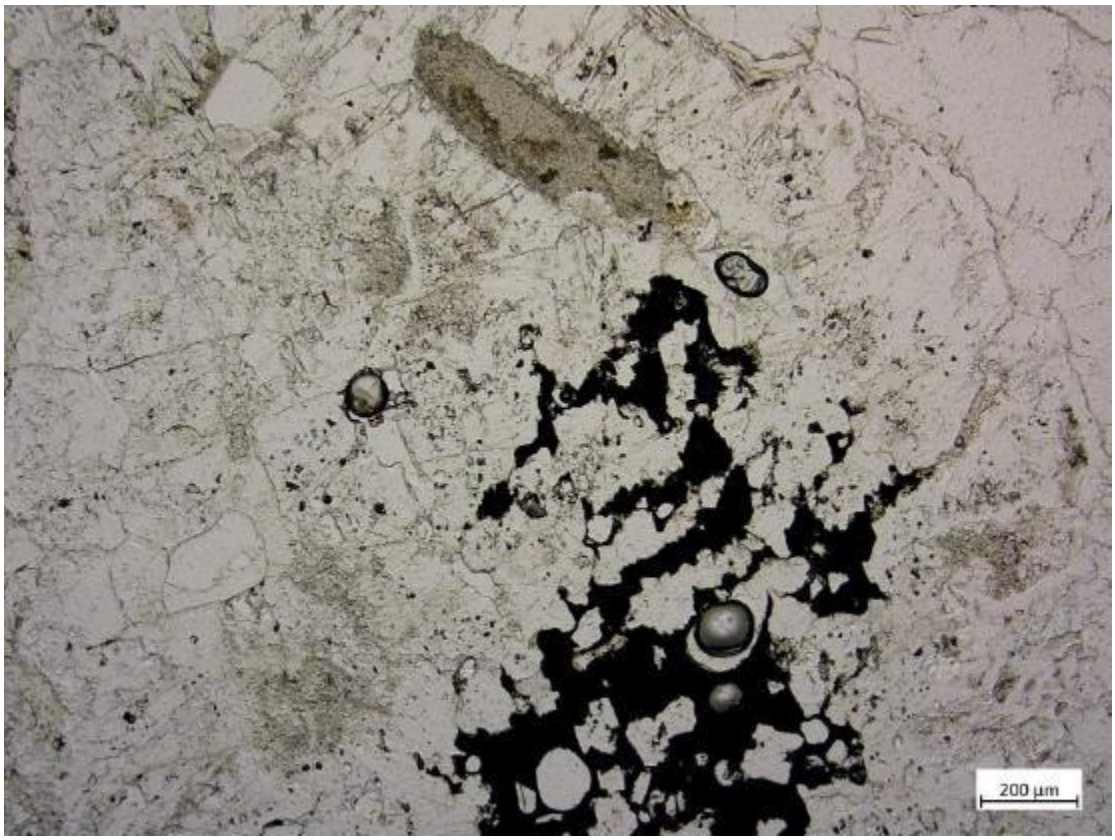

Figure 151: Section 461(i), 1.4. Plagioclase with perthitic structure and twinning in // Nicols,

Figure 152: Section 461(i), 3.1 Annealing structure of quartz in // Nicols.

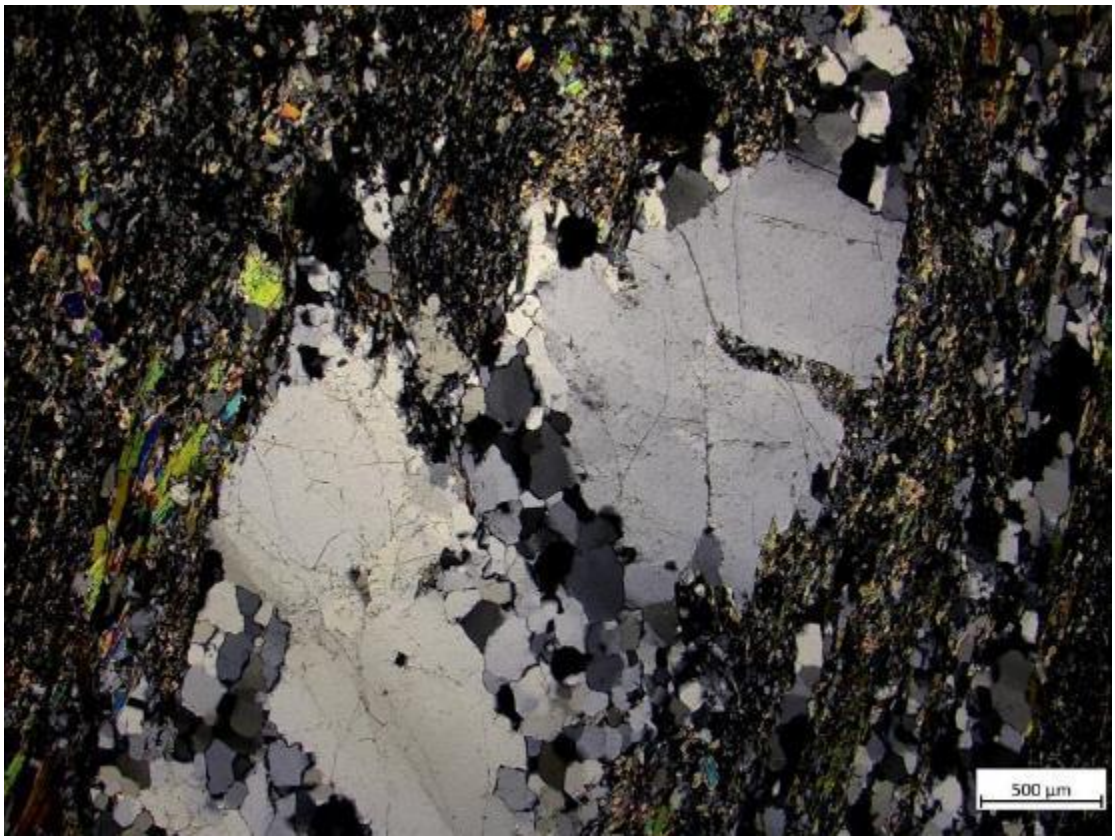

Figure 153: Section 461(i), 3.2 Annealing structure of quartz in crossed Nicols

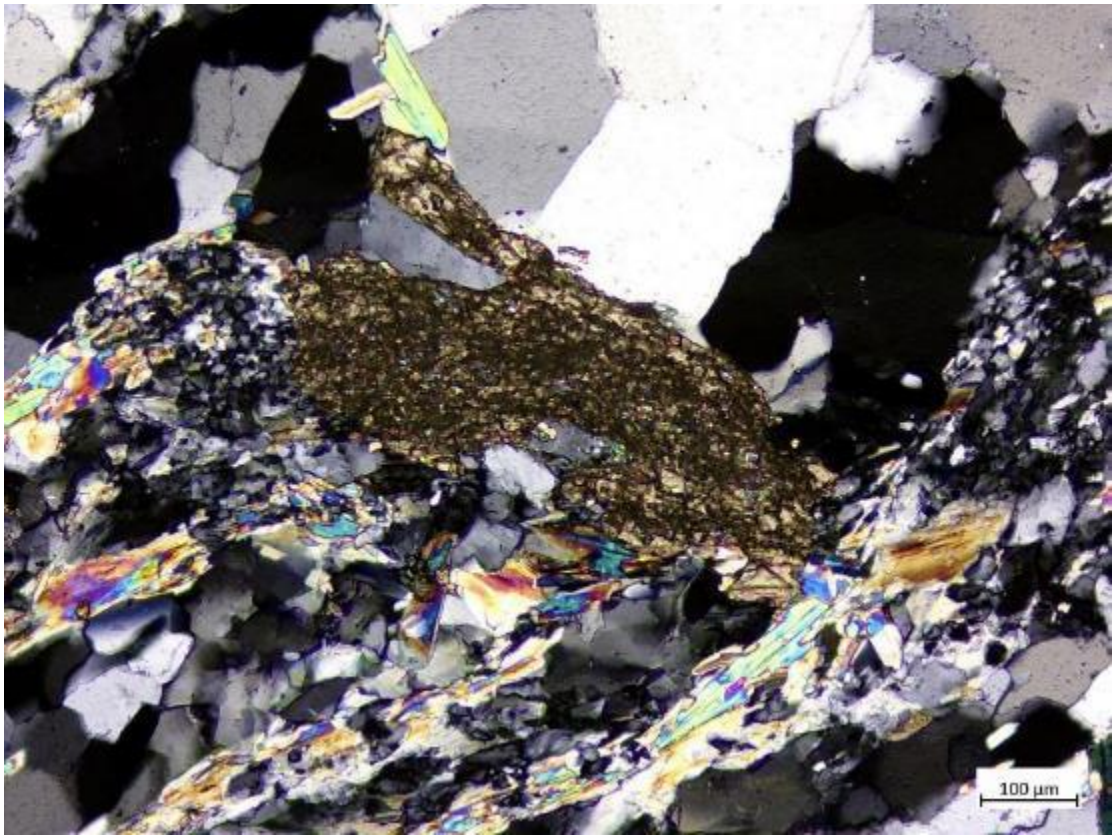

Figure 154: Section 461(i), 4.1. Titanite granules.

Figure 155: Section 461(I), Marked areas of minerals reported in section 461(I).

Continuing with the microscope images of sample 461(ii):

Figure 156: Section 461(ii), 1.1. Altered plagioclase with perthitic structure and twinning.

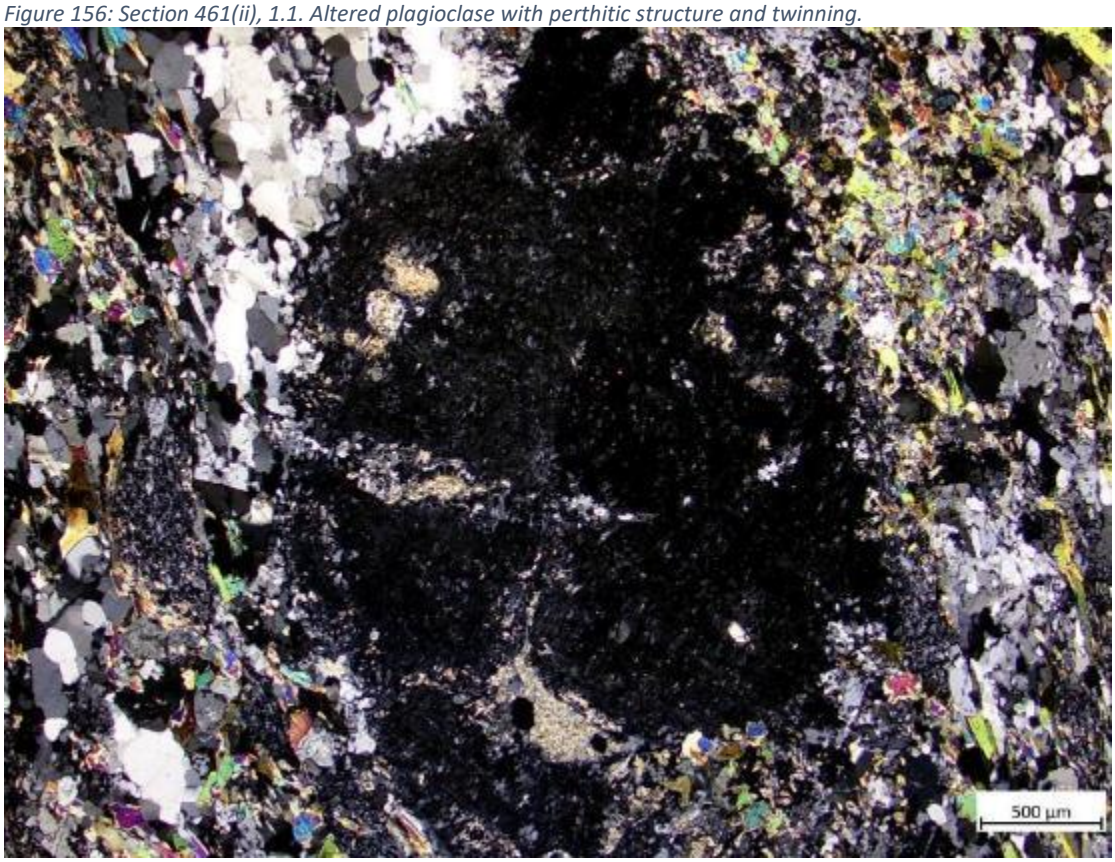

Figure 157: Section 461(ii), 1.2. Altered plagioclase with perthytic structure and twinning.

Figure 158: Section 461(ii), 1.3. Altered plagioclase with perthytic structure and twinning.

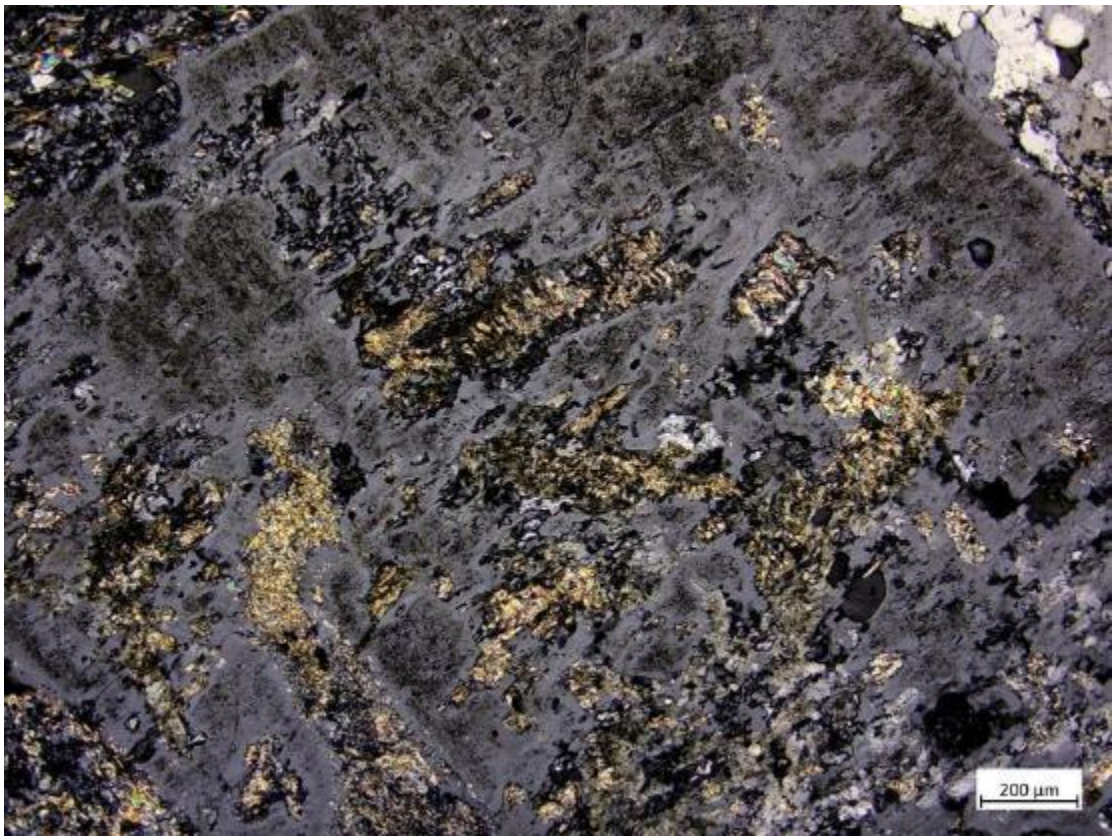

Figure 159: Section 461(ii), 1.4. Altered plagioclase with perthytic structure and twinning.

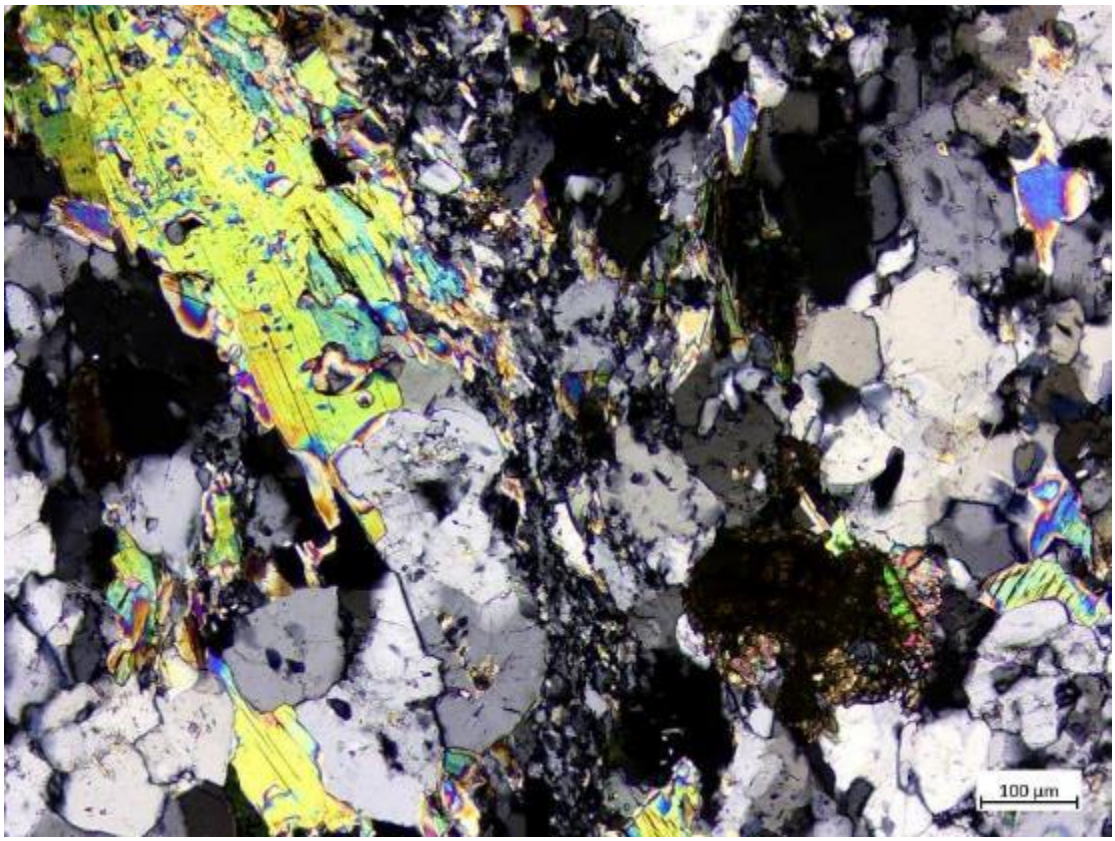

Figure 160: Section 461(ii), 4.1 Existence of titanite and mica grains in crossed Nicols.

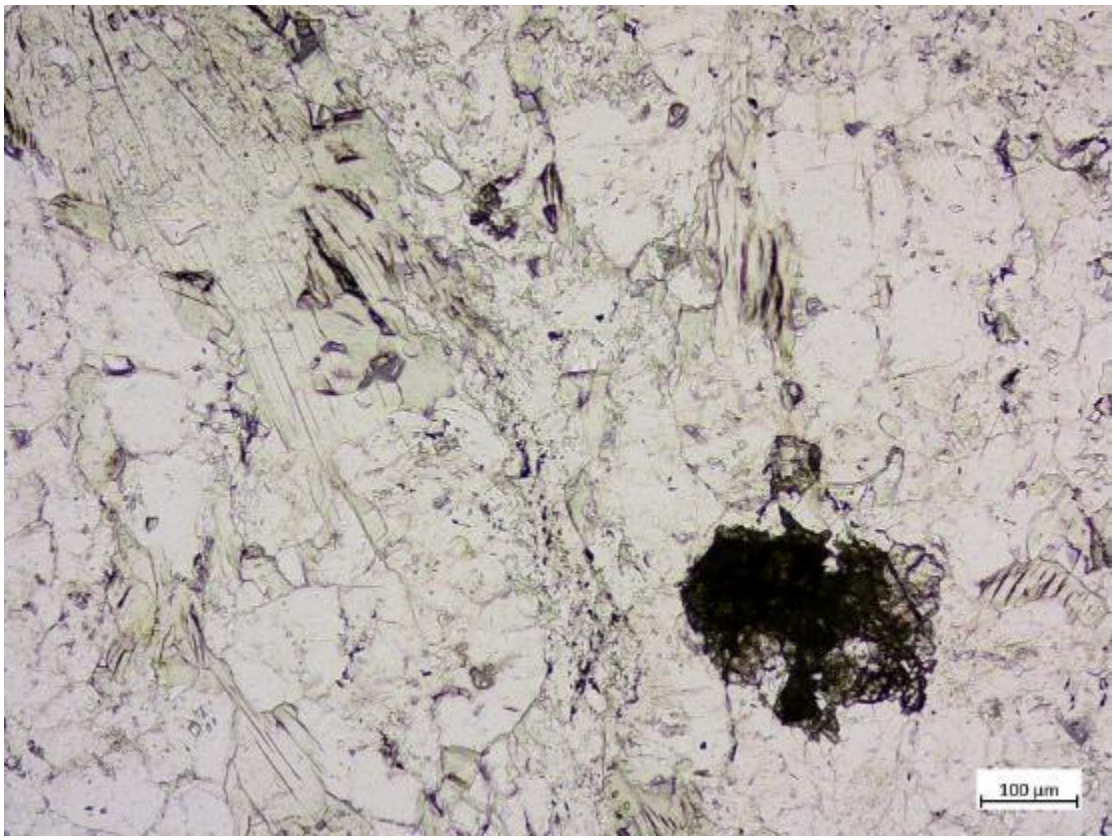

Figure 161: Section 461(ii), 4.2. Existence of titanite and mica grains in // Nicols.

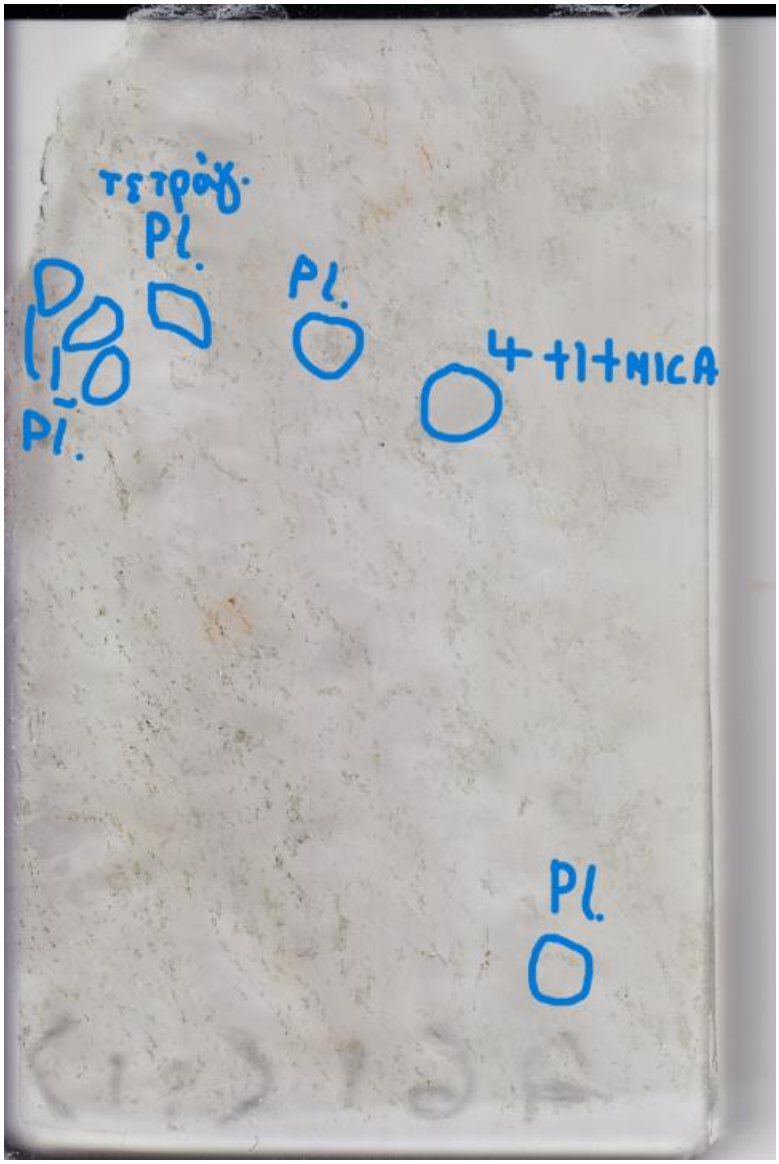

Figure 162: Section 461(ii), Marked areas in the transect, mainly of the laterals observed.

Sample 464(i) has an anisocrystalline structure, is all-crystalline with minerals such as quartz (foliation parallel zones with slightly more developed grains, with anisotropic and parallel grain arrangement (foliation parallel), calcite, plagioclase, intergranular mica with slight cleavage and an aggregate of clay-silicate minerals. Characteristic is the intense mineralization which is observed macroscopically and in the main mass between the grains as we have hyprimorphic grains of metallic minerals.

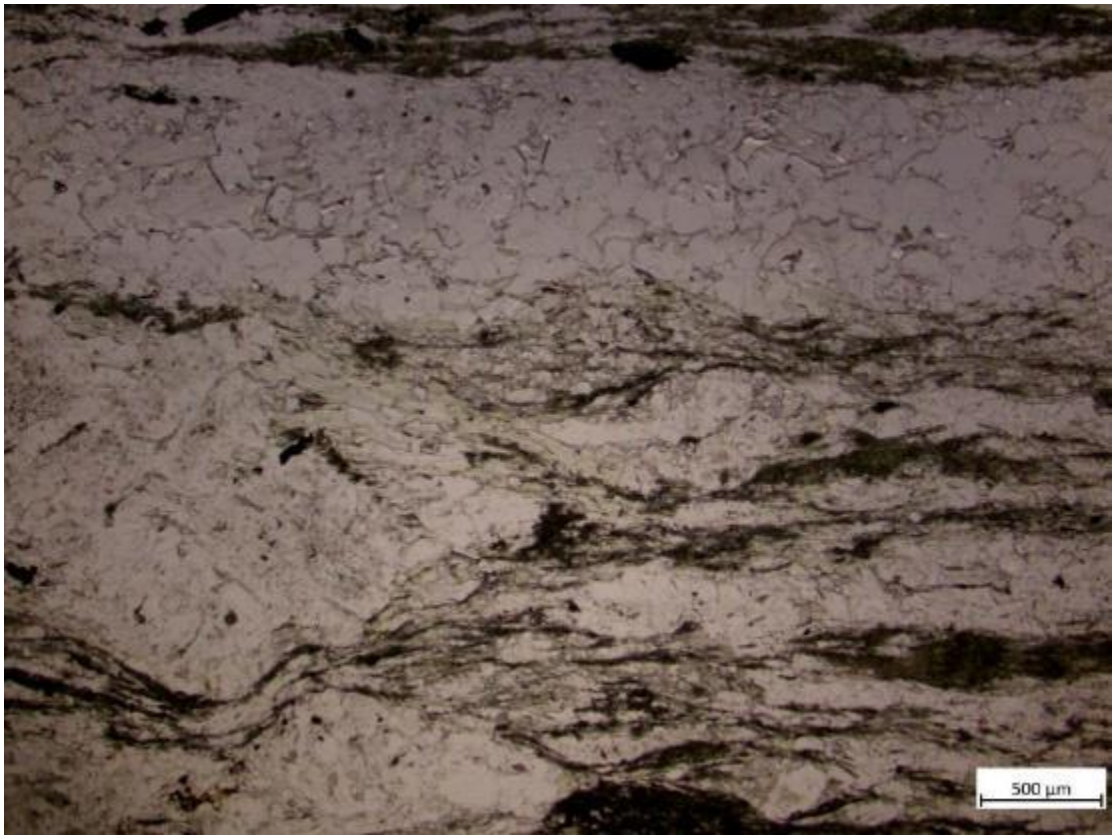

Figure 163: Section 464(i), Quartz zones (stressed Quartz) in // Nicols.

Figure 164: Section 464(i), Quartz zones (stressed Quartz) in crossed Nicols.

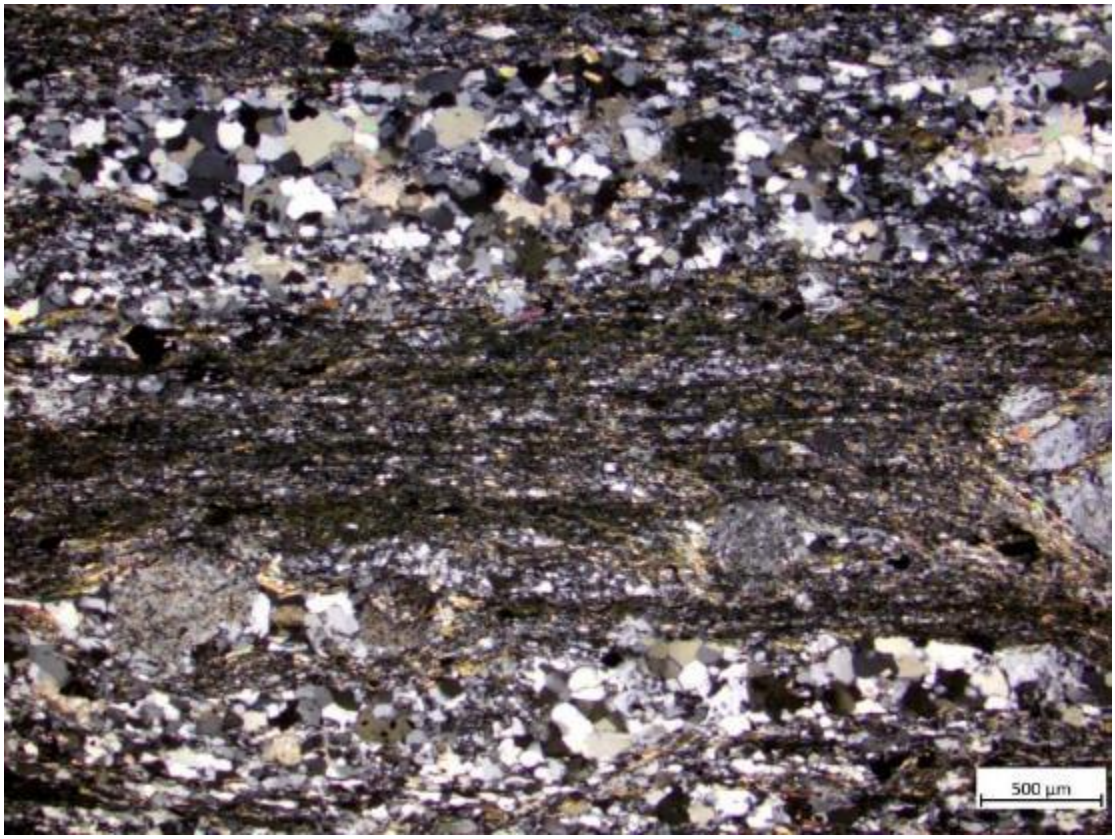

Figure 165: Section 464(i), Quartz belts (stressed Quartz) in crossed Nicols.

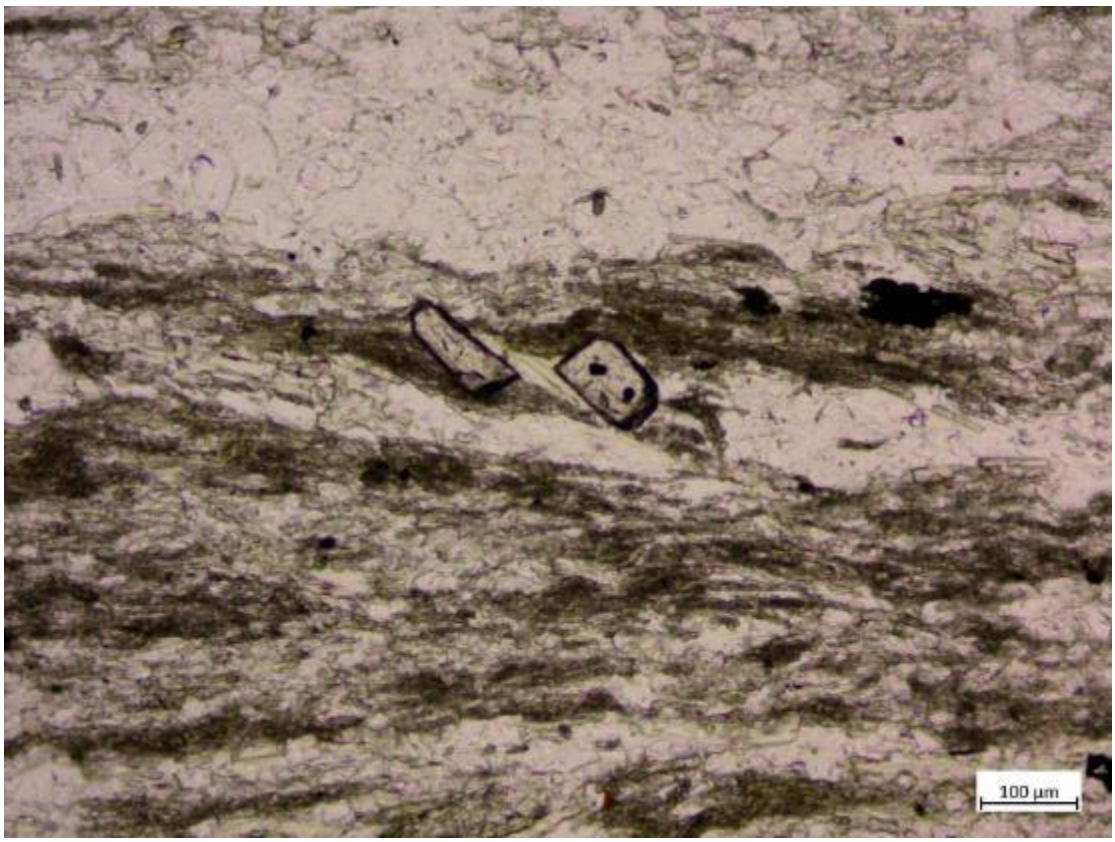

Figure 166: Section 464(i), //Nicols

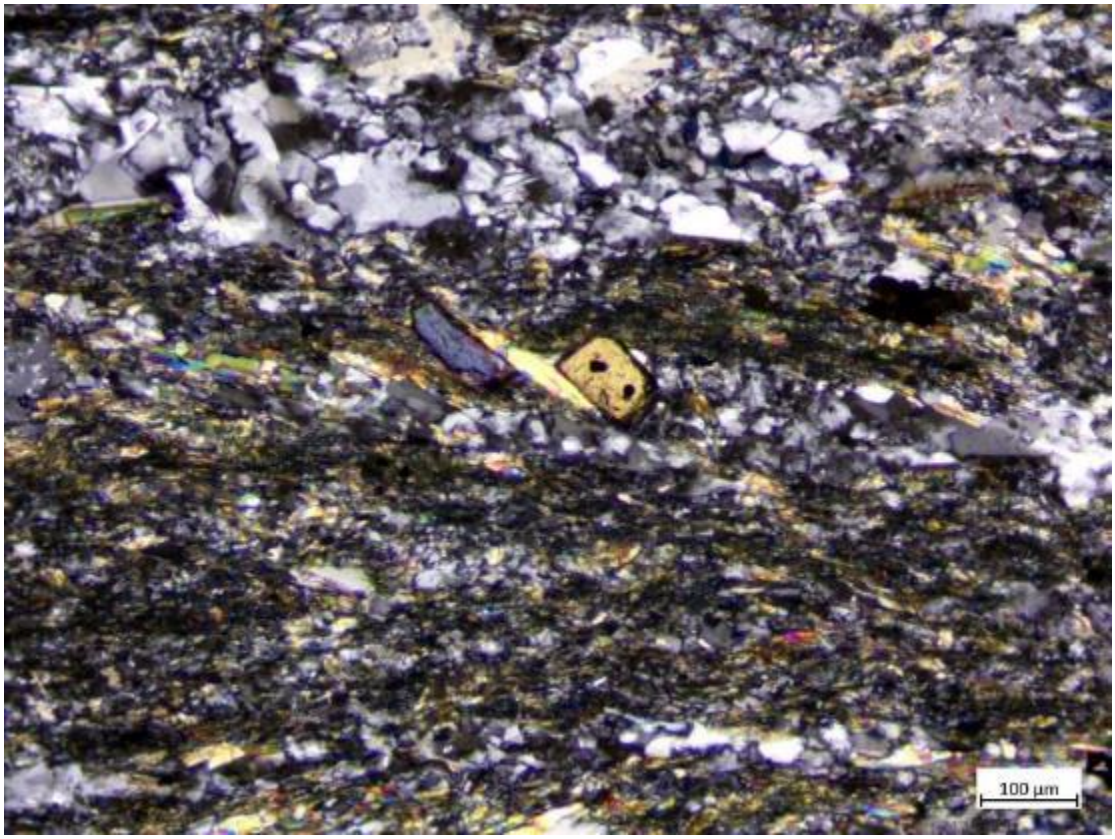

Figure 167: Section 464(i), Crossed Nicols.

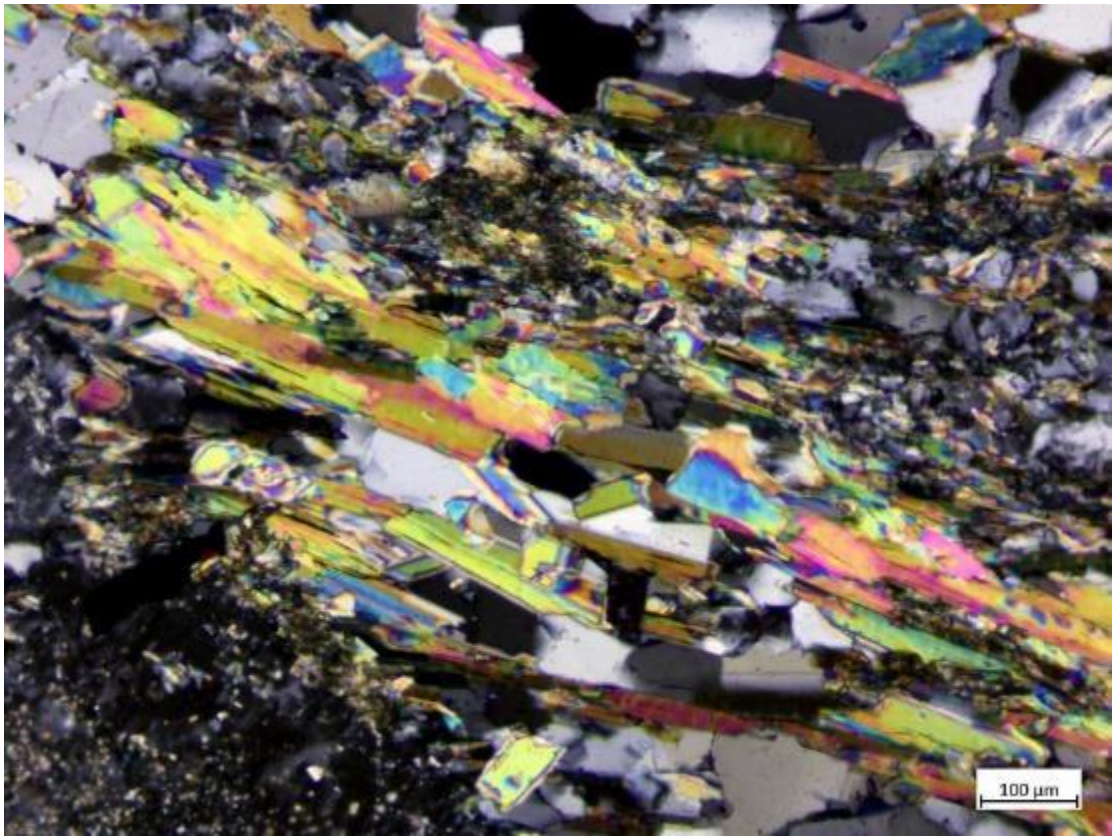

Figure 168: Section 464(i), Velloid mica crystals in crossed Nicols.

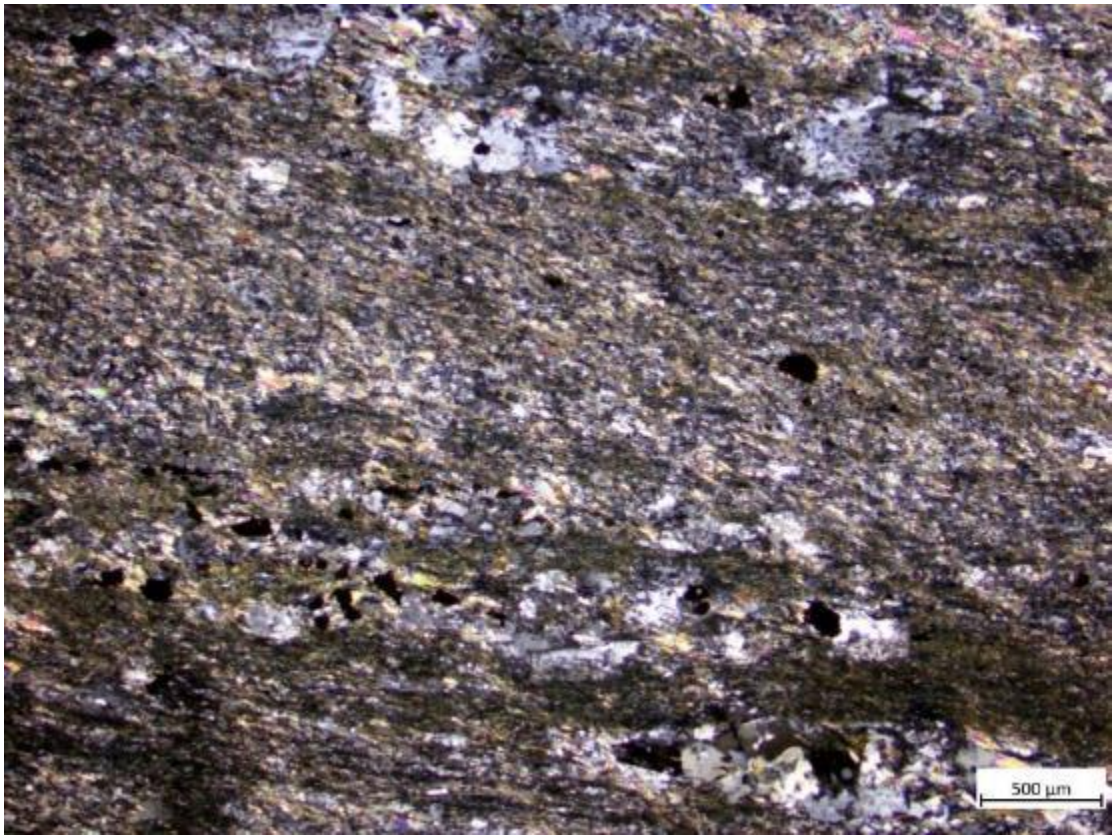

Figure 169: Section 464(i), Dark grains of metallic minerals in crossed Nicols.

Sample 464(ii) has been collected from exactly the same location and is part of exactly the same rock as (Felsic Rock). The quartz is stressed quartz with a characteristic undulating quench, the presence of many micas, plagioclase and of course carbonate minerals.

The above images were obtained from the Matscope program installed on the computer connected to the microscope. The sections were scanned and used as a map to locate the above minerals.

Unit 4.3 Microprobe Analysis of Mainz

After microscopic reconnaissance, the most interesting mineralogically interesting sections were selected that contained mineral phases that had been altered by others as little as possible and that could not justify a schist rock.

Below are the Microprobe photos for each sample:

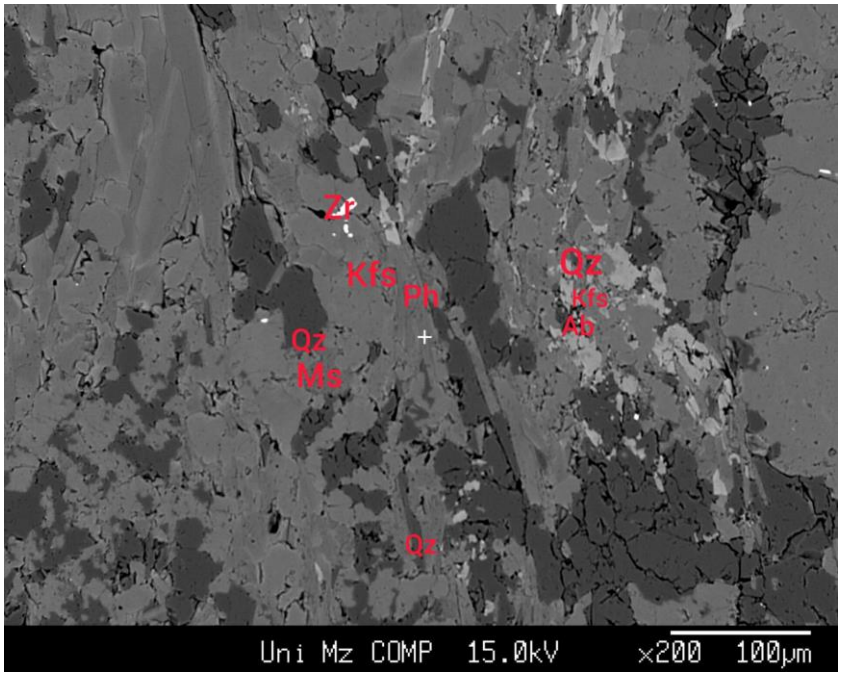

Figure 170: Sample 456 a1-a11

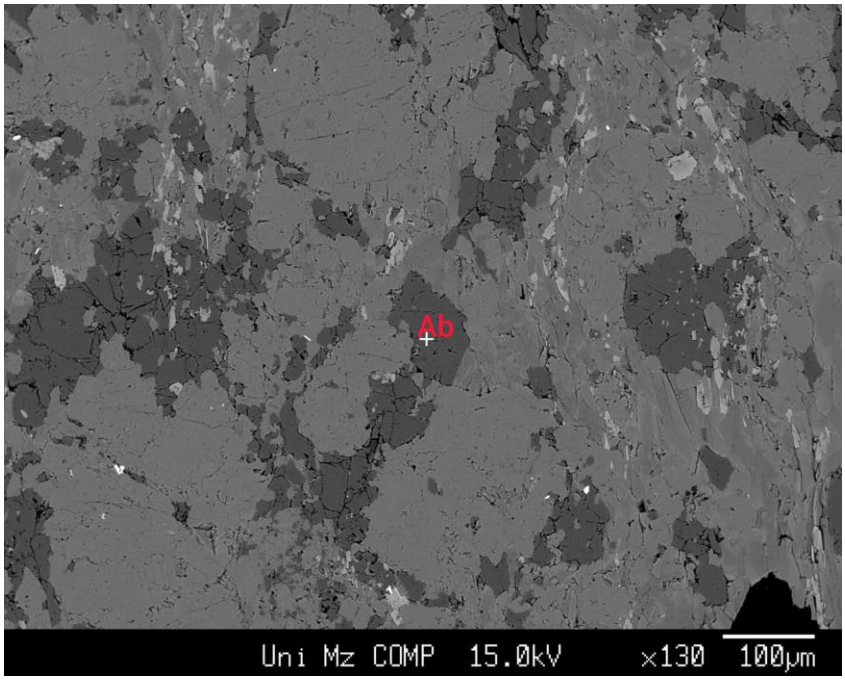

Figure 171: Sample 456 a12

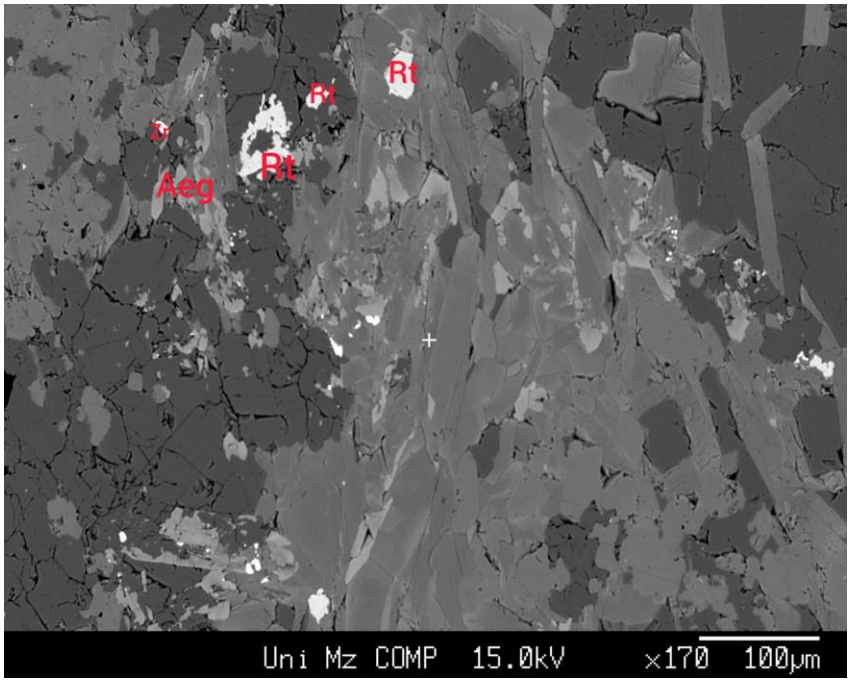

Figure 172: Sample 456 a13-a15

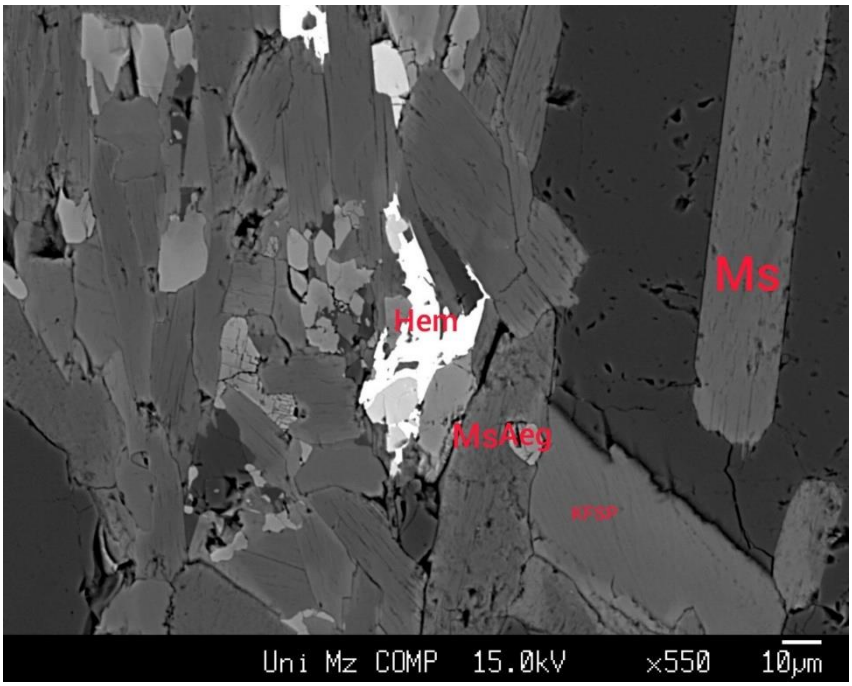

Figure 173: Sample 456 a16-a20

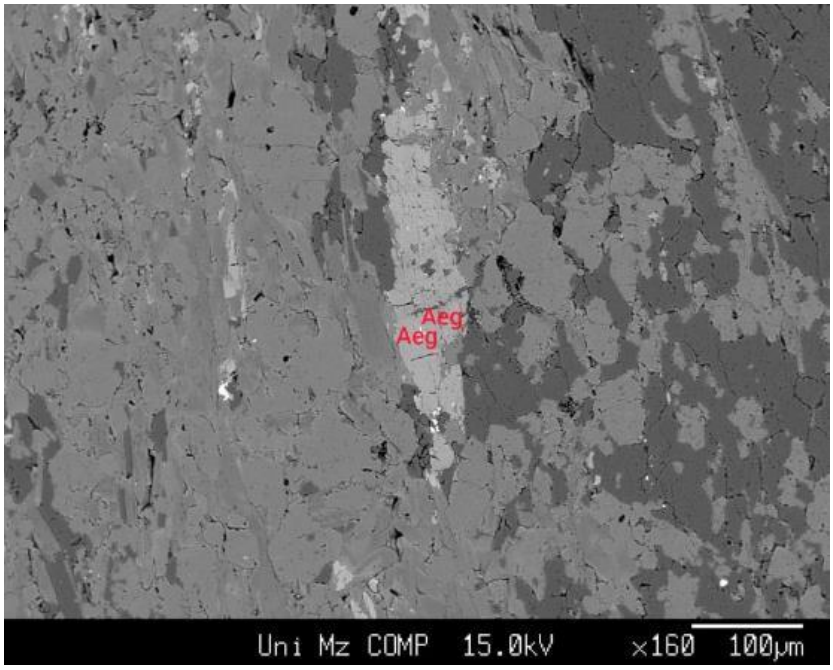

Figure 174: Sample 456 a21-a22

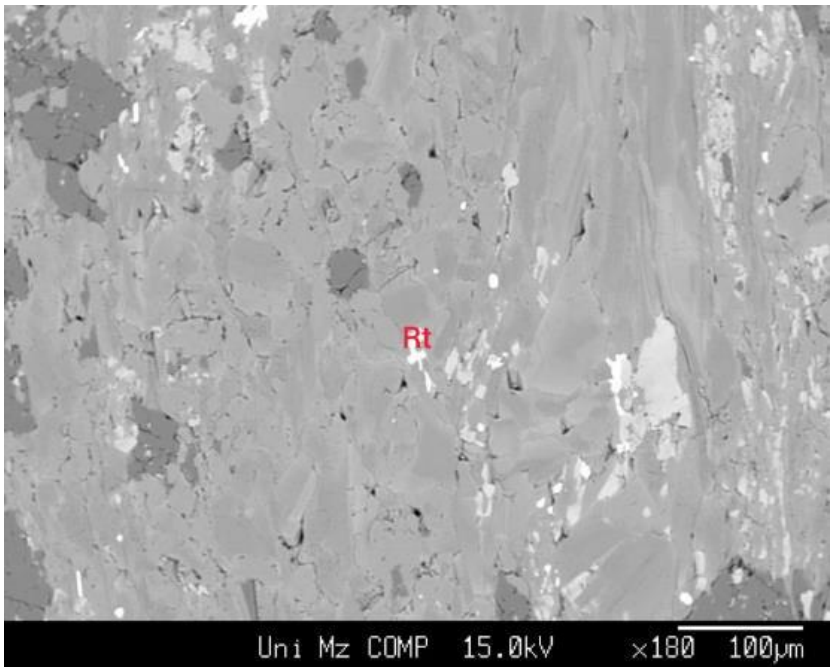

Figure 175: Sample 456 a23

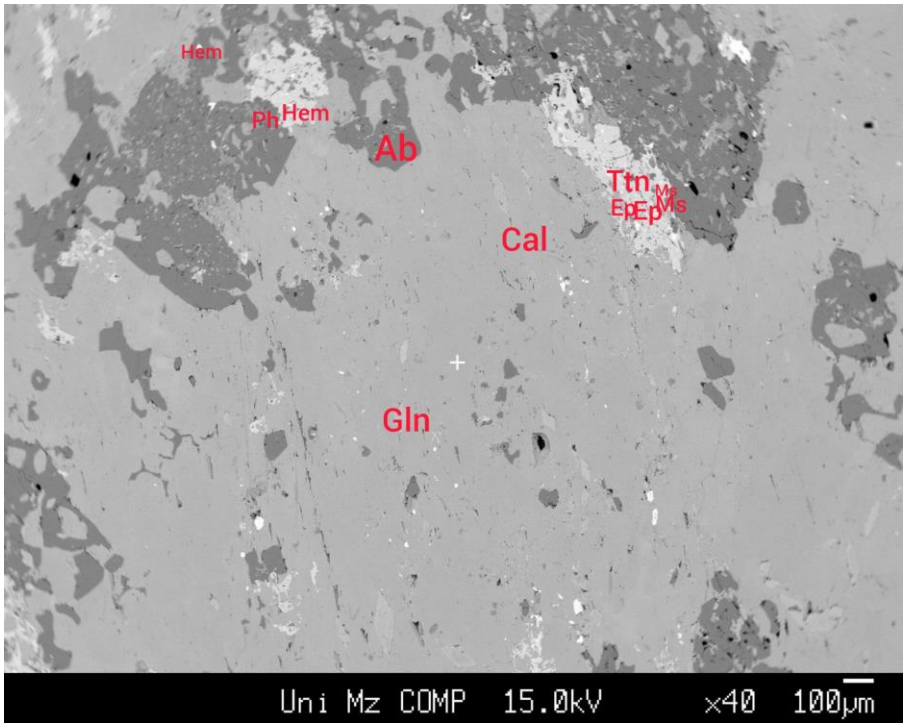

Figure 176: Sample 457 a24-a35

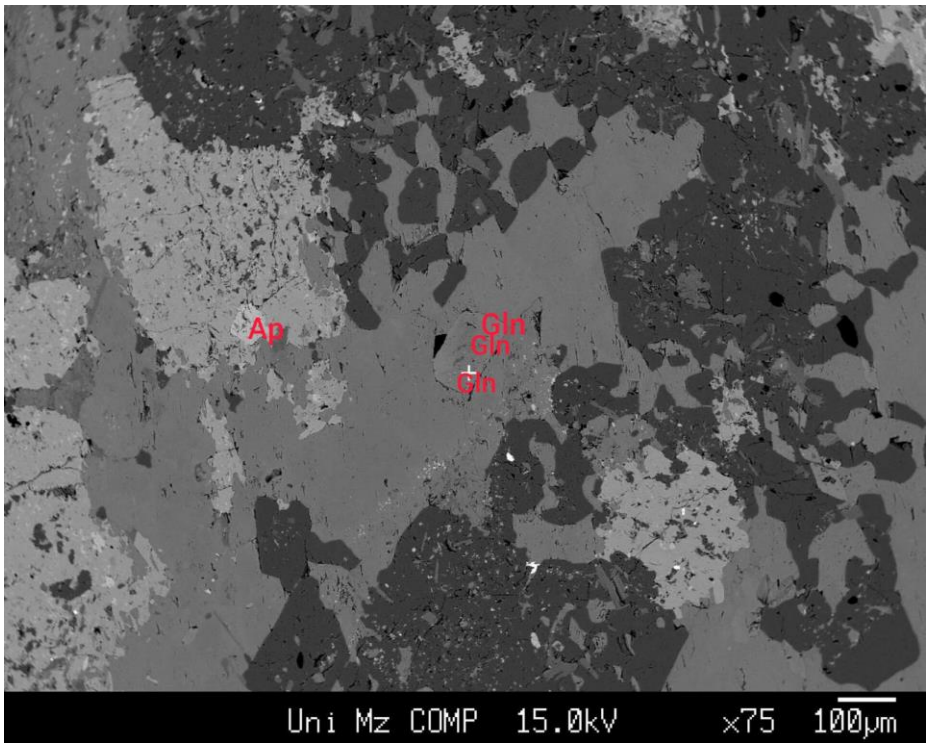

Figure 177: Sample 457 a36-a38

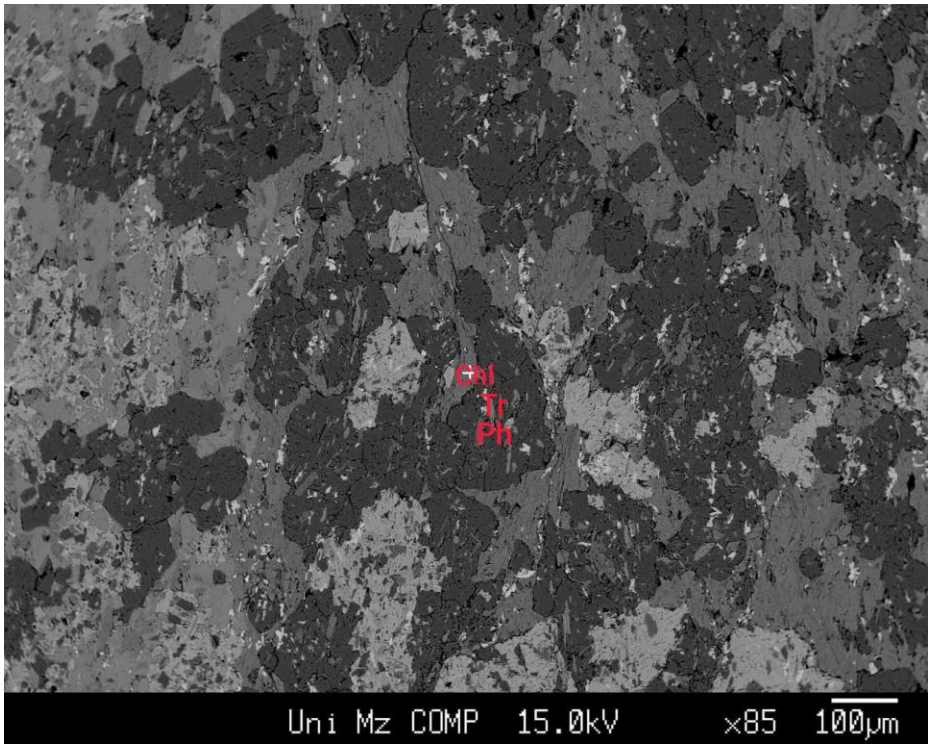

Figure 178: Sample 458 a39-a41

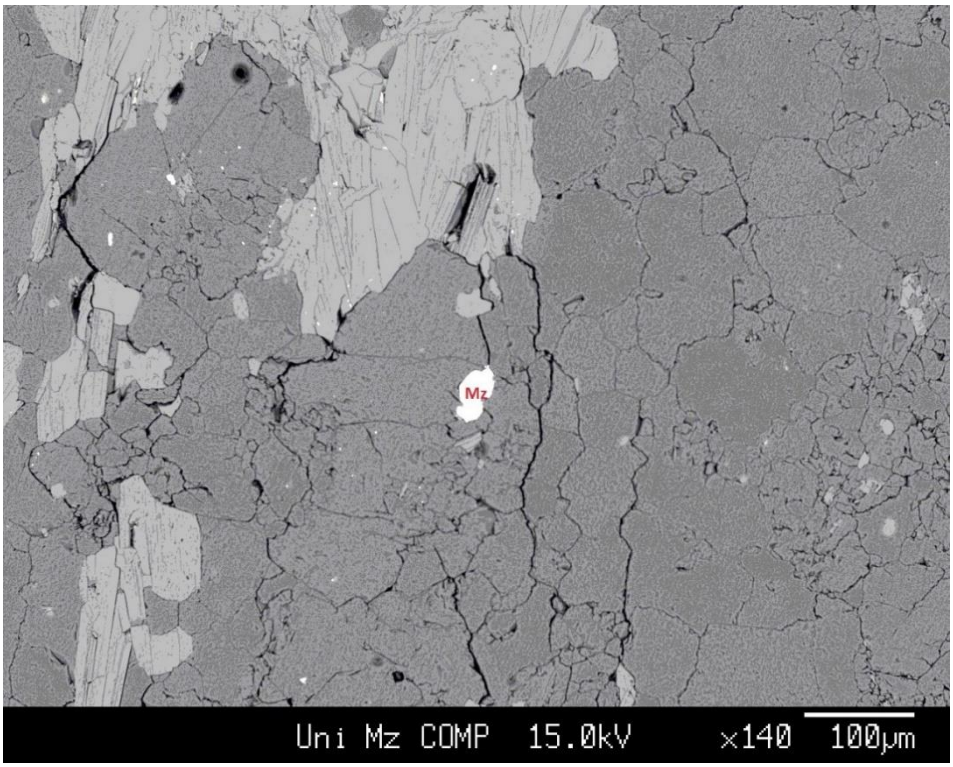

Figure 179: Sample 458

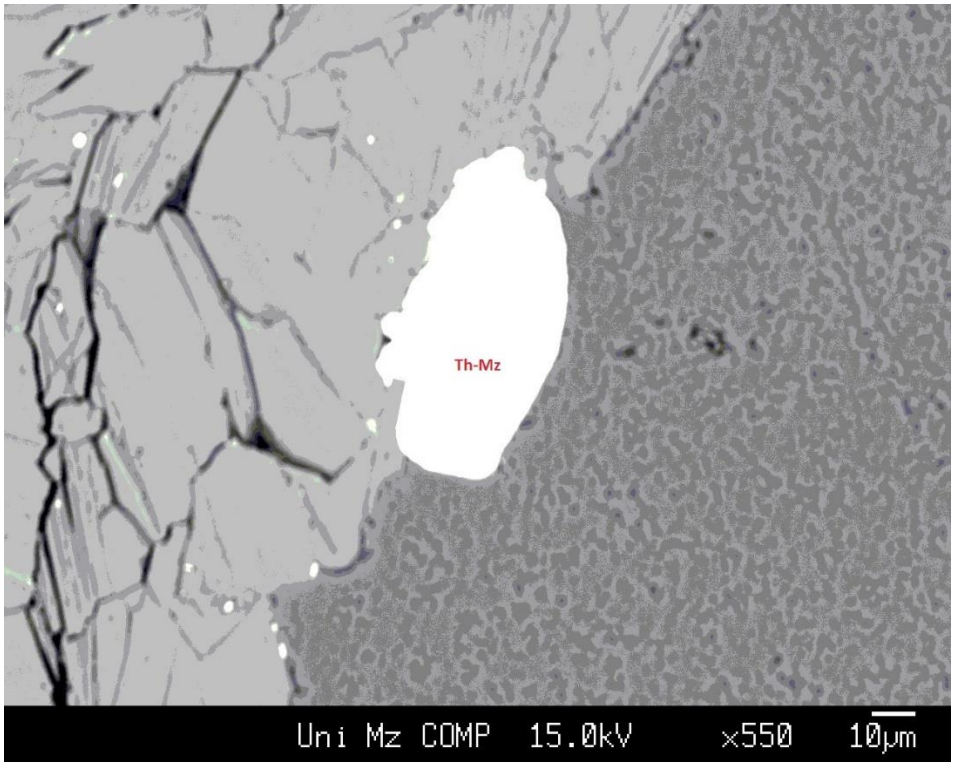

Figure 180: Sample 458

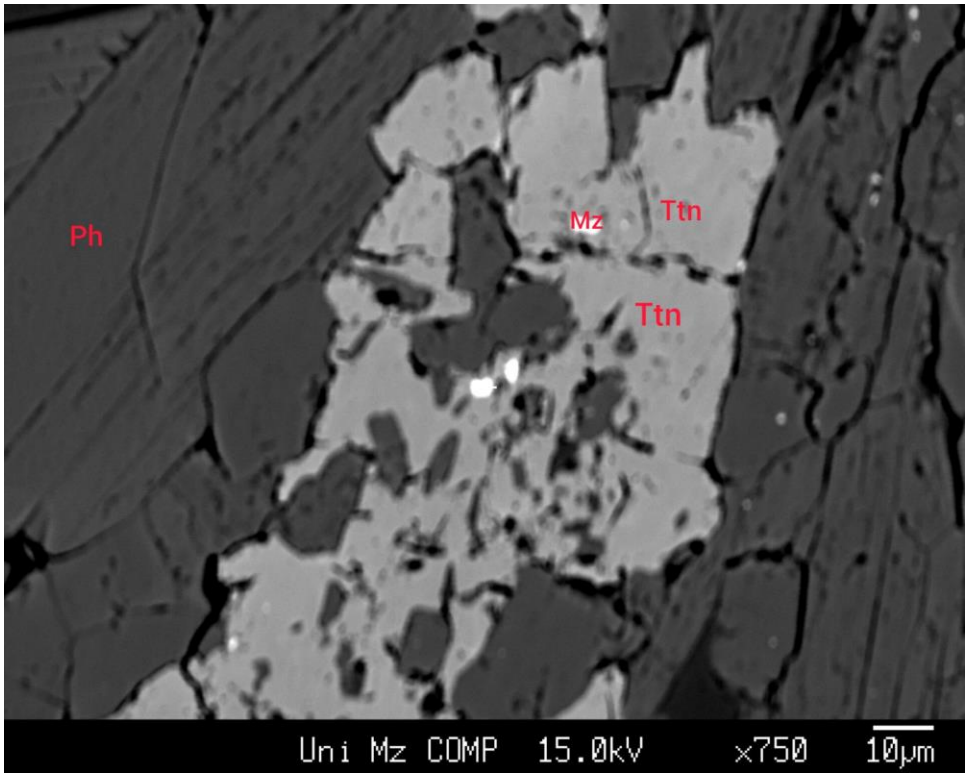

Figure 181: Sample 461 b1-b2

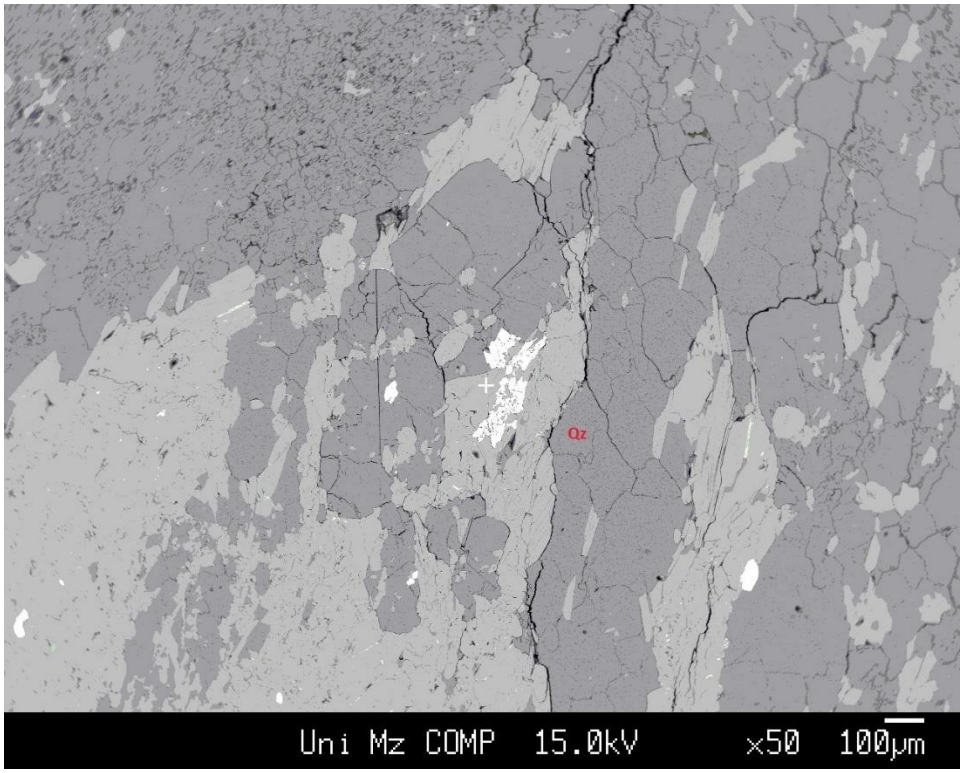

Figure 182: Sample 461

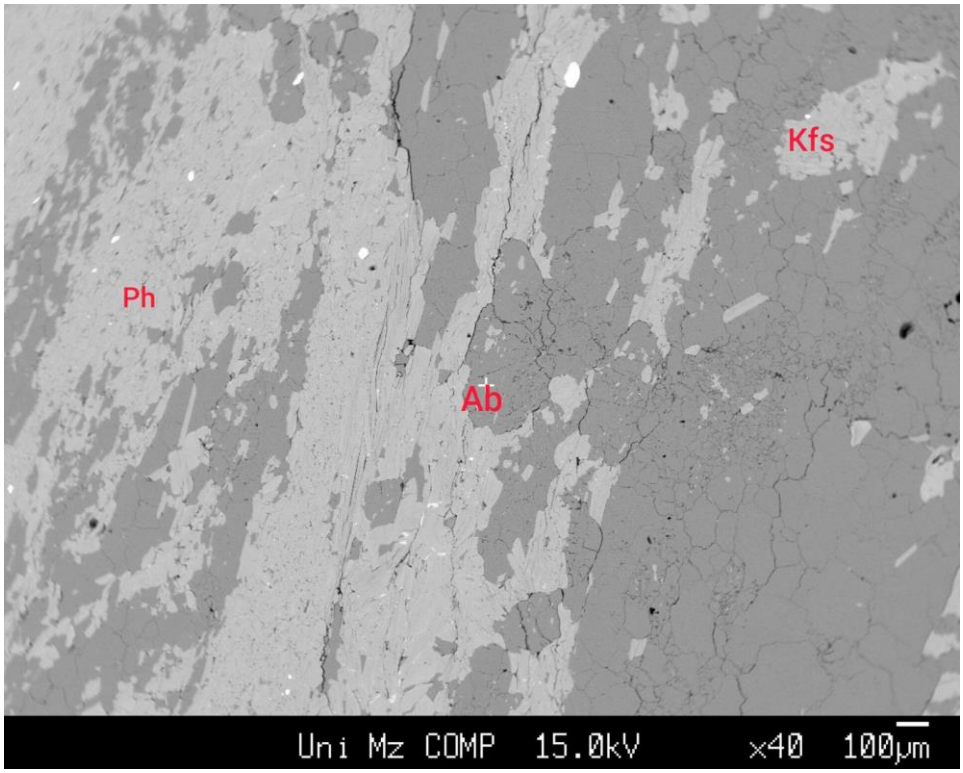

Figure 183: Sample 461 b3-b5

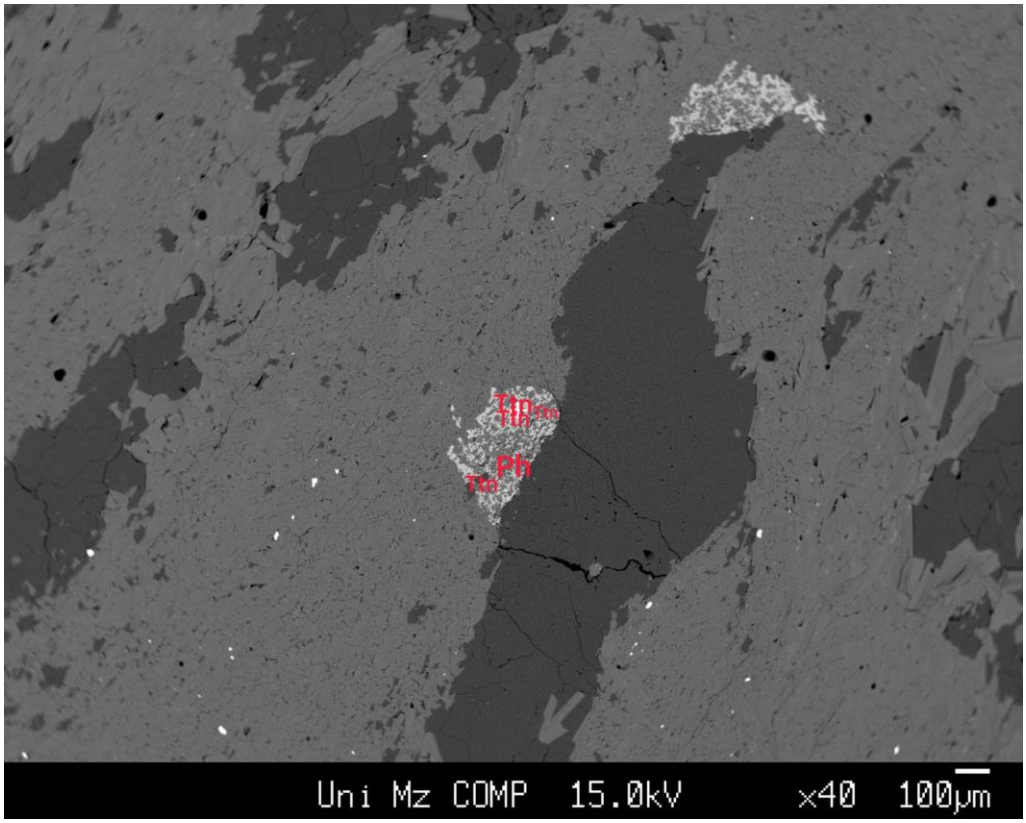

Figure 184: Sample 461 b6-b10

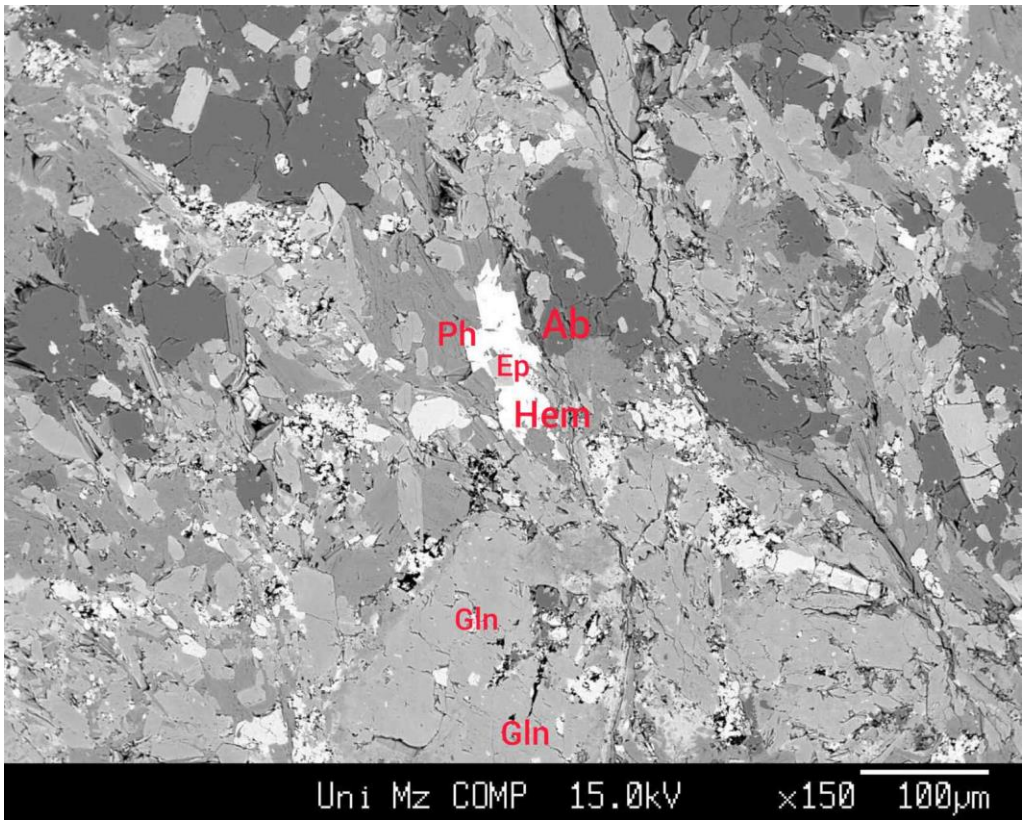

Figure 185: Sample 460 b12-b17

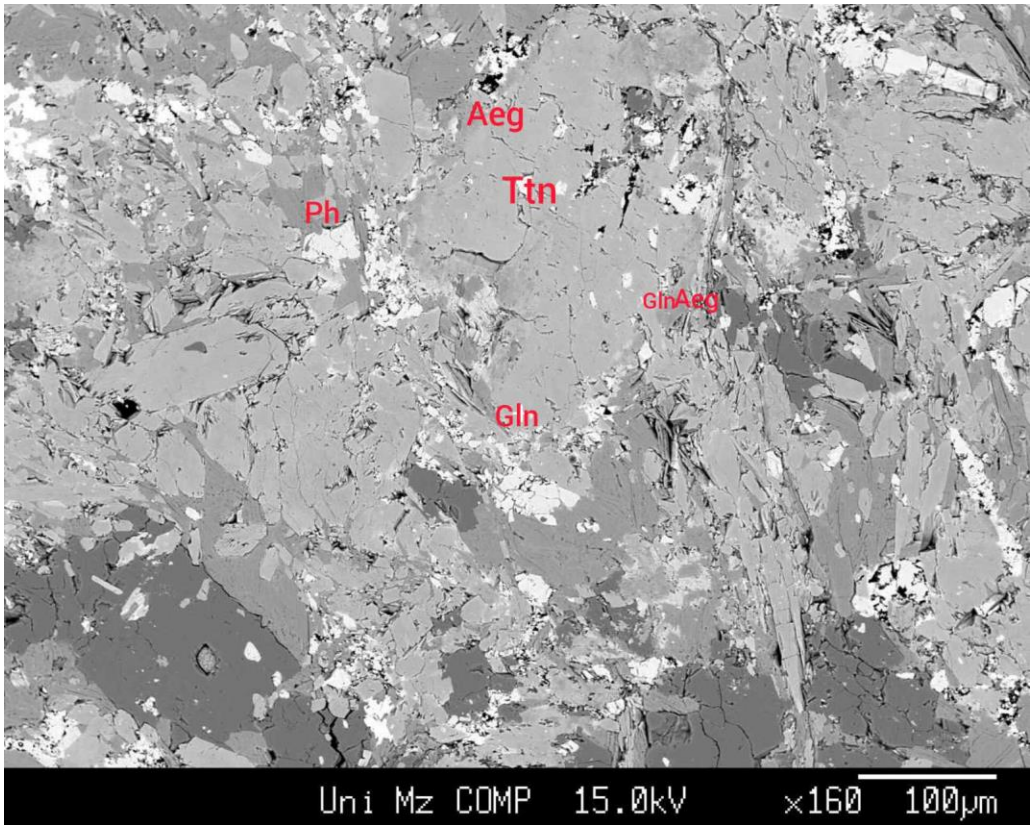

Figure 186: Sample 460 b18-b23

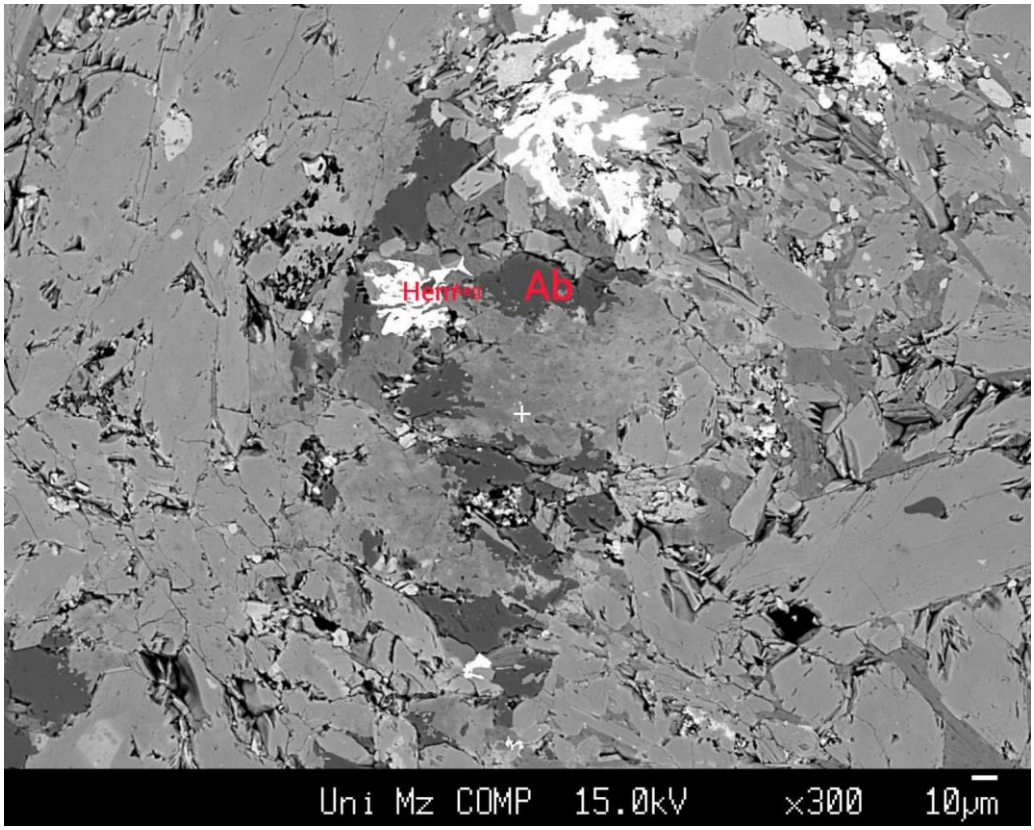

Figure 187: Sample 460 b24-b26

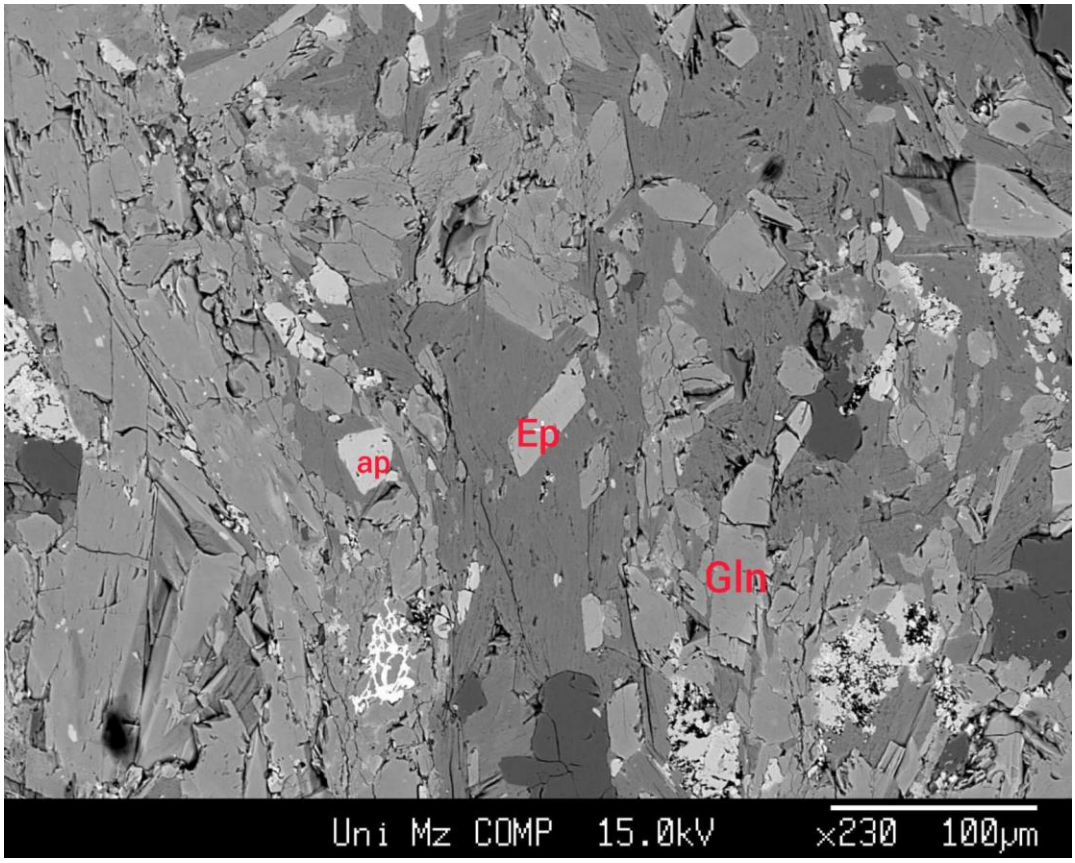

Figure 188: Sample 460 b27-b28

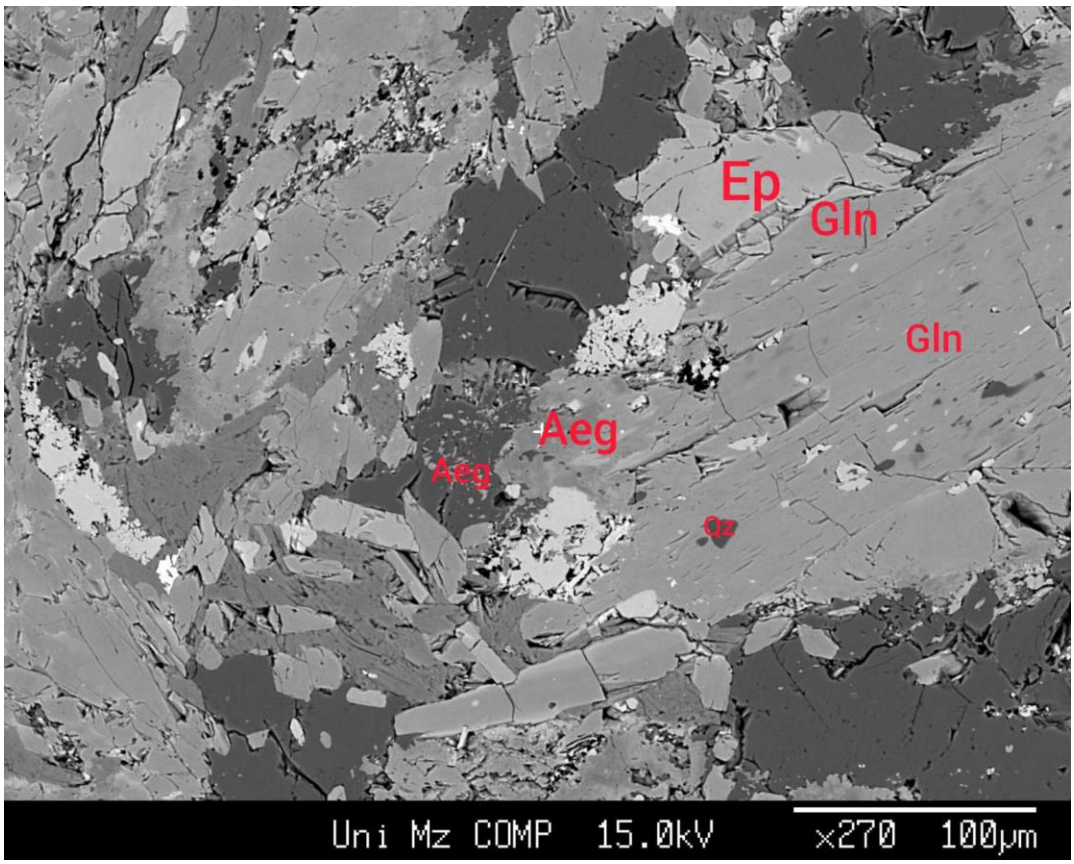

Figure 189: Sample 460 b29-b33

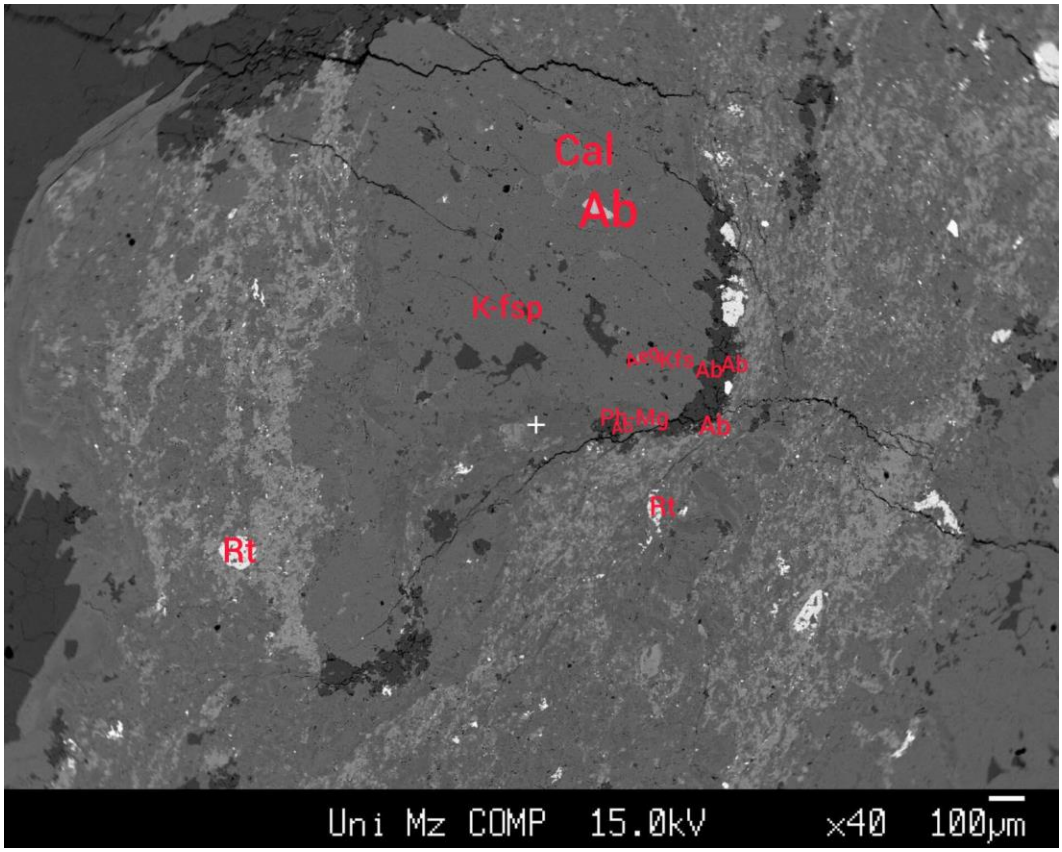

Figure 190: Sample 464 b34-b38

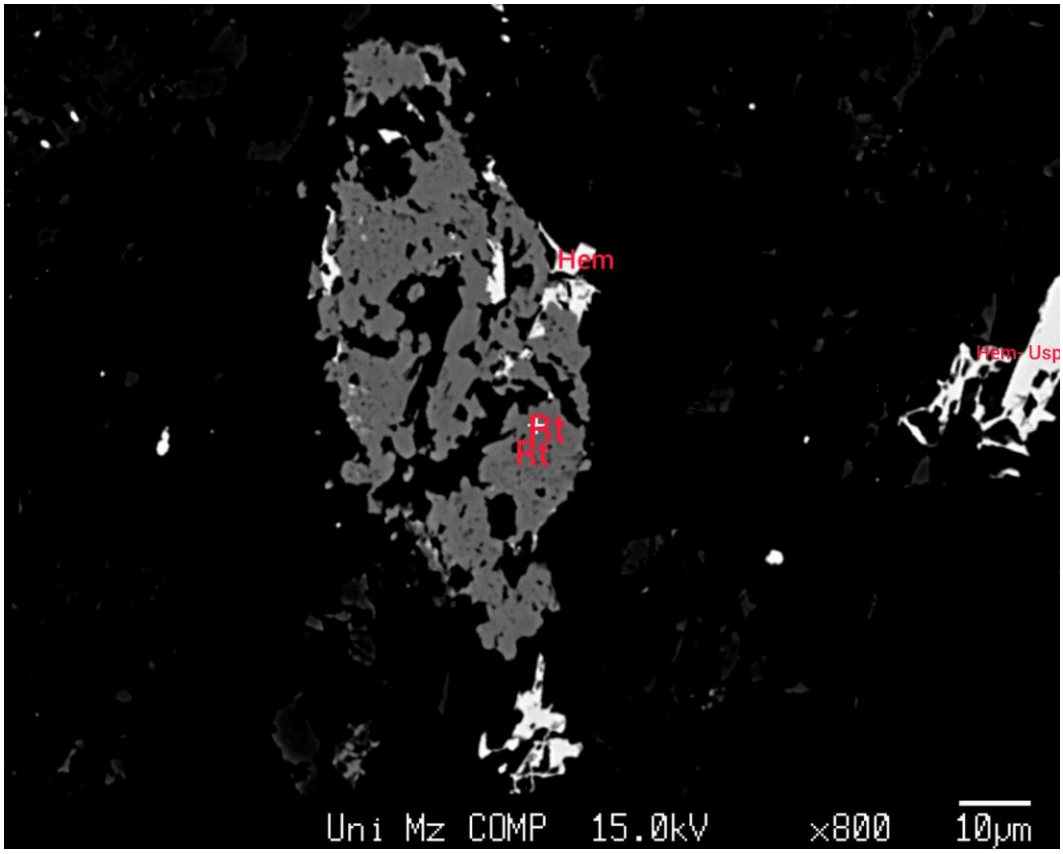

Figure 191: Sample 464 b38-b39

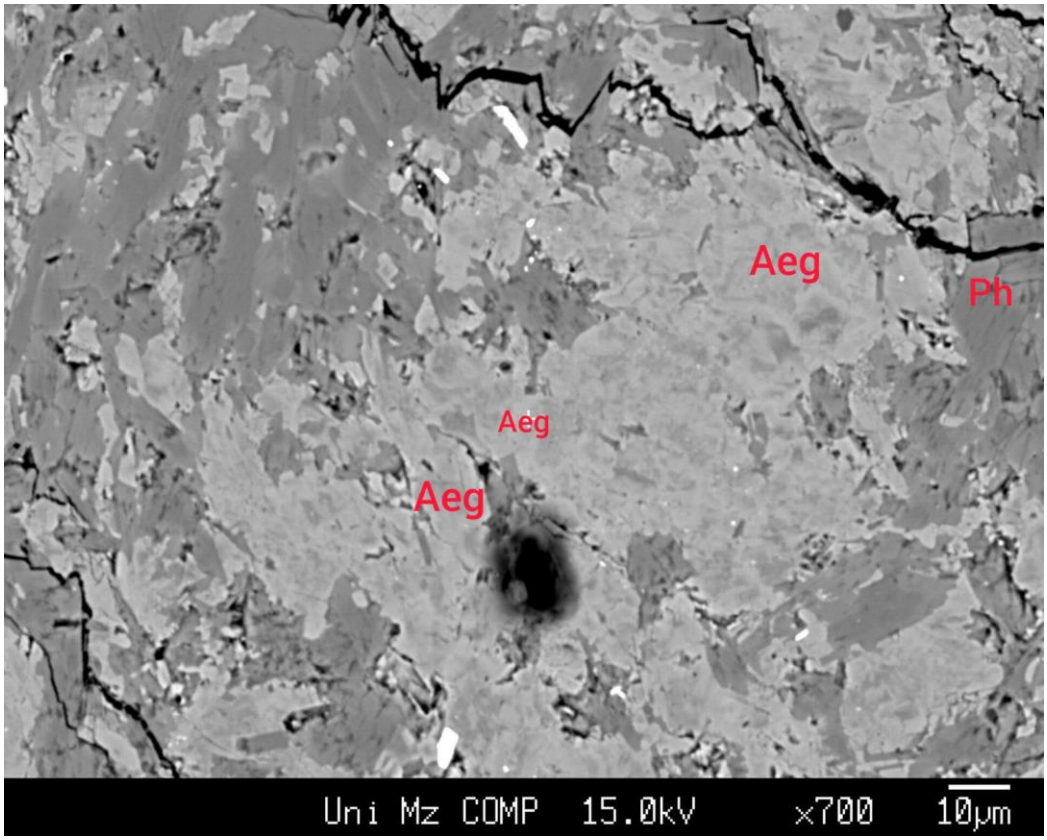

Figure 192: Sample 464 b40-b43

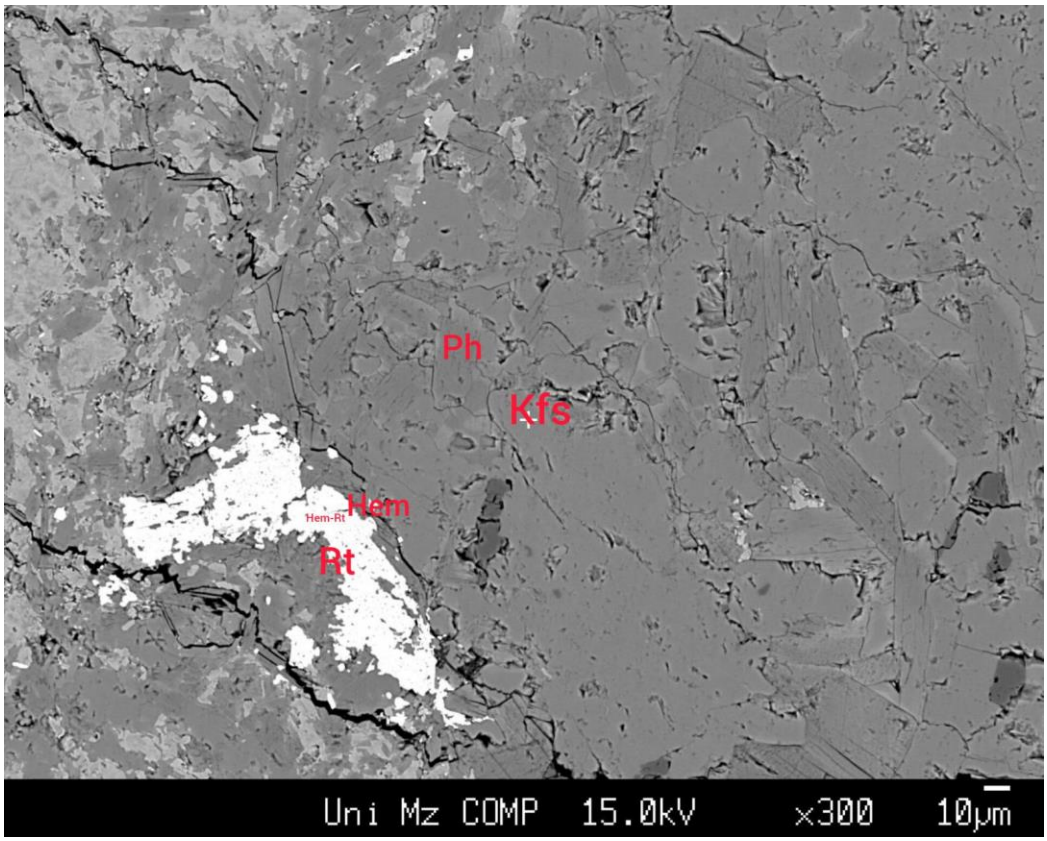

Figure 193: Sample 464 b44-b46

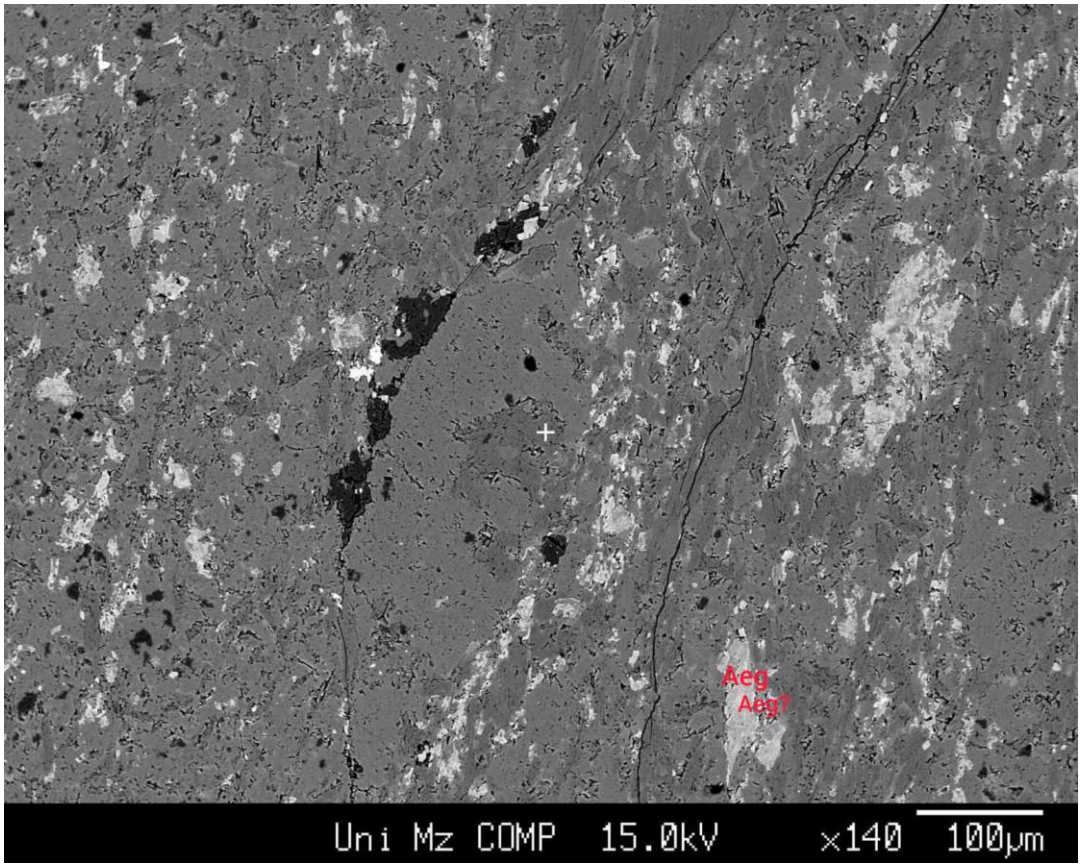

Figure 194: Sample 464 b47-b48

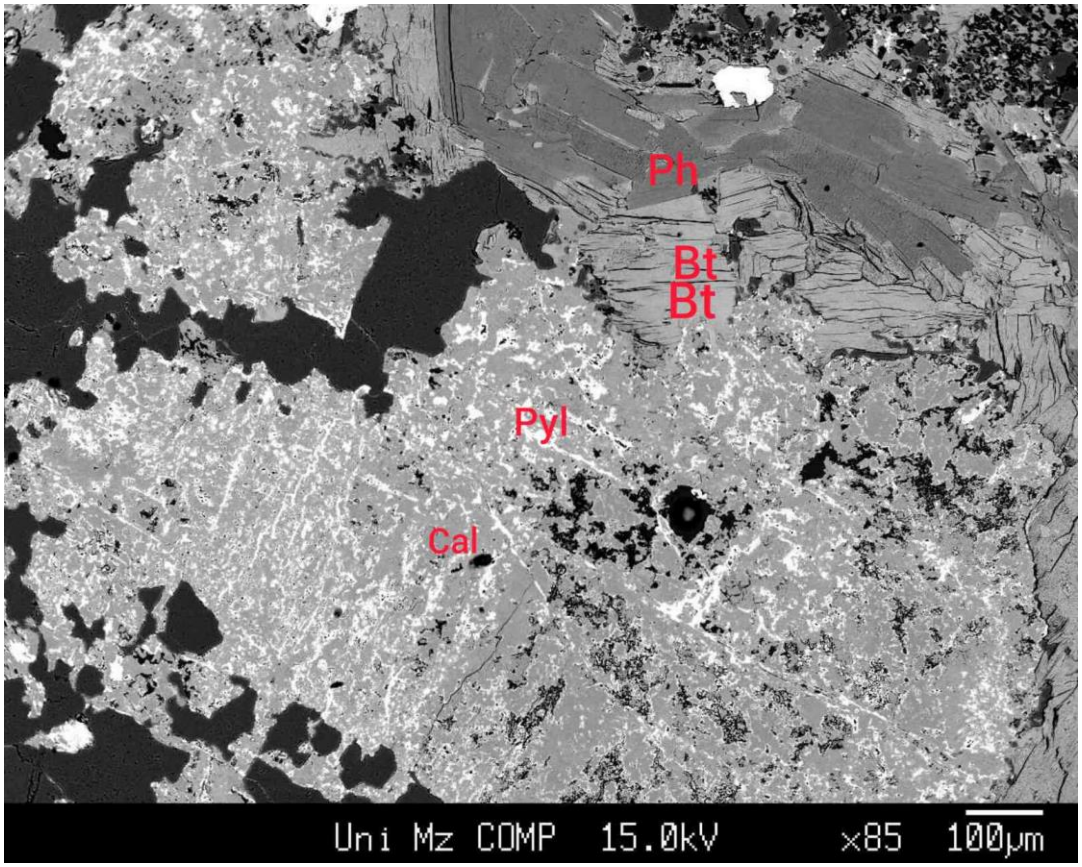

Figure 195: Sample 464 b49-b53

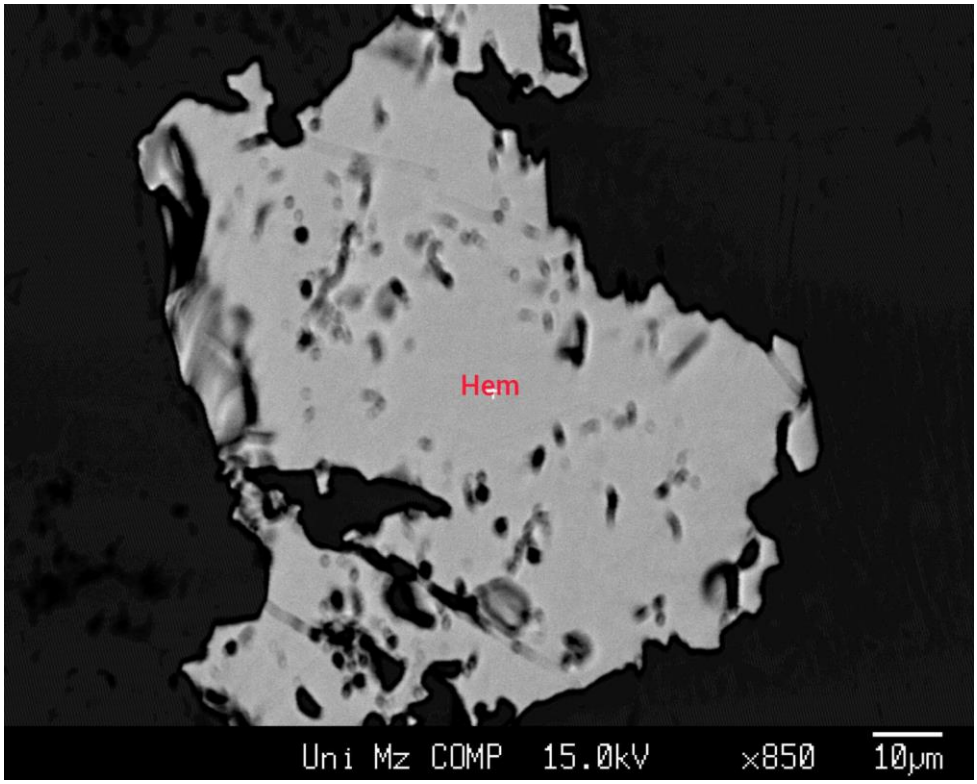

Figure 196: Sample 464 b50

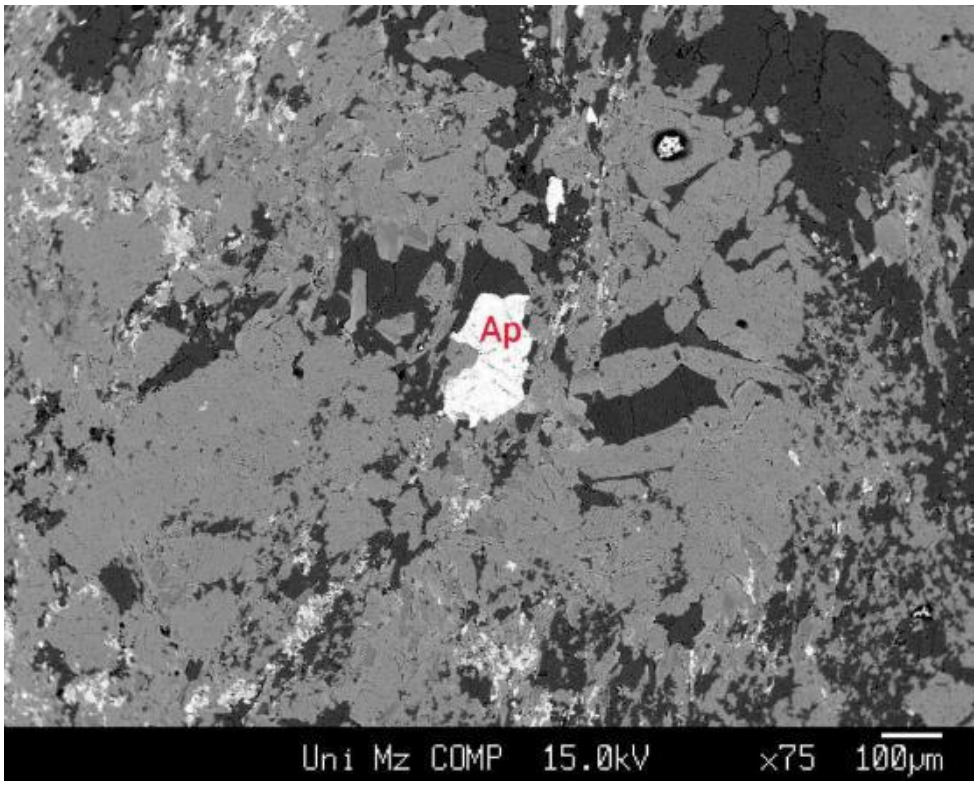

Figure 197: Sample 464

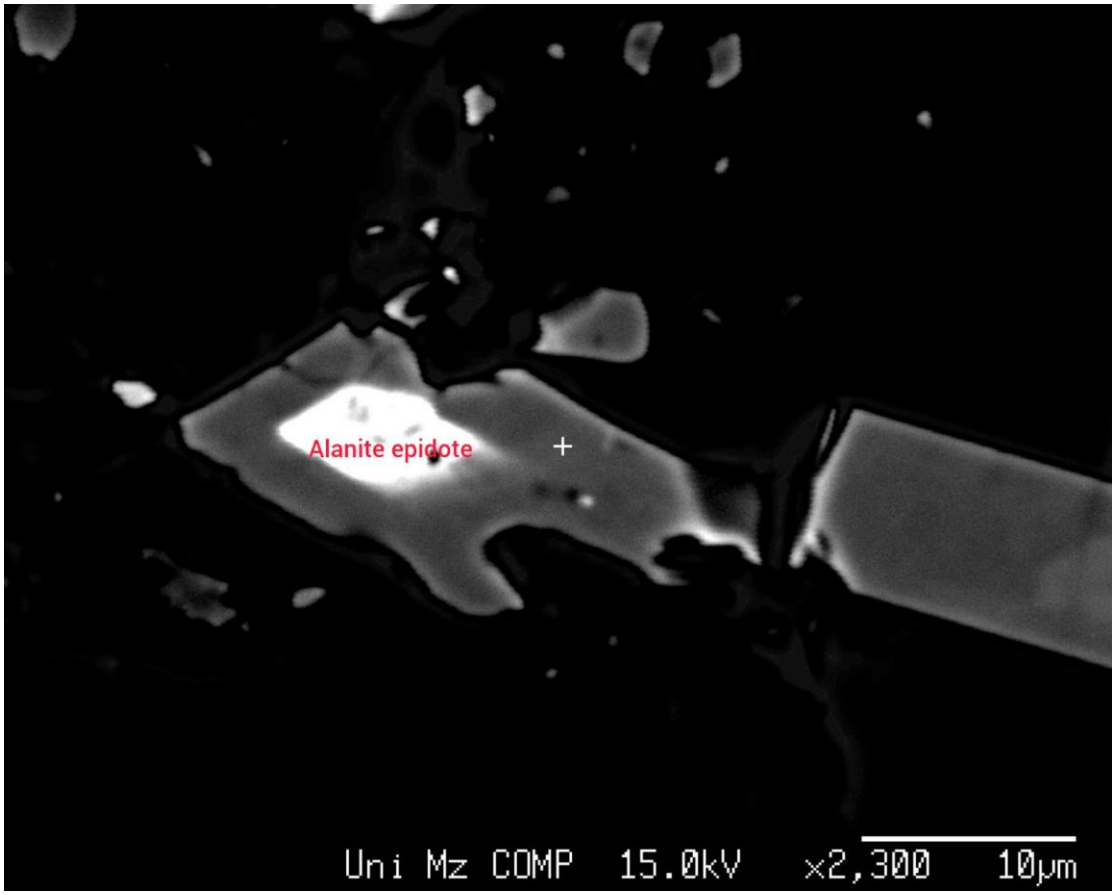

Figure 198: Sample 464

Unit 4.4 Sodic clinopyroxenes and amphiboles.

Samples analysed at the microprobe in Mainz yielded sodium-rich clinopyroxene and amphibole samples characterising the blueschist phase of metamorphism in the subduction zone. The glaucophane with chemical formula $Na_2(Mg_3Al_2)\ Si_8O_{22}(OH)_2$ as its name implies has a cyan-blue color whose shades change depending on the pressure condition, as shown in the microscope. Our region is characterized by strong oxidizing conditions and this is evidenced by the presence of ferroglaucophane ($Na_2(Fe,\ Mg)_3Al_2Si_8O_{22}(OH)_2$) which projects near the top of the iron trivalent.

The presence of a strongly sodium-rich clinopyroxene residing in the aegirine family (Fig.198) is also pronounced. The jadeite as shown in the diagram from the microprobe analysis database is also sodic and not calcium.

The presence of both sodic amphibole and pyroxene increases the concentration of Na in the rock and in combination with the oxidizing conditions of the alkaline (aegirine) orthogneiss increases the chances for replacement of sodium in the lattice of these minerals with elements of large ionic radius and valence 3^+ which are the rare earth elements (REE).

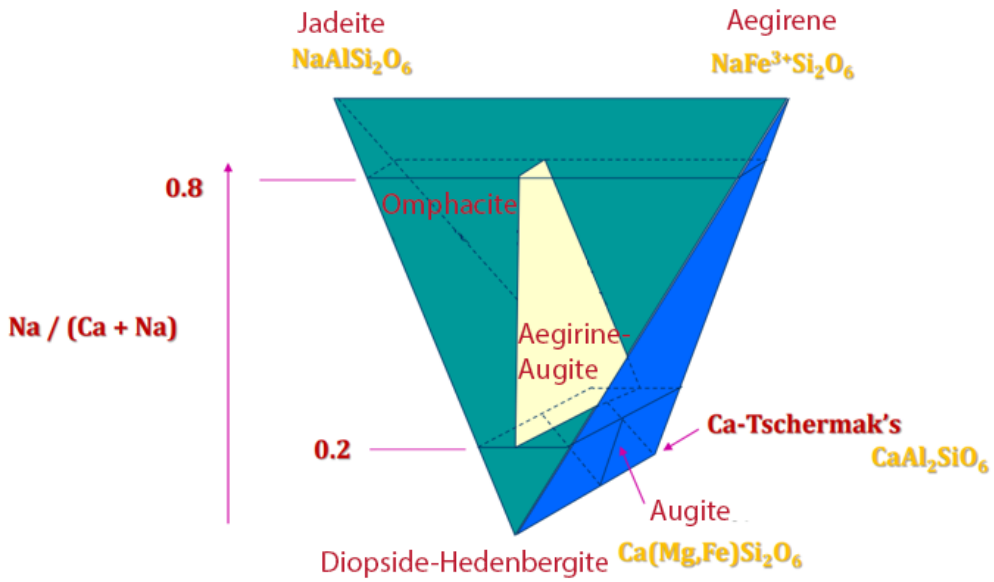

Figure 199: Clinopyroxenes diagram.

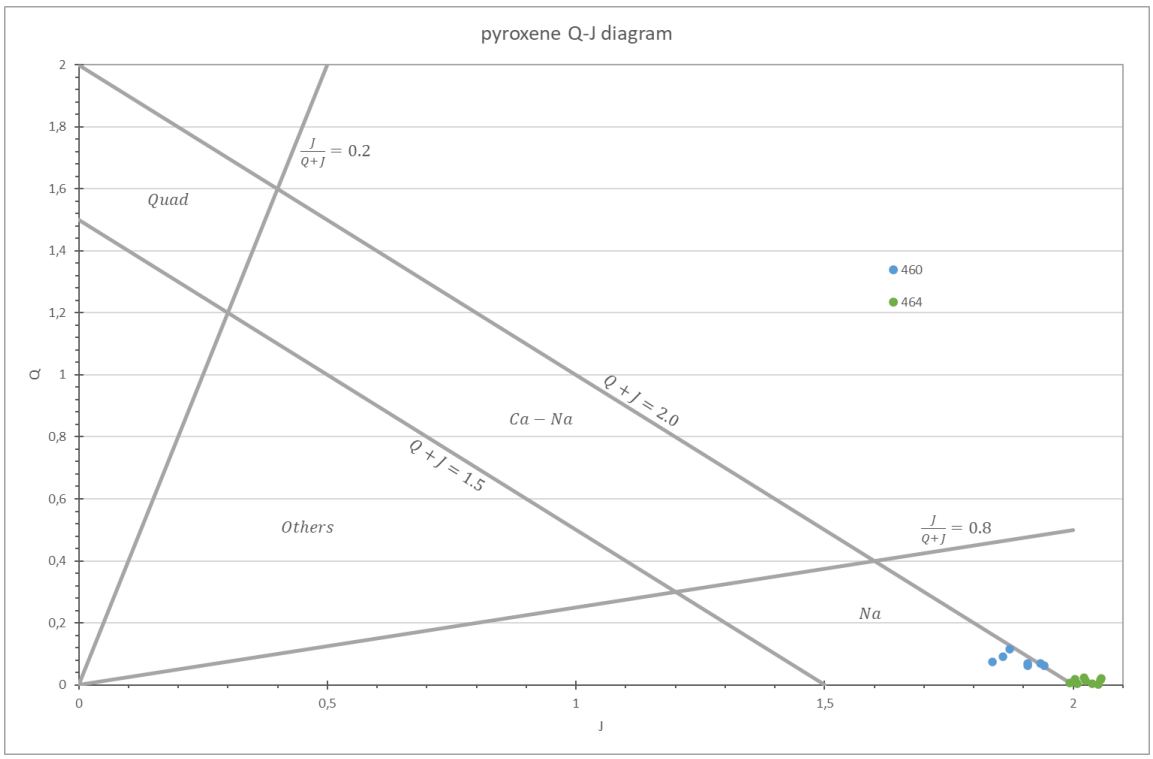

Figure 200: Quartz (axes y) - Jadeite (axes x) projection diagram.

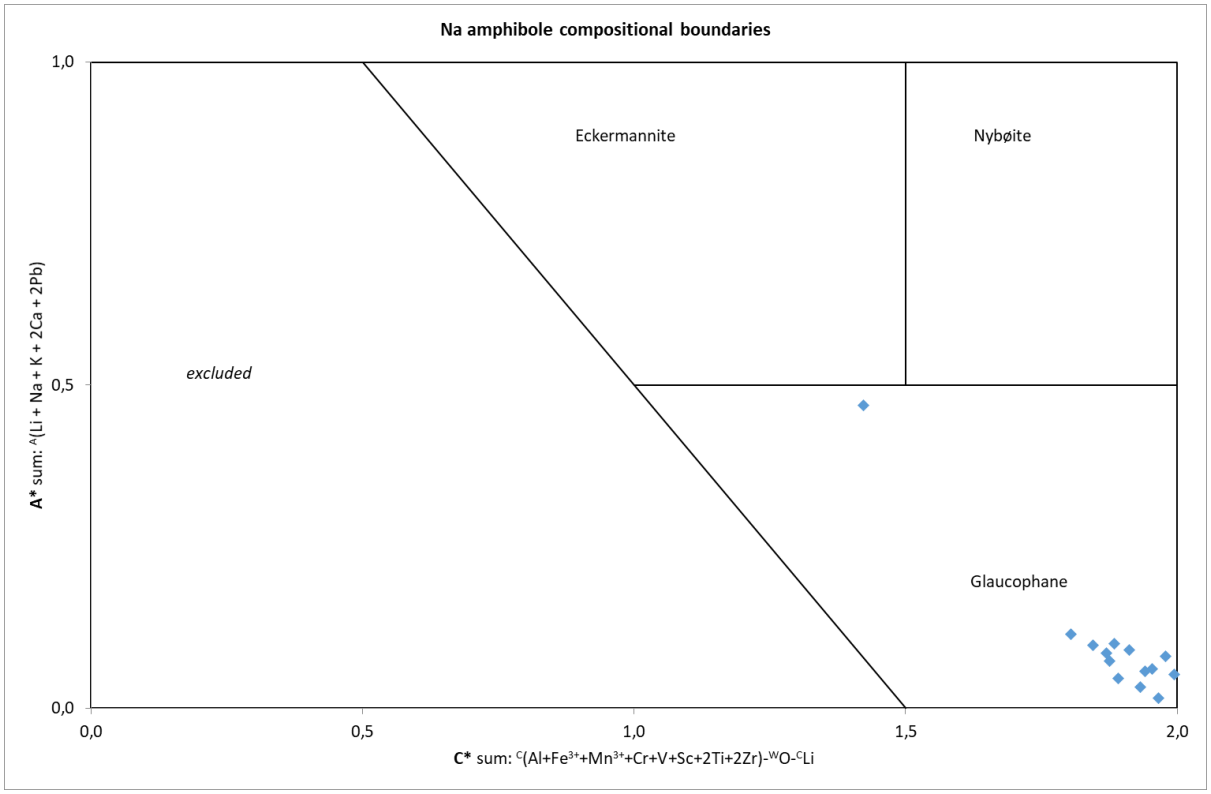

Figure 201: Sodic Amphiboles projection chart.

Database of chemical analysis in (unit 5.3)

Unit 4.5 XRD analysis of ΕΚΠΑ

The next method of analysis to check the presence of minerals per sample, to perform a qualitative analysis, is X Ray Diffraction (XRD). Steps of sample tapering for XRD are explained below:

Preparation of representative fine-grained material (powder) by coning samples of rock slices into powder for use in the X-ray diffraction (XRD) instrument. Use of a press to break sample into approximately gravel-sized grains. Then collecting this and the resulting fine-grained material for coning in an agate mortar. Collection of material in sample bags for XRD. Finally, rinsing utensils after each sample fusion.

Preparation and evaluation of samples in XRD:

Using a spatula, spread the powder as evenly as possible on the surface of a special sample holder (tablet) so that it is homogeneous. Then place it on the magnetic base and finally into the XRD instrument. The X-ray beam (laser) come from the x-ray tube and heat the tablet. Using software, we analyze the pics of the diagrams of each sample obtained from the different radiation intensities at the different 2θ angles received by the analyzer, which result from the diffraction of x-rays due to the different distances of the crystal fields of the different minerals contained in each sample. For this reason, then comes the evaluation, matching the mineral pics we know from various databases with the pics of our in-situ analysis.

Chapter 5 Identification and interpretation of the geotectonic environment

Unit 5.1 Diagrams of geotectonic environments

The following plots and charts were obtained after normalization to ORG (ocean ridge granite) for each (Evia) literature sample to be understood the tectonic setting.

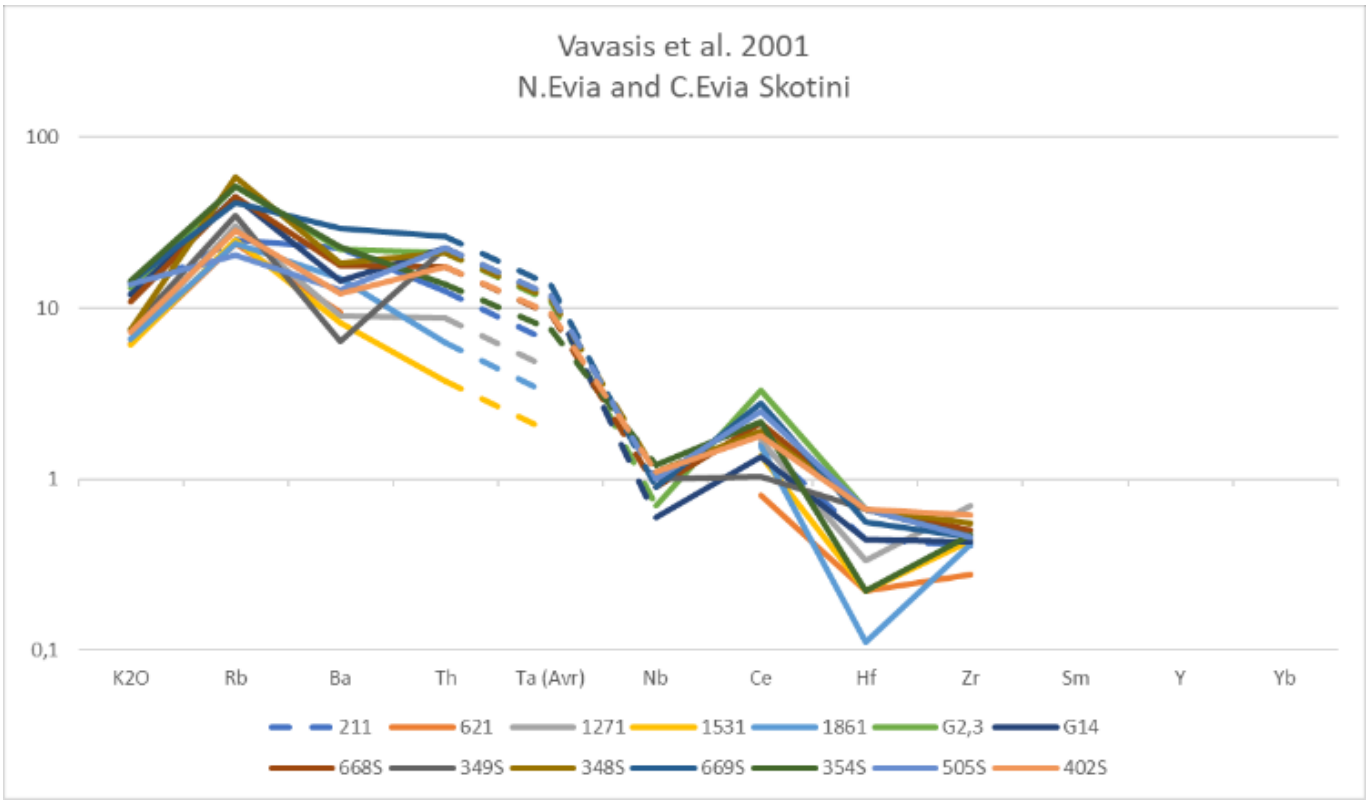

Figure 202: Typical pattern of WPG (within plates granites) in Central and North Evia.

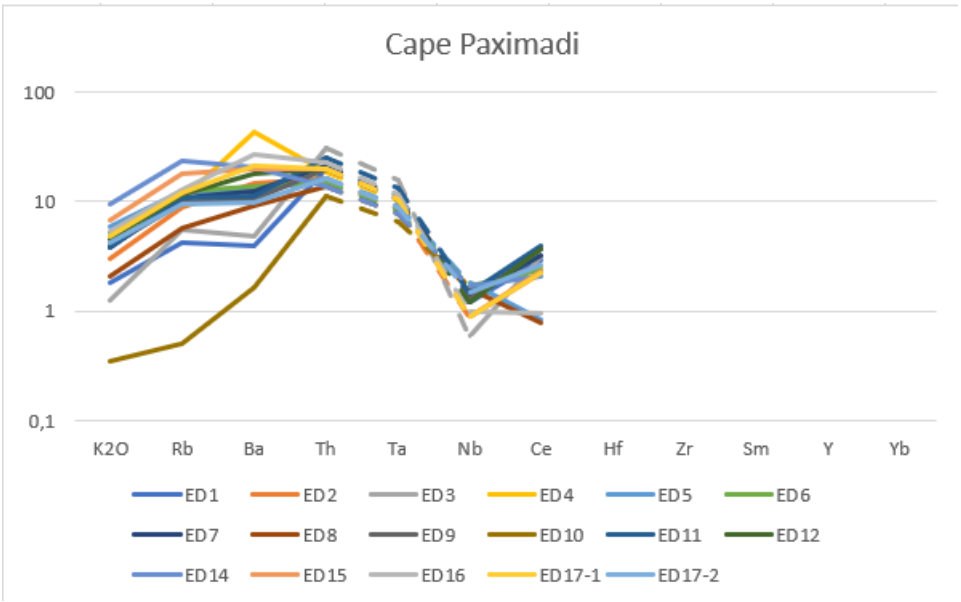

Figure 203: Typical pattern of WPG in South Evia (Cape Paximadi near to Karistos).

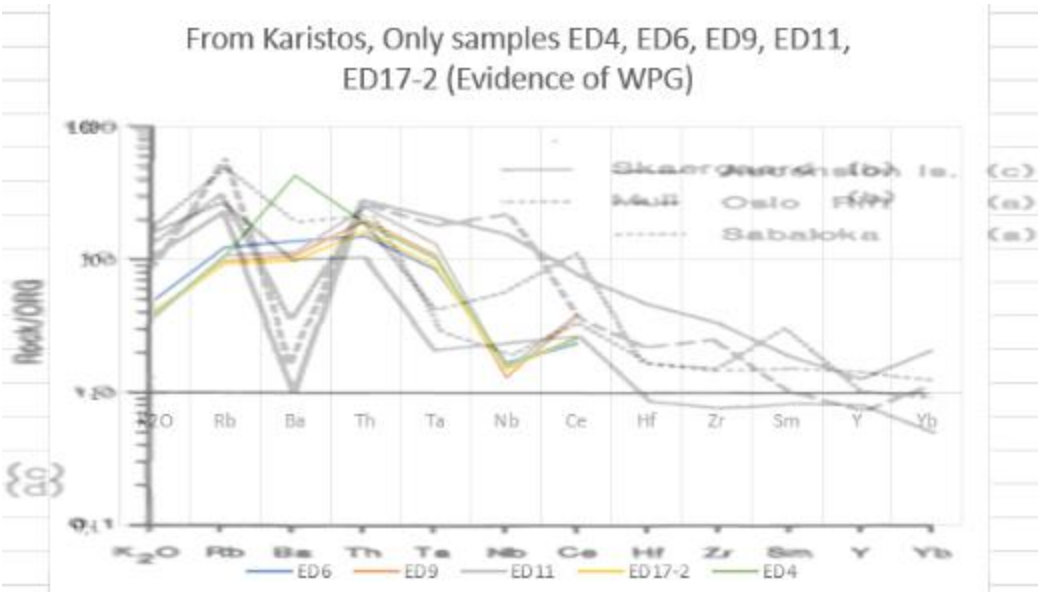

Figure 204: Comparative WPG (Within plate granites) from literature diagram (Ascension Is., Oslo rift, Sabaloka) with samples diagram from South Evia (Cape Paximadi-Karistos).

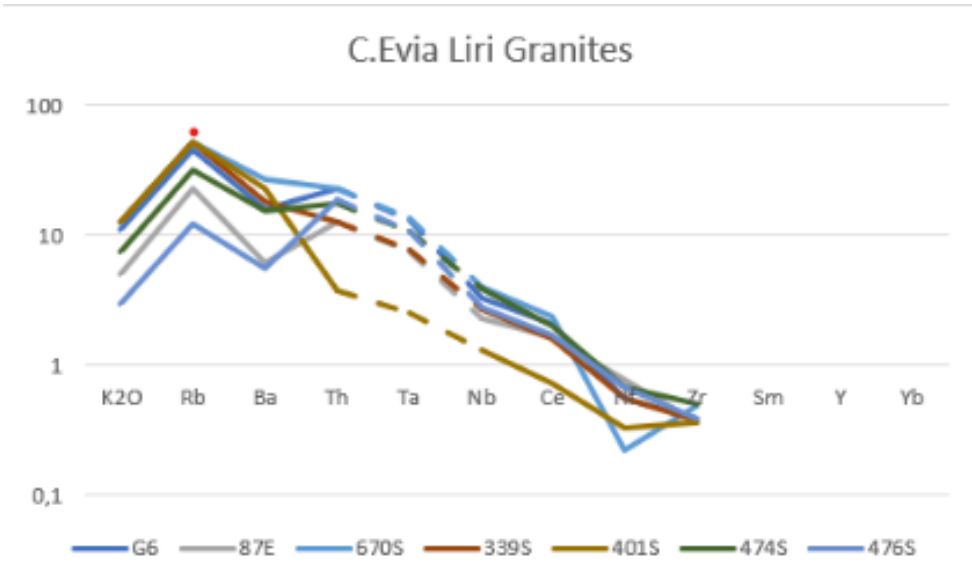

Figure 205: Intermidiate pattern between WPG and Post-COLG (post-collision granites) in Central Evia.

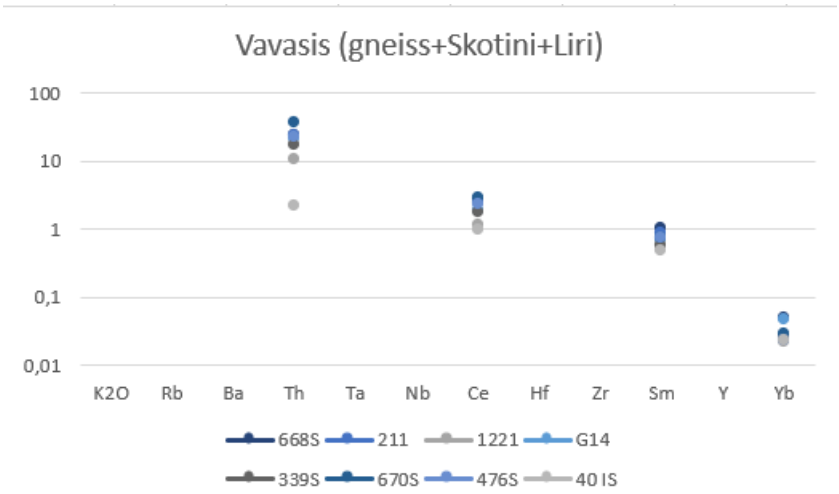

Figure 206: Intermediate pattern between WPG and Post-COLG (post-collision granites) in Central Evia.

By applying and synthesizing analysis matrices of only Rb, Nb, Y elements, we arrive at some diagrams which, if inserted in a common diagram with geotectonic fields, we can draw conclusions about the geotectonic environment of our various areas in Evia. The following diagram was constructed from Pearce's literature.

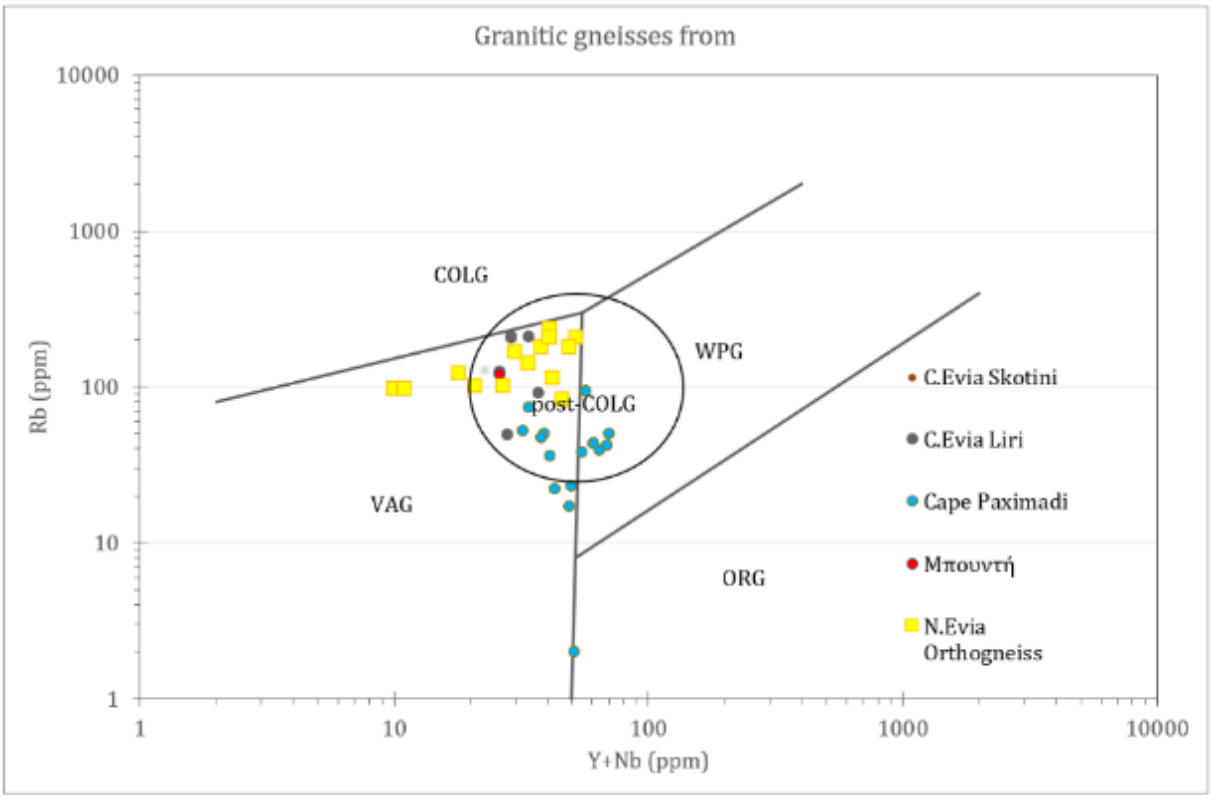

Figure 207: Tectonic type setting diagram.

In Pearce's diagram above most of the granitic samples are projected in the post-collision granite area and this fact leads us to the following thoughts and interpretation of the geotectonic environment of our area.

Post-collisions settings can be of considerable scope. At the beginning a large cause of magmatism is believed to be the detachment of the thickened lithosphere, where lithospheric mantle is removed from below by convection. (Either progressively or catastrophically), while the thickness of the crust is unaffected. This allows the hot asthenosphere to come into contact with the post-embedded mantle lithosphere, which then undergoes a small amount of melting. The result is the production of incompatible elements in magma. Because of the thickened crust, the interaction of the derived mantle with the crust is extensive and all post-collision explosive rocks show evidence of significant crustal assimilation. There are two type of melting lithosphere character, an intraplate or subduction zone, depending on the pre-collision history of the lithosphere. The post-collision granites probably form some of the largest granite fibro genic zones in terms of volume. There are many specimens that are at the surface and can be identified in many past orogenic zones (e.g., Caledonides, Heracynides) mainly by their ages and deformational episodes. granites are often (sensu stricto) and they can range between type A and type I. The origin from a mantle above an earlier subduction zone gives type I character and below passive margin gives type A character. Due to the large thickness of the crust, extensive magma-crust interaction further modifies the composition because a heat is generated by the large volumes of mafic magma formed by crustal attenuation; the fluids are groundwater put into circulation by magmatic heat. And so, we have post-collision extension. This is the evidence for example that the sequence of

peraluminous biotite granites, grading upwards into leucogranites and migmatites, was created by liquid melting of sedimentary rocks.

So, in the best examples of post-collisional magmatism today can be considered (continent-rear-arc collision) and (continent-fore arc collision) in Papua New Guinea and Bolivia respectively. However, 5 samples from Karistos are projected into the field of within-plate granites. In (Fig.207) it is checked whether the diagram having the curve resulting from analyses of these samples meets the conditions of a WPG that is valid. About within plates granites there are two principal causes for intraplate magma generation. First cause is mantle plume activity and the second one is passive rifting. Passive rifting (Fig.208) is typically linked to ocean opening or to the formation of extensional, intracontinental basins that never developed into oceans. Which means that magmatism can mainly be attributed to decompression of depleted asthenosphere. Passive rifting may also be related to subduction in an sialic back-arc setting. Within-plate granites (WPG) typically comprise small-volume intrusions in continental rift and ocean island settings, where they are typically alkali granites with peralkaline compositions containing sodic pyroxenes and amphiboles. Geochemically, they show a strong enrichment in both LIL and HFS elements, characteristic of the derivation of an enriched mantle source, although crustal assimilation can selectively increase the LIL element content. Volatile-related processes, either supra-or sub solidus may also redistribute many elements. Many of the granites from such settings show evidence of significant magma-crust interaction and bimodal, basic-acid magmatic products (Julian Pearce et. al. 1996).

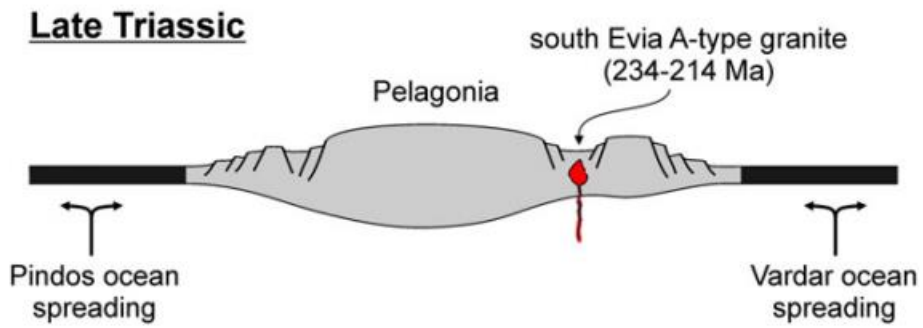

Figure 208: Age of 5 (WPG) samples from (Cape Paximadi-Karistos) and a picture of tectonic setting for the Late Triassic metagranitoid rocks from the Attic-Cycladic zone on south Evia Island.

Unit 5.2 Tables with notes and observations, microprobe and XRD analysis charts

Sample number	Latitude	Longitude	Rock type	Day	Description	Comments	Tectonic-Structural measurements
439	38°34'29.07"B	24°10'11.91"A	Micalgheng(te) Marbles	29/9/2023	recrystallization phengite, sugary texture, green colour	Thick banks, thickly layers, highly foliated marbles, plastic behavour-deformation (phengite 300-400°C) and synfolial parallel Quarz veins(probably relative) and S-mylonite, boudinaged courts	Foliation 010/45 Lineation 056/20 , sense of shear top to the NE
440	38°30'7.05"B	24° 0'58.92"A	Basalts and overlying limestones	29/9/2023	Compact ultramafic-mafic rock	East of the road there are Serpentines	
442	38°30'25.53"B	24° 0'30.97"A	Basalt flows	29/9/2023	Basalt rock		
443	38°30'54.25"B	24° 0'38.48"A	Basalt (flows)	29/9/2023	Altered basalt rock	The sample was taken from the corner	
444	38°24'44.05"B	24° 2'2.50"A	?	29/9/2023		We do not know for sure what it is...	
445	38°31'1.34"B	24°10'54.20"A	_	29/9/2023	Metalliferous zone begins, fine grained clays minerals	Something like argilic alteration	
445A, 446	38°30'56.47"B	24°11'1.50"A	Metalliferous basalt	29/9/2023			
No sample 447	38°30'50.72"B	24°11'11.32"A	_	29/9/2023	Hydrothermally altered rocks in this area		
448	38°30'51.06"B	24°11'10.71"A	_	29/9/2023	Hydrothermal breccia	H.W. B.X.	
449	38°30'52.26"B	24°11'6.10"A	Basalt and (kaolinite probably)	29/9/2023	White color, fine grained	Metallic minerals replace basalt	
450	38°30'54.84"B	24°11'4.93"A	Metalliferous basalt	29/9/2023			
No sample 451	38°30'55.01"B	24°11'4.56"A	_	29/9/2023			
No sample 452	38°31'7.63"B	24°10'44.61"A	_	29/9/2023		Hydrothermal environment begins	
453	38°22'12.46"B	24°11'51.71"A	Micro granite - Orthogneiss	30/9/2023	Acid igneous rock, fine graded, Biotite granite and we can see Quarz, Potassium feldspars, white mica	L-mylonite, synfolial (thick) and post tectonic (cm) Quarz veins	Foliation: 050/43 Lineation: 080/65, Lineation: 058/65, sense of shear top to the SW
454	38°21'55.31"B	24°12'43.91"A	Micro granite - Orthogneiss	30/9/2023	Acid igneous rock, fine graded, MINERALS: Biotite, Quarz, Potassium feldspars, white mica, (Plagioclases)	L-mylonite, synfolial (thick) and post tectonic (cm) Quarz veins	
No sample 455	38°22'1.47"B	24°12'37.63"A	Micro granite - Orthogneiss	30/9/2023	Acid igneous rock, fine graded, MINERALS: Biotite, Quarz, Potassium feldspars, white mica, (Plagioclases)	L-mylonite, synfolial (thick) and post tectonic (cm) Quarz veins	Foliation: 060/33 Lineation: 042/38
456	38°22'40.42"B	24°11'24.55"A	Micro granite - Orthogneiss	30/9/2023	Acid igneous rock, fine graded, MINERALS: Biotite, Quarz, Potassium feldspars, white mica, (Plagioclases)	Horizontal foliation and lineation	Foliation: 061/10 Lineation: 061/03
457	38°23'33.73"B	24°10'3.23"A	Orthogneiss and basalt	30/9/2023	Gneiss and Fine-grained metamorphosed mafic rock (Epidote)	Mafic sills clearly folded, highly foliated or boudinaged, syntectonic during metamorphism in their host rocks (orthogneiss). 30m length of mafic "eye"	
458	38°23'33.65"B	24°10'3.61"A	Orthogneiss and basalt	30/9/2023	Gneiss and Fine-grained metamorphosed mafic rock	Basaltic sills highly foliated and syntectonic	
459	38°22'48.13"B	24°10'45.65"A	Orthogneiss and basalt	30/9/2023	Chlorination basaltic sill	Mafic sills clearly folded, highly foliated or boudinaged, syntectonic during metamorphism in their host rocks (orthogneiss)	
460	38°22'43.38"B	24°10'53.05"A	Orthogneiss and basalt	30/9/2023	Gneiss and Fine-grained metamorphosed mafic rock	Mafic sills clearly folded, highly foliated or boudinage, syntectonic during metamorphism in their host rocks (orthogneiss)	
461	38°22'44.56"B	24°10'50.39"A	Orthogneiss	30/9/2023	Orthogneiss Augen-Eyes	Polished plate of "Augen gneiss" or "Eye gneiss" with lenticular clusters of quartz and feldspars (white) wrapped around by fine-grained matrix	
No sample 462	38°22'47.26"B	24°10'47.37"A	Orthogneiss	30/9/2023		Orthogneiss and synfolial (thick) Quarz veins	Sense of shear top to the SW from 1 delta but there are more deltas of sense of shear top to the NW
No sample 463	38°22'47.92"B	24°10'50.16"A	Orthogneiss and 2 mafic sills	30/9/2023	Gneiss and Fine-grained metamorphosed mafic rock	2 mafic sills parallel to gneiss foliation, syntectonic and deformed	Foliation 163/03
464	38°22'50.02"B	24°10'49.57"A	Orthogneiss	30/9/2023	Quarz and sulfides	Orthogneiss and metalliferous Quarz veins	

Figure 209: Excel sheet, background with notes and observations of samples and locations.

Figure 210: Table of mineral observations point by point in each sample in microprobe analysis.

Table matching minerals with samples found by XRD (XRD Pic charts in Appendix):

Minerals	Sample number														
	440	442	443	448	448-3-20	450	453	454	456	457	458	461	464 (I)	464(II)	460
Albite	√	√	√	√		√	√	√			√				√
Anorthite		√	√				√	√					√		
Apatite										√					
Biotite					√								√		
Calcite	√	√	√	√		√	√		√	√	√			√	
Chlorite										√					
Clinochlore	√	√	√			√				√	√				
Diopside		√					√								
Dolomite															√
Glauconite					√										
Glaucophane										√					
Hematite															√
Illite			√	√							√				
Kaolinite	√				√										
Lepidolite															
Lepidolite					√										
Lopezite								√							
Magnesioriebeckite															√
Microcline								√	√			√			
Montmorillonite	√														
Muscovite	√		√	√	√	√	√	√	√	√		√	√	√	√
Orthoclase								√	√					√	
Phlogopite					√										
Quartz		√		√		√	√	√	√		√	√	√	√	
Riebeckite										√	√				
Sanidine								√							
Taeniolite					√										
Weissbergite				√											
Zinnwaldite				√											
Zircon				√											

Figure 211: XRD mineral inventory table.

Unit 5.3 Database chemical analysis

From the literature all the chemical analyses of (Whole Rock analysis) of both granitic and basaltic composition from Central and Southern Evia were collected.

Sample	ED1	ED2	ED3	ED4	ED5	ED6	ED7	ED8	ED9	ED10	ED11	ED12	ED14	ED15	ED16	ED17-1	ED17-2
Majorelementswt,%																	
SiO2	75,93	76,72	78,42	76,18	76,71	75,66	76,98	77,95	79	79,02	77,68	78,74	68,17	76,87	77,57	77,46	71,75
TiO2	0,15	0,06	0,1	0,08	0,21	0,22	0,09	0,09	0,15	0,15	0,1	0,14	0,44	0,1	0,09	0,11	0,26
Al2O3	13,02	13,09	12,02	12,85	12,4	13,27	13,27	12,75	11,93	12,62	12,79	12,24	15,51	12,86	12,6	12,36	13,21
Fe2O3(tot	1,94	1,05	0,95	1,55	1,46	1,4	1,18	0,62	1,08	0,33	1,01	0,99	3,87	1,18	1,07	1,12	2,47
MnO	0,05	0,02	0,01	0,02	0,03	0,02	0,02	0,01	0,01	0,01	0,01	0,02	0,06	0,03	0,02	0,02	0,04
MgO	1,08	0,42	0,15	0,5	1,24	1,02	0,49	0,26	0,65	0,1	0,59	0,56	1,45	0,76	0,73	0,55	0,7
CaO	0,13	0,23	0,13	0,22	0,06	0,17	0,15	0,09	0,15	0,17	0,08	0,02	0,51	0,11	0,01	0,02	0,35
Na2O	5,67	5,48	6,08	5,06	4,25	5,03	4,9	5,89	5,04	6,26	4,7	4,71	3,78	3,62	4,09	4,28	5,03
K2O	0,73	1,21	0,5	1,6	2,38	2,04	1,55	0,82	1,57	0,14	1,51	1,82	3,8	2,69	2,15	1,95	1,69
P2O5	0,03	0,03	0,01	0,01	0,02	0,04	0,01	0,01	0,01	0,01	0,01	0,01	0,13	0,02	0,01	0,02	0,06
LOI	1,68	1,63	1,36	1,95	1,79	1,63	1,43	1,41	1,08	1,29	1,7	1,58	2,26	1,67	1,73	1,84	1,77
Total	100,41	99,94	99,73	100,02	100,55	100,5	100,07	99,9	100,67	100,1	100,18	100,83	99,98	99,91	100,07	99,73	97,33
A/CNK	1,26	1,22	1,12	1,23	1,28	1,23	1,33	1,19	1,16	1,17	1,35	1,26	1,38	1,42	1,39	1,35	1,23
Trace elements (ppm)																	
Ba	197	743	242	2131	616	693	615	465	532	82	564	907	1044	997	1366	1069	491
Ce	101	78	111	88	29	83	112	27	130	bdl	137	128	74	80	33	77	91
Cl	34	474	116	54	19	51	35	74	58	41	139	55	23	17	44	190	61
Co	2	3	1	2	2	2	2	1	2	1	1	5	4	2	1	bdl	3
Cr	1	2	bdl	2	5	bdl	3	1	1	bdl	bdl	1	11	0	3	bdl	bdl
Ga	12	12	12	17	14	16	18	9	14	12	15	13	19	13	13	11	16
Gd	9	6	7	6	7	7	10	4	9	2	10	9	6	6	3	4	7
La	48	34	39	41	22	34	54	29	58	10	33	41	34	37	26	34	40
Nb	12	9	6	16	18	17	14	16	13	17	15	12	17	9	10	9	15
Nd	42	34	41	49	21	29	55	22	47	bdl	27	56	22	34	18	33	23
Ni	3	4	2	3	4	3	3	2	4	1	1	2	5	2	3	2	3
Pb	39	1	9	7	3	4	7	1	7	2	5	5	4	bdl	4	7	5
Rb	17	36	22	42	50	50	43	23	39	2	43	47	94	73	52	48	38
Sc	6	bdl	6	2	7	9	4	2	5	6	5	6	8	2	6	3	9
Sn	2	12	12	12	12	6	6	8	6	13	15	4	10	16	7	9	9
Sr	10	28	22	53	17	17	17	17	18	23	12	10	22	14	9	13	28
Th	16	13	25	15	13	12	17	11	16	9	20	16	11	16	18	16	13
U	7	6	8	8	8	4	6	2	10	8	6	7	3	5	9	7	7
V	1	5	8	2	1	5	1	2	bdl	5	6	bdl	35	4	5	12	35
Y	37	32	37	53	21	53	47	34	51	34	46	26	40	25	22	20	40
Zn	116	18	10	13	27	20	13	12	19	7	13	19	42	15	15	15	22
Zr	234	98	103	203	289	250	186	234	199	250	217	183	326	104	114	114	254

Figure 212: Chatzaras et al. 2012. Chemical data for the Evia metagranitoid rocks. Major elements in wt.% oxides, trace elements in ppm. LOI: loss on ignition; bdl: below detection limit; A/CNK is the molar Al2O3/ CaO+ Na2O+K2O ratio.

Rock type	Amphibolites				Orthogneisses					C. Evia Skotini granites									
Samples	201	1221	1231	1241	211	621	1271	1531	1861	G2,3	G14	668S	349S	348S	669S	354S	505S	402S	
major wt-%																			
SiO2	50,25	53,59	49,33	49,55	77,85	69,23	65,39	63,38	65,62	68,34	68,69	68,48	65,82	67,6	68,12	68,46	63,93	68,17	
MO2	0,52	0,53	1	1,16	0,11	0,38	0,74	0,58	0,48	0,44	0,4	0,42	0,53	0,44	0,41	0,4	0,49	0,5	
Al2O3	16,46	12,79	16,23	20,55	12,33	15,68	16,7	16,59	16,44	15,83	16,06	15,6	16,89	15,71	15,9	15,49	17,49	15,24	
Fe2O3	8,48	8,46	10,61	10,14	0,87	3,1	4,18	4,66	3,87	2,94	2,96	3,6	4,15	3,78	3,32	3,43	4,23	4,58	
FeO										0,81	0,37								
MnO	0,13	0,14	0,15	0,12	0	0,04	0,03	0,06	0,06	0,06	0,02	0,06	0,03	0,05	0,05	0,04	0,07	0,05	
MgO	7,65	9,71	5,36	4,1	0,34	1,02	0,98	1,91	1,35	1,27	1,22	1,62	2,24	1,23	1,29	1,28	1,67	1,66	
CaO	10,34	8,16	9,5	7,77	0,61	2,5	2,54	3,33	2,49	0,19	0,23	0,14	0,04	0,17	0,16	0,13	0,07	0,31	
Na2O	2,34	1,09	1,35	1,25	2,21	3,79	3,47	3,88	4,17	2,35	3,24	2,48	4,38	5,46	2,59	1,79	2,37	3,24	
K2O	1,56	2,94	2,63	4,03	4,87	2,49	2,65	2,42	2,62	5,23	4,77	4,34	3,01	3	5,71	5,78	5,56	2,88	
P2O5	0,04	0,13	0,15	0,26	0,02	0,07	0,23	0,11	0,14	0,13	0,12	0,13	0,1	0,13	0,16	0,1	0,08	0,18	
LOI	2,07	2,04	2,88	0,22	0,77	1,6	2,14	2,6	1,95	2,13	1,7	2,39	2,79	1,71	2,12	2,16	3,08	2,27	
Cr2O3	0,03	0,12	0,01	0	0	0	0	0	0	0	0	0	0	0	0	0	0	0	
NiO	0,01	0,03	0	0	0	0	0	0	0	0	0	0	0	0	0	0	0	0	
Total	99,88	99,73	99,2	99,15	99,98	99,9	99,05	99,52	99,19	98,91	99,41	99,26	99,98	99,28	99,83	99,06	99,04	99,08	
traces	ppm)																		
Nb	0	0	0	2	0	0	0	0	0	7	6	9	10	11	9	12	10	11	
Zr	32	75	87	131	140	94	236	149	141	157	146	171	157	188	154	159	156	210	
Y	14	12	23	30	21	10	18	27	11	45	32	40	24	30	21	29	36	31	
Sr	109	115	488	521	159	254	388	197	203	40	56	30	38	47	65	53	76	84	
U	0	0	0	3	0	0	0	0	0	3	2	4	6	4	4	3	4	4	
Rb	88	135	126	151	101	96	121	101	96	207	178	178	139	233	166	207	82	113	
Th	0	4	2	9	10	0	7	3	5	17	18	14	18	17	21	11	18	14	
Pb	0	0	0	0	30	0	0	0	0	35	28	27	31	30	37	22	24	17	
Ga	12	11	11	19	15	17	19	17	15	20	18	19	20	21	19	18	18	18	
Zn	75	86	89	121	20	43	68	62	51	59	59	51	63	72	50	53	66	57	
Cu	0	0	0	0	0	0	0	0	0	13	10	14	11	11	9	7	16	12	
Ni	77	166	4	0	0	0	1	1	0	6	4	5	5	9	4	5	4	7	
Co	52	46	46	51	26	35	32	29	28	28	28	35	29	38	45	32	31	46	
Cr	216	862	73	16	0	7	6	15	13	25	18	16	22	18	17	18	23	17	
V	194	190	281	297	3	56	67	97	65	56	46	53	94	62	49	51	62	81	
Ce	0	31	29	65	56	28	59	48	54	116	47	75	36	67	98	76	87	63	
Nd	0	13	8	33	15	1	22	21	17	79	26	36	15	36	45	40	33	27	
Ba	99	505	325	987	1130	475	452	411	744	1110	721	882	320	921	1473	1149	635	613	
La	0	18	10	43	33	13	38	25	33	84	33	39	24	46	64	43	39	32	
S	68	81	66	72	55	34	39	38	34	7	8	14	3	67	68	28	2	26	
Hf	0	0	0	1	4	2	3	2	1	6	4	6	6	6	5	2	6	6	
Sc								<0<	<0<	7	7	5	7	6	6	6	10	13	
As								<0<	<0<	<3<	<3<	3	<0<	4	3	6	11	27	

Figure 213: Vavassis et al. 2000. Whole rock geochemical analyses of Evia samples. N. Evia amphibolites & orthogneisses

	N. Evia granites & amphibolites		C.Evia Skotini granites		C.Evia Liri granites			
Samples	211	1221	G14	668S	339S	670S	476S	40 IS
REE (ppm)	granite	amphibolite						
La	48,8	20,2	30,7	46,9	30,01	58,6	42,2	17,8
Ce	84,3	38,9	65,6	92,9	59,9	101	81,3	33,6
Pr	10,4	5,8	7,4	11,5	6,8	11,5	9,7	4,3
Nd	37,7	22	29,6	40,5	23,2	36,3	32,2	16,7
Sm	7,6	5,2	6,2	9,2	5,1	6,6	6,6	4,2
Eu	1,55	1,57	0,99	1,22	1,21	1,61	1,38	1,24
Gd	6,2	4	6,4	7,6	4,1	5,4	4,9	3,9
Tb	0,9	0,6	0,9	1,3	0,6	0,9	0,7	0,7
Dy	4,8	3,4	6	7,4	3,6	4,5	3,7	3,8
Ho	0,94	0,69	1,25	1,62	0,71	0,93	0,71	0,75
Er	2,2	1,8	3,6	4,3	2	2,4	1,9	1,9
Tm	0,3	0,3	0,5	0,6	0,3	0,4	0,3	0,3
Yb	1,9	1,7	3,6	4	2	2,3	1,8	1,8
Lu	0,29	0,29	0,51	0,58	0,31	0,37	0,28	0,23
Th	18,3	8,2	16,8	18,9	13,3	28,7	17,7	1,7
U	2,9	2,4	3,2	3,5	2,6	2,8	1,8	1,1

Figure 214: Vavassis et al. 2000. Whole rock geochemical analyses of Evia samples.

						C. Evia Liri granites					
samples		G6		87E		670S		339S	401S	474S	476S
major wt-%											
Si02		68,86		72,61		62,96		63,26	64,3	61,98	68,19
Ti02		0,4		0,21		0,66		0,6	0,72	0,65	0,33
Al203		14,9		14,89		16,06		16,49	18,09	16,76	13,35
Fe203		2,94		2,41		5,04		4,92	4,37	5,26	2,3
FeO		0,38									
MnO		0,06		0,03		0,08		0,08	0,04	0,08	0,05
MgO		1,31		0,92		2,79		2,93	1,87	2,51	1,06
CaO		0,31		0,19		2,49		2,24	0,33	2,34	3,95
Na20		3,61		4,39		1,39		1,59	1,68	2,76	4,88
K2O		4,38		1,99		5,07		5,09	5,04	3,01	1,18
P2O5		0,13		0,07		0,16		0,14	0,26	0,11	0,13
LOI		2,11		1,68		2,67		2,75	2,83	4,05	4,09
Cr203		0				0,01		0	0,01	0,01	
NiO		0		0				0		0	0
Total		99,39		99,39		99,38		100,09	99,54	99,52	99,51
	traces (ppm)										
Nb		7		7		8		6	3	6	9
Zr		130		122		165		129	123	169	132
Y		31		30		26		23	26	20	19
Sr		98		53		128		240	43	135	303
U		2		3		3		3	2	3	1
Rb		183		91		209		205	210	125	49
Th		18		10		18		10	3	14	15
Pb		34		15		13		16	7	12	14
Ga		18		15		20		21	23	20	13
Zn		51		41		67		62	55	69	36
Cu		8		11		10		11	10	18	8
Ni		4		4		14		13	19	16	1
Co		30		81		46		49	46	41	47
Cr		18		10		46		40	49	61	12
V		51		37		103		100	117	143	43
Ce		72		57		83		56	25	70	59
Nd		33		23		40		27	13	38	28
Ba		799		309		1329		905	1146	776	276
La		42		21		70		38	24	31	31
S		<3<		<0<		7		8	14	«0<	5
Hf		5		7		2		5	3	6	6
Sc		9		6		9		8	s	13	8
As		4		5		7		4	23	12	4

Figure 215: Vavassis et al. 2000. Whole rock geochemical analyses of Evia samples.

	N. Evia granites & amphibolites		C.Evia Skotini granites		C.Evia Liri granites			
Samples	211	1221	G14	668S	339S	670S	476S	40 IS
REE (ppm)	granite	amphibolite						
La	48,8	20,2	30,7	46,9	30,01	58,6	42,2	17,8
Ce	84,3	38,9	65,6	92,9	59,9	101	81,3	33,6
Pr	10,4	5,8	7,4	11,5	6,8	11,5	9,7	4,3
Nd	37,7	22	29,6	40,5	23,2	36,3	32,2	16,7
Sm	7,6	5,2	6,2	9,2	5,1	6,6	6,6	4,2
Eu	1,55	1,57	0,99	1,22	1,21	1,61	1,38	1,24
Gd	6,2	4	6,4	7,6	4,1	5,4	4,9	3,9
Tb	0,9	0,6	0,9	1,3	0,6	0,9	0,7	0,7
Dy	4,8	3,4	6	7,4	3,6	4,5	3,7	3,8
Ho	0,94	0,69	1,25	1,62	0,71	0,93	0,71	0,75
Er	2,2	1,8	3,6	4,3	2	2,4	1,9	1,9
Tm	0,3	0,3	0,5	0,6	0,3	0,4	0,3	0,3
Yb	1,9	1,7	3,6	4	2	2,3	1,8	1,8
Lu	0,29	0,29	0,51	0,58	0,31	0,37	0,28	0,23
Th	18,3	8,2	16,8	18,9	13,3	28,7	17,7	1,7
U	2,9	2,4	3,2	3,5	2,6	2,8	1,8	1,1

Figure 216: Vavassis et al. 2000. Whole rock geochemical analyses of Evia samples.

		ΓΕΩΧΗΜΙΚΕΣ ΑΝΑΛΥΣΕΙΣ ΟΛΙΚΟΥ ΠΕΤΡΩΜΑΤΟΣ ΚΥΡΙΩΝ ΣΤΟΙΧΕΙΩΝ ΚΑΙ						
			ΙΧΝΟΣΤΟΙΧΕΙΩΝ					
		EV-2	EV-6		EV-8	EV-9	EV-11	
SiO2	(%)	68,2	55,1		56,4	69,9	69,8	
TiO2	(%)	0,23	0,59		0,38	0,7	0,28	
Al2O3	(%)	14,8	17,9		17,6	13,1	12,6	
Fe2O3	(%)	4,05	8,4		9,15	4,9	4,7	
MgO	(%)	1,5	3,65		4,55	2,4	0,95	
CaO	(%)	0,8	3,1		0,95	1,05	0,65	
Na2O	(%)	2,75	3,15		1,55	2,9	1,65	
K2O	(%)	4,6	4,55		3	1,35	7,3	
LOI	(%)	1,87	2,86		5,4	2,92	1,23	
SUM	(%)	98,8	99,3		98,98	99,22	99,16	
V	(ppm)	32	43		150	100	36	
Co	(ppm)	5	4		46	20	6	
Ni	(ppm)	14	13		310	150	21	
Cu	(ppm)	20	28		100	35	20	
Zn	(ppm)	180	190		235	190	160	
Rb	(ppm)	120	67		118	60	120	
Nb	(ppm)	10					9	
Sr	(ppm)	18	140		31	25	18	
Y	(ppm)	16	29		8	21	12	
Pb	(ppm)	47	50		27	33	245	
As	(ppm)	16	7		11	7	7	
Mn	(ppm)	460	80		1065	720	185	

Figure 217: Mpounti et al. 2011. Table: Geochemical analyses of major elements and trace elements of South Evia.

Volcanic analysis:

	Evia	
Sample	E24	E22
Major elements by XRF or AA1		
SiO2	47,3	47,7
TiO2	2,13	1,98
Al2O3	17,5	17,2
Fe2O3	10,67	8,61
FeO^{1}	0	0
MnO	0,12	0,08
MgO	8,18	6,57
CaO	2,62	5,29
Na	4,62	4,51
K	1,29	1,89
P	0,45	0,44
L,O,I,	5,1	6,2
Total	100	100,52

Trace elements by XRF		
Ba	66	100
Rb	14	24
Sr	48	97
Y	28	28
Zr	168	165
Nb	51	48
Th	5	2
Pb	9	6
Ga	21	19
Zn	88	75
Cu	10	14
Ni	40	51
V	286	255
Cr	145	141

REE and trace elements by INAA		
La	33	33
Ce	68	61
Nd	25	27
Sm	5,7	5,3
Eu	1,9	1,7
Tb	0,8	0,9
Yb	2,9	2,4
Lu	0,46	0,42
Co	35	n,d,
Cs	0,7	0,6
Hf	3,6	3,4
Sb	0,3	0,2
Sc	28	27
Ta	2,4	2,4
Th	5,1	4,4
U	1,5	1,6

Sample	Ev Central Evia	
	Rock Type	
E24[5]	Alk. Basalt	
SiO2	47,31	
TiO2	2,13	
K2O	1,29	
Nb ppm	51	
Th ppm	5,1	
U ppm	1,5	
Pb ppm	9	
Pb 206/204	19,601	
Pb 207/204	15,668	
Pb 208/204	39,541	

Figure 218: Pe Piper et al. 1998, geochemical analysis of selected Triassic alkaline rocks.

				amphibolites			
samples	201		1221		1231		1241
major wt-%							
Si02	50,25		53,59		49,33		49,55
M02	0,52		0,53		1		1,16
Al203	16,46		12,79		16,23		20,55
Fe203	8,48		8,46		10,61		10,14
FeO							
MnO	0,13		0,14		0,15		0,12
MgO	7,65		9,71		5,36		4,1
CaO	10,34		8,16		9,5		7,77
Na2O	2,34		1,09		1,35		1,25
K2O	1,56		2,94		2,63		4,03
P2O5	0,04		0,13		0,15		0,26
LOI	2,07		2,04		2,88		0,22
Cr2O3	0,03		0,12		0,01		0
NiO	0,01		0,03		0		0
Total	99,88		99,73		99,2		99,15
traces	ppm)						
Nb	0		0		0		2
Zr	32		75		87		131
Y	14		12		23		30
Sr	109		115		488		521
U	0		0		0		3
Rb	88		135		126		151
Th	0		4		2		9
Pb	0		0		0		0
Ga	12		11		11		19
Zn	75		86		89		121
Cu	0		0		0		0
Ni	77		166		4		0
Co	52		46		46		51
Cr	216		862		73		16
V	194		190		281		297
Ce	0		31		29		65
Nd	0		13		8		33
Ba	99		505		325		987
La	0		18		10		43
S	68		81		66		72
Hf	0		0		0		1
Sc							
As							

Figure 219: Vavassis et al. 2000, whole rock geochemical analyses of Evia samples.

Trace elements-REE (ppm)

		N. Evia amphibolites	
Samples	1221		
REE (ppm)	amphibolite		
La	20,2		
Ce	38,9		
Pr	5,8		
Nd	22		
Sm	5,2		
Eu	1,57		
Gd	4		
Tb	0,6		
Dy	3,4		
Ho	0,69		
Er	1,8		
Tm	0,3		
Yb	1,7		
Lu	0,29		
Th	8,2		
U	2,4		

Figure 220: Vavassis et al. 2000, whole rock geochemical analyses of Evia samples.

Chemical analyses normalized to orogenetic granites (ORG):

Rock/ORG	211	621	1271	1531	1861	G2,3	G14	668S	349S	348S	669S	354S	505S	402S
K_2O	12,175	6,225	6,625	6,05	6,55	13,075	11,925	10,85	7,525	7,5	14,275	14,45	13,9	7,2
Rb	25,25	24	30,25	25,25	24	51,75	44,5	44,5	34,75	58,25	41,5	51,75	20,5	28,25
Ba	22,6	9,5	9,04	8,22	14,88	22,2	14,42	17,64	6,4	18,42	29,46	22,98	12,7	12,26
Th	12,5	0	8,75	3,75	6,25	21,25	22,5	17,5	22,5	21,25	26,25	13,75	22,5	17,5
Ta (Avr)	6,25	0	4,375	1,875	3,125	10,975	11,55	9,2	11,75	11,175	13,575	7,475	11,75	9,3
Nb	0	0	0	0	0	0,7	0,6	0,9	1	1,1	0,9	1,2	1	1,1
Ce	1,6	0,8	1,685714	1,371429	1,542857	3,314286	1,342857	2,142857	1,028571	1,914286	2,8	2,171429	2,485714	1,8
Hf	0,444444	0,222222	0,333333	0,222222	0,111111	0,666667	0,444444	0,666667	0,666667	0,666667	0,555556	0,222222	0,666667	0,666667
Zr	0,411765	0,276471	0,694118	0,438235	0,414706	0,461765	0,429412	0,502941	0,461765	0,552941	0,452941	0,467647	0,458824	0,617647
Sm														
Y	0,3	0,142857	0,257143	0,385714	0,157143	0,642857	0,457143	0,571429	0,342857	0,428571	0,3	0,414286	0,514286	0,442857
Yb														

Figure 221: Table of analyses of samples from N. Evia and C. Evia (Skotini) normalized to ORG (Vavassis et al. 2000).

Rock/ORG	ED1	ED2	ED3	ED4	ED5	ED6	ED7	ED8	ED9	ED10	ED11	ED12	ED14	ED15	ED16	ED17-1	ED17-2
K_2O	1,825	3,025	1,25	4	5,95	5,1	3,875	2,05	3,925	0,35	3,775	4,55	9,5	6,725	5,375	4,875	4,225
Rb	4,25	9	5,5	10,5	12,5	12,5	10,75	5,75	9,75	0,5	10,75	11,75	23,5	18,25	13	12	9,5
Ba	3,94	14,86	4,84	42,62	12,32	13,86	12,3	9,3	10,64	1,64	11,28	18,14	20,88	19,94	27,32	21,38	9,82
Th	20	16,25	31,25	18,75	16,25	15	21,25	13,75	20	11,25	25	20	13,75	20	22,5	20	16,25
Ta	10,6	8,575	15,925	10,175	9,025	8,35	11,325	7,675	10,65	6,475	13,25	10,6	7,725	10,45	11,75	10,45	8,875
Nb	1,2	0,9	0,6	1,6	1,8	1,7	1,4	1,6	1,3	1,7	1,5	1,2	1,7	0,9	1	0,9	1,5
Ce	2,885714	2,228571	3,171429	2,514286	0,828571	2,371429	3,2	0,771429	3,714286	#VALUE!	3,914286	3,657143	2,114286	2,285714	0,942857	2,2	2,6
Hf																	
Zr	0,688235	0,288235	0,302941	0,597059	0,85	0,735294	0,547059	0,688235	0,585294	0,735294	0,638235	0,538235	0,958824	0,305882	0,335294	0,335294	0,747059
Sm																	
Y	0,528571	0,457143	0,528571	0,757143	0,3	0,757143	0,671429	0,485714	0,728571	0,485714	0,657143	0,371429	0,571429	0,357143	0,314286	0,285714	0,571429
Yb																	

Figure 222: Table of analyses of samples from Cape Paximadi, Karistos normalized to ORG (Chatzaras et al. 2012).

Rock/ORG	G6	87E	670S	339S	401S	474S	476S
K_2O	10,95	4,975	12,675	12,725	12,6	7,525	2,95
Rb	45,75	22,75	52,25	51,25	52,5	31,25	12,25
Ba	15,98	6,18	26,58	18,1	22,92	15,52	5,52
Th	22,5	12,5	22,5	12,5	3,75	17,5	18,75
Ta	12,9	7,4	13,25	7,6	2,525	10,65	10,775
Nb	3,3	2,3	4	2,7	1,3	3,8	2,8
Ce	2,057143	1,628571	2,371429	1,6	0,714286	2	1,685714
Hf	0,555556	0,777778	0,222222	0,555556	0,333333	0,666667	0,666667
Zr	0,382353	0,358824	0,485294	0,379412	0,361765	0,497059	0,388235
Sm							
Y	0,442857	0,428571	0,371429	0,328571	0,371429	0,285714	0,271429
Yb							

Figure 223: Table of analyses of samples from C. Evia (Liri) normalized to ORG (Vavassis et al. 2000).

Rock/ORG	211	1221	G14	668S	339S	670S	476S	40 IS
K_2O								
Rb								
Ba								
Th	22,875	10,25	21	23,625	16,625	35,875	22,125	2,125
Ta								
Nb								
Ce	2,408571	1,111429	1,874286	2,654286	1,711429	2,885714	2,322857	0,96
Hf								
Zr								
Sm	0,844444	0,577778	0,688889	1,022222	0,566667	0,733333	0,733333	0,466667
Y								
Yb	0,02375	0,02125	0,045	0,05	0,025	0,02875	0,0225	0,0225

Figure 224: Table of analyses of samples from C. Evia (N.Evia granites, Skotini and Liri) normalized to ORG (Vavassis et al. 2000).

N.Evia, Orthogneiss	211	621	1271	1531	1861	G2,3	G14	668S	349S	348S	669S	354S	505S	402S		
Y+Nb	21	10	18	27	11	52	38	49	34	41	30	41	46	42		
Rb	101	96	121	101	96	207	178	178	139	233	166	207	82	113		
C.Evia (Skotini Granites)	G2,3	G14	668S	349S	348S	669S	354S	505S								
Rb	207	178	178	139	233	166	207	82								
Y+Nb	52	38	49	34	41	30	41	46								
C.Evia (Liri Granites)	G6	87E	670S	339S	401S	474S	476S									
Rb	183	91	209	205	210	125	49									
Y+Nb	38	37	34	29	29	26	28									
S.Evia, Karistos	ED1	ED2	ED3	ED4	ED5	ED6	ED7	ED8	ED9	ED10	ED11	ED12	ED14	ED15	ED16	ED17-2
Rb	17	36	22	42	50	50	43	23	39	2	43	47	94	73	52	38
Y+Nb	49	41	43	69	39	70	61	50	64	51	61	38	57	34	32	55
C.Evia (Ochi unit), S.Evia	EV-2	EV-6		EV-8	EV-9	EV-11										
Rb	120	67		118	60	120										
Y+Nb	26					21										

Figure 225: Table of chemical analyses (Rb, Y+Nb) of samples from all previous locations in Evia. The synthesis of these in Pearce's diagram (Fig. 206) concludes the geotectonic environment as shown below.

Spot analysis carried out in Mainz:

Chemical analysis from Day 1:

No.	2	3	4	5	6	7	8	9	10	11	12	13	14	15
Comment	a1	a2	a3	a4	a5	a6	a7	a8	a9	a10	a11	a12	a13	a14
SiO2	65,42	49,82	53,38	101,1	35,81	53,71	64,62	96,97	52,88	69,05	101,57	68,97	0,05	0,1258
TiO2	0,0015	0,8322	0,8679	0,0608	0	0,0124	0	0	2,74	0	0	0	78,43	97,33
Al2O3	18,16	24,52	24,66	0,0136	0,1205	2,87	18,17	0,4417	4,2	19,37	0,0607	19,27	0,0944	0,0836
Cr2O3	0	0,0214	0,0277	0	0,0674	0	0,0419	0	0	0,0071	0,0065	0,0271	0,0787	0,0436
FeO	0,0641	3,76	2,74	0,092	0,3509	27,13	0,2678	1,48	23,65	0,2317	0,1257	0,035	1,0498	1,1617
MnO	0	0,109	0,0334	0,0289	0,0465	0,0131	0	0,0125	0	0,0212	0,0371	0,0116	0,0386	0,0131
MgO	0	3,65	3,65	0,0009	0,0975	0,0439	0,0229	0,0023	0,0857	0,0042	0	0	0,0029	0
NiO	0	0	0,026	0	0	0	0	0,0086	0,009	0	0	0,0055	0	0
CaO	0	0,0368	0,0576	0	0,0587	0,1219	0	0,0324	0,0081	0,0013	0	0,0038	0,0203	0,0136
Na2O	0,3528	0,0357	0,1138	0	0	14,34	0,4129	0,5368	13,9	11,87	0	11,72	0,0335	0
K2O	16,61	11,22	11,36	0,0361	0,1532	0,0574	16,49	0,1151	0,0513	0,1141	0,0434	0,0619	0,1368	0,097
Total	100,6084	94,0052	96,9165	101,3323	36,7048	98,2988	100,0255	99,5994	97,5242	100,6696	101,8434	100,1048	79,9351	98,8685

16	17	18	19	20	21	22	23	24	25	26	27	28	29	30
a15	a16	a17	a18	a19	a20	a21	a22	a23	a24	a25	a26	a27	a28	a29
54,51	0,1156	0,1509	50,93	54,06	50,29	54,46	54,13	0,1368	57,72	37,92	37,88	30,97	45,44	46,44
0,0518	0,9541	1,97	0,9105	0,0686	0,7406	2,04	1,91	97,04	0,0363	0,1119	0,0237	39,24	2,4	0,0733
3,2	0,0154	0,0201	23,21	2,01	22,64	4,8	6,23	0,033	5,53	22,48	22,94	0,7332	34,17	35,23
0,0096	0	0,0385	0,0085	0,03	0	0,0537	0,0054	0,0717	0,0274	0,0747	0,1388	0,0085	0,033	0,034
27,2	89,06	88,86	4,78	28,01	5,94	23,85	22,65	1,51	18,03	13,21	12,53	0,6188	1,0228	1,38
0,0364	0,0129	0,0143	0,0256	0,022	0	0	0,0179	0	0,2437	0,4385	0,2917	0,0497	0,0472	0
0,0805	0	0	3,78	0,1151	3,86	0,0565	0,0726	0,0191	9,2	0,0076	0	0	0,3322	0,4703
0	0,0197	0	0,0032	0	0,0049	0	0	0	0	0,0386	0	0	0,0123	0
0,0611	0	0,024	0	0,1827	0	0	0	0,0298	0,5281	23,15	23,43	28,87	2,2	0,3639
13,77	0	0,0568	0,0471	13,95	0,0057	14,13	15	0	7,02	0	0,02	0,016	0,6674	0,7044
0,0548	0,0839	0,0636	11,28	0,0272	11,26	0,0005	0,0527	0,2556	0,0091	0	0,0013	0	8,76	8,88
98,9743	90,2617	91,1983	94,9749	98,4757	94,7413	99,3908	100,0686	99,0961	98,3446	97,4313	97,2556	100,5061	95,085	93,576

Figure 226: spot a1-a29

No.	31	32	33	34	35	36	37	38	39	40	41	42	43	44
Comment	a30	a31	a32	a33	a34	a35	a36	a37	a38	a39	a40	a41	a42	a43
SiO2	0,1058	0,0448	68,63	50,54	1,9789	0,111	57,15	57,27	56,67	27,97	50,53	56,97	58,65	38,39
TiO2	0	0	0,0276	0,0406	0,01	1,1886	0	0,1236	0,0401	0,008	0,0775	0,0505	0,9733	0,1272
Al2O3	0,0805	0,006	18,94	26,09	0,1241	0,0746	6,85	7,53	5,35	19,37	26,24	2,37	17,5	23,32
Cr2O3	0,0639	0	0,0438	0,0523	0,0896	0,0632	0,0475	0,0216	0,0675	0,1644	0	0,0018	0,0497	0,1018
FeO	0,4694	0,1421	0,0437	3,9	88,31	87,74	16,23	15,22	18,33	19,32	3,59	12,48	0,1761	12,04
MnO	0,1632	0,0307	0,0009	0,0329	0,0427	0	0,2376	0,2191	0,2853	0,3441	0,0316	0,4047	0,0097	0,4157
MgO	0,1504	0	0	3,24	0,0043	0,013	9,41	9,39	8,94	20,51	3,38	15,1	0,0276	0
NiO	0	0	0	0	0,0272	0	0,0742	0,0752	0	0,0068	0	0	0	0
CaO	54,71	59,33	0,0787	0,0464	0,5856	0,3407	0,3046	0,3978	0,9216	0,0882	0	7,47	1,1508	23,21
Na2O	0	0	11,92	0,1945	0,0627	0,1385	7,35	7,27	6,96	0	0,1786	2,98	7,07	0
K2O	0,0095	0	0,0107	11,16	0,0546	0	0	0,023	0,0136	0,0241	11,23	0,0622	0,0413	0
Total	55,7528	59,5537	99,6954	95,2968	91,2898	89,6696	97,654	97,5404	97,5782	87,8057	95,2577	97,8893	85,6486	97,6048

45	46	47	48	49	50	51	52	53	54	55	56	57	58	59	60
a44	a45	a46	a47	a48	a49	a50	a51	a52	a53	a54	a55	a56	a57	a58	a59
68,14	0,0047	36,47	27,35	30,17	55,97	52,47	45,12	37,78	28,66	31,17	100,79	50,72	56,57	19,06	56,34
0	0	0,0148	0	38,51	0,0334	0,026	0	0,0345	0,0116	38,17	0,0138	0,0778	0,0444	30,81	0,0419
19,19	0,0112	22,29	19,72	0,9961	3,96	20,06	28,82	23,28	19,54	1,1226	0,0217	25,99	6,45	10,51	6,46
0,0252	0,0413	0,0697	0,0495	0,0527	0,0425	0,0367	0,0903	0,088	0,0872	0,0446	0,0102	0,0453	0,0779	0,1001	0,0443
0,0863	0,3306	12,55	18,74	0,6072	15,07	6,25	2,57	12,03	19,27	0,8089	0,1195	3,5	15,35	1,1092	16,33
0,0147	0,1199	0,1884	0,6358	0,0477	0,3628	0,1506	0,0133	0,1609	0,3262	0,0531	0	0,0096	0,2066	0,0435	0,2666
0	0,1174	0	20,43	0	12,78	6,28	2,7	0,0179	20,24	0	0	3,2	10,29	0,4012	9,67
0	0	0	0,0333	0	0,0012	0	0	0	0,0284	0	0	0	0	0	0
0,1706	53,93	23,46	0,1309	29,14	4,64	0,2039	1,73	23,84	0,1658	28,42	0,2981	0,0635	1,44	25,1	0,7055
12,12	0,0037	0,0204	0,0622	0,0275	4,79	7,92	0,1609	0,0438	0,0356	0	0,0025	0,7913	7,06	0,0186	7,17
0,026	0,0005	0	0,0207	0,0121	0,079	0,0217	9,84	0	0,0527	0,0123	0,0261	10,65	0,0112	0,1329	0,0498
99,7729	54,5593	95,0634	87,1725	99,5633	97,729	93,419	91,0445	97,2751	88,4175	99,8016	101,2819	95,0475	97,5002	87,2856	97,0782

Figure 227: spot a30-a59

No.	61	62	63	64	65	66	67	68	69	70	71	72	73	74	75	76	77	78	79	80	81
Comment	a60	a61	a62	a63	a64	a65	a66	a67	a68	a69	a70	a71	a72	a73	a74	a75	a76	a77	a78	a79	a80	
SiO2	55,87	54,91	29,34	38,2	56,95	31,4	36,36	27,64	38,44	49,67	46,42	32,6	38,09	38,18	0,0207	27,88	37,73	57,2	56,88	41,25	29,95
TiO2	0,0492	0	0,0118	0	0	36,04	31,03	0	0,081	0,0557	0,119	34,43	0	0,0145	0	0,0283	0	0	0	0,0392	0,0657
Al2O3	1,1077	1,2354	18,96	23,12	5,91	2,65	4,8	19,37	23,86	28,09	27,39	5,18	25,79	22,87	0	18,98	22,64	6,59	6,86	20,34	19,1
Cr2O3	0,0115	0,0407	0,0656	0,1023	0,0607	0,0454	0,0276	0,0553	0,1211	0,0705	0,0652	0,0373	0,0886	0,1149	0,0139	0,0105	0,0998	0,0586	0,0212	0,1518	0,1205
FeO	10,96	9,97	18,86	12,04	16,09	1,2594	0,5468	19,47	11,3	3,15	1,73	1,1537	7,7	12,49	0,3213	19,28	12,81	16,31	16,68	11,89	19,07
MnO	0,2561	0,3101	0,3687	0,1643	0,1815	0,0492	0,059	0,4322	0,2177	0,022	0,0587	0	0,2077	0,2354	0,4474	0,3559	0,2323	0,263	0,2779	0,1697	0,2336
MgO	17,55	17,11	20,72	0,0191	10,26	0	0	20,49	0,013	2,63	0,2606	0,0166	0,1257	0,0129	0,1829	20,61	0	9,49	8,87	10,9	18,66
NiO	0	0	0	0,003	0	0	0	0,0233	0	0	0	0	0,0047	0	0	0,0213	0	0,0447	0	0	0,0157
CaO	11,61	11,38	0,1414	23,41	1,2362	28,29	22,93	0,092	23,62	0,0162	6,25	25,1	23,02	23,21	54,89	0,2907	23,23	0,6982	0,7485	0,1208	0,2152
Na2O	0,9134	0,9482	0,0161	0,0191	6,81	0	2,71	0,0574	0	0,2301	2,66	1,65	0,1403	0,014	0	0,0193	0	7,19	7	0,0424	0
K2O	0,0527	0,0515	0,021	0	0,0085	0	0,0133	0,0179	0,0068	11,12	4,01	0,0304	0,0041	0,0193	0,0198	0,0101	0,0169	0,0292	0,021	5,81	0,7827
Total	98,3807	95,9559	88,5047	97,0778	97,507	99,7341	98,4767	87,6482	97,6597	95,0546	88,9635	100,198	95,1712	97,1611	55,8955	87,4862	96,7591	97,8737	97,3587	90,714	88,2134

82	83	84	85	86	87	88	89	90	91	92	93	94	95	96	97	98	99	100	101	102
a81	a82	a83	a84	a85	a86	a87	a88	a89	a90	a91	a92	a93	a94	a95	a96	a97	a98	a99	a100	a101
50	0,0555	27,22	38,08	0,0333	56,67	41,76	0,0343	68,71	50,32	50,36	56,7	44,17	56,57	51,95	27,95	56,54	61,35	56,54	27,48	56,45
0,0232	0,081	0,0357	0,0093	0,0233	0,0328	0,1079	0	0,0107	0,0109	0,0356	0	0,051	0,0223	0,0749	0	0,056	0,0015	0,0433	0,0173	0,0026
25,32	0,0014	19,36	22,37	0	4,2	18,09	0,0089	19,28	25,95	25,67	6,76	26,33	6,39	23,26	19,17	5,91	11,19	6,28	18,44	5,93
0,1331	0,036	0,1421	0,1097	0	0,061	0	0,0537	0,0273	0,0892	0,0634	0,0146	0,0172	0,0697	0,1023	0,1313	0,0887	0,044	0,0612	0,0166	0,1045
4,06	0,1883	21,36	12,7	0,3407	19,6	14,75	0,3381	0,0762	3,25	3,63	16,28	4,77	16,57	4,46	20,83	16,85	9,57	16,96	21,89	17,04
0,0282	0,0247	0,4112	0,1951	0,0886	0,2681	0,2665	0,1317	0	0,0653	0,0326	0,2349	0,17	0,3269	0,087	0,3297	0,3315	0,0717	0,301	0,1902	0,2657
3,38	0	19,15	0,0058	0,1529	9,08	6,43	0,2148	0,0026	3,45	3,39	9,48	0	9,64	4,1	19,51	9,55	6,11	9,42	18,98	9,31
0	0	0,009	0	0	0,037	0,0389	0	0	0	0	0	0	0,0247	0	0	0	0	0,0039	0,0324	0
0,0562	55,57	0,1461	23,29	54,7	0,1893	0,856	53,46	0,0417	0,0092	0	0,3919	18,96	1,1747	0,0157	0,0793	0,8477	2,01	0,5401	0,0683	0,4795
0,1746	0	0	0,0452	0,0623	7,13	3,89	0	11,89	0,1882	0,1907	7,28	2,31	6,79	0,1076	0	6,99	7,83	7,2	0	7,15
11,04	0,0165	0	0	0,0057	0,0123	0,157	0,0006	0,0035	11,28	11,1	0,0055	0,0151	0,0073	11,17	0,0037	0,0464	0,0132	0,0079	0,001	0
94,2153	55,9234	87,8342	96,8052	55,4068	97,2805	86,3464	54,2421	100,0419	94,6128	94,4724	97,1469	96,7984	97,5856	95,3276	88,0041	97,2104	98,1905	97,3575	87,1159	96,7324

Figure 228: spot a60-a101

Chemical analysis from Day 2:

No.	15	24	82	83	19	22	25	29	33	89	91	72	13	27	32	71	75	80	87	16	17	18	20	28	30	31	68
Comment	460_b15	460_b24	460_b82	460_b83	460_b19	460_b22	460_b25	460_b29	460_b33	460_b89	460_b91	460_b72	460_b13	460_b27	460_b32	460_b71	460_b75	460_b80	460_b87	460_b16	460_b17	460_b18	460_b20	460_b28	460_b30	460_b31	460_b68
Sample #	460	460	460	460	460	460	460	460	460	460	460	460	460	460	460	460	460	460	460	460	460	460	460	460	460	460	460
Spot	b15	b24	b82	b83	b19	b22	b25	b29	b33	b89	b91	b72	b13	b27	b32	b71	b75	b80	b87	b16	b17	b18	b20	b28	b30	b31	b68
Mineral	Ab	Ab	Ab	Ab	Aeg	Aeg	Aeg	Aeg	Aeg	Aeg	Aeg	Cal	Ep	Ep	Ep	Ep	Ep	Ep	Ep	Gln	Gln	Gln	Gln	Gln	Gln	Gln	Gln
Comment																											
SiO2	68,69	68,37	68,54	68,99	57,23	55,79	56,19	56,24	57,11	54,15	56,33	0,0771	37,78	38,22	37,86	38,79	37,87	38,31	37,87	55,22	55,75	55,89	55,8	55,89	55,79	56,01	55,95
TiO2	0	0	0,0534	0,0334	0,1886	0,0749	0,1326	0,4743	0,2106	0,3523	0,0135	0,1098	0	0,1021	0,0074	0,0507	0,0706	0,0441	0,0309	0,048	0,0274	0,1236	0,1121	0,0324	0	0,0234	0,0706
Al2O3	19,06	19,42	19,18	19,19	13,91	11,93	13,2	11,97	8,76	5,21	13,56	0	23,68	23,68	23,27	22,93	23,18	22,87	22,48	8,67	8,59	8	7,93	7,65	7,5	7,93	8,64
Cr2O3	0,0065	0,0646	0,0484	0	0,0047	0	0	0,0278	0,0343	0	0	0,0666	0,0128	0	0,0096	0,0152	0,0527	0,067	0,0301	0,0358	0,0377	0,0225	0,069	0,0258	0,0291	0,0011	0
Fe2O3	0,471434	0,408865	0,152699	0,100466	14,43641	17,73711	16,62576	16,71467	21,46012	26,29448	15,65889		14,30304	13,48065	13,1917	13,54733	13,66958	13,43619	14,19191								
FeO	0,4242	0,3679	0,1374	0,0904	12,99	15,96	14,96	15,04	19,31	23,66	14,09	0,3134	12,87	12,13	11,87	12,19	12,3	12,09	12,77	20,85	20,65	20,03	21,08	20,82	21,6	21,14	19,81
MnO	0	0,014	0	0	0,06	0,0394	0,0703	0,0186	0,1158	0,0941	0,0148	0,0279	0,2231	0,2986	0,2918	0,3426	0,3193	0,2811	0,5593	0,3691	0,3737	0,2874	0,3572	0,329	0,3402	0,3315	0,3453
MgO	0,0039	0	0	0,0118	0,4076	0,3792	0,3475	0,5468	0,7823	0,7093	0,4109	0	0	0,0065	0	0	0	0	0,0034	5,04	5,03	5,45	4,97	5,78	5,07	5,02	5,35
NiO																											
CaO	0,0565	0,0298	0,0225	0,0315	1,3775	1,3163	1,1816	1,0748	1,339	1,96	1,0691	55,44	23,06	23,12	23,33	22,57	22,54	22,83	22,48	0,2077	0,2278	0,0634	0,2771	0,1522	0,1885	0,2969	0,1626
Na2O	11,71	11,86	11,74	11,8	13,5	14	14,22	13,84	13,6	13,18	13,91	0	0	0	0	0	0,0006	0,1303	0,0058	7,36	7,41	7,49	7,29	7,36	7,38	7,45	7,47
K2O	0,0588	0,0211	0,0472	0,0299	0	0,0072	0,0192	0,0021	0,0092	0	0,0118	0,0249	0,0517	0,0608	0	0,0915	0,0291	0,0076	0	0,0223	0,0143	0,0144	0,0129	0,0236	0,01	0,011	0,0342
Total	100,0098	100,1473	99,769	100,177	99,6684	99,4971	100,3211	99,2345	101,2711	99,3158	99,4102	56,0597	97,6777	97,6181	96,6389	96,98	96,3624	96,6301	96,2296	97,823	98,1109	97,3713	97,8984	98,0631	97,9079	98,2139	97,8327
Total	100,0571	100,1884	99,7842	100,1871									99,11064	98,96865	97,9605	98,33733	97,73188	97,97629	97,65141								
moles																											
SiO2	1,143237	1,137911	1,14074	1,14823	0,952503	0,928536	0,935194	0,936026	0,950506	0,901241	0,937524	0,001283	0,628788	0,636112	0,63012	0,645598	0,630286	0,637609	0,630286	0,91905	0,927871	0,930201	0,928703	0,930201	0,928536	0,932198	0,931199
TiO2	0	0	0,000669	0,000418	0,002361	0,000938	0,00166	0,005939	0,002637	0,004411	0,000169	0,001375	0	0,001278	9,27E-05	0,000635	0,000884	0,000552	0,000387	0,000601	0,000343	0,001548	0,001404	0,000406	0	0,000293	0,000884
Al2O3	0,186934	0,190464	0,188111	0,188209	0,136424	0,117005	0,129461	0,117398	0,085915	0,051098	0,132992	0	0,232245	0,232245	0,228224	0,224889	0,227341	0,224301	0,220476	0,085032	0,084248	0,078461	0,077775	0,075028	0,073557	0,077775	0,084738
Cr2O3	4,28E-05	0,000425	0,000318	0	3,09E-05	0	0	0,000183	0,000226	0	0	0,000438	8,42E-05	0	6,32E-05	0,0001	0,000347	0,000441	0,000198	0,000236	0,000248	0,000148	0,000454	0,00017	0,000191	7,24E-06	0
Fe2O3	0,002952	0,00256	0,000956	0,000629	0,090404	0,111073	0,104114	0,104671	0,134388	0,164661	0,098059		0,089569	0,084419	0,082609	0,084836	0,085602	0,08414	0,088873								
FeO												0,004362								0,290211	0,287427	0,278797	0,293412	0,289793	0,30065	0,294247	0,275735
MnO	0	0,000197	0	0	0,000846	0,000555	0,000991	0,000262	0,001632	0,001327	0,000209	0,000393	0,003145	0,004209	0,004113	0,00483	0,004501	0,003963	0,007884	0,005203	0,005268	0,004051	0,005035	0,004638	0,004796	0,004673	0,004868
MgO	9,68E-05	0	0	0,000293	0,010113	0,009408	0,008622	0,013567	0,01941	0,017598	0,010195	0	0	0,000161	0	0	0	0	8,44E-05	0,125047	0,124799	0,135219	0,12331	0,143407	0,125791	0,124551	0,132738
NiO	0	0	0	0	0	0	0	0	0	0	0	0	0	0	0	0	0	0	0	0	0	0	0	0	0	0	0
CaO	0,001008	0,000531	0,000401	0,000562	0,024564	0,023473	0,021071	0,019166	0,023878	0,034952	0,019065	0,988634	0,411217	0,412287	0,416032	0,402479	0,401944	0,407116	0,400875	0,003704	0,004062	0,001131	0,004941	0,002714	0,003361	0,005294	0,0029
Na2O	0,188935	0,191355	0,189419	0,190387	0,217816	0,225883	0,229433	0,223302	0,219429	0,212653	0,224431	0	0	0	0	0	9,68E-06	0,002102	9,36E-05	0,11875	0,119557	0,120848	0,117621	0,11875	0,119073	0,120202	0,120525
K2O	0,000624	0,000224	0,000501	0,000317	0	7,64E-05	0,000204	2,23E-05	9,77E-05	0	0,000125	0,000264	0,000549	0,000645	0	0,000971	0,000309	8,07E-05	0	0,000237	0,000152	0,000153	0,000137	0,000251	0,000106	0,000117	0,000363
cations																											
Si	1,143237	1,137911	1,14074	1,14823	0,952503	0,928536	0,935194	0,936026	0,950506	0,901241	0,937524	0,001283	0,628788	0,636112	0,63012	0,645598	0,630286	0,637609	0,630286	0,91905	0,927871	0,930201	0,928703	0,930201	0,928536	0,932198	0,931199
Ti	0	0	0,000669	0,000418	0,002361	0,000938	0,00166	0,005939	0,002637	0,004411	0,000169	0,001375	0	0,001278	9,27E-05	0,000635	0,000884	0,000552	0,000387	0,000601	0,000343	0,001548	0,001404	0,000406	0	0,000293	0,000884
Al	0,373867	0,380929	0,376221	0,376417	0,272849	0,23401	0,258922	0,234795	0,17183	0,102196	0,265983	0	0,46449	0,46449	0,456448	0,449779	0,454682	0,448602	0,440952	0,170065	0,168495	0,156922	0,155549	0,150057	0,147115	0,155549	0,169476
Cr	8,55E-05	0,00085	0,000637	0	6,18E-05	0	0	0,000366	0,000451	0	0	0,000876	0,000168	0	0,000126	0,0002	0,000693	0,000882	0,000396	0,000471	0,000496	0,000296	0,000908	0,000339	0,000383	1,45E-05	0
Fe^{3+}	0,005904	0,005121	0,001912	0,001258	0,180807	0,222147	0,208228	0,209341	0,268775	0,329323	0,196118		0,179137	0,168837	0,165218	0,169672	0,171203	0,16828	0,177745								
Fe^{2+}	0	0	0	0	0	0	0	0	0	0	0	0,004362	0	0	0	0	0	0	0	0,290211	0,287427	0,278797	0,293412	0,289793	0,30065	0,294247	0,275735
Mn	0	0,000197	0	0	0,000846	0,000555	0,000991	0,000262	0,001632	0,001327	0,000209	0,000393	0,003145	0,004209	0,004113	0,00483	0,004501	0,003963	0,007884	0,005203	0,005268	0,004051	0,005035	0,004638	0,004796	0,004673	0,004868
Mg	9,68E-05	0	0	0,000293	0,010113	0,009408	0,008622	0,013567	0,01941	0,017598	0,010195	0	0	0,000161	0	0	0	0	8,44E-05	0,125047	0,124799	0,135219	0,12331	0,143407	0,125791	0,124551	0,132738
Ni	0	0	0	0	0	0	0	0	0	0	0	0	0	0	0	0	0	0	0	0	0	0	0	0	0	0	0
Ca	0,001008	0,000531	0,000401	0,000562	0,024564	0,023473	0,021071	0,019166	0,023878	0,034952	0,019065	0,988634	0,411217	0,412287	0,416032	0,402479	0,401944	0,407116	0,400875	0,003704	0,004062	0,001131	0,004941	0,002714	0,003361	0,005294	0,0029
Na	0,37787	0,382711	0,378838	0,380775	0,435632	0,451766	0,458866	0,446603	0,438859	0,425306	0,448862	0	0	0	0	0	1,94E-05	0,004205	0,000187	0,2375	0,239113	0,241695	0,235241	0,2375	0,238145	0,240404	0,24105
K	0,001248	0,000448	0,001002	0,000635	0	0,000153	0,000408	4,46E-05	0,000195	0	0,000251	0,000529	0,001098	0,001291	0	0,001943	0,000618	0,000161	0	0,000473	0,000304	0,000306	0,000274	0,000501	0,000212	0,000234	0,000726
oxygens																											
SiO2	2,286473	2,275821	2,28148	2,296459	1,905006	1,857073	1,870388	1,872052	1,901012	1,802483	1,875048	0,002566	1,257577	1,272223	1,26024	1,291197	1,260573	1,275219	1,260573	1,838099	1,855741	1,860402	1,857406	1,860402	1,857073	1,864396	1,862399
TiO2	0	0	0,001337	0,000836	0,004723	0,001876	0,003321	0,011877	0,005274	0,008822	0,000338	0,00275	0	0,002557	0,000185	0,00127	0,001768	0,001104	0,000774	0,001202	0,000686	0,003095	0,002807	0,000811	0	0,000586	0,001768
Al2O3	0,560801	0,571393	0,564332	0,564626	0,409273	0,351016	0,388383	0,352193	0,257745	0,153293	0,398975	0	0,696735	0,696735	0,684672	0,674668	0,682024	0,672903	0,661428	0,255097	0,252743	0,235383	0,233324	0,225085	0,220672	0,233324	0,254214
Cr2O3	0,000128	0,001275	0,000955	0	9,28E-05	0	0	0,000549	0,000677	0	0	0,001315	0,000253	0	0,000189	0,0003	0,00104	0,001322	0,000594	0,000707	0,000744	0,000444	0,001362	0,000509	0,000574	2,17E-05	0
Fe2O3	0,008857	0,007681	0,002869	0,001887	0,271211	0,33322	0,312342	0,314012	0,403163	0,493984	0,294177		0,268706	0,253256	0,247827	0,254508	0,256805	0,252421	0,266618								
FeO	0	0	0	0	0	0	0	0	0	0	0	0,004362	0	0	0	0	0	0	0	0,290211	0,287427	0,278797	0,293412	0,289793	0,30065	0,294247	0,275735
MnO	0	0,000197	0	0	0,000846	0,000555	0,000991	0,000262	0,001632	0,001327	0,000209	0,000393	0,003145	0,004209	0,004113	0,00483	0,004501	0,003963	0,007884	0,005203	0,005268	0,004051	0,005035	0,004638	0,004796	0,004673	0,004868
MgO	9,68E-05	0	0	0,000293	0,010113	0,009408	0,008622	0,013567	0,01941	0,017598	0,010195	0	0	0,000161	0	0	0	0	8,44E-05	0,125047	0,124799	0,135219	0,12331	0,143407	0,125791	0,124551	0,132738
NiO	0	0	0	0	0	0	0	0	0	0	0	0	0	0	0	0	0	0	0	0	0	0	0	0	0	0	0
CaO	0,001008	0,000531	0,000401	0,000562	0,024564	0,023473	0,021071	0,019166	0,023878	0,034952	0,019065	0,988634	0,411217	0,412287	0,416032	0,402479	0,401944	0,407116	0,400875	0,003704	0,004062	0,001131	0,004941	0,002714	0,003361	0,005294	0,0029
Na2O	0,188935	0,191355	0,189419	0,190387	0,217816	0,225883	0,229433	0,223302	0,219429	0,212653	0,224431	0	0	0	0	0	9,68E-06	0,002102	9,36E-05	0,11875	0,119557	0,120848	0,117621	0,11875	0,119073	0,120202	0,120525
K2O	0,000624	0,000224	0,000501	0,000317	0	7,64E-05	0,000204	2,23E-05	9,77E-05	0	0,000125	0,000264	0,000549	0,000645	0	0,000971	0,000309	8,07E-05	0	0,000237	0,000152	0,000153	0,000137	0,000251	0,000106	0,000117	0,000363
Total	3,046923	3,048479	3,041295	3,055368	2,843645	2,802581	2,834753	2,807002	2,832317	2,725112	2,822563	1,000284	2,638182	2,642074	2,613259	2,630223	2,608974	2,61623	2,598923	2,638256	2,651179	2,639523	2,639355	2,64636	2,632096	2,647412	2,655509

Figure 229: Spots of chemical analysis and classification into minerals.

oxygens	8	8	8	8	6	6	6	6	6	6	6	3	12,5	12,5	12,5	12,5	12,5	12,5	12,5	8	8	8	8	8	8	8	8
cations																											
Si	3,0017	2,9862	3,0007	3,0065	2,0098	1,9879	1,9794	2,0008	2,0136	1,9843	1,9929	0,0038	2,9793	3,0095	3,0141	3,0682	3,0198	3,0464	3,0315	2,7868	2,7999	2,8193	2,8149	2,8120	2,8222	2,8169	2,8053
Ti	0,0000	0,0000	0,0018	0,0011	0,0050	0,0020	0,0035	0,0127	0,0056	0,0097	0,0004	0,0041	0,0000	0,0060	0,0004	0,0030	0,0042	0,0026	0,0019	0,0018	0,0010	0,0047	0,0043	0,0012	0,0000	0,0009	0,0027
Al	0,9816	0,9997	0,9896	0,9856	0,5757	0,5010	0,5480	0,5019	0,3640	0,2250	0,5654	0,0000	2,2008	2,1976	2,1833	2,1375	2,1785	2,1434	2,1208	0,5157	0,5084	0,4756	0,4715	0,4536	0,4471	0,4700	0,5106
Cr	0,0002	0,0022	0,0017	0,0000	0,0001	0,0000	0,0000	0,0008	0,0010	0,0000	0,0000	0,0026	0,0008	0,0000	0,0006	0,0010	0,0033	0,0042	0,0019	0,0014	0,0015	0,0009	0,0028	0,0010	0,0012	0,0000	0,0000
Fe^{3+}	0,0155	0,0134	0,0050	0,0033	0,3815	0,4756	0,4407	0,4475	0,5694	0,7251	0,4169		0,8488	0,7988	0,7903	0,8064	0,8203	0,8040	0,8549								
Fe^{2+}	0,0000	0,0000	0,0000	0,0000	0,0000	0,0000	0,0000	0,0000	0,0000	0,0000	0,0000	0,0131	0,0000	0,0000	0,0000	0,0000	0,0000	0,0000	0,0000	0,8800	0,8673	0,8450	0,8893	0,8760	0,9138	0,8892	0,8307
Mn	0,0000	0,0005	0,0000	0,0000	0,0018	0,0012	0,0021	0,0006	0,0035	0,0029	0,0004	0,0012	0,0149	0,0199	0,0197	0,0230	0,0216	0,0189	0,0379	0,0158	0,0159	0,0123	0,0153	0,0140	0,0146	0,0141	0,0147
Mg	0,0003	0,0000	0,0000	0,0008	0,0213	0,0201	0,0182	0,0290	0,0411	0,0387	0,0217	0,0000	0,0000	0,0008	0,0000	0,0000	0,0000	0,0000	0,0004	0,3792	0,3766	0,4098	0,3738	0,4335	0,3823	0,3764	0,3999
Ni	0,0000	0,0000	0,0000	0,0000	0,0000	0,0000	0,0000	0,0000	0,0000	0,0000	0,0000	0,0000	0,0000	0,0000	0,0000	0,0000	0,0000	0,0000	0,0000	0,0000	0,0000	0,0000	0,0000	0,0000	0,0000	0,0000	0,0000
Ca	0,0026	0,0014	0,0011	0,0015	0,0518	0,0503	0,0446	0,0410	0,0506	0,0770	0,0405	2,9651	1,9484	1,9506	1,9900	1,9128	1,9258	1,9451	1,9281	0,0112	0,0123	0,0034	0,0150	0,0082	0,0102	0,0160	0,0087
Na	0,9921	1,0043	0,9965	0,9970	0,9192	0,9672	0,9712	0,9546	0,9297	0,9364	0,9542	0,0000	0,0000	0,0000	0,0000	0,0000	0,0001	0,0201	0,0009	0,7202	0,7215	0,7325	0,7130	0,7180	0,7238	0,7265	0,7262
K	0,0033	0,0012	0,0026	0,0017	0,0000	0,0003	0,0009	0,0001	0,0004	0,0000	0,0005	0,0016	0,0052	0,0061	0,0000	0,0092	0,0030	0,0008	0,0000	0,0014	0,0009	0,0009	0,0008	0,0015	0,0006	0,0007	0,0022
Total	4,9973	5,0089	4,9990	4,9973	3,9662	4,0056	4,0087	3,9888	3,9787	3,9991	3,9929	2,9915	7,9981	7,9893	7,9984	7,9610	7,9765	7,9856	7,9783	5,3136	5,3053	5,3045	5,3006	5,3192	5,3159	5,3107	5,3009
X_{Ab}	0,9941	0,9974	0,9963	0,9969																							
X_{Or}	0,0033	0,0012	0,0026	0,0017																							
X_{An}	0,0027	0,0014	0,0011	0,0015																							
X_{Ps}													0,2783	0,2666	0,2658	0,2739	0,2735	0,2728	0,2873								
J_{ex}					1,838339	1,934359	1,942457	1,90924	1,859363	1,872829	1,908317																
Q_{ex}					0,0732	0,0704	0,0628	0,0700	0,0917	0,1157	0,0622																

																				55,22	55,75	55,89	55,8	55,89	55,79	56,01	55,95
P2O5																											
TiO2																				0,048	0,0274	0,1236	0,1121	0,0324	0	0,0234	0,0706
ZrO2																											
Al2O3																				8,67	8,59	8	7,93	7,65	7,5	7,93	8,64
Sc2O3																											
V2O3																											
Cr2O3																				0,0358	0,0377	0,0225	0,069	0,0258	0,0291	0,0011	0
MnO																				0,3691	0,3737	0,2874	0,3572	0,329	0,3402	0,3315	0,3453
Mn2O3																											
FeO																				20,85	20,65	20,03	21,08	20,82	21,6	21,14	19,81
Fe2O3																											
CoO																											
NiO																											
ZnO																											
BeO																											
MgO																				5,04	5,03	5,45	4,97	5,78	5,07	5,02	5,35
CaO																				0,2077	0,2278	0,0634	0,2771	0,1522	0,1885	0,2969	0,1626
SrO																											
Li2O																											
Na2O																				7,36	7,41	7,49	7,29	7,36	7,38	7,45	7,47
PbO																											
K2O																				0,0223	0,0143	0,0144	0,0129	0,0236	0,01	0,011	0,0342
H2O+																											
F																											
Cl																											

Group																				OH,F,Cl	OH,F,Cl	OH,F,Cl	OH,F,Cl	OH,F,Cl	OH,F,Cl	OH,F,Cl	OH,F,Cl
Subgroup of (OH,F,Cl)																				Na	Na	Na	Na	Na	Na	Na	Na
Species																				ferro-glau	ferro-glau	ferro-glau	ferro-glau	ferro-glau	ferro-glau	ferro-glau	ferro-glau
Formula																				(Na0,076K	(Na0,087K	(Na0,095K	(Na0,07K0	(Na0,056K	(Na0,083K	(Na0,113K	(Na0,093K
Formula Assignments																											
T (ideally 8 apfu)																											
Si																				7,909	7,963	8,024	8,004	7,962	8,008	8,017	7,991
P																											
Be																											
Al																				0,091	0,037			0,038			0,009
Ti																											
Fe3+																											
T subtotal																				8	8	8,024	8,004	8	8,008	8,017	8
C (ideally 5 apfu)																											
Ti																				0,005	0,003	0,013	0,012	0,003		0,003	0,008
Zr																											
Al																				1,372	1,41	1,354	1,341	1,246	1,269	1,338	1,445
Sc																											
V																											
Cr																				0,004	0,004	0,003	0,008	0,003	0,003		
Mn3+																											
Fe3+																				0,593	0,492	0,462	0,504	0,699	0,597	0,461	0,424
Co																											
Ni																											
Zn																											
Mn2+																				0,045	0,045	0,035	0,043	0,04	0,041	0,04	0,042
Fe2+																				1,905	1,975	1,943	2,025	1,782	1,996	2,069	1,942
Mg																				1,076	1,071	1,166	1,063	1,227	1,085	1,071	1,139
Li																											
C subtotal																				5	5	4,976	4,996	5	4,991	4,982	5
B (ideally 2 apfu)																											
Mn2+																											
Fe2+																											
Mg																											
Li																											
Ca																				0,032	0,035	0,01	0,043	0,023	0,029	0,046	0,025
Sr																											
Na																				1,968	1,965	1,99	1,957	1,977	1,971	1,954	1,975
B subtotal																				2	2	2	2	2	2	2	2
A (from 0 to 1 apfu)																											
Ca																											
Li																											
Na																				0,076	0,087	0,095	0,07	0,056	0,083	0,113	0,093
Pb																											
K																				0,004	0,003	0,003	0,002	0,004	0,002	0,002	0,006
A subtotal																				0,08	0,09	0,098	0,072	0,06	0,085	0,115	0,099
O (non-W)																				22	22	22	22	22	22	22	22
W (ideally 2 apfu)																											
OH																				2	2	2	2	2	2	2	2
F																											
Cl																											
O																											
W subtotal																				2	2	2	2	2	2	2	2

Sum T,C,B,A																				15,08	15,09	15,098	15,072	15,06	15,084	15,114	15,099
$Fe^{3+}/\Sigma Fe$																				0,23739	0,199433	0,1921	0,199288	0,281741	0,230235	0,182213	0,179205

Figure 229: Spots of chemical analysis and classification into minerals.

No.	69	70	76	78	84	86	12	26	14	23	73	74	77	79	85	88	90	21	81
Comment	460_b69	460_b70	460_b76	460_b78	460_b84	460_b86	460_b12	460_b26	460_b14	460_b23	460_b73	460_b74	460_b77	460_b79	460_b85	460_b88	460_b90	460_b21	460_b81
Sample #	460	460	460	460	460	460	460	460	460	460	460	460	460	460	460	460	460	460	460
Spot	b69	b70	b76	b78	b84	b86	b12	b26	b14	b23	b73	b74	b77	b79	b85	b88	b90	b21	b81
Mineral	Gln	Gln	Gln	Gln	Gln	Gln	Hm	Hm	Phe	Phe	Phe	Phe	Phe	Phe	Phe	Phe	Phe	Ttn	Ttn
Comment																			
SiO2	55,37	56,37	54,92	55,6	55,87	55,35	0,0504	0,0949	51,22	52,55	50,79	52,06	50,37	51,03	51,59	51,28	50,68	31,22	29,89
TiO2	0,072	0	0,0347	0,0591	0,0472	0,0823	0,7974	1,4786	0,0582	0,0746	0,0603	0,0135	0,1044	0,115	0,0463	0,0815	0,1217	36,29	38,4
Al2O3	7,79	8,87	8,29	8	7,59	8,15	0,0927	0,001	24,67	22,43	23,9	22,28	23,58	24,32	24,44	24,05	23,37	1,6381	2,69
Cr2O3	0,0151	0	0,0764	0,0345	0,0421	0,0765	0,0632	0,0004	0,0171	0,0059	0,0165	0,0719	0,0083	0,0586	0,0073	0,0095	0,0585	0	0,0301
Fe2O3							99,42115	98,53208										1,878177	1,130018
FeO	20,94	19,24	20,54	20,52	21,07	20,4	89,46	88,66	4,73	5,73	6,71	6,29	6,9	4,46	4,5	6,05	6,47	1,69	1,0168
MnO	0,3235	0,2858	0,3253	0,3516	0,2907	0,2919	0,0418	0,0095	0,0676	0,1415	0,0825	0,1894	0,0827	0,068	0,0643	0,085	0,1508	0,0782	0,0419
MgO	5,11	5,66	5,51	5,44	5,23	4,6	0,0335	0	3,13	3,17	2,63	2,94	2,58	3,11	3,18	2,63	2,97	0,0412	0
NiO																			
CaO	0,2487	0,1133	0,3846	0,1938	0,1297	0,6732	0,0956	0,007	0,0344	0	0,0214	0,063	0,0306	0,0253	0	0,084	0,0971	27,99	27,86
Na2O	7,08	7,25	7,13	7,28	7,28	8,39	0,0257	0,0525	0,0704	0,01	0,0756	0,0114	0,0854	0,1117	0,0821	0,0568	0,0148	0,1566	0
K2O	0,0675	0,0174	0,0306	0,0213	0	0,0081	0,0251	0,0113	10,61	11,11	11,07	10,75	10,94	11,09	10,97	10,82	10,65	0,0139	0
Total	97,0169	97,8065	97,2417	97,5004	97,5498	98,022	90,6854	90,3153	94,6077	95,2221	95,3564	94,6693	94,6815	94,3886	94,8801	95,1468	94,583	99,118	99,9289
Total							100,6466	100,1873										99,30618	100,042
moles																			
SiO2	0,921546	0,93819	0,914057	0,925374	0,929868	0,921213	0,000839	0,001579	0,852476	0,874612	0,845319	0,866457	0,838329	0,849314	0,858634	0,853475	0,843489	0,519608	0,497472
TiO2	0,000902	0	0,000434	0,00074	0,000591	0,00103	0,009984	0,018514	0,000729	0,000934	0,000755	0,000169	0,001307	0,00144	0,00058	0,00102	0,001524	0,454387	0,480807
Al2O3	0,076402	0,086994	0,081305	0,078461	0,07444	0,079932	0,000909	9,81E-06	0,241955	0,219985	0,234403	0,218514	0,231264	0,238522	0,239699	0,235874	0,229205	0,016066	0,026383
Cr2O3	9,93E-05	0	0,000503	0,000227	0,000277	0,000503	0,000416	2,63E-06	0,000113	3,88E-05	0,000109	0,000473	5,46E-05	0,000386	4,8E-05	6,25E-05	0,000385	0	0,000198
Fe2O3							0,622595	0,617028										0,011762	0,007076
FeO	0,291463	0,267801	0,285896	0,285617	0,293273	0,283947			0,065837	0,079756	0,093396	0,08755	0,096041	0,062079	0,062635	0,08421	0,090056		
MnO	0,00456	0,004029	0,004586	0,004956	0,004098	0,004115	0,000589	0,000134	0,000953	0,001995	0,001163	0,00267	0,001166	0,000959	0,000906	0,001198	0,002126	0,001102	0,000591
MgO	0,126784	0,14043	0,136708	0,134971	0,129761	0,11413	0,000831	0	0,077658	0,07865	0,065253	0,072944	0,064012	0,077162	0,078899	0,065253	0,073688	0,001022	0
NiO	0	0	0	0	0	0	0	0	0	0	0	0	0	0	0	0	0	0	0
CaO	0,004435	0,00202	0,006858	0,003456	0,002313	0,012005	0,001705	0,000125	0,000613	0	0,000382	0,001123	0,000546	0,000451	0	0,001498	0,001732	0,499132	0,496813
Na2O	0,114232	0,116975	0,115039	0,117459	0,117459	0,135369	0,000415	0,000847	0,001136	0,000161	0,00122	0,000184	0,001378	0,001802	0,001325	0,000916	0,000239	0,002527	0
K2O	0,000717	0,000185	0,000325	0,000226	0	8,6E-05	0,000266	0,00012	0,112637	0,117946	0,117521	0,114124	0,116141	0,117733	0,116459	0,114867	0,113062	0,000148	0
cations																			
Si	0,921546	0,93819	0,914057	0,925374	0,929868	0,921213	0,000839	0,001579	0,852476	0,874612	0,845319	0,866457	0,838329	0,849314	0,858634	0,853475	0,843489	0,519608	0,497472
Ti	0,000902	0	0,000434	0,00074	0,000591	0,00103	0,009984	0,018514	0,000729	0,000934	0,000755	0,000169	0,001307	0,00144	0,00058	0,00102	0,001524	0,454387	0,480807
Al	0,152803	0,173988	0,162611	0,156922	0,14888	0,159865	0,001818	1,96E-05	0,483909	0,439971	0,468805	0,437029	0,462529	0,477044	0,479398	0,471748	0,458409	0,032132	0,052765
Cr	0,000199	0	0,001005	0,000454	0,000554	0,001007	0,000832	5,26E-06	0,000225	7,76E-05	0,000217	0,000946	0,000109	0,000771	9,61E-05	0,000125	0,00077	0	0,000396
Fe^{3+}							1,245191	1,234056										0,023523	0,014153
Fe^{2+}	0,291463	0,267801	0,285896	0,285617	0,293273	0,283947	0	0	0,065837	0,079756	0,093396	0,08755	0,096041	0,062079	0,062635	0,08421	0,090056	0	0
Mn	0,00456	0,004029	0,004586	0,004956	0,004098	0,004115	0,000589	0,000134	0,000953	0,001995	0,001163	0,00267	0,001166	0,000959	0,000906	0,001198	0,002126	0,001102	0,000591
Mg	0,126784	0,14043	0,136708	0,134971	0,129761	0,11413	0,000831	0	0,077658	0,07865	0,065253	0,072944	0,064012	0,077162	0,078899	0,065253	0,073688	0,001022	0
Ni	0	0	0	0	0	0	0	0	0	0	0	0	0	0	0	0	0	0	0
Ca	0,004435	0,00202	0,006858	0,003456	0,002313	0,012005	0,001705	0,000125	0,000613	0	0,000382	0,001123	0,000546	0,000451	0	0,001498	0,001732	0,499132	0,496813
Na	0,228465	0,23395	0,230078	0,234919	0,234919	0,270737	0,000829	0,001694	0,002272	0,000323	0,00244	0,000368	0,002756	0,003604	0,002649	0,001833	0,000478	0,005053	0
K	0,001433	0,000369	0,00065	0,000452	0	0,000172	0,000533	0,00024	0,225275	0,235891	0,235042	0,228247	0,232282	0,235466	0,232919	0,229734	0,226124	0,000295	0
oxygens																			
SiO2	1,843092	1,876379	1,828113	1,850748	1,859736	1,842427	0,001678	0,003159	1,704952	1,749224	1,690639	1,732913	1,676658	1,698628	1,717268	1,706949	1,686977	1,039215	0,994944
TiO2	0,001803	0	0,000869	0,00148	0,001182	0,002061	0,019968	0,037027	0,001457	0,001868	0,00151	0,000338	0,002614	0,00288	0,001159	0,002041	0,003048	0,908774	0,961613
Al2O3	0,229205	0,260981	0,243916	0,235383	0,22332	0,239797	0,002728	2,94E-05	0,725864	0,659956	0,703208	0,655543	0,693793	0,715566	0,719097	0,707622	0,687614	0,048198	0,079148
Cr2O3	0,000298	0	0,001508	0,000681	0,000831	0,00151	0,001247	7,9E-06	0,000338	0,000116	0,000326	0,001419	0,000164	0,001157	0,000144	0,000188	0,001155	0	0,000594
Fe2O3							1,867786	1,851084										0,035285	0,021229
FeO	0,291463	0,267801	0,285896	0,285617	0,293273	0,283947	0	0	0,065837	0,079756	0,093396	0,08755	0,096041	0,062079	0,062635	0,08421	0,090056	0	0
MnO	0,00456	0,004029	0,004586	0,004956	0,004098	0,004115	0,000589	0,000134	0,000953	0,001995	0,001163	0,00267	0,001166	0,000959	0,000906	0,001198	0,002126	0,001102	0,000591
MgO	0,126784	0,14043	0,136708	0,134971	0,129761	0,11413	0,000831	0	0,077658	0,07865	0,065253	0,072944	0,064012	0,077162	0,078899	0,065253	0,073688	0,001022	0
NiO	0	0	0	0	0	0	0	0	0	0	0	0	0	0	0	0	0	0	0
CaO	0,004435	0,00202	0,006858	0,003456	0,002313	0,012005	0,001705	0,000125	0,000613	0	0,000382	0,001123	0,000546	0,000451	0	0,001498	0,001732	0,499132	0,496813
Na2O	0,114232	0,116975	0,115039	0,117459	0,117459	0,135369	0,000415	0,000847	0,001136	0,000161	0,00122	0,000184	0,001378	0,001802	0,001325	0,000916	0,000239	0,002527	0
K2O	0,000717	0,000185	0,000325	0,000226	0	8,6E-05	0,000266	0,00012	0,112637	0,117946	0,117521	0,114124	0,116141	0,117733	0,116459	0,114867	0,113062	0,000148	0
Total	2,616589	2,668801	2,623818	2,634979	2,631973	2,635446	1,897214	1,892533	2,691445	2,689672	2,674617	2,668809	2,652512	2,678415	2,697893	2,684741	2,659696	2,535402	2,554932
oxygens	8	8	8	8	8	8	3	3	11	11	11	11	11	11	11	11	11	5	5
cations																			
Si	2,8175	2,8123	2,7870	2,8095	2,8264	2,7964	0,0013	0,0025	3,4841	3,5769	3,4766	3,5713	3,4766	3,4881	3,5009	3,4969	3,4885	1,0247	0,9736
Ti	0,0028	0,0000	0,0013	0,0022	0,0018	0,0031	0,0158	0,0293	0,0030	0,0038	0,0031	0,0007	0,0054	0,0059	0,0024	0,0042	0,0063	0,8961	0,9409
Al	0,4672	0,5215	0,4958	0,4764	0,4525	0,4853	0,0029	0,0000	1,9777	1,7994	1,9281	1,8013	1,9181	1,9592	1,9546	1,9329	1,8959	0,0634	0,1033
Cr	0,0006	0,0000	0,0031	0,0014	0,0017	0,0031	0,0013	0,0000	0,0009	0,0003	0,0009	0,0039	0,0005	0,0032	0,0004	0,0005	0,0032	0,0000	0,0008
Fe^{3+}							1,9690	1,9562										0,0464	0,0277
Fe^{2+}	0,8911	0,8028	0,8717	0,8672	0,8914	0,8619	0,0000	0,0000	0,2691	0,3262	0,3841	0,3609	0,3983	0,2550	0,2554	0,3450	0,3725	0,0000	0,0000
Mn	0,0139	0,0121	0,0140	0,0150	0,0125	0,0125	0,0009	0,0002	0,0039	0,0082	0,0048	0,0110	0,0048	0,0039	0,0037	0,0049	0,0088	0,0022	0,0012
Mg	0,3876	0,4210	0,4168	0,4098	0,3944	0,3464	0,0013	0,0000	0,3174	0,3217	0,2684	0,3007	0,2655	0,3169	0,3217	0,2674	0,3048	0,0020	0,0000
Ni	0,0000	0,0000	0,0000	0,0000	0,0000	0,0000	0,0000	0,0000	0,0000	0,0000	0,0000	0,0000	0,0000	0,0000	0,0000	0,0000	0,0000	0,0000	0,0000
Ca	0,0136	0,0061	0,0209	0,0105	0,0070	0,0364	0,0027	0,0002	0,0025	0,0000	0,0016	0,0046	0,0023	0,0019	0,0000	0,0061	0,0072	0,9843	0,9723
Na	0,6985	0,7013	0,7015	0,7132	0,7140	0,8218	0,0013	0,0027	0,0093	0,0013	0,0100	0,0015	0,0114	0,0148	0,0108	0,0075	0,0020	0,0100	0,0000
K	0,0044	0,0011	0,0020	0,0014	0,0000	0,0005	0,0008	0,0004	0,9207	0,9647	0,9667	0,9408	0,9633	0,9670	0,9497	0,9413	0,9352	0,0006	0,0000
Total	5,2972	5,2781	5,3140	5,3066	5,3017	5,3675	1,9974	1,9916	6,9886	7,0025	7,0442	6,9966	7,0461	7,0158	6,9995	7,0066	7,0242	3,0296	3,0196

Figure 230: Spots of chemical analysis and classification into minerals.

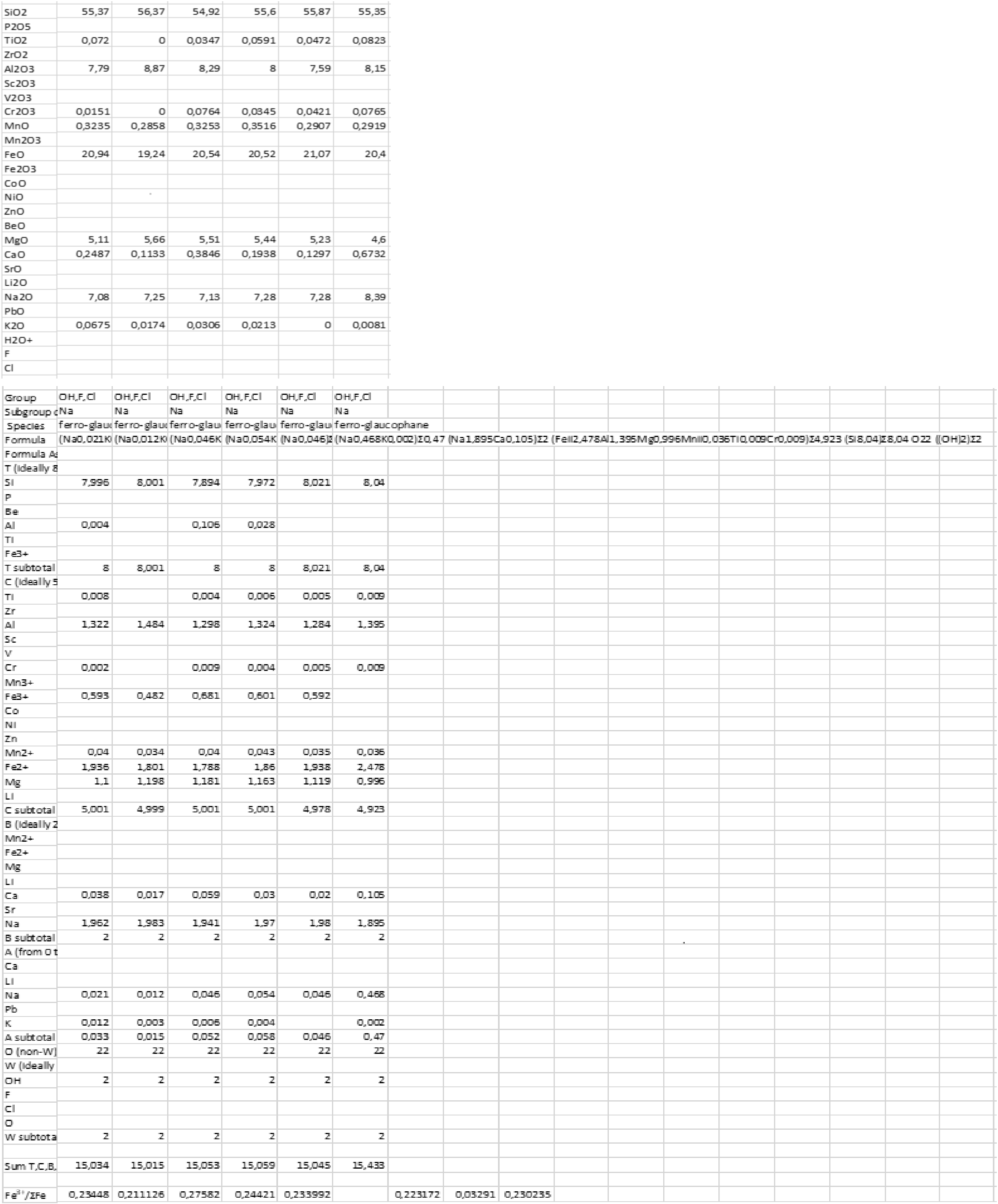

SiO2	55,37	56,37	54,92	55,6	55,87	55,35
P2O5						
TiO2	0,072	0	0,0347	0,0591	0,0472	0,0823
ZrO2						
Al2O3	7,79	8,87	8,29	8	7,59	8,15
Sc2O3						
V2O3						
Cr2O3	0,0151	0	0,0764	0,0345	0,0421	0,0765
MnO	0,3235	0,2858	0,3253	0,3516	0,2907	0,2919
Mn2O3						
FeO	20,94	19,24	20,54	20,52	21,07	20,4
Fe2O3						
CoO						
NiO						
ZnO						
BeO						
MgO	5,11	5,66	5,51	5,44	5,23	4,6
CaO	0,2487	0,1133	0,3846	0,1938	0,1297	0,6732
SrO						
Li2O						
Na2O	7,08	7,25	7,13	7,28	7,28	8,39
PbO						
K2O	0,0675	0,0174	0,0306	0,0213	0	0,0081
H2O+						
F						
Cl						

Group	OH,F,Cl	OH,F,Cl	OH,F,Cl	OH,F,Cl	OH,F,Cl	OH,F,Cl			
Subgroup c	Na	Na	Na	Na	Na	Na			
Species	ferro-glau	ferro-glau	ferro-glau	ferro-glau	ferro-glau	ferro-glaucophane			
Formula	(Na0,021K	(Na0,012K	(Na0,046K	(Na0,054K	(Na0,046)Σ	(Na0,468K0,002)Σ0,47 (Na1,895Ca0,105)Σ2 (FeII2,478Al1,395Mg0,996MnII0,036Ti0,009Cr0,009)Σ4,923 (Si8,04)Σ8,04 O22 ((OH)2)Σ2			
Formula As									
T (ideally 8									
Si	7,996	8,001	7,894	7,972	8,021	8,04			
P									
Be									
Al	0,004		0,106	0,028					
Ti									
Fe3+									
T subtotal	8	8,001	8	8	8,021	8,04			
C (ideally 5									
Ti	0,008		0,004	0,006	0,005	0,009			
Zr									
Al	1,322	1,484	1,298	1,324	1,284	1,395			
Sc									
V									
Cr	0,002		0,009	0,004	0,005	0,009			
Mn3+									
Fe3+	0,593	0,482	0,681	0,601	0,592				
Co									
Ni									
Zn									
Mn2+	0,04	0,034	0,04	0,043	0,035	0,036			
Fe2+	1,936	1,801	1,788	1,86	1,938	2,478			
Mg	1,1	1,198	1,181	1,163	1,119	0,996			
Li									
C subtotal	5,001	4,999	5,001	5,001	4,978	4,923			
B (ideally 2									
Mn2+									
Fe2+									
Mg									
Li									
Ca	0,038	0,017	0,059	0,03	0,02	0,105			
Sr									
Na	1,962	1,983	1,941	1,97	1,98	1,895			
B subtotal	2	2	2	2	2	2			
A (from 0 t									
Ca									
Li									
Na	0,021	0,012	0,046	0,054	0,046	0,468			
Pb									
K	0,012	0,003	0,006	0,004		0,002			
A subtotal	0,033	0,015	0,052	0,058	0,046	0,47			
O (non-W)	22	22	22	22	22	22			
W (ideally									
OH	2	2	2	2	2	2			
F									
Cl									
O									
W subtota	2	2	2	2	2	2			
Sum T,C,B,	15,034	15,015	15,053	15,059	15,045	15,433			
Fe^{3+}/ΣFe	0,23448	0,211126	0,27582	0,24421	0,233992		0,223172	0,03291	0,230235

Figure 231: Spots of chemical analysis and classification into minerals.

No.	1	2	3	4	5	6	7	8	9	10	11	92	93	94
Comment	461_b1	461_b2	461_b3	461_b4	461_b5	461_b6	461_b7	461_b8	461_b9	461_b10	461_b11	461_b92	461_b93	461_b94
Sample #	461	461	461	461	461	461	461	461	461	461	461	461	461	461
Spot	b1	b2	b3	b4	b5	b6	b7	b8	b9	b10	b11	b92	b93	b94
Mineral	Ttn	Phe	Ab	Phe	Kfs	Ttn	Ttn	Kfs	Phe	Ttn	Phe	Phe	Phe	Ab
Comment														
SiO2	30,86	52,02	68,82	52,14	65,09	30,48	30,85	65,01	52,11	30,76	51.99	52,4	49,06	69,01
TiO2	39,36	0,3075	0	0,4647	0	38,58	38,89	0,2003	0,7191	39,02	0,5749	0,2761	0,4899	0
Al2O3	0,8294	23,55	19,17	22,47	18,15	0,9242	0,9502	18,02	23,04	0,7477	21.76	23,36	22,62	19,12
Cr2O3	0,0143	0,0196	0,0082	0	0	0,0154	0,02	0	0,0428	0,0466	0,0173	0,0256	0,0247	0,0456
Fe2O3			0,041787		0,135029			0,002556						0,041564
FeO	0,0836	5,08	0,0376	5,65	0,1215	0,0815	0,062	0,0023	5,31	0,0736	6.98	5,23	5,74	0,0374
MnO	0	0,0885	0	0,0921	0,0168	0	0,0169	0,0074	0,1121	0,0214	0,0517	0,0698	0,1296	0,0561
MgO	0	2,46	0	2,67	0	0	0	0	2,5	0	2.64	2,71	2,47	0
NiO														
CaO	27,57	0	0,0057	0	0	26,41	27,03	0,0475	0,0595	27,77	0,0053	0	0,0358	0
Na2O	0,3246	0	11,91	0,0328	0,3305	0,6788	0,3944	0,2545	0,0407	0,3636	0,0526	0,0407	0,0643	11,88
K2O	0,1308	11,48	0,0581	11,27	16,56	0,22	0,1991	16,57	11,07	0,1762	11.25	11,3	10,87	0,0496
Total	99,1728	95,0057	100,0095	94,7896	100,2687	97,39	98,4127	100,1119	95,0043	98,9792	95,3619	95,4123	91,5044	100,1986
Total														

moles												
SiO2	0,865791	1,1454	0,867788	1,08332			1,081989	0,867289		0,865291	0,872115	0,816526	1,148563
TiO2	0,00385	0	0,005819	0			0,002508	0,009004		0,007198	0,003457	0,006134	0
Al2O3	0,23097	0,188013	0,220378	0,178009			0,176734	0,225968		0,213414	0,229107	0,221849	0,187522
Cr2O3	0,000129	5,4E-05	0	0			0	0,000282		0,000114	0,000168	0,000163	0,0003
Fe2O3		0,000262		0,000846			1,6E-05						0,00026
FeO	0,070708		0,078642					0,07391		0,097154	0,072796	0,079895	
MnO	0,001248	0	0,001298	0,000237			0,000104	0,00158		0,001293	0,000984	0,001827	0,000791
MgO	0,061035	0	0,066245	0			0	0,062027		0,065501	0,067237	0,061283	0
NiO	0	0	0	0			0	0		0	0	0	0
CaO	0	0,000102	0	0			0,000847	0,001061		9,45E-05	0	0,000638	0
Na2O	0	0,192162	0,000529	0,005332			0,004106	0,000657		0,000849	0,000657	0,001037	0,191678
K2O	0,121874	0,000617	0,119644	0,175804			0,17591	0,117521		0,119432	0,119963	0,115398	0,000527

cations												
Si	0,865791	1,1454	0,867788	1,08332			1,081989	0,867289		0,865291	0,872115	0,816526	1,148563
Ti	0,00385	0	0,005819	0			0,002508	0,009004		0,007198	0,003457	0,006134	0
Al	0,46194	0,376025	0,440756	0,356018			0,353468	0,451936		0,426829	0,458213	0,443698	0,375044
Cr	0,000258	0,000108	0	0			0	0,000563		0,000228	0,000337	0,000325	0,0006
Fe^{3+}		0,000523		0,001691			3,2E-05						0,000521
Fe^{2+}	0,070708	0	0,078642	0			0	0,07391		0,097154	0,072796	0,079895	0
Mn	0,001248	0	0,001298	0,000237			0,000104	0,00158		0,001293	0,000984	0,001827	0,000791
Mg	0,061035	0	0,066245	0			0	0,062027		0,065501	0,067237	0,061283	0
Ni	0	0	0	0			0	0		0	0	0	0
Ca	0	0,000102	0	0			0,000847	0,001061		9,45E-05	0	0,000638	0
Na	0	0,384324	0,001058	0,010665			0,008212	0,001313		0,001697	0,001313	0,002075	0,383356
K	0,243747	0,001234	0,239288	0,351607			0,35182	0,235042		0,238864	0,239925	0,230795	0,001053

oxygens												
SiO2	1,731582	2,290801	1,735576	2,166641			2,163978	1,734577		1,730583	1,744231	1,633053	2,297125
TiO2	0,0077	0	0,011637	0			0,005016	0,018008		0,014397	0,006914	0,012268	0
Al2O3	0,69291	0,564038	0,661133	0,534026			0,530201	0,677904		0,640243	0,68732	0,665547	0,562567
Cr2O3	0,000387	0,000162	0	0			0	0,000845		0,000341	0,000505	0,000488	0,0009
Fe2O3		0,000785		0,002537			4,8E-05						0,000781
FeO	0,070708	0	0,078642	0			0	0,07391		0,097154	0,072796	0,079895	0
MnO	0,001248	0	0,001298	0,000237			0,000104	0,00158		0,001293	0,000984	0,001827	0,000791
MgO	0,061035	0	0,066245	0			0	0,062027		0,065501	0,067237	0,061283	0
NiO	0	0	0	0			0	0		0	0	0	0
CaO	0	0,000102	0	0			0,000847	0,001061		9,45E-05	0	0,000638	0
Na2O	0	0,192162	0,000529	0,005332			0,004106	0,000657		0,000849	0,000657	0,001037	0,191678
K2O	0,121874	0,000617	0,119644	0,175804			0,17591	0,117521		0,119432	0,119963	0,115398	0,000527
Total	2,687443	3,048666	2,674705	2,884577			2,88021	2,68809		2,669887	2,700607	2,571433	3,054368

oxygens	11	8	11	8			8	11		11	11	11	8
cations													
Si	3,5438	3,0056	3,5689	3,0044			3,0053	3,5491		3,5650	3,5523	3,4929	3,0083
Ti	0,0158	0,0000	0,0239	0,0000			0,0070	0,0368		0,0297	0,0141	0,0262	0,0000
Al	1,8908	0,9867	1,8127	0,9874			0,9818	1,8494		1,7585	1,8664	1,8980	0,9823
Cr	0,0011	0,0003	0,0000	0,0000			0,0000	0,0023		0,0009	0,0014	0,0014	0,0016
Fe^{3+}		0,0014		0,0047			0,0001						0,0014
Fe^{2+}	0,2894	0,0000	0,3234	0,0000			0,0000	0,3024		0,4003	0,2965	0,3418	0,0000
Mn	0,0051	0,0000	0,0053	0,0007			0,0003	0,0065		0,0053	0,0040	0,0078	0,0021
Mg	0,2498	0,0000	0,2724	0,0000			0,0000	0,2538		0,2699	0,2739	0,2622	0,0000
Ni	0,0000	0,0000	0,0000	0,0000			0,0000	0,0000		0,0000	0,0000	0,0000	0,0000
Ca	0,0000	0,0003	0,0000	0,0000			0,0024	0,0043		0,0004	0,0000	0,0027	0,0000
Na	0,0000	1,0085	0,0044	0,0296			0,0228	0,0054		0,0070	0,0053	0,0089	1,0041
K	0,9977	0,0032	0,9841	0,9751			0,9772	0,9618		0,9841	0,9773	0,9873	0,0028
Total	6,9934	5,0060	6,9951	5,0019			4,9968	6,9719		7,0211	6,9911	7,0292	5,0025

X_{Ab}	0,9965		0,0294				0,0228				0,9973
X_{Or}	0,0032		0,9706				0,9749				0,0027
X_{An}	0,0003		0,0000				0,0023				0,0000
X_{Fs}											
J_{px}											
Q_{px}											

Figure 232: Spots of chemical analysis and classification into minerals.

No.	95	96	97	98	99	100	101	102	103	104	105	106	107	
Comment	461_b95	461_b96	461_b97	461_b98	461_b99	461_b100	461_b101	461_b102	461_b103	461_b104	461_b105	461_b106	461_b107_unfocused	
Sample #	461	461	461	461	461	461	461	461	461	461	461	461	461	
Spot	b95	b96	b97	b98	b99	b100	b101	b102	b103	b104	b105	b106	b107	
Mineral	Kfs	Kfs	Phe	Phe	Phe	Kfs	Ab	Kfs	Phe	Ab	Kfs	Phe	Hm in Cal?	Cal-Sd?
Comment													defocused_beam_ca_	
SiO2	65,35	64,95	51,61	52,1	52,26	64,98	68,99	64,95	51,55	68,01	64,68	52,01	3,39	
TiO2	0,012	0	0,2764	0,1951	0,7099	0,0225	0,0131	0	0,5308	0	0,0195	0,341	0	
Al2O3	18,13	17,95	24,01	23,53	22,34	18,2	19,06	18,19	23,05	19,34	17,86	22,82	0,4686	
Cr2O3	0	0,077	0,0599	0	0,0097	0,0336	0,0192	0	0,0141	0	0,0626	0	0	
Fe2O3	0,005334	0,072904				0,089241	0,032007	0,059457		0,054011	0,038341			
FeO	0,0048	0,0656	5,02	5,39	5,63	0,0803	0,0288	0,0535	5,39	0,0486	0,0345	5,34	33,01	
MnO	0,0146	0,0094	0,0979	0,0606	0,0732	0,0128	0	0,0345	0,1171	0	0,0055	0,1348	0,2481	
MgO	0	0,0205	2,51	2,61	2,61	0,0009	0	0,021	2,53	0	0,023	2,59	0,8839	
NiO														
CaO	0	0	0,0165	0	0,0185	0	0,0077	0	0,1486	0,0109	0	0,0041	26,37	
Na2O	0,2551	0,221	0	0	0	0,3499	11,59	0,2766	0,0294	12,02	0,2992	0,0082	0	
K2O	16,43	16,58	11,25	11,37	11,23	16,4	0,049	16,47	9,68	0,0731	16,3	11,22	0	
Total	100,1964	99,8736	94,8508	95,2558	94,8813	100,08	99,7579	99,9957	93,0401	99,5027	99,2844	94,4682	64,3707	
Total														
moles														
SiO2	1,087648	1,08099	0,858967	0,867122	0,869785	1,08149	1,14823	1,08099	0,857968	1,131919	1,076496	0,865624		
TiO2	0,00015	0	0,003461	0,002443	0,008889	0,000282	0,000164	0	0,006646	0	0,000244	0,00427		
Al2O3	0,177813	0,176047	0,235482	0,230774	0,219103	0,178499	0,186934	0,178401	0,226066	0,18968	0,175165	0,22381		
Cr2O3	0	0,000507	0,000394	0	6,38E-05	0,000221	0,000126	0	9,28E-05	0	0,000412	0		
Fe2O3	3,34E-05	0,000457				0,000559	0,0002	0,000372		0,000338	0,00024			
FeO			0,069873	0,075023	0,078364				0,075023			0,074327		
MnO	0,000206	0,000133	0,00138	0,000854	0,001032	0,00018	0	0,000486	0,001651	0	7,75E-05	0,0019		
MgO	0	0,000509	0,062275	0,064756	0,064756	2,23E-05	0	0,000521	0,062772	0	0,000571	0,06426		
NiO	0	0	0	0	0	0	0	0	0	0	0	0		
CaO	0	0	0,000294	0	0,00033	0	0,000137	0	0,00265	0,000194	0	7,31E-05		
Na2O	0,004116	0,003566	0	0	0	0,005645	0,186999	0,004463	0,000474	0,193937	0,004827	0,000132		
K2O	0,174424	0,176016	0,119432	0,120706	0,119219	0,174105	0,00052	0,174848	0,102764	0,000776	0,173043	0,119113		
cations														
Si	1,087648	1,08099	0,858967	0,867122	0,869785	1,08149	1,14823	1,08099	0,857968	1,131919	1,076496	0,865624		
Ti	0,00015	0	0,003461	0,002443	0,008889	0,000282	0,000164	0	0,006646	0	0,000244	0,00427		
Al	0,355625	0,352094	0,470963	0,461548	0,438206	0,356998	0,373867	0,356802	0,452132	0,37936	0,350329	0,447621		
Cr	0	0,001013	0,000788	0	0,000128	0,000442	0,000253	0	0,000186	0	0,000824	0		
Fe^{3+}	6,68E-05	0,000913				0,001118	0,000401	0,000745		0,000676	0,00048			
Fe^{2+}	0	0	0,069873	0,075023	0,078364	0	0	0	0,075023	0	0	0,074327		
Mn	0,000206	0,000133	0,00138	0,000854	0,001032	0,00018	0	0,000486	0,001651	0	7,75E-05	0,0019		
Mg	0	0,000509	0,062275	0,064756	0,064756	2,23E-05	0	0,000521	0,062772	0	0,000571	0,06426		
Ni	0	0	0	0	0	0	0	0	0	0	0	0		
Ca	0	0	0,000294	0	0,00033	0	0,000137	0	0,00265	0,000194	0	7,31E-05		
Na	0,008232	0,007131	0	0	0	0,011291	0,373998	0,008926	0,000949	0,387874	0,009655	0,000265		
K	0,348847	0,352032	0,238864	0,241412	0,238439	0,34821	0,00104	0,349696	0,205529	0,001552	0,346087	0,238227		

Figure 233: Spots of chemical analysis and classification into minerals.

No.	95	96	97	98	99	100	101	102	103	104	105	106	107	
Comment	461_b95	461_b96	461_b97	461_b98	461_b99	461_b100	461_b101	461_b102	461_b103	461_b104	461_b105	461_b106	461_b107_unfocused	
Sample #	461	461	461	461	461	461	461	461	461	461	461	461	461	
Spot	b95	b96	b97	b98	b99	b100	b101	b102	b103	b104	b105	b106	b107	
Mineral	Kfs	Kfs	Phe	Phe	Phe	Kfs	Ab	Kfs	Phe	Ab	Kfs	Phe	Hm in Cal?	Cal-Sd?
Comment													defocused_beam_ca_	
oxygens														
SiO2	2,175295	2,16198	1,717934	1,734245	1,73957	2,162979	2,296459	2,16198	1,715937	2,263838	2,152993	1,731249		
TiO2	0,000301	0	0,006922	0,004886	0,017777	0,000563	0,000328	0	0,013292	0	0,000488	0,008539		
Al2O3	0,533438	0,528142	0,706445	0,692322	0,657308	0,535497	0,560801	0,535203	0,678199	0,56904	0,525494	0,671431		
Cr2O3	0	0,00152	0,001182	0	0,000191	0,000663	0,000379	0	0,000278	0	0,001236	0		
Fe2O3	0,0001	0,00137				0,001677	0,000601	0,001117		0,001015	0,00072			
FeO	0	0	0,069873	0,075023	0,078364	0	0	0	0,075023	0	0	0,074327		
MnO	0,000206	0,000133	0,00138	0,000854	0,001032	0,00018	0	0,000486	0,001651	0	7,75E-05	0,0019		
MgO	0	0,000509	0,062275	0,064756	0,064756	2,23E-05	0	0,000521	0,062772	0	0,000571	0,06426		
NiO	0	0	0	0	0	0	0	0	0	0	0	0		
CaO	0	0	0,000294	0	0,00033	0	0,000137	0	0,00265	0,000194	0	7,31E-05		
Na2O	0,004116	0,003566	0	0	0	0,005645	0,186999	0,004463	0,000474	0,193937	0,004827	0,000132		
K2O	0,174424	0,176016	0,119432	0,120706	0,119219	0,174105	0,00052	0,174848	0,102764	0,000776	0,173043	0,119113		
Total	2,887879	2,873234	2,685737	2,692792	2,678549	2,881333	3,046225	2,878619	2,65304	3,0288	2,85945	2,671026		
oxygens	8	8	11	11	11	8	8	8	11	8	8	11		
cations														
Si	3,0130	3,0098	3,5181	3,5422	3,5719	3,0027	3,0155	3,0042	3,5573	2,9897	3,0118	3,5649		
Ti	0,0004	0,0000	0,0142	0,0100	0,0365	0,0008	0,0004	0,0000	0,0276	0,0000	0,0007	0,0176		
Al	0,9852	0,9803	1,9289	1,8854	1,7996	0,9912	0,9819	0,9916	1,8746	1,0020	0,9801	1,8434		
Cr	0,0000	0,0028	0,0032	0,0000	0,0005	0,0012	0,0007	0,0000	0,0008	0,0000	0,0023	0,0000		
Fe^{3+}	0,0002	0,0025				0,0031	0,0011	0,0021		0,0018	0,0013			
Fe^{2+}	0,0000	0,0000	0,2862	0,3065	0,3218	0,0000	0,0000	0,0000	0,3111	0,0000	0,0000	0,3061		
Mn	0,0006	0,0004	0,0057	0,0035	0,0042	0,0005	0,0000	0,0014	0,0068	0,0000	0,0002	0,0078		
Mg	0,0000	0,0014	0,2551	0,2645	0,2659	0,0001	0,0000	0,0014	0,2603	0,0000	0,0016	0,2646		
Ni	0,0000	0,0000	0,0000	0,0000	0,0000	0,0000	0,0000	0,0000	0,0000	0,0000	0,0000	0,0000		
Ca	0,0000	0,0000	0,0012	0,0000	0,0014	0,0000	0,0004	0,0000	0,0110	0,0005	0,0000	0,0003		
Na	0,0228	0,0199	0,0000	0,0000	0,0000	0,0313	0,9822	0,0248	0,0039	1,0245	0,0270	0,0011		
K	0,9664	0,9802	0,9783	0,9862	0,9792	0,9668	0,0027	0,9718	0,8522	0,0041	0,9683	0,9811		
Total	4,9885	4,9973	6,9908	6,9982	6,9811	4,9978	4,9848	4,9973	6,9055	5,0227	4,9933	6,9869		
X_{Ab}	0,0231	0,0199				0,0314	0,9969	0,0249		0,9955	0,0271			
X_{Or}	0,9769	0,9801				0,9686	0,0028	0,9751		0,0040	0,9729			
X_{An}	0,0000	0,0000				0,0000	0,0004	0,0000		0,0005	0,0000			
X_{Ps}														
J_{px}														
Q_{px}														

Figure 234: Spots of chemical analysis and classification into minerals.

No.	34	35	36	37	38	39	40	41	42	43	44	45	46	47	48	49	50	51	52	53	54	55
Comment	464_b34	464_b35	464_b36	464_b37	464_b38	464_b39	464_b40	464_b41	464_b42	464_b43	464_b44	464_b45	464_b46	464_b47	464_b48	464_b49	464_b50	464_b51	464_b52	464_b53	464_b54	464_b55
Sample #	464	464	464	464	464	464	464	464	464	464	464	464	464	464	464	464	464	464	464	464	464	464
Spot	b34	b35	b36	b37	b38	b39	b40	b41	b42	b43	b44	b45	b46	b47	b48	b49	b50	b51	b52	b53	b54	b55
Mineral	Ab	Kfs	Aeg	Phe	Rt	Hm	Aeg	Aeg	Aeg	Phe	Kfs	Phe	Rt	Aeg	Aeg	Rds-Sd?	Hm	Bt	Bt	Phe	Kfs	Ab
Commen_mn																						
SiO2	69,26	65,35	53,95	52,96	0,1112	0,0787	53,55	54,96	54,52	54,02	65,27	52,59	0,1367	53,5	54,16	0,7131	0,096	41,1	41,63	53,73	64,86	67,8
TiO2	0,0114	0,017	0,2484	0,7276	98,5	2,56	0,0682	0,9204	0,9631	0,6283	0,052	0,8443	98,95	1,0427	0,7825	0,083	0,1015	0,1086	0,1233	0,3268	0,004	0
Al2O3	19,21	18,34	3,76	22,8	0,136	0,0321	3,67	7,43	5,54	21,77	18,05	22,69	0,0526	2,03	7,08	0,2474	0,0406	11,18	11,07	21,6	17,93	19,02
Cr2O3	0,0283	0	0,0918	0,0656	0,0631	0,0495	0,0105	0,0556	0,0419	0,0484	0	0,0052	0,0683	0,0448	0,0567	0,0956	0,0852	0	0,0244	0,0251	0,015	0
Fe2O3	0,049455	0,016892	28,60609				29,42848	23,49389	26,58343		0,141919			30,91769	24,38297						0,018337	0,039675
FeO	0,0445	0,0152	25,74	3,63	1,158	87,37	26,48	21,14	23,92	3,53	0,1277	3,58	0,9945	27,82	21,94	11,74	90,6	13,92	13,6	3,88	0,0165	0,0357
MnO	0,0346	0,0269	0	0,0039	0,0161	0,0488	0,0078	0,0219	0,0378	0,0061	0	0,0495	0,0188	0	0	48,89	0,0325	0,2503	0,2306	0,167	0	0,0079
MgO	0,0051	0	0,1597	4,22	0,0334	0,0337	0,2102	0,0803	0,1318	4,76	0	3,97	0	0,0339	0,0776	1,1642	0	17,83	18,04	4,6	0	0,0001
NiO																						
CaO	0	0	0,2765	0	0,0198	0	0,3189	0,0487	0,2529	0	0	0	0,0162	0,0107	0,0188	2,82	0,0273	0,1708	0,2436	0	0	0,0541
Na2O	11,69	0,2383	14,3	0	0	0,0411	14,01	14,13	14,57	0,0183	0,2923	0,037	0	14,19	14,34	0,2777	0	0,0323	0,0632	0	0,2364	11,24
K2O	0,0717	16,74	0,1596	11,48	0,1745	0,1595	0,0234	0,0263	0	11,45	16,6	11,4	0,1389	0,0586	0,0574	0,1315	0,0275	9,38	8,22	11,23	16,52	0,0894
Total	100,3555	100,7273	98,686	95,8871	100,212	90,3734	98,349	98,8132	99,9775	96,2312	100,3919	95,1661	100,3759	98,7308	98,5131	66,1626	91,0107	93,972	93,2451	95,5589	99,5819	98,2473
Total																						
moles																						
SiO2	1,152723	1,087648	0,897913	0,881436			0,891255	0,914722	0,907399	0,899078	1,086316	0,875278		0,890423	0,901408					0,894251	1,079492	1,128424
TiO2	0,000143	0,000213	0,00311	0,00911			0,000854	0,011524	0,012059	0,007867	0,000651	0,010571		0,013056	0,009798					0,004092	5,01E-05	0
Al2O3	0,188405	0,179872	0,036877	0,223614			0,035994	0,072871	0,054334	0,213512	0,177028	0,222535		0,01991	0,069438					0,211845	0,175851	0,186541
Cr2O3	0,000186	0	0,000604	0,000432			6,91E-05	0,000366	0,000276	0,000318	0	3,42E-05		0,000295	0,000373					0,000165	9,87E-05	0
Fe2O3	0,00031	0,000106	0,179137				0,184287	0,147124	0,166471		0,000889			0,193613	0,152691						0,000115	0,000248
FeO				0,050526						0,049134		0,04983								0,054006		
MnO	0,000488	0,000379	0	5,5E-05			0,00011	0,000309	0,000533	8,6E-05	0	0,000698		0	0					0,002354	0	0,000111
MgO	0,000127	0	0,003962	0,104702			0,005215	0,001992	0,00327	0,1181	0	0,098499		0,000841	0,001925					0,11413	0	2,48E-06
NiO	0	0	0	0			0	0	0	0	0	0		0	0					0	0	0
CaO	0	0	0,004931	0			0,005687	0,000868	0,00451	0	0	0		0,000191	0,000335					0	0	0,000965
Na2O	0,188612	0,003845	0,230724	0			0,226045	0,227981	0,23508	0,000295	0,004716	0,000597		0,228949	0,231369					0	0,003814	0,181352
K2O	0,000761	0,177715	0,001694	0,121874			0,002248	0,002279	0	0,121555	0,176228	0,121024		0,000622	0,000609					0,119219	0,175379	0,000949
cations																						
Si	1,152723	1,087648	0,897913	0,881436			0,891255	0,914722	0,907399	0,899078	1,086316	0,875278		0,890423	0,901408					0,894251	1,079492	1,128424
Ti	0,000143	0,000213	0,00311	0,00911			0,000854	0,011524	0,012059	0,007867	0,000651	0,010571		0,013056	0,009798					0,004092	5,01E-05	0
Al	0,37681	0,359744	0,073753	0,447229			0,071988	0,145742	0,108669	0,427025	0,354056	0,445071		0,039819	0,138876					0,42369	0,351702	0,373083
Cr	0,000372	0	0,001208	0,000863			0,000138	0,000732	0,000551	0,000637	0	6,84E-05		0,00059	0,000746					0,00033	0,000197	0
Fe^{3+}	0,000619	0,000212	0,358274				0,368574	0,294247	0,332942		0,001777			0,387226	0,305382						0,00023	0,000497
Fe^{2+}	0	0	0	0,050526			0	0	0	0,049134	0	0,04983		0	0					0,054006	0	0
Mn	0,000488	0,000379	0	5,5E-05			0,00011	0,000309	0,000533	8,6E-05	0	0,000698		0	0					0,002354	0	0,000111
Mg	0,000127	0	0,003962	0,104702			0,005215	0,001992	0,00327	0,1181	0	0,098499		0,000841	0,001925					0,11413	0	2,48E-06
Ni	0	0	0	0			0	0	0	0	0	0		0	0					0	0	0
Ca	0	0	0,004931	0			0,005687	0,000868	0,00451	0	0	0		0,000191	0,000335					0	0	0,000965
Na	0,377225	0,00769	0,461447	0			0,452089	0,455961	0,47016	0,000591	0,009432	0,001194		0,457897	0,462738					0	0,007628	0,362704
K	0,001522	0,355429	0,003389	0,243747			0,000497	0,000558	0	0,24311	0,352457	0,242048		0,001244	0,001219					0,238439	0,350758	0,001898
oxygens																						
SiO2	2,305447	2,175295	1,795825	1,762871			1,78251	1,829445	1,814799	1,798155	2,172632	1,750555		1,780846	1,802815					1,788502	2,158985	2,256848
TiO2	0,000285	0,000426	0,00622	0,018221			0,001708	0,023049	0,024118	0,015734	0,001302	0,021143		0,026111	0,019595					0,008184	0,0001	0
Al2O3	0,565215	0,539617	0,11063	0,670843			0,107982	0,218612	0,163003	0,640537	0,531084	0,667606		0,059729	0,208314					0,635535	0,527553	0,559624
Cr2O3	0,000559	0	0,001812	0,001295			0,000207	0,001097	0,000827	0,000955	0	0,000103		0,000884	0,001119					0,000495	0,000296	0
Fe2O3	0,000929	0,000317	0,537411				0,552861	0,441371	0,499413		0,002666			0,580839	0,458073						0,000344	0,000745
FeO	0	0	0	0,050526			0	0	0	0,049134	0	0,04983		0	0					0,054006	0	0
MnO	0,000488	0,000379	0	5,5E-05			0,00011	0,000309	0,000533	8,6E-05	0	0,000698		0	0					0,002354	0	0,000111
MgO	0,000127	0	0,003962	0,104702			0,005215	0,001992	0,00327	0,1181	0	0,098499		0,000841	0,001925					0,11413	0	2,48E-06
NiO	0	0	0	0			0	0	0	0	0	0		0	0					0	0	0
CaO	0	0	0,004931	0			0,005687	0,000868	0,00451	0	0	0		0,000191	0,000335					0	0	0,000965
Na2O	0,188612	0,003845	0,230724	0			0,226045	0,227981	0,23508	0,000295	0,004716	0,000597		0,228949	0,231369					0	0,003814	0,181352
K2O	0,000761	0,177715	0,001694	0,121874			0,000248	0,000279	0	0,121555	0,176228	0,121024		0,000622	0,000609					0,119219	0,175379	0,000949
Total	3,062422	2,897593	2,69321	2,730386			2,682574	2,745003	2,745552	2,744552	2,888629	2,710055		2,679012	2,724156					2,722426	2,866472	3,000597
oxygens	8	8	6	11			6	6	6	11	8	11		6	6					11	8	8
cations																						
Si	3,0113	3,0029	2,0004	3,5511			1,9934	1,9994	1,9830	3,6034	3,0085	3,5527		1,9942	1,9854					3,6132	3,0127	3,0085
Ti	0,0004	0,0006	0,0069	0,0367			0,0019	0,0252	0,0264	0,0315	0,0018	0,0429		0,0292	'0,0216					0,0165	0,0001	0,0000
Al	0,9843	0,9932	0,1643	1,8018			0,1610	0,3186	0,2375	1,7115	0,9806	1,8065		0,0892	0,3059					1,7119	0,9816	0,9947
Cr	0,0010	0,0000	0,0027	0,0035			0,0003	0,0016	0,0012	0,0026	0,0000	0,0003		0,0013	0,0016					0,0013	0,0006	0,0000
Fe^{3+}	0,0016	0,0006	0,7982				0,8244	0,6432	0,7276		0,0049			0,8672	0,6726						0,0006	0,0013
Fe^{2+}	0,0000	0,0000	0,0000	0,2036			0,0000	0,0000	0,0000	0,1969	0,0000	0,2023		0,0000	0,0000					0,2182	0,0000	0,0000
Mn	0,0013	0,0010	0,0000	0,0002			0,0002	0,0007	0,0012	0,0003	0,0000	0,0028		0,0000	0,0000					0,0095	0,0000	0,0003
Mg	0,0003	0,0000	0,0088	0,4218			0,0117	0,0044	0,0071	0,4733	0,0000	0,3998		0,0019	0,0042					0,4611	0,0000	0,0000
Ni	0,0000	0,0000	0,0000	0,0000			0,0000	0,0000	0,0000	0,0000	0,0000	0,0000		0,0000	0,0000					0,0000	0,0000	0,0000
Ca	0,0000	0,0000	0,0110	0,0000			0,0127	0,0019	0,0099	0,0000	0,0000	0,0000		0,0004	0,0007					0,0000	0,0000	0,0026
Na	0,9854	0,0212	1,0280	0,0000			1,0112	0,9966	1,0275	0,0024	0,0261	0,0048		1,0255	1,0192					0,0000	0,0213	0,9670
K	0,0040	0,9813	0,0075	0,9820			0,0011	0,0012	0,0000	0,9744	0,9761	0,9825		0,0028	0,0027					0,9634	0,9789	0,0051
Total	4,9896	5,0009	4,0279	7,0006			4,0179	3,9927	4,0213	6,9964	4,9981	6,9946		4,0118	4,0139					6,9953	4,9959	4,9795
X_{Ab}	0,9960	0,0212									0,0261										0,0213	0,9922
X_{Or}	0,0040	0,9788									0,9739										0,9787	0,0052
X_{An}	0,0000	0,0000									0,0000										0,0000	0,0026
X_{Ps}																						
J_{px}			2,056046				2,022337	1,993271	2,05493					2,051044	2,038376							
Q_{px}			0,0198				0,0244	0,0063	0,0170					0,0023	0,0050							

Figure 235: Spots of chemical analysis and classification into minerals.

No.	56	57	58	59	60	61	62	63	64	65	66	67	108			
Comment	464_b56	464_b57	464_b58	464_b59	464_b60_l	464_b61_c	464_b62	464_b63	464_b64	464_b65_c	464_b66_l	464_b67_v	464_b108_bright_phase_spectra_3			
Sample #	464	464	464	464	464	464	464	464	464	464	464	464	464			
Spot	b56	b57	b58	b59	b60	b61	b62	b63	b64	b65	b66	b67	b108			
Mineral	Aeg	Phe	Kfs	Kfs	Cal	Cal	Cal	Kfs	Qz	Aeg	Aeg	Cal	Rds?			
Comment					light core	dark rim				dark patch	light patch	with mn	bright phase spectra 3			
SiO2	53,47	52,17	64,35	64,81	0,0141	0,0174	0	65,3	100,81	54,52	55,16	0,0358	0,549			
TiO2	2,31	0,3103	0	0	0	0	0,0095	0,0112	0	0,1303	0,2919	0	0,4583			
Al2O3	3,54	23,86	18,06	18,11	0	0,0104	0,0184	18,1	0	8,46	8,93	0,0141	0,3575			
Cr2O3	0,0682	0	0,0593	0,0095	0,0106	0,0709	0,0051	0,0616	0,0707	0	0,0288	0,0892	0,0858			
Fe2O3	27,98373		0,07446	0,019782				0,044454		23,01601	22,43811					
FeO	25,18	3,22	0,067	0,0178	0,0214	0	0,026	0,04	0,0286	20,71	20,19	0,3367	0,7228			
MnO	0,0677	0,0158	0,0009	0,0283	0,0185	0,022	0,0398	0,0262	0,0203	0,0311	0,0232	0	67,01			
MgO	0,048	4,07	0	0	0	0	0	0,0086	0	0,1932	0,1498	0,7895	0,3004			
NiO																
CaO	0,0035	0	0,0015	0	52,55	55,05	53,47	0	0,037	0,1748	0,1611	55,93	1,1524			
Na2O	13,99	0,0537	0,3349	0,3082	0,6403	0,1817	0	0,2752	0	14,18	14,48	0,0217	0,1636			
K2O	0,0263	11,6	16,44	16,57	0,0099	0,0416	0,0058	16,57	0,0059	0,3145	0,0065	0,0066	0,0281			
Total	98,7038	95,2999	99,3137	99,8538	53,2649	55,394	53,5746	100,3927	100,9725	98,7139	99,4214	57,2236	70,828			
Total																
moles																
SiO2	0,889924	0,868287	1,071004	1,07866				1,086815		0,907399	0,918051					
TiO2	0,028924	0,003885	0	0				0,00014		0,001631	0,003655					
Al2O3	0,034719	0,23401	0,177126	0,177616				0,177518		0,082973	0,087582					
Cr2O3	0,000449	0	0,00039	6,25E-05				0,000405		0	0,000189					
Fe2O3	0,17524		0,000466	0,000124				0,000278		0,144131	0,140512					
FeO		0,044819														
MnO	0,000954	0,000223	1,27E-05	0,000399				0,000369		0,000438	0,000327					
MgO	0,001191	0,10098	0	0				0,000213		0,004793	0,003717					
NiO	0	0	0	0				0		0	0					
CaO	6,24E-05	0	2,67E-05	0				0		0,003117	0,002873					
Na2O	0,225722	0,000866	0,005403	0,004973				0,00444		0,228787	0,233628					
K2O	0,000279	0,123147	0,17453	0,17591				0,17591		0,003339	6,9E-05					
cations																
Si	0,889924	0,868287	1,071004	1,07866				1,086815		0,907399	0,918051					
Ti	0,028924	0,003885	0	0				0,00014		0,001631	0,003655					
Al	0,069438	0,468021	0,354252	0,355233				0,355037		0,165945	0,175165					
Cr	0,000897	0	0,00078	0,000125				0,000811		0	0,000379					
Fe^{3+}	0,35048		0,000933	0,000248				0,000557		0,288262	0,281024					
Fe^{2+}	0	0,044819	0	0				0		0	0					
Mn	0,000954	0,000223	1,27E-05	0,000399				0,000369		0,000438	0,000327					
Mg	0,001191	0,10098	0	0				0,000213		0,004793	0,003717					
Ni	0	0	0	0				0		0	0					
Ca	6,24E-05	0	2,67E-05	0				0		0,003117	0,002873					
Na	0,451444	0,001733	0,010807	0,009945				0,00888		0,457575	0,467256					
K	0,000558	0,246295	0,349059	0,35182				0,35182		0,006678	0,000138					
oxygens																
SiO2	1,779847	1,736575	2,142008	2,15732				2,173631		1,814799	1,836102					
TiO2	0,057847	0,007771	0	0				0,00028		0,003263	0,00731					
Al2O3	0,104157	0,702031	0,531378	0,532849				0,532555		0,248918	0,262747					
Cr2O3	0,001346	0	0,00117	0,000188				0,001216		0	0,000568					
Fe2O3	0,525719		0,001399	0,000372				0,000835		0,432393	0,421536					
FeO	0	0,044819	0	0				0		0	0					
MnO	0,000954	0,000223	1,27E-05	0,000399				0,000369		0,000438	0,000327					
MgO	0,001191	0,10098	0	0				0,000213		0,004793	0,003717					
NiO	0	0	0	0				0		0	0					
CaO	6,24E-05	0	2,67E-05	0				0		0,003117	0,002873					
Na2O	0,225722	0,000866	0,005403	0,004973				0,00444		0,228787	0,233628					
K2O	0,000279	0,123147	0,17453	0,17591				0,17591		0,003339	6,9E-05					
Total	2,697126	2,716412	2,855928	2,87201				2,88945		2,739848	2,768877					
oxygens	6	11	8	8				8		6	6					
cations																
Si	1,9797	3,5161	3,0001	3,0046				3,0091		1,9871	1,9894				3,5673	0,0404
Ti	0,0643	0,0157	0,0000	0,0000				0,0004		0,0036	0,0079					
Al	0,1545	1,8952	0,9923	0,9895				0,9830		0,3634	0,3796					
Cr	0,0020	0,0000	0,0022	0,0003				0,0022		0,0000	0,0008					
Fe^{3+}	0,7797		0,0026	0,0007				0,0015		0,6313	0,6090					
Fe^{2+}	0,0000	0,1815	0,0000	0,0000				0,0000		0,0000	0,0000					
Mn	0,0021	0,0009	0,0000	0,0011				0,0010		0,0010	0,0007					
Mg	0,0026	0,4089	0,0000	0,0000				0,0006		0,0105	0,0081					
Ni	0,0000	0,0000	0,0000	0,0000				0,0000		0,0000	0,0000					
Ca	0,0001	0,0000	0,0001	0,0000				0,0000		0,0068	0,0062					
Na	1,0043	0,0070	0,0303	0,0277				0,0246		1,0020	1,0125					
K	0,0012	0,9974	0,9778	0,9800				0,9741		0,0146	0,0003					
Total	3,9906	7,0227	5,0054	5,0040				4,9965		4,0203	4,0144					
X_{Ab}			0,0300	0,0275				0,0246								
X_{Or}			0,9699	0,9725				0,9754								
X_{An}			0,0001	0,0000				0,0000								
X_{Ps}																
J_{px}	2,008554									2,004089	2,025033					
Q_{px}	0,0028									0,0173	0,0143					

Figure 236: Spots of chemical analysis and classification into minerals.

			Sr (ppm)	87/86 Sr	87/86 Sr
Unmetamorphosed limestones, northern and central Evia					
5913	Late Cretaceous		986	0,70733	0,7075
				0,70756±0,00012	
5879	Late Cretaceous		285	0,70736	0,7073
				0,70712±0,00012	
2100E	Late Jurassic		225	0,70684	0,7067
		(Kimmeridgian)		0,70649±0,00018	
2529	Late Triassic		205	0,70698	0,7076
				0,70804±0,00053	
2101E	Permian		690	0,70737	0,7076
				0,7077±0,00017	
Marbles of southern Evia					
3148	Styra Marble	Late Cretaceous	559	0,70877	0,7088
2747	Styra Marble	Late Cretaceous	789	0,70817	0,7082
E100K	Styra Marble	Late Cretaceous	184	0,70929	0,7093
3328	Styra Marble	Late Cretaceous	664	0,70758	0,7076
2592	Panagia Marble	Late Cretaceous	235	0,70867	0,7087
				0,70869±0,00001	
3126	Argyron Marble	Jurassic or Turonian	214	0,7068	0,7069
3145	Argyron Marble	Jurassic or Turonian	200	0,70685	0,7069
3152	Argyron Marble	Jurassic or Turonian	391	0,70651	0,7067
				0,70685±0,00017	
3171	Argyron Marble	Jurassic or Turonian	266	0,70671	0,707
				0,707190,00024	
2447	St. George Marble	Late Triassic	170	0,70713	0,7072
2448	St. George Marble	Late Triassic	143	0,70822	0,7081
				0,70791±0,00015	

Figure 237: Strontium isotope ratio for dating limestones and marbles in Evia.

Conclusions:

Initially, we have a crystalline basement in the Permian-Carboniferous which is fractured by uplift of the asthenosphere due to density differences in the form of basaltic vein-solutions in a metamorphic granitoid sequence. Without the paper containing ages of this tectonic episode, all other geological evidence proves that this rupture occurred during the well-known Triassic rift. Then our tectonic environment after being rifted evolved into a subduction zone where the oceanic lithosphere that had been created entered entirely into the subduction zone and the continental crust was next in line. This is exactly what the rocks of the Lower Plate units south of the Pelagonian fault in central Evia form. According to the latest data of the present study, it is possible that the Lower Plate area, due to intense deformation, acquired an anticlinal structure and was subsequently eroded. Therefore, the Ochi unit is not finally, tectonically overlying the other units (Almyropotamos, Styron) but is a reclamation of the crystalline Permo-Carboniferous basement, while until today it was known from the stratigraphic columns of ΙΓΜΕ and Mr. Katsikatsos that the Ochi unit is tectonically overlying all the units in the Lower Plate of Evia. Therefore, in the area of Petries where there are occurrences of the Ochi unit, we do not have any sedimentary sequence as mapped so far but we are on a metamorphic sequence of granitoid rocks with characteristic minerals of blueschist phase. The fact that the ΙΓΜΕ referred to rocks of sedimentary origin with characteristic minerals of the epidote, lawsonite, and glaucophane, would only have a basis if they were found in metamorphic carbonate rocks such as marbles but only in the case that there were some residual elements such as e.g. Na from a source and thus the rock under the necessary conditions to create e.g. glaucophane, which is rare. But in our case, this is not the case. What seems to happen is that we have orthogneisses metamorphosed from alkaline

basaltic veins and sills in an oxidizing environment and in a geotectonic environment between post and within plates tectonic since the extension of granitoids by tectonic elements is observed. Ultimately, it is reasonably hypothesized that, since it is demonstrated by data that the Attica fault geologically correlates the Lower Plate Central's Evia granitoids and the orthogneisses of Penteli and agrees with the petrology-mineralogy, the tectonics and the age of the Penteli area as reported in this paper, then it is likely that these two areas are part of the same subduction zone, except that Central Evia was closer to the subduction zone and was found at slightly greater depths.

Acknowledgements:

I would like to thank my supervisors Dr. P. Pomonis (Professor) and Dr. D. Kostopoulos (Associate professor) for their guidance, help, and time they offered me, both in the field, in research and information gathering. I would also like to thank Mrs. I. Megremi for her help and time on the XRD instrument, Mr. B. Skounakis for showing me the preparatory steps for the creation of thin section microscope sections, as well as ΙΓΜΕ for their cooperation and Mr. D. Moutzouris for his help (in microprobe analysis) at the University of Mainz. Thanks to Mrs M. Chondrokouki for her bibliography assistance. I would like to point out that the information about the geology of Penteli was taken from the field guide within the course of metamorphic rocks by Dr. D. Kostopoulos and the information about the methodology mentioned was taken from the notes of the elective course: (Methods of rock and ore analysis - Fluid inclusions) by Dr. A. Papoutsa. Last but not least, I would like to thank the one and only person in my life who always supports me and helps me on all levels, my girlfriend Nefeli Kollia.

Abstract:

In the present thesis the study of granitic rocks which occupy a significant area of the geological unit of Ochi, in the region of Central Evia, is carried out. The Ochi Unit is located in the footwall of the N. Attica-S. Evia fault and (in Central Evia) has undergone high-pressure/low-temperature metamorphism in the blueschist facies. Kinematic indicators clearly indicate exhumation tectonics with a top-to-the-NE sense of shear. The granitic rocks of the Ochi Unit are considered to be the products of crystallization of an alkaline granitic melt under oxidizing conditions as testified by the abundance of the mineral aegirine (sodic clinopyroxene with a high content of ferric iron) and the ubiquitous presence of hematite. Such granites are typical in areas of continental rifting (e.g. Oslo Rift). The granitic paragenesis is complemented by the minerals: phengite, albite, K-feldspar, biotite and quartz. Metamorphic conditions were calculated as 9-11 kbar and 400-450°C based on the equilibrium reaction: phlogopite + 2 K-feldspar + 3 quartz = 3 Mg-Al celadonite and the silica content of the phengite (3.6 a.p.f.u.).

According to the geological map of the area (ΙΓΜΕ - Aliveri sheet - scale 1:50.000), the Ochi Unit is mainly characterized by muscovite, epidote, chlorite, glaucophane and quartz schists whose protolith was interpreted as being of sedimentary origin. The petrological findings of

the present thesis contradict the above interpretation of the Ochi unit in central Evia and argue for a purely igneous origin for the unit, which justifies the absence of marbles from it. Fieldwork also showed that the Ochi Unit underlies (and not overlies) the marbles and cipolines of the Styra Unit.

The new findings lead to the conclusion that the geological structure of the Styra-Ochi Unit in central Evia has strong similarities with that of Mount Pendelikon in Attica, where the granitoids underlying the marbles have been dated as being of Lower Triassic age, i.e., they have been emplaced during the pervasive continental rifting of the Greek area at that time.

Περίληψη:

Στην παρούσα διπλωματική εργασία γίνεται η μελέτη γρανιτικών πετρωμάτων τα οποία καταλαμβάνουν σημαντική έκταση της γεωλογικής ενότητας Όχης, στην περιοχή της Κεντρικής Εύβοιας. Η ενότητα Όχης βρίσκεται στο υποκείμενο τέμαχος του ρήγματος Β. Αττικής-Ν. Εύβοιας και (στην κεντρική Εύβοια) έχει υποστεί μεταμόρφωση υψηλών πιέσεων/χαμηλών θερμοκρασιών στην κυανοσχιστολιθική φάση. Οι κινηματικοί δείκτες μαρτυρούν σαφώς τεκτονική εκταφής με σχετική κίνηση του άνω τεμάχους προς τα βορειοανατολικά (top-to-the-NE). Τα γρανιτικά πετρώματα της ενότητας Όχης θεωρούνται προϊόντα κρυστάλλωσης ενός αλκαλικού γρανιτικού τήγματος υπό οξειδωτικές συνθήκες όπως προκύπτει από την αφθονία του ορυκτού αιγιρίνη (νατρούχος κλινοπυρόξενος με μεγάλη περιεκτικότητα σε τρισθενή σίδηρο) και τον πασίδηλο αιματίτη. Τέτοιοι γρανίτες είναι τυπικοί σε περιοχές ηπειρωτικής διάρρηξης (π.χ. Oslo Rift). Η γρανιτική παραγένεση συμπληρώνεται από τα ορυκτά: φεγγίτης, αλβίτης, καλιούχος άστριος, βιοτίτης και χαλαζίας. Οι συνθήκες μεταμόρφωσης υπολογίσθηκαν ως 9-11 kbar και 400-450°C με βάση την αντίδραση ισορροπίας: φλογοπίτης + 2 K-άστριος + 3 χαλαζίας = 3 Mg-Al σελαδονίτης και το περιεχόμενο σε πυρίτιο του φεγγίτη (3,6 a.p.f.u.).

Σύμφωνα με τον γεωλογικό χάρτη της περιοχής (ΙΓΜΕ – Φύλλο Αλιβέρι – κλίμακα 1:50.000), η ενότητα Όχης χαρακτηρίζεται κυρίως από μοσχοβιτικούς, επιδοτικούς, χλωριτικούς, γλαυκοφανιτικούς και χαλαζιακούς σχιστόλιθους των οποίων ο πρωτόλιθος ερμηνεύθηκε ως ιζηματογενούς προέλευσης. Τα πετρολογικά ευρήματα της παρούσας διπλωματικής εργασίας έρχονται σε αντίθεση με την ανωτέρω ερμηνεία της ενότητας Όχης στην κεντρική Εύβοια και συνηγορούν υπέρ μίας καθαρά πυριγενούς προέλευσης για την ενότητα, γεγονός που δικαιολογεί και την απουσία μαρμάρων από αυτή. Η εργασία στο πεδίο έδειξε επίσης ότι η ενότητα Όχης υπόκειται (και όχι υπέρκειται) της ενότητας μαρμάρων-σιπολινών Στύρων.

Τα νέα ευρήματα οδηγούν στο συμπέρασμα ότι η γεωλογική δομή της ενότητας Στύρων-Όχης στην κεντρική Εύβοια παρουσιάζει μεγάλες ομοιότητες με αυτή του Πεντελικού όρους στην Αττική, όπου τα υποκείμενα των μαρμάρων γρανιτοειδή έχουν χρονολογηθεί ως Κατω-Τριαδικής ηλικίας, τοποθετημένα δηλαδή κατά την διαμπερή ηπειρωτική διάρρηξη του ελληνικού χώρου την εποχή εκείνη.

References:

Bono, A. D., Martini, R., Zaninetti, L., Hirsch, F., Stampfli, G. M., & Vavassis, I. (2001). Permo-Triassic stratigraphy of the Pelagonian zone in central Evia Island (Greece). *Eclogae Geol.*, *94*, 289–311. http://doi.org/10.5169/seals-168895

Bradley, K. E. (2012). *The Roof of the Cyclades: A structural, stratigraphic, and paleomagnetic study of neogene extensional tectonics in Central Greece* [Thesis]. M.I.T.

Chatzaras, V., Dörr, W., Finger, F., Xypolias, P., & Zulauf, G. (2012). Tectonophysics: U–PB Single Zircon Ages and Geochemistry of Metagranitoid rocks in the Cycladic Blueschists (Evia Island): Implications for the Triassic Tectonic setting of Greece. *ELSEVIER*. https://doi.org/10.1016/j.tecto.2012.05.016

Faucher, A., Gueydan, F., Jolivet, M., Alsaif, M., & Célérier, B. (2021). Dextral Strike-Slip and normal faulting during middle Miocene Back-Arc extension and westward Anatolia extrusion in central Greece. *Tectonics*. https://doi.org/10.1029/2020TC006615

Jolivet, L., & Brun, J. P. (2008). Cenozoic geodynamic evolution of the Aegean. *Int J Earth Sci (Geol Rundsch)*, *99*, 109–138. https://doi.org/10.1007/s00531-008-0366-4

Katsikatsos, G. (1991). *Aliveri Sheet* [Dataset; Map scale 1:50.000]. Hellenic Survey of Geology and Mineral Exploration- I.Γ.Μ.Ε.

Katsikatsos, G. (1992). *Γεωλογία της Ελλάδας*. Οργανισμός Εκδόσεως Διδακτικών Βιβλίων.

Katsikatsos, G., Fytika, M., Kouki, G., & Anastopoulos, I. (1981). *Kymi Sheet* [Dataset; Map scale 1:50.000]. Hellenic Survey of Geology and Mineral Exploration- I.Γ.Μ.Ε.

Mpounti, D. (2011). *Τεκτονική ανάλυση των μεταμορφωμένων ενοτήτων Αλμυροπόταμου και Στύρων, Νότια Εύβοια*. Εθνικό και Καποδιστριακό Πανεπιστήμιο Αθηνών.

Parra, T., Vidal, O., & Agard, P. (2002). A thermodynamic model for FE–MG dioctahedral K white micas using data from phase-equilibrium experiments and natural pelitic assemblages. *Contrib Mineral Petrol*, *143*, 706–732. https://doi.org/10.1007/s00410-002-0373-6

Pearce, J. (1996). Sources and settings of granitic rocks. *Episodes*, *19*, 120–125.

Pearce, J. A., Harris, N. B. W., & Tindle, A. G. (1984). Trace element discrimination diagrams for the tectonic interpretation of granitic rocks. *Journal of Petrology*, *25*, 956–983. http://petrology.oxfordjournals.org/

Pe-Piper, G. (1998). The nature of Triassic extension-related magmatism in Greece: Evidence from ND and PB isotope Geochemistry. *Geol. Mag.*, *135*, 331–348.

Ring, U., Glodny, J., Will, T., & Thomson, S. (2010). The Hellenic Subduction System: High-Pressure Metamorphism, Exhumation, Normal Faulting, and Large-Scale Extension. *The Annual Review of Earth and Planetary Sciences*, 45. https://doi.org/10.1146/annurev.earth.050708.170910

Robertson, A. H. F. (2006). Sedimentary evidence from the South Mediterranean region (Sicily, Crete, Peloponnese, Evia) used to test alternative models for the regional tectonic

setting of Tethys during late Paleozoic-Early Mesozoic time. *Geological Society*, *260*, 91–154. https://doi.org/10.1144/GSL.SP.2006.260.01.06

Robertson, A. H. F. (2007). Overview of tectonic settings related to the rifting and opening of Mesozoic Ocean basins in the eastern Tethys: Oman, Himalayas and eastern Mediterranean regions. *Geological Society*, *282*, 325–388. https://doi.org/10.1144/SP282.15

Schmid, S. M., Fügenschuh, B., Kounov, A., Matenco, L., Nievergelt, P., Oberhansli, R., Pleuger, J., Schefer, S., Schuster, R., Tomljenovic, B., Ustaszewski, K., & Van Hinsbergen, D. J. J. (2019). Gondwana Research: Tectonic units of the alpine collision zone between Eastern Alps and Western Turkey. *ELSEVIER*. https://www.sciencedirect.com/science/article/abs/pii/S1342937X19302199?via%3Dihub

Shaked, Y., Avigad, D., & Garfunkel, Z. (2000). Alpine high-pressure metamorphism at the Almyropotamos Window (Southern Evia, Greece). *Geol. Mag.*, *137*, 367–380.

Stampfli, G. M. (2005). Plate tectonics of the Apulia–Adria microcontinents. *CROP PROJECT: Deep Seismic Exploration of the Central Mediterranean and Italy*.

Stampfli, G. M., Borel, G. D., & Earth and Planetary Science Letters [EPSL]. (2001). *A plate tectonic model for the paleozoic and mesozoic constrained by dynamic plate boundaries and restored synthetic oceanic isochrons*. Institute of Geology and Paleontology, University of Lausanne.

Van Hinsbergen*, D. J. J., Hafkenscheid, E., Spakman, W., Meulenkamp, J. E., Wortel, R., & Geological Society of America. (2005). Nappe stacking resulting from subduction of oceanic and continental lithosphere below Greece. *Geology*, *33*.

Vavassis, I., Bono, A. D., Stampfli, G. M., Giorgis, D., Valloton, A., & Amelin, Y. (2000). U-PB and AR-AR geochronological data from the Pelagonian basement in Evia (Greece) : Geodynamic implications for the evolution of PaleoTethys. *SCHWEIZ. MINERAL.*, *80*, 21–43. http://dx.doi.org/10.5169/seals-60948

Appendix:

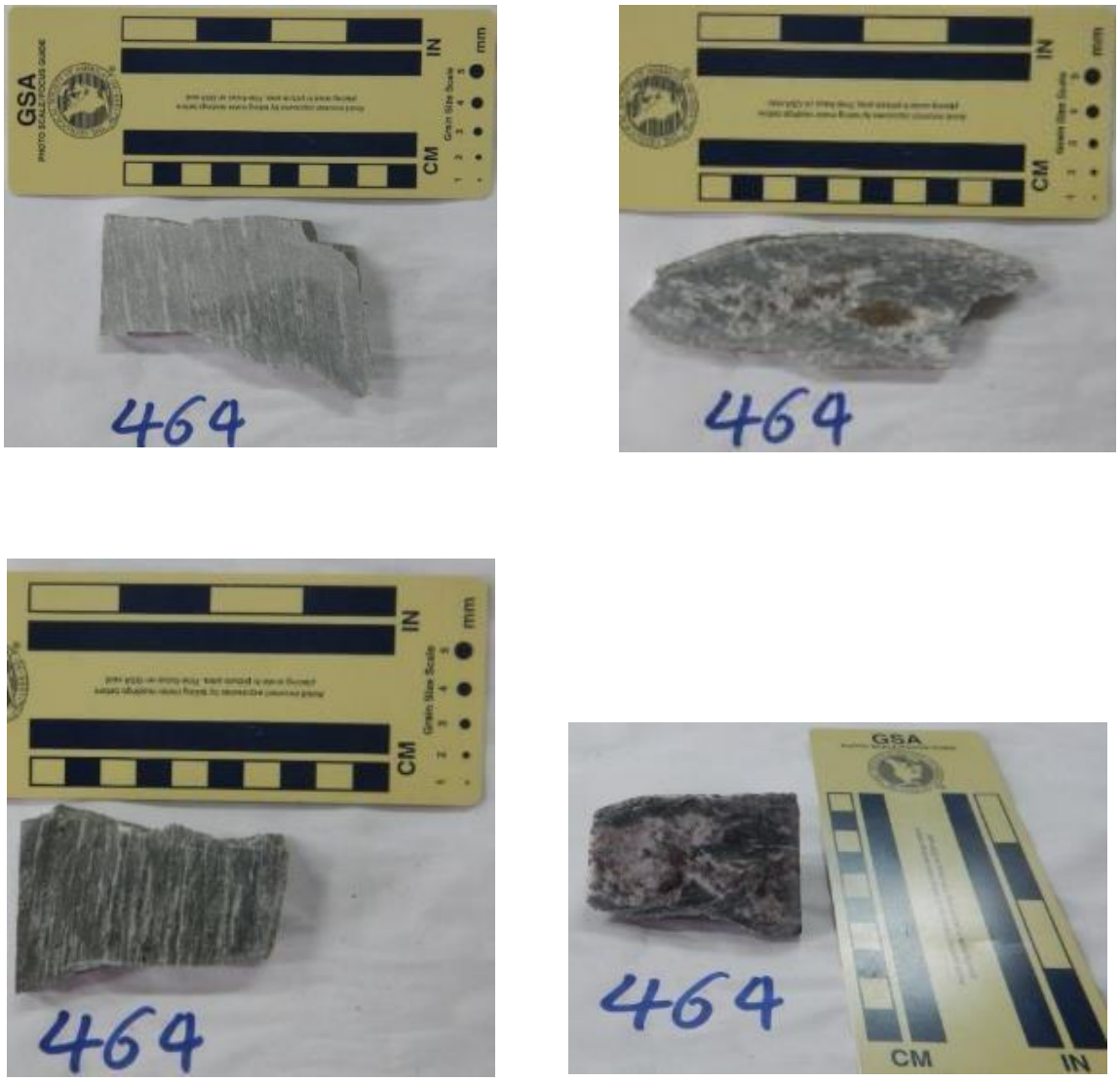

Figure 1: slabs 464

Figure 2: slabs 461

:

Figure 3: slabs 460

Figure 4: slabs 458

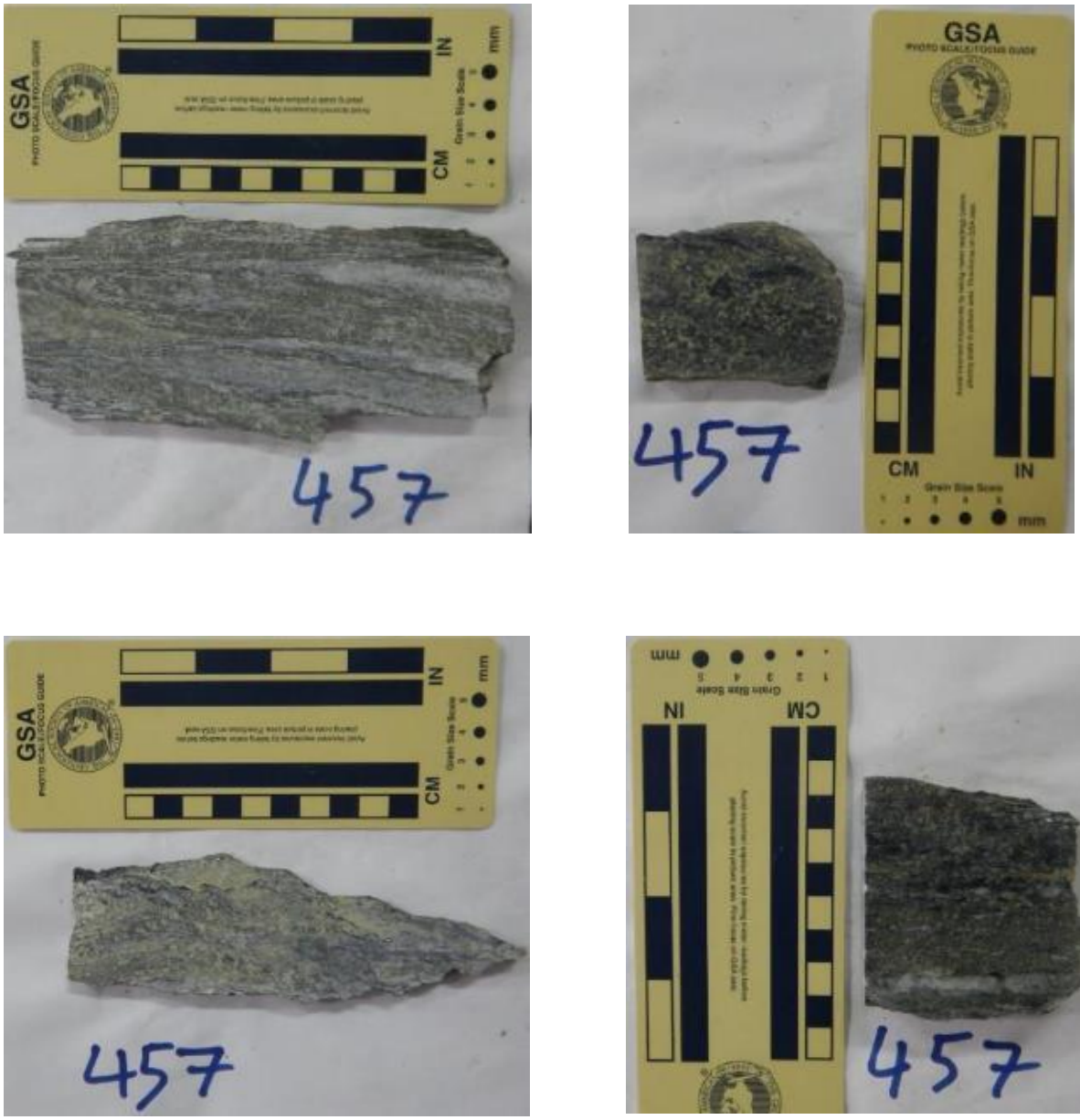

Figure 5: slabs 457

Figure 6: slab 456

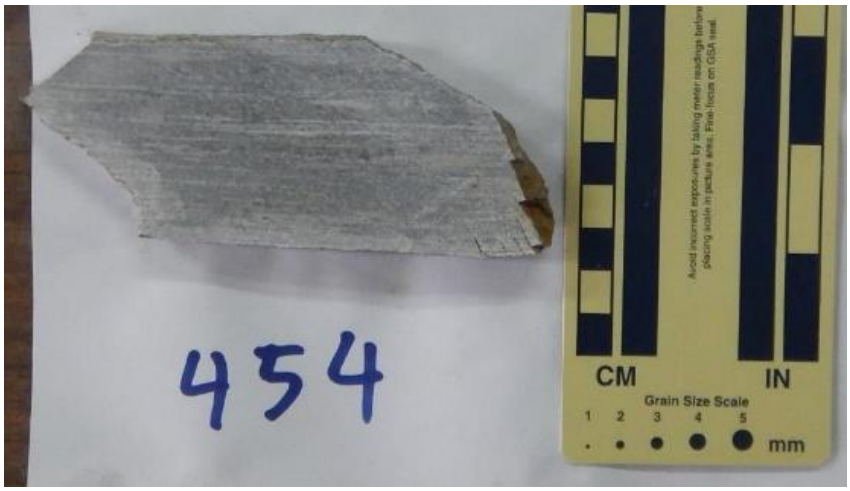

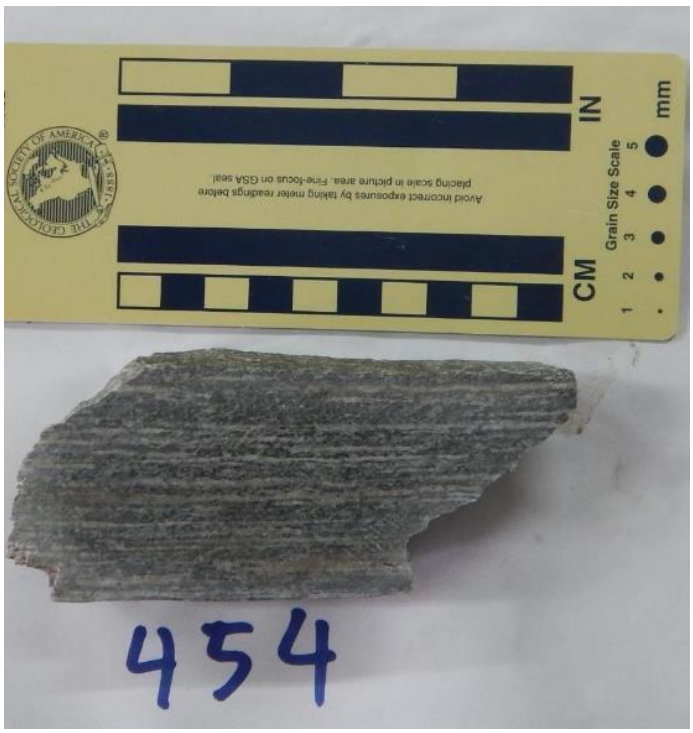

Figure 7: slabs 454

Figure 8: slabs 453

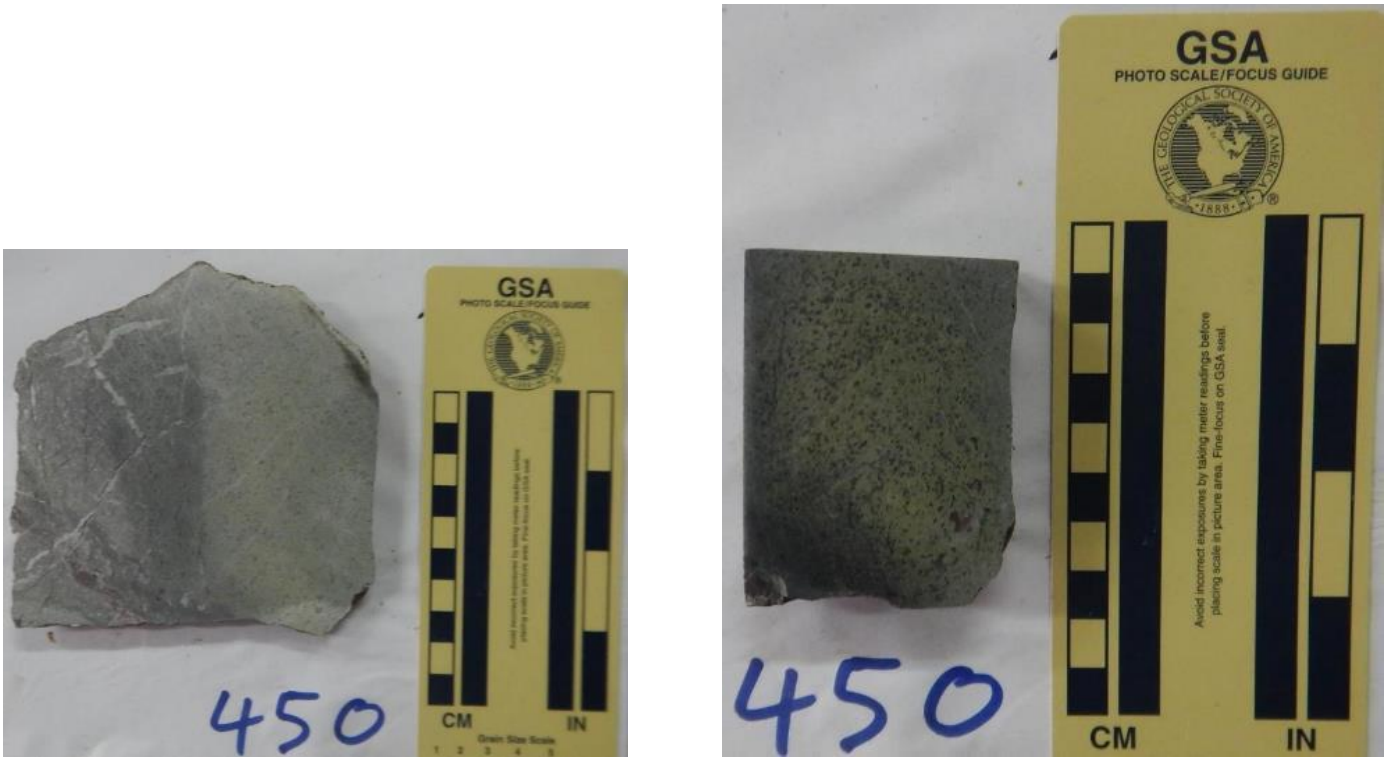

Figure 9: slabs 450

Figure 10: slabs 443

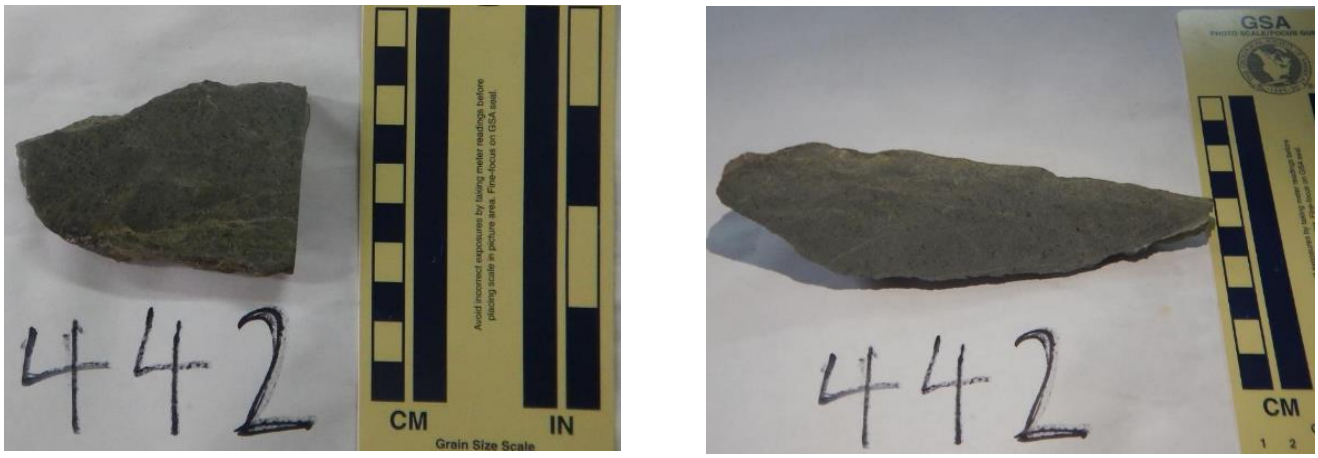

Figure 11: slabs 442

Figure 12: slabs 440

XRD Pic Charts:

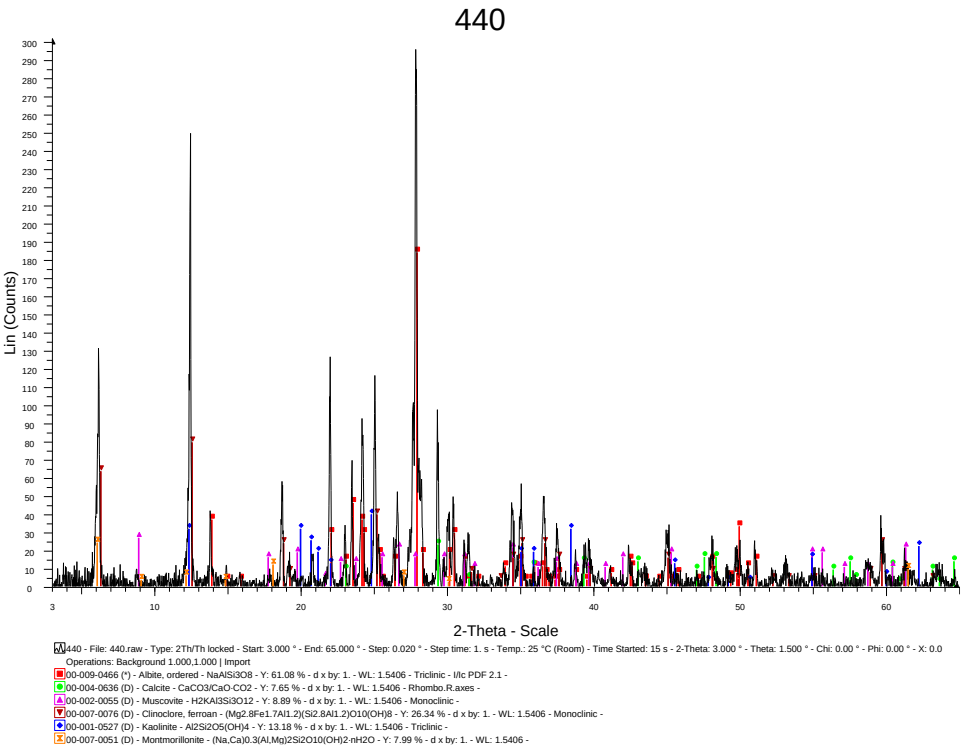

Figure 13: XRD chart 440

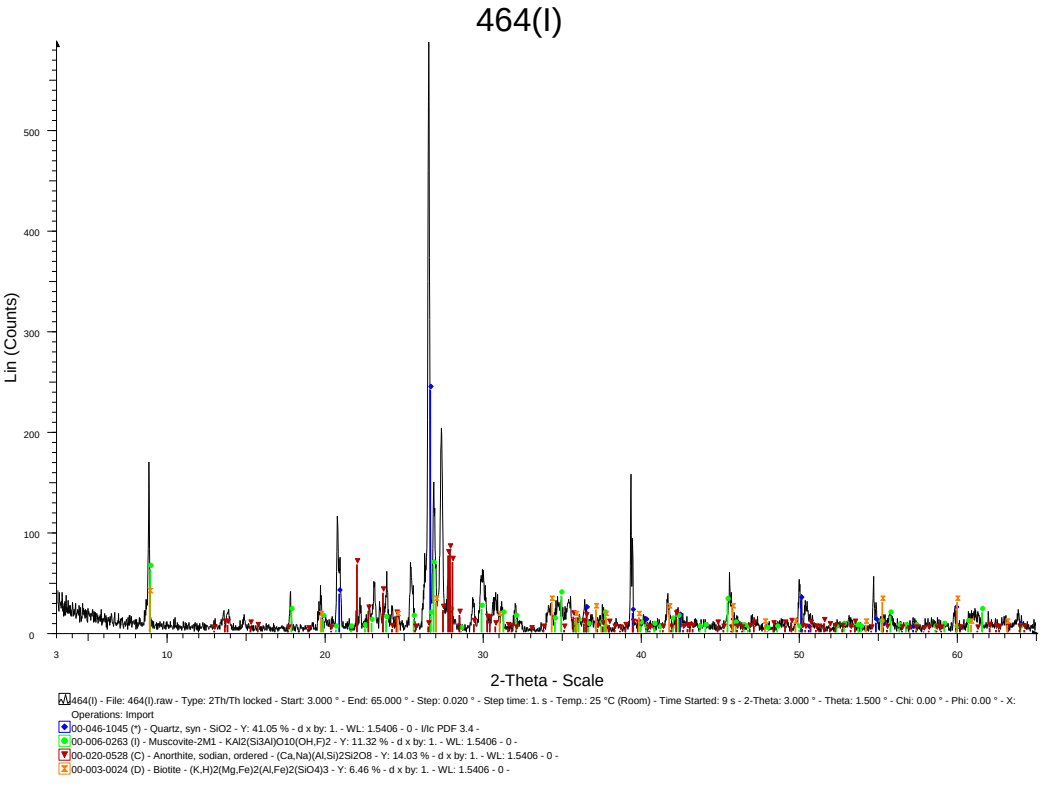

Figure 14: XRD chart 464 (I)

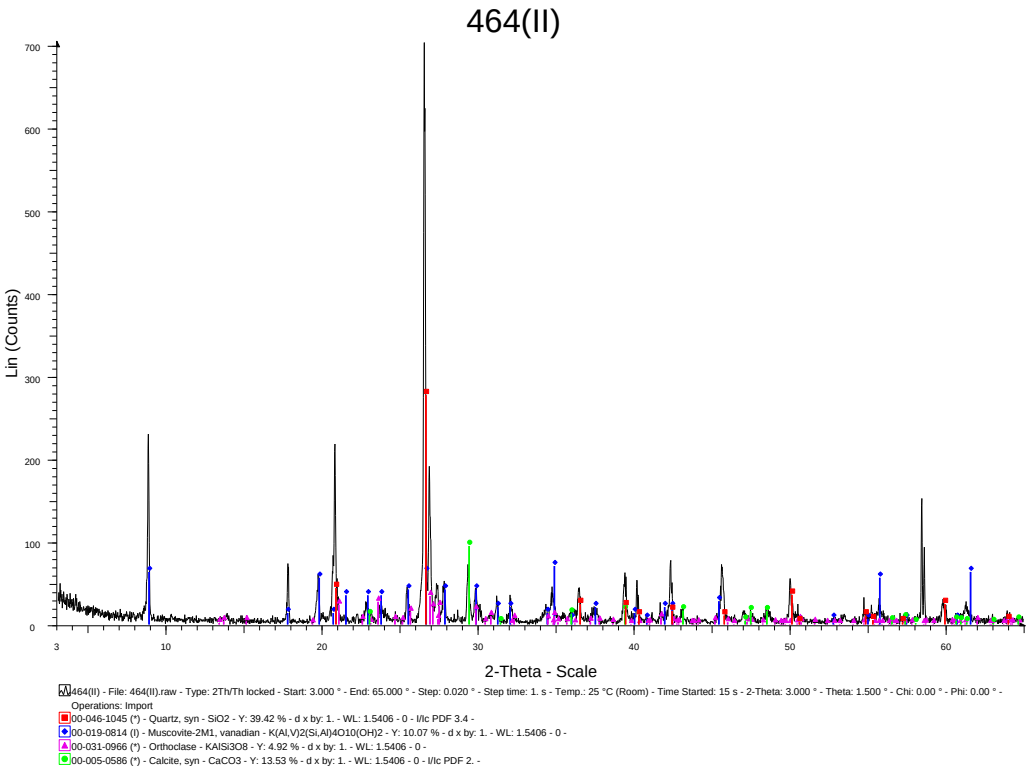

Figure 15: XRD chart 464 (II)

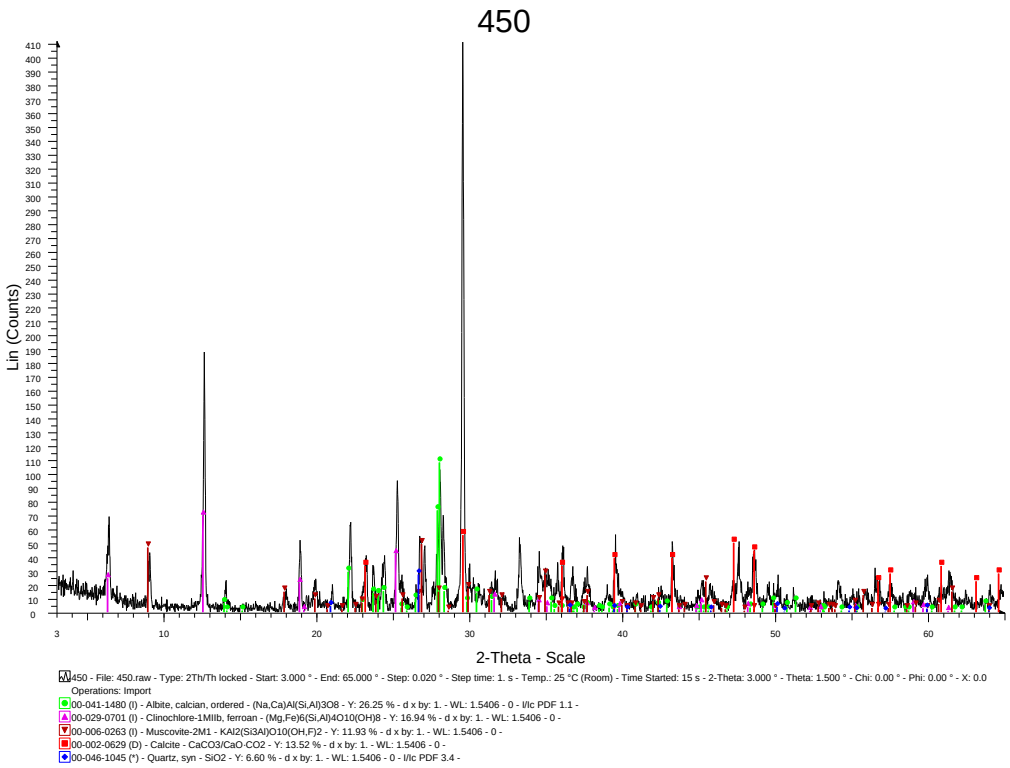

Figure 16: XRD chart 450

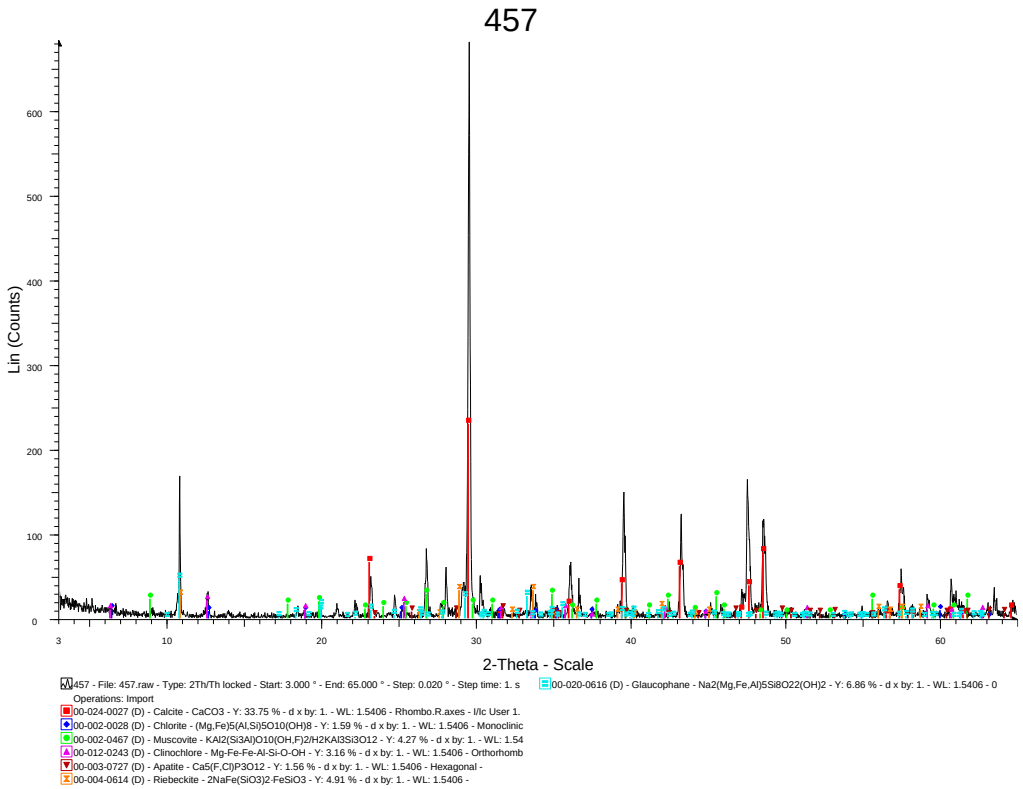

Figure 17: XRD chart 457

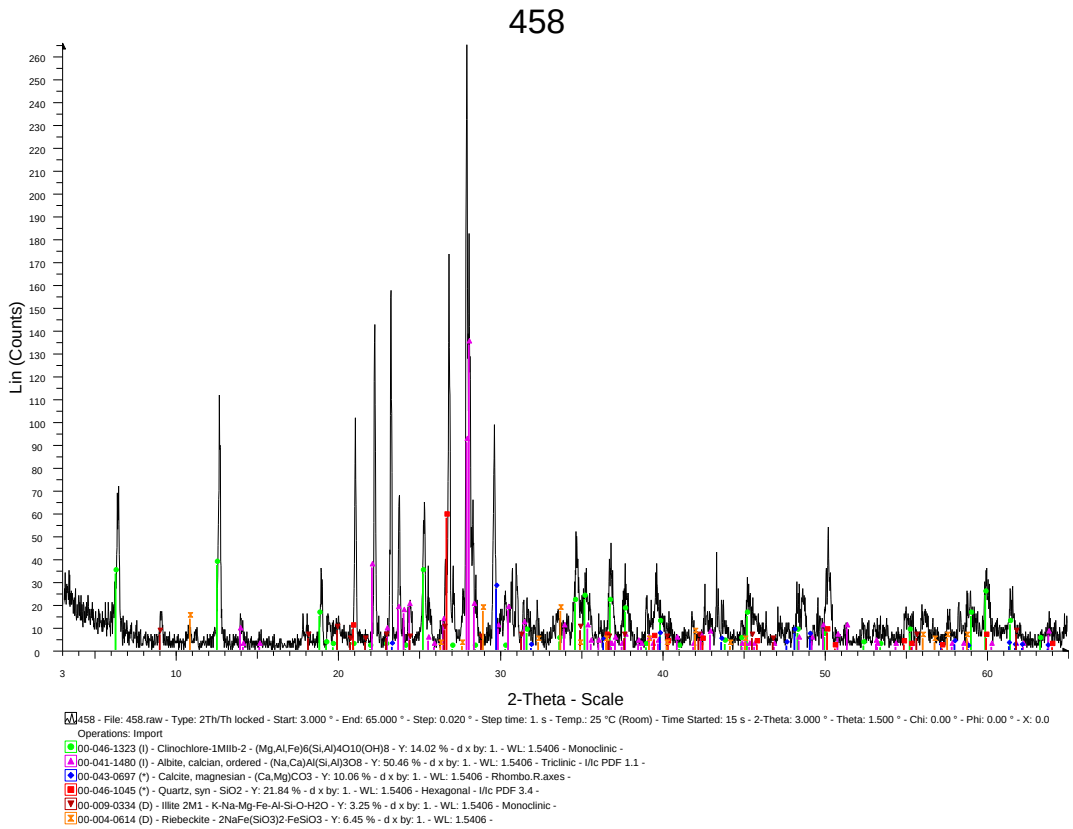

Figure 18: XRD chart 458

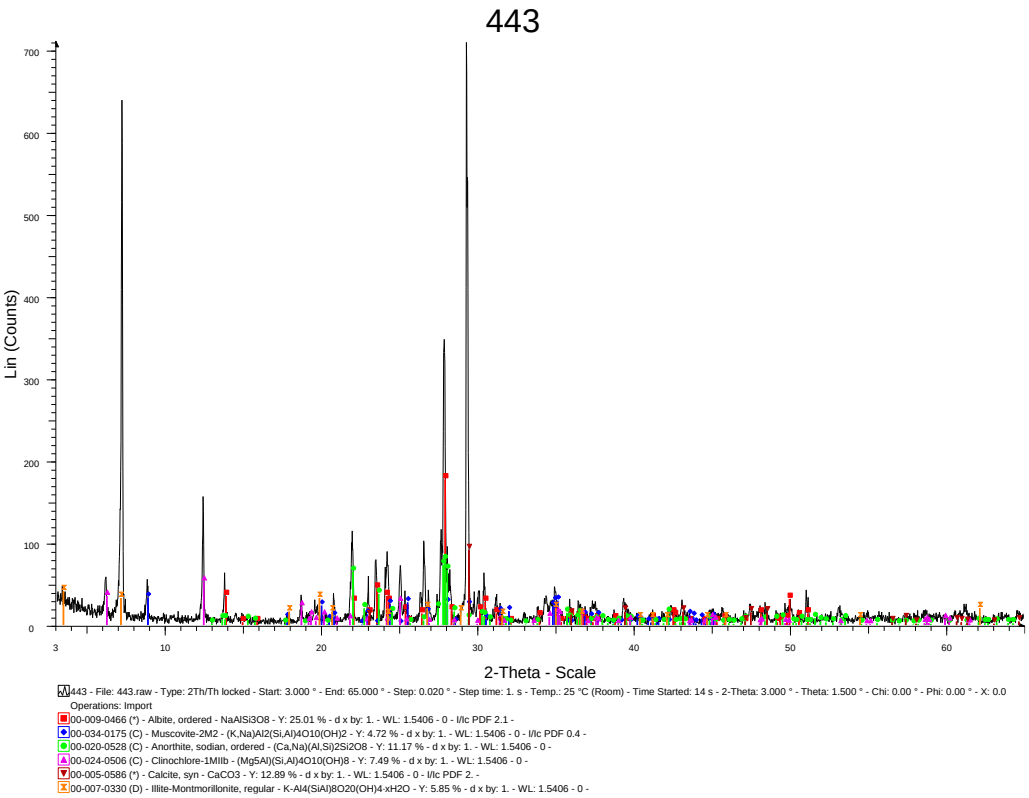

Figure 19: XRD chart 443

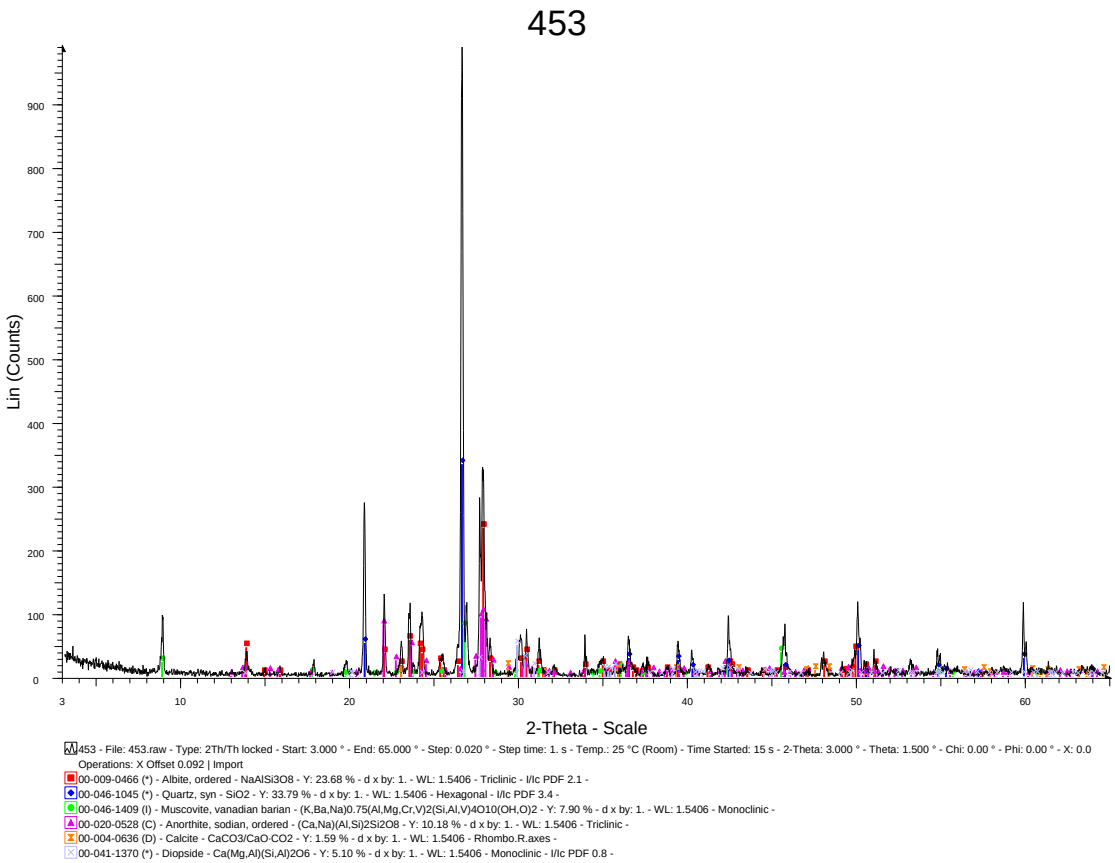

Figure 20: XRD chart 453

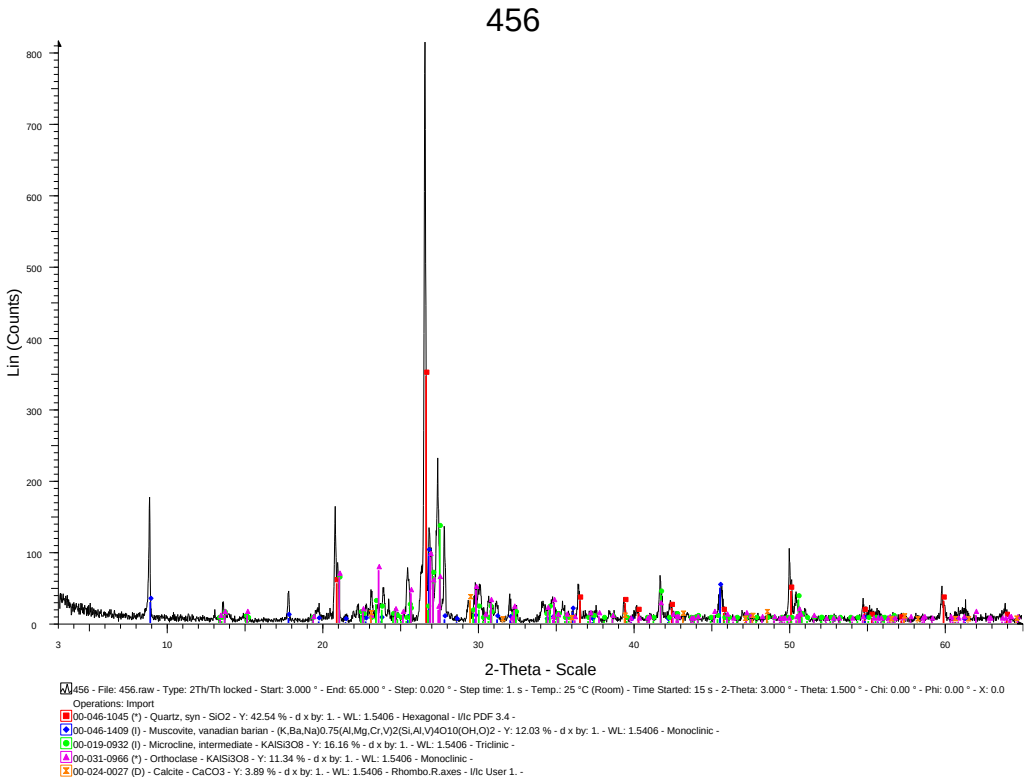

Figure 21: XRD chart 456

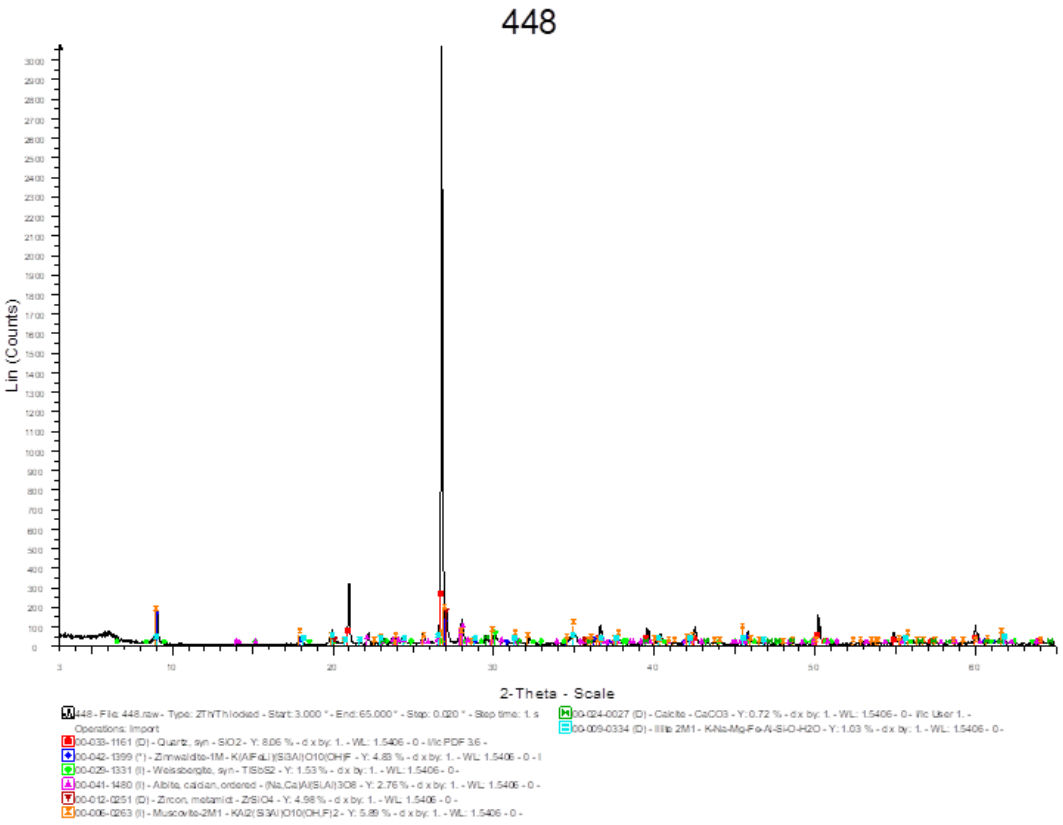

Figure 22: XRD chart 448

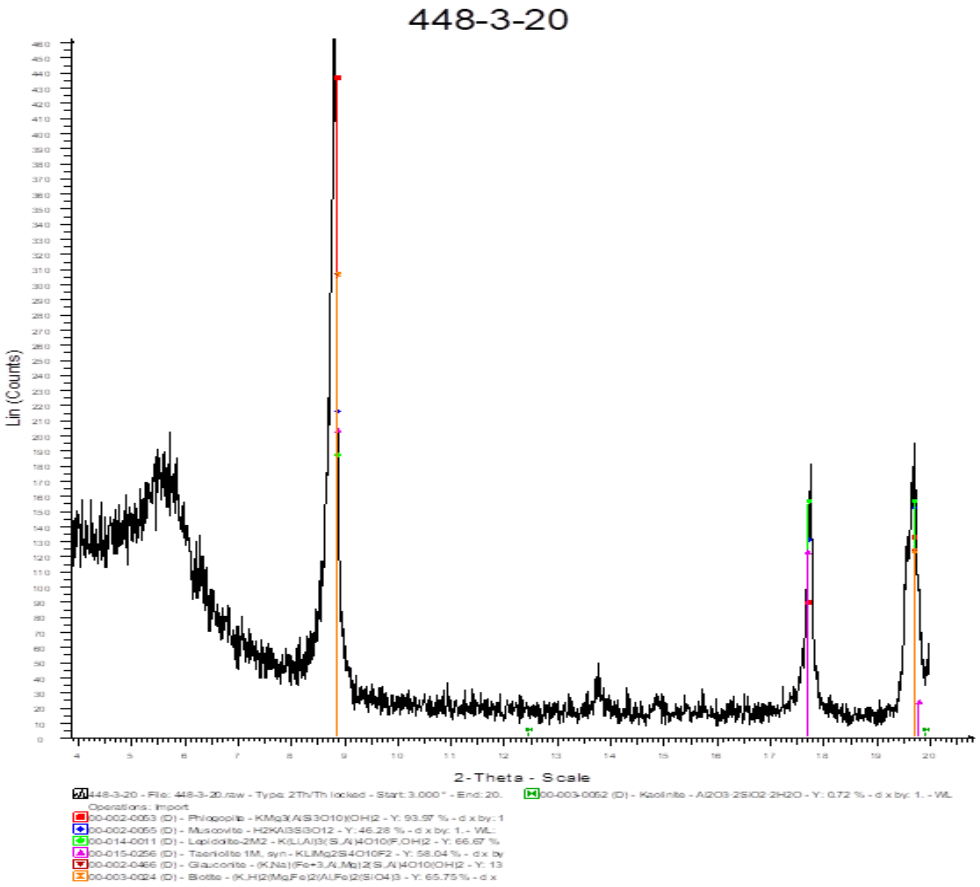

Figure 23: XRD chart 448 (Low degrees)

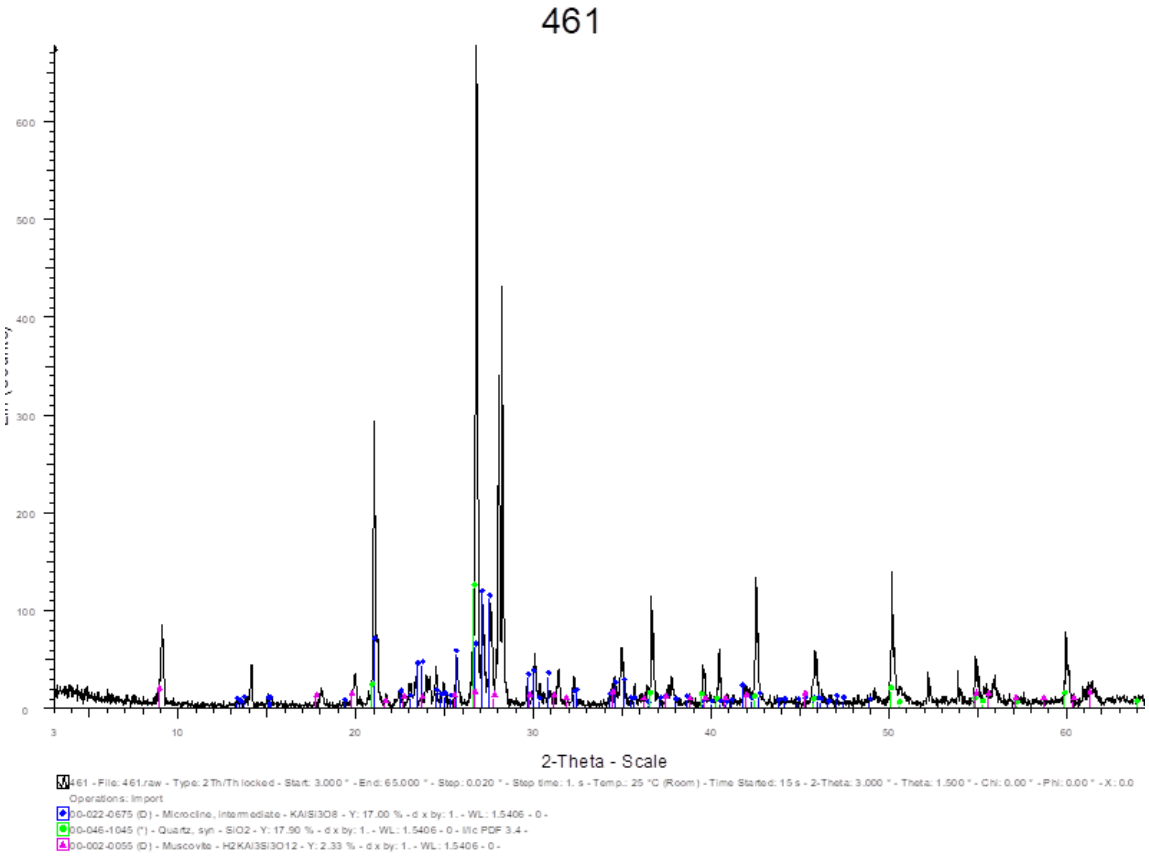

Figure 24: XRD chart 461

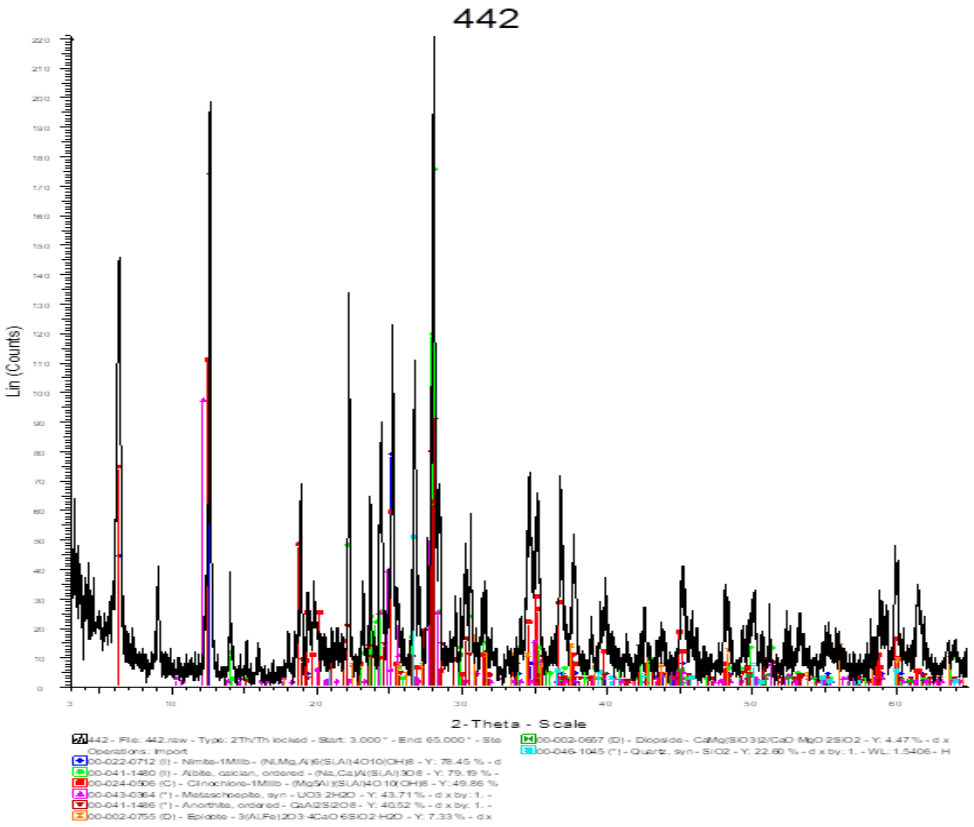

Figure 25: XRD chart 442

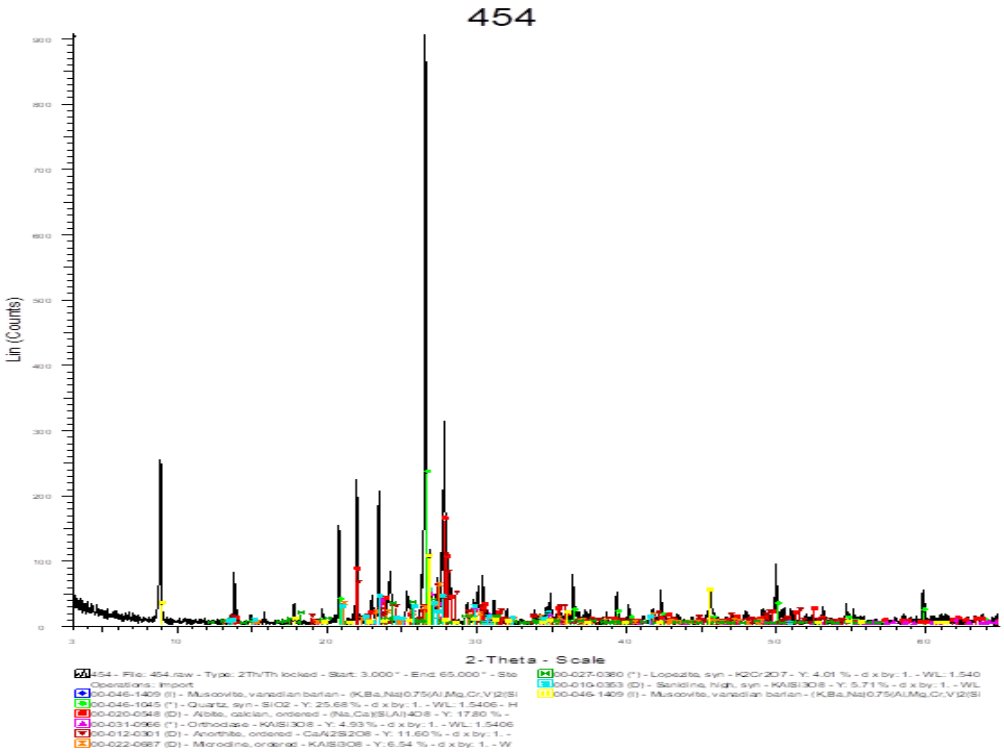

Figure 26: XRD chart 454

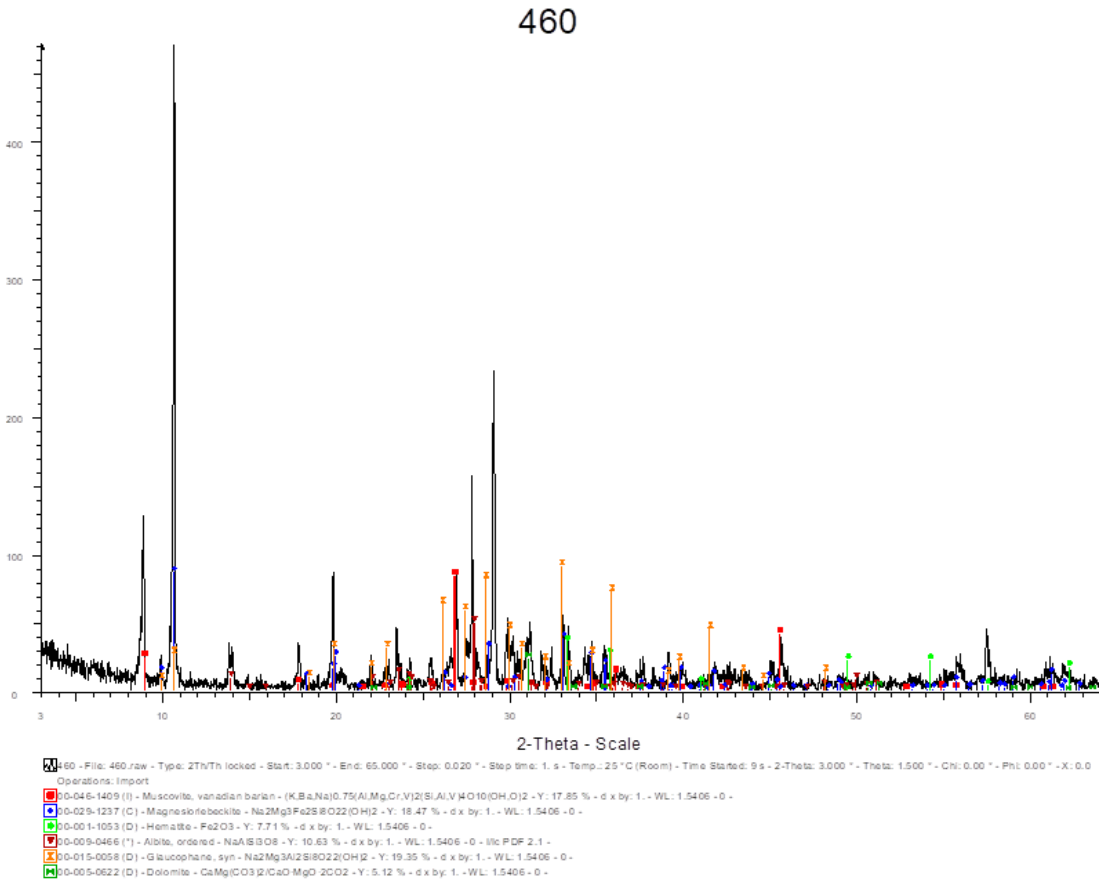

Figure 27: XRD chart 460

Pic Charts of chemical operation analysis from Mainz Microprobe:

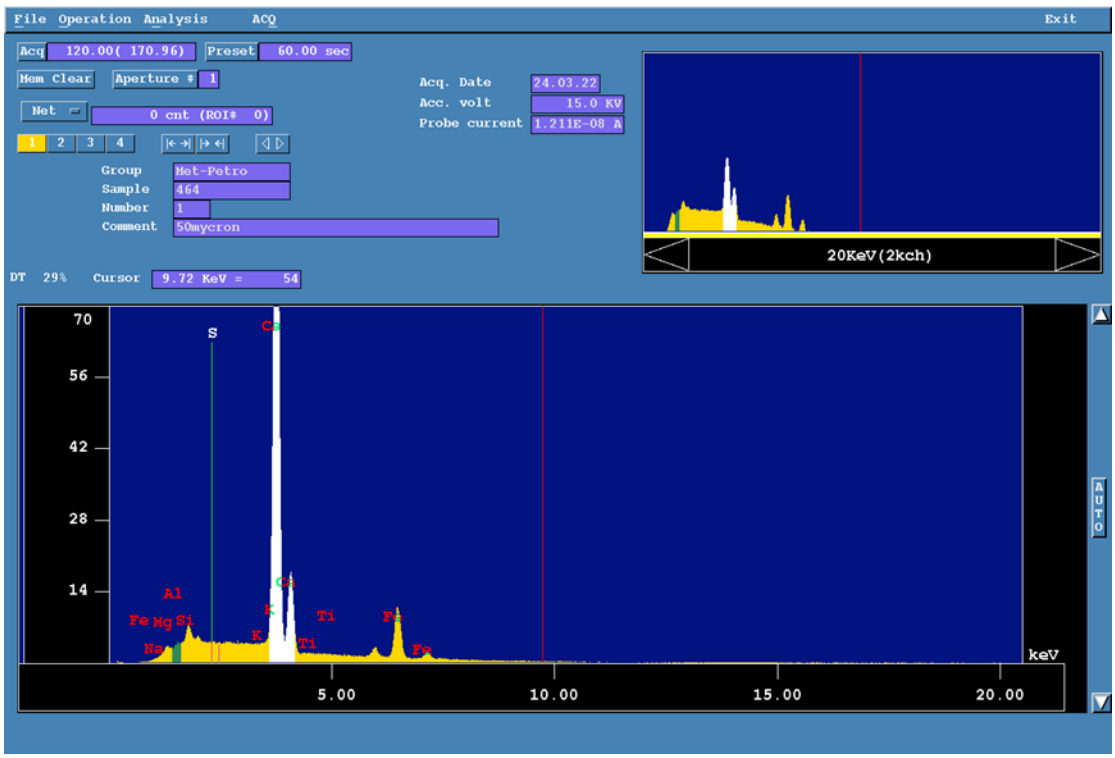

Figure 28: Microprobe chart1 464

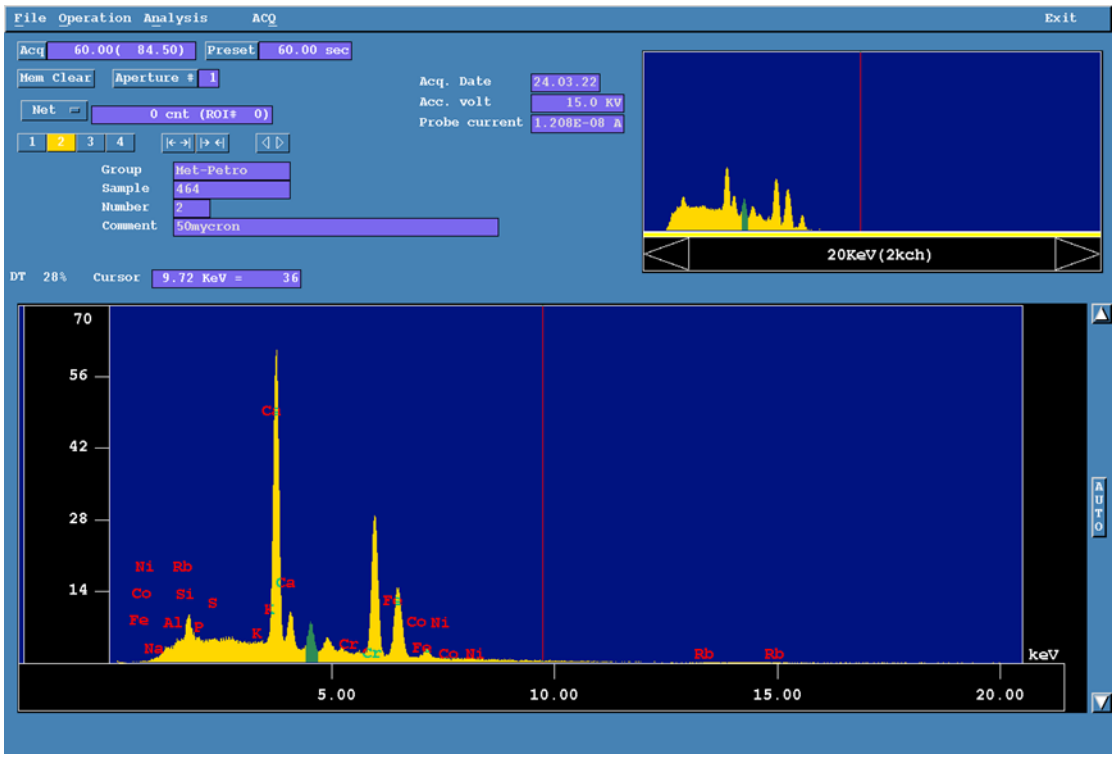

Figure 29: Microprobe chart2 464

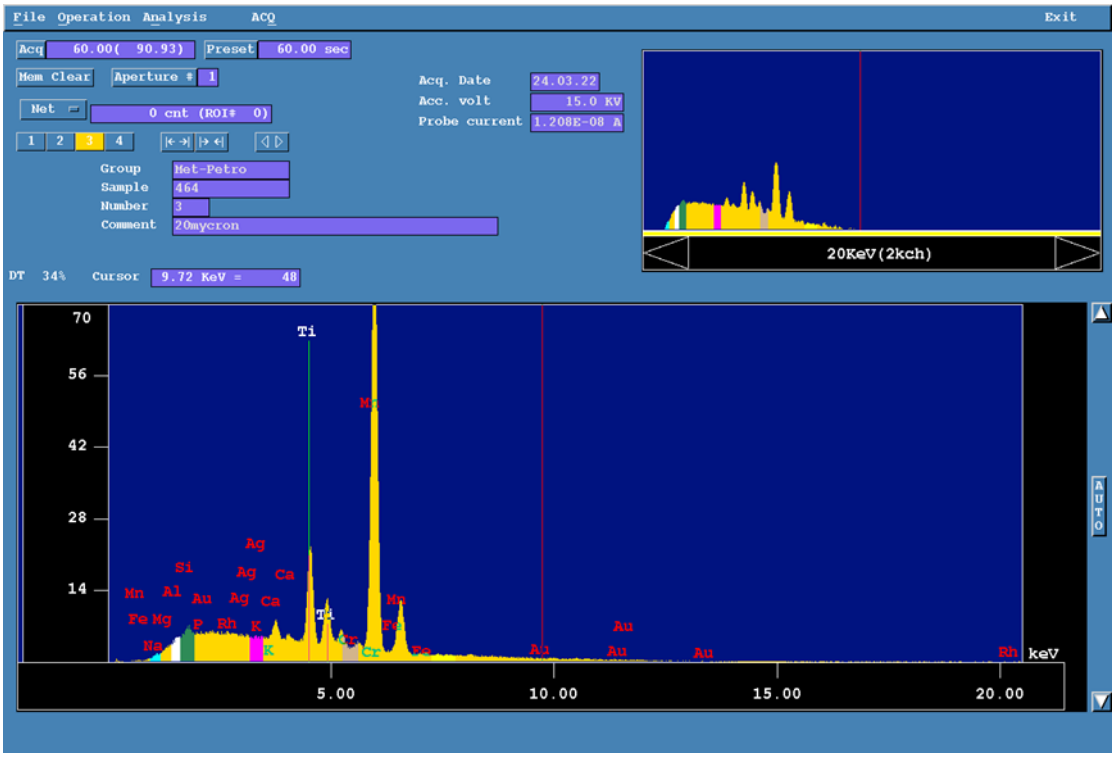

Figure 30: Microprobe chart3 464